Application of Thermally-Sprayed Coatings as Heat Tracers for Carbon Steel Pipes to Mitigate the Effect of Ice Accumulation and Freezing Damage

by

Milad Rezvani Rad

A thesis submitted in partial fulfillment of the requirements for the degree of

Doctor of Philosophy

Department of Mechanical Engineering

University of Alberta

Abstract

Application of Thermally-Sprayed Coatings as Heat Tracers for Carbon Steel Pipes to Mitigate the Effect of Ice Accumulation and Freezing Damage

Milad Rezvani Rad
Doctor of Philosophy
Department of Mechanical Engineering
University of Alberta
2020

The bursting of pipes due to freezing of contained liquid is considerably costly in industrial applications, resulting in over $4 billion in damage over the last decade alone in the United States. The high values of pressure in these circumstances are often so dangerous that the safety of workers may be at risk. Given the detrimental effects of freezing of water in closed systems, further study of this phenomenon is of considerable importance. Considering the consequences of the above-mentioned problem, it seems that more emphasis should be placed on finding a solution to this unwanted phenomenon.

This doctoral research program attempted to study the root cause of the failure of pipes due to freezing and then propose a novel solution to overcome this undesirable occurrence. Furthermore, various aspects regarding fabrication of the coating-based heating system, as the novel heating system for protection of pipelines, were investigated. In this regard, to understand better the failure mechanism of the steel pipes due to internal pressurization and impact of pressure on freezing behavior of water in pipes, several experiments were performed in an 18 m^3 cold room in the first phase of this project. It was found that the freezing temperature of water is greatly dependent on the internal pressure of the pipe, which is itself dependent on pipe material, diameter, and thickness. Then, to mitigate the problems caused by ice formation and accumulation, a novel heating system was developed for usage in pipelines. The flame spraying process was used to deposit the coatings, which possess favorable mechanical and electrical characteristics, onto the carbon steel pipes to heat and melt the ice formed within pipes by the way of Joule heating. The results suggest that the proposed novel heating system can be used on an industrial scale to mitigate the detrimental effects of ice accumulation in steel pipes.

The third phase of this project was focused on developing a mathematical model that can predict the performance of the coating system by estimating the transient temperature of ice, the times that were required to heat and melt ice, and the transient location of the moving solid-liquid interface during the melting process. The results suggest that the mathematical models that were developed based on one-dimensional conduction in cylindrical coordinates can be employed to provide reasonable predictions of coating system performance up to maximum 16% and 9% relative difference between the experimental measurements and model predictions for ice heating and melting stages, respectively.

The final phase of this project was on developing a techno-economic model to assess the feasibility of manufacturing and utilization of the coating-based heating systems. A data-intensive model was developed to compare the technical and economic implications associated with fabrication, installation, operation, and maintenance of multi-layered coatings with those of conventional tracers. It was found that the total cost of fabrication of the coating system was about 7 times that of the tracers due mainly to the labor cost. However, the efficiency of the coating system was about 30% higher than conventional heat tracers. The results suggest that end-users must weigh the improved performance of the coatings against the increased fabrication and installation costs for large-scale protection of pipes against bursting in industrial applications.

Preface

A few of the sections presented in this thesis document have been or will be published in peer reviewed journal revues or conference proceedings as follows:

- Section 1.3 of the work presented in Chapter 1 of this thesis document has been published in peer reviewed journal Paper No. 1 as shown below.
- All sections of the work presented in Chapter 2 of this thesis document have been published in peer reviewed conference Paper No. 6.
- Sections 3.1.2, 3.1.3, 3.1.4, 3.1.5, 3.1.7, 3.2.1, 3.2.2, and 3.2.4 of the work presented in this chapter, especially with regards to the fabrication of coating system on cylindrical samples, have been published in conference proceedings Papers No. 7. In addition, sections 3.1.2, 3.1.3, 3.1.4, 3.1.5, 3.1.6, 3.1.7, 3.2.1, 3.2.2 and 3.2.4 of this chapter, especially with regards to the fabrication of coating system on flat samples, have been published in conference proceedings Papers No. 8. In addition, sections 3.1.1, 3.1.7, and 3.2.3, of this chapter have been published in conference proceedings Papers No. 10. The extended versions of these papers that includes all the sections will be published in peer reviewed journal Paper No. 3 and 4.
- All sections of the work presented in Chapter 4 of this thesis document have been published in peer reviewed journal Paper No. 2.
- Sections 5.1.1, 5.2.1, 5.3.1, and 5.3.4 of the work presented in Chapter 5 of this thesis document have been published in conference proceedings Papers No. 9. The extended version that includes all the sections in this chapter will be published in peer reviewed journal Paper No. 5.

Paper No. 1: D. Tejero-Martin, M. Rezvani Rad, A. McDonald, T. Hussain, “Beyond traditional coatings: A review on thermal-sprayed functional and smart coatings”, J. Thermal Spray Technol., 28, 2019, 598 – 644.

Paper No. 2: M. Rezvani Rad, A. McDonald, “Mathematical simulation of heating and melting of solid ice in a carbon steel pipe coated with a resistive heating system”, Int. J. Heat Mass Transfer, 138, 2019, 923 – 940.

Paper No. 3: M. Rezvani Rad, M. Mohammadian Bajgiran, C. Moreau, A. McDonald, “Fabrication of Thermally Sprayed Coating Systems for Mitigation of Ice Accumulation in Carbon Steel Pipes and Prevention of Pipe Bursting — Part I: Fabrication and characterization”, *Surface and Coatings Technology*, Under Review, 2019.

Paper No. 4: M. Rezvani Rad, M. Mohammadian Bajgiran, C. Moreau, A. McDonald, “Fabrication of Thermally Sprayed Coating Systems for Mitigation of Ice Accumulation in Carbon Steel Pipes and Prevention of Pipe Bursting — Part II: Performance and Analysis”, *Surface and Coatings Technology*, Under Review, 2019.

Paper No. 5: M. Rezvani Rad, K. Ngaokere, S. Lloyd, A. McDonald, “Techno-Economic Assessment of Multi-Layered Coating-Based Resistive Heating Systems and Conventional Heat Tracers for Industry Pipes”, *Cold Regions Science and Technology*, Under Review, 2019.

Paper No. 6: M. Rezvani Rad, R. Marsden, A. McDonald, “Testing and analysis of freezing phenomenon in conventional carbon steel pipes”, in: Proceedings of the Canadian Society for Mechanical Engineering International Congress 2018, May 27-30, 2018 (Toronto, ON, Canada), The Canadian Society for Mechanical Engineering, (2018), 6 pages on compact disk.

Paper No. 7: M. Rezvani Rad, A. McDonald, “Development of a flame-sprayed coating system to mitigate ice accumulation and freezing damage in carbon steel pipes”, in:

International Thermal Spray Conference, May 7-10, 2018 (Orlando, FL, USA), ASM International, (2018), #44600, 6 pages on compact disk.

Paper No. 8: M. Rezvani Rad, M. Mohammadian Bajgiran, C. Moreau, A. McDonald, "Microstructural and performance analyses of thermal-sprayed electric resistance heating systems deposited onto steel pipes as de-icing elements", in: International Thermal Spray Conference, May 26-29, 2019 (Yokohama, Japan), ASM International, (2019), # 47189, 6 pages on compact disk.

Paper No. 9: M. Rezvani Rad, K. Ngaokere, D. Hayden, A. Kumar, A. McDonald, "Techno economic assessment of coating-based resistive heating systems versus conventional heat tracers", in: International Thermal Spray Conference, May 26-29, 2019 (Yokohama, Japan), ASM International, (2019), # 47224, 6 pages on compact disk.

Paper No. 10: Morvarid Mohammadian Bajgiran, Milad Rezvani Rad, André McDonald, Christian Moreau, "On Reliability of Thermally-Sprayed Alumina Dielectric Layers in a Multi-layered Coating-based Heating System", in: Proceedings of the Joint Canadian Society for Mechanical Engineering and CFD Society of Canada International Congress 2019, June 2-5, 2019 (London, ON, Canada), The Canadian Society for Mechanical Engineering, (2019), 8 pages on compact disk.

All the authors contributed to the preparation of the listed papers. I conducted the research work under the guidance of Dr. André McDonald and Dr. Christian Moreau in their roles as research supervisors. I collaborated with Ms. Morvarid Mohammadian-Bajgiran on producing several conference papers and Journal papers. Other collaboration with Mr. Kingsley Ngaokere also resulted in publication of a conference and a journal article. I benefited from valuable guidance and advice of Professor S. Lloyd in preparation of the journal article. I also collaborated with Mr. Daniel Tejero-Martin and Professor T. Hussain on writing a review article on the thermal-sprayed functional and smart coatings.

Acknowledgments

First and foremost, I wish to express my sincerest gratitude to my supervisors, Prof. A. McDonald and Prof. C. Moreau for their guidance, continuous support and excellent supervision throughout the course of my doctoral program. Completion of this research program would have been impossible without their support, hard work, and encouragement. I would like to thank the members of my doctoral supervisory committee, Prof. B. Jar and Prof. C. Ayranci for their time, valuable advice, and suggestions. I am also thankful to the members of the examining committee, Prof. A. Agarwal and Prof. M. Sadrzadeh for their valuable time.

I would like to thank technical support from the machine shop technicians. In particular, I am thankful to Mr. D. Mooney for his assistance in assembly of some of the experimental equipment needed for my doctoral program. I am also very thankful to Mr. R. Conrad for his invaluable advice and guidance regarding electrical assembly of my coating systems. I am also very grateful to Mr. R. Marsden for his continuous technical support and valuable advice.

Last, but certainly not the least, I would like to thank my parents, Mr. A. Rezvani-Rad and Ms. S. Jafari-Azad, and my brother, Mr. M. Rezvani-Rad, for their encouragement and support for my studies towards graduate degree and all accomplishments that I have made.

Table of Contents

Table of Contents

List of Tables

List of Figures

Chapter 1

Introduction

1.1 Background

1.1.1 Failure of Pipes Due to Ice Accumulation

Formation and accumulation of ice inside closed piping systems are pervasive phenomena in both residential and industrial sectors where the pipes are exposed to temperatures below the freezing point of the enclosed water. The pressurization of the liquid phase inside the pipe due to the freezing of the liquid water that is followed by bulging and rupture of the steel pipes. It is known that the failure occurs at the location where unfrozen water is entrapped between plugs of ice [1]. Failure of piping systems due to internal pressurization is not only restricted to the metallic pipes and can also be observed in plastic piping systems as well [2].

It is well-established that the detrimental effects of such undesired phenomenon are perilous and costly, especially in the industry due to the significant non-productive downtime and production loss. The financial losses due to the damages that stemmed from the frozen pipes were estimated to be $450 million/year during the 1985 to 1995 period only in the United States [3]. Based on an investigation conducted by the Insurance Information Institute (I.I.I.) [4], one of the main problems that occur during winter is freezing of enclosed liquid in pipes. The financial losses caused by ice, freezing, and related issues averaged $1.2 billion annually only in the United States over the last 20 years [4]. The detrimental effects of frozen pipes are not only limited to financial losses. Due to the tremendous pressure and energy that is stored inside the closed pressure vessels and piping systems, bursting of the pressurized pipes sometimes result in explosive ruptures that can pose a threat to the well-being of the workers in the field and endanger their safety. Given the prevalence, severity, and financial losses associated with the formation and accumulation of ice in closed piping systems, it stands to reason that a great emphasis should be placed on finding a practical solution.

Installing insulation material around the pipes is the most widespread and cost-efficient strategy to decrease the wind chill effect and the rate of heat loss. It also increases the total time required for cooling and freezing of water within the pipes and reduces the extent of losses associated with burst pipes [5]. However, this solution is a suitable burst protection strategy when the pipes are exposed to frigid environments for periods of limited duration [5]. Therefore, it stands to reason that an efficient heating system must be accompanied by suitable insulation to protect the piping systems properly against prolonged exposures to frigid environments.

1.2 Utilization of Heating Systems

Electric heat tracing has been suggested as an efficient means for temperature control of water distribution pipes and protection against freezing where process steam and waste heat are not available [6]. Furthermore, heat tracers are widely used for pipelines that carry high viscosity fluids where temperature protection is required. The provision of clean heat sources, compared to the low-pressure steam, on a large scale for both industrial and residential applications is another advantage of the electric heat tracing method [7]. Electric tracing systems also have the advantage of precise temperature control and economic, environmental, and safety benefits when compared to steam-based heat tracing [8]. Furthermore, utilization of electric resistance heating systems is not only limited to pipelines; they have been used successfully in other areas such as power-line de-icing [9], cementitious composites for removal of snow from the surface of transportation infrastructures [10], carbon fiber resistance heating for mitigation of ice accumulation on road surfaces [11], and anti-icing and de-icing of wind turbines [12].

It is well-established that the power supplied to electric tracing systems can be adjusted by controlling the input voltage. Therefore, the performance of the heating system can be modified based on the environmental conditions and the required working conditions in the field at any specific moment. In this regard, a controller can be employed to adjust the output of the electric heating systems and make the heating system adaptable to environmental conditions [13]. Not only does the application of a controlling system improve the efficiency of the electric heating system for temperature protection of the lines, but it also reduces energy consumption. The wide range of power that can be supplied by self-regulating heat tracers that start from 4 Watt per foot (W/ft) up to 30 W/ft at 10°C at operating voltages from 24 VAC up to 750 VDC is another advantage of electric heating systems [14].

Other alternative electric resistive heating systems that are not based on conventional heat tracers for pipelines haves been proposed recently. These include use of multi-layered thermally sprayed coatings. Utilization of thermal-sprayed coatings has already been investigated extensively for various heating applications, substrate geometries and materials, and temperature ranges [15 - 20].

1.3 Fabrication and Utilization of Coating-Based Resistive Heating Systems

Thermal spraying has been present for over a century, being greatly refined and optimized during this time, becoming nowadays a reliable and cost-efficient method to deposit thick coatings with a wide variety of feedstock materials and substrates. Thermal sprayed coatings have been successfully applied in fields such as aerospace or electricity production, becoming an essential component of today's industry. The usage of thermal-sprayed coatings as electric resistance heating systems has received increasing attention in recent years. However, the application of thermal-sprayed coatings in electronics was proposed around five decades ago when planar ferrite microwave integrated circuits (MIC's) were successfully fabricated by using arc-plasma spraying (APS) process [21]. Smyth and Anderson [22] studied the effect of spraying parameters on the physical and electrical properties of the produced film resistors. It was shown that APS process can be used as an alternative method for producing electrical components and circuit. It was found that a film with sheet resistivity from 5-500 Ω/sq could be obtained by using a mixture of NiO and Fe_3O_4 powders with a particle size range of 1 – 20 μm and that APS can be used for cheap quantity production of resistors and conductors with satisfactory long-term stability [22].

Sampath, *et al.* [23], investigated the application of thermal spray techniques in fabrication of meso-electronics. It was found that multilayer deposits of ceramics and metals that have appropriate electrical properties can be produced by thermal spray methods to fabricate electrical components ranging from insulators, conductors, and resistors. Fabrication of resistor was conducted by deposition of NiCr alloy over alumina by plasma or HVOF processes. The sheet resistance of the fabricated resistor was reported to be in the range of 17-54 KΩ/sq. Low cost, high production rate, flexibility of use of thermal spray process, and capability of producing millimeter-thick layers of conductors and insulators made this process an alternative for fabrication of components for power electronics [23]. Similarly, deposition of ceramic feedstock particles by using HVOF process that is accompanied by oxygen-rich flames and the use of cold spray process have been found to be appropriate methods in synthesis of high-quality dielectrics and conductors, respectively [24].

In an early effort [25], air plasma spraying process was used to fabricate the resistance heaters. The metal film heater (molybdenum), which was isolated from the faceplate by a plasma-sprayed ceramic film, was able to generate heat fluxes up to 7.2 MW/m^2 over an area of 10.3 cm^2 [25]. Therefore, it was shown that thermal-sprayed coatings can be used as heating systems. Given the direct deposition of the films atop the test surface, as opposed to mechanically attaching the heater to the surface, the thermal contact resistance between the thermal-sprayed heating element and the substrate is minimized [26]. This results in fabrication of more efficient heating elements. The structure of the heating system depends on the electrical resistance of the metallic alloy that is required to be achieved, the substrate material and its electrical conductivity. Owing to the high thickness required to achieve the appropriate electrical resistance, thermal spraying techniques are preferred over vapor deposition for fabrication of the coating-based heating elements [26]. It is well-established that for the cases in which the substrate is electrically conductive, an intermediary ceramic layer, which possesses dielectric properties, is required to prevent short circuiting and leakage current in the heating system. Therefore, it is required to develop a multi-layered coating system that consists of the two main elements, namely the heating element that is usually a metallic alloy and an electrically insulating ceramic layer.

1.3.1 Deposition of ceramic coating as an electrically insulating layer

Alumina is widely used as an electrical insulator due to the dielectric properties that this material possesses. Given the rapid and simple coating of large surfaces by using plasma spraying process, deposition of electrically insulating coatings have been an appealing option in electronics industry. It has been shown that the volume resistivity of plasma-sprayed alumina coating can be very high within the range of 10^9 - 10^{10} Ω cm [27]. It has been reported in the literature that the electrical resistivity of alumina depends on several parameters including applied pressure, humidity, microstructural characteristics, and phase composition of alumina [28 – 32].

Lue *et al.* [28] demonstrated that the surface resistivity of alumina coating decreases by applying pressure on it, but it still was larger than 10^6 Ω cm when it was compressed at pressures up to 250 MPa. High humidity levels also affect resistivity of the alumina coating [29 – 31]. In a study by Toma *et al.* [29] a dramatic decrease about five orders of magnitude in the resistivity of alumina coating was observed when the relative humidity level was increased to 95%. The deterioration of the insulating properties of alumina coating with increasing humidity was explained by increase in the surface conductance of the oxide layer because of absorption and accumulation of water molecules on the coating surface [30].

Furthermore, the different microstructural features of the coatings due to use of different thermal spray processes affect the electrical resistivity of alumina layer. It was found that the electrical resistivity of the alumina coating that was obtained from HVOF process was slightly better than the one that was fabricated by APS process, which was likely due to the lower open porosity and presence of defects [29]. Furthermore, it was shown that the alumina that is sprayed by suspension HVOF (SHVOF) has better electrical resistance stability than the alumina coating deposited by the conventional HVOF process due to the retention of higher content of α-alumina [31].

The phase transformation of alumina is also another well-known, but neglected factor that can negatively affect the electrical properties of the thermally sprayed alumina coatings. The deterioration of electrical properties of alumina is due to the phase change from α-alumina (corundum) to γ-alumina, which is a metastable phase with undesired properties [31, 32]. The phase change is attributed to the rapid cooling of the molten alumina particles below the temperature at which the atomic rearrangement can occur before the stable phase of corundum is reached [33]. It was found by McPherson [34] that the metastable form is retained during cooling of particles that are less than 10 μm diameter due to higher cooling rates and the particles larger than that may transform to α-Al_2O_3 during the solidification.

It has been shown that plasma-sprayed deposits of cordierite ($2MgO$-$2Al_2O_3$-$5SiO_2$) can also be used as the electrically insulating layers due to the high electrical resistivity and chemical durability of this material [35, 36]. Alumina-titania coatings are other alternatives that can be used as electrically insulating layers. In addition to the dielectric properties, they benefit from enhanced toughness, which increase their performance durability [37]. However, the electrical resistivity of the alumina-titania coatings is partially compromised. As an example, it was observed by Golnka and Pawlowski [38] that the surface resistivity of arc plasma sprayed alumina was 10^9 Ω cm, but that of alumina-2wt. % titania was 10^7 Ω cm.

The main challenge associated with the coating-based insulators is the dielectric breakdown mechanism of the coating, which is indicative of the failure of the electrically insulating layer, and is caused by electrical discharge when high local fields are produced. This leads to physical degradation of the ceramic layer by formation of a complete failure path. It has been found that voltage at which the breakdown of the APS-sprayed Al_2O_3-13% TiO_2 coating, which is one of the compositions of alumina-titania systems that is widely used as an electrical insulator, occurs is linearly related to the thickness of the coating. In this respect, the average dielectric strength of the coating was measured to be 20 kV/mm [39].

It was observed by Killinger *et al*. [40] that the two most important factors regarding the electrically insulating layer are breakthrough voltage and leakage current, which depended heavily on the internal morphology of the coating that was related to the thermal spraying process that was used for deposition of the coating. The difference in the breakdown voltage versus coating thickness of the alumina coating that was deposited with HVOF and APS process can be seen in Fig. 1-1(a). The pin hole that was produced by the voltage breakdown mechanism is also shown in Fig. 1-1(b).

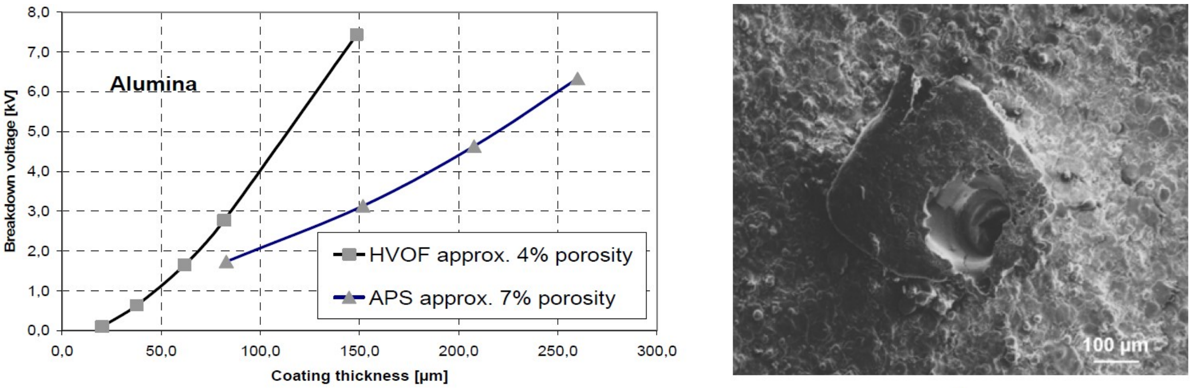

a b

Figure 1-1 (a) Breakdown voltage of alumina as a function of coating thickness and (b) Pin hole formed due to high voltage breakdown [40]

1.3.2 Deposition of the metallic alloy coating as the heating element

A material that is electrically conductive and has high electrical resistivity is required to be deposited onto the intermediary ceramic layer with dielectric properties to fabricate the heating element. Deposition of several different thermal-sprayed metal alloys, namely Molybdenum (Mo), nickel (Ni), nickel-20 wt.% chromium (Ni-20Cr), nickel-5 wt.% aluminium (Ni-5Al), iron-13 wt.% chromium (Fe-13Cr), and Iron-chromium-aluminium (FeCrAl), by using various thermal spraying processes including APS, VPS, HVOF, wire arc, combustion spray, and wire flame spray, has been reported in the literature for usage as the heating elements [25, 26, 40 – 45].

Michels, *et al*. [26], used three thermal spray techniques, namely air plasma spray (APS), vacuum plasma spray (VPS), and high-velocity oxygen fuel (HVOF), to produce resistance heating elements that can generate uniform and easily controlled flux. It was found that HVOF and VPS processes compared to the APS could manufacture consistent coatings with physical properties that are close to the bulk materials. In this study, a metallic layer (nickel-chromium alloy Ni80-Cr20), which served as the heating element, was deposited onto a ceramic layer (alumina) that served as the electrically insulating layer. The layers had a thickness in the range of 75 to 300 µm. The configuration of the studied resistive heating system is shown in Fig. 1-2.

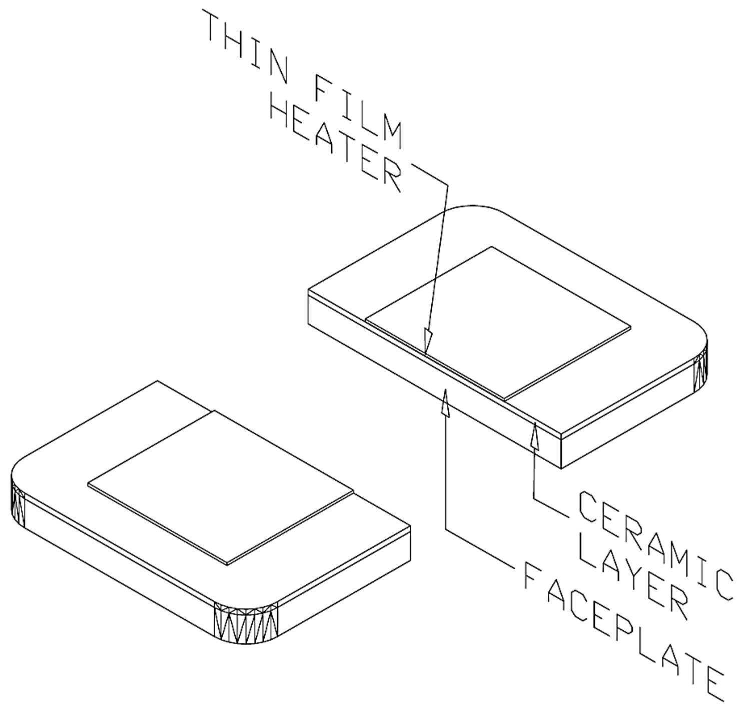

Figure 1-2 Configuration of heater and insulator films [26]

It was found that the thickness of alumina that was required to isolate the heating element from the substrate was around 100 µm for HVOF, but 200 µm for APS [26]. Furthermore, the highest fluxes that could be generated from the fabricated heating system before failure was as high as 10.6 MW/m^2 and 17.2 MW/m^2 for HVOF and VPS films, respectively. The heaters failed at very high level electrical currents. It was found that the failure mode of the thermal-sprayed heating system was delamination of the Ni-Cr layer from the insulating ceramic layer. Therefore, the evolved thermal stresses between the deposited ceramic and metallic films due to the mismatch between the thermal expansion coefficients were suggested as the root cause of the failures [26].

Tong, *et al.* [41] investigated fabrication of microheaters by micromachining thermal-sprayed 80Ni-20Cr coatings. In this study, thermal spray, as an additive manufacturing process, was combined with micromachining, as a subtractive manufacturing process, to produce functional microheaters. This technique shows considerable potential in fabricating small scale embedded functional parts within thermal-sprayed coatings. In this study, both combustion and plasma thermal spray techniques were used to deposit the NiCr coating with thickness in the range of 25 to 75 μm on alumina substrate. Ultrafast laser direct-wire technique was used to fabricate patterns based on which uniform heat flux can be produced. Several different patterns for fabrication of the micro heaters are shown in Fig. 1-3.

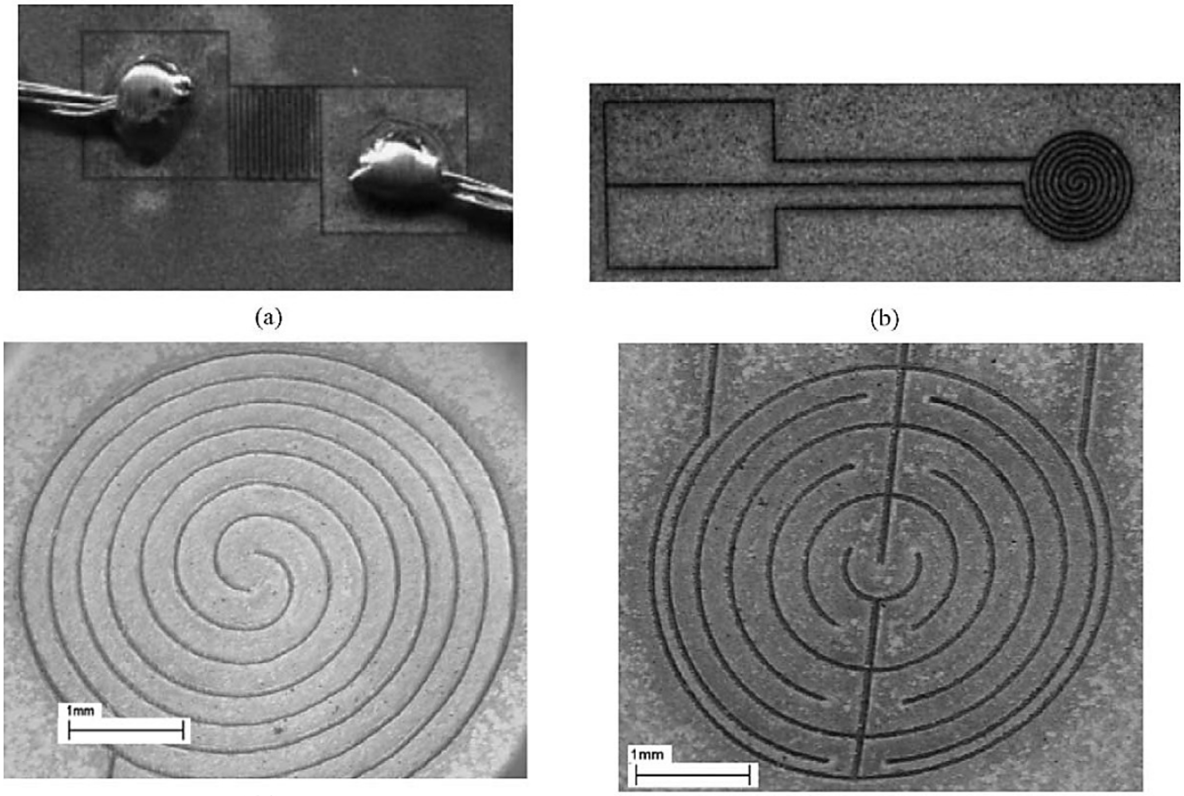

(a) (b) (c) (d)

Figure 1-3 Microheater designs: (a) square-meander, (b) circular-spiral, (c) SEM image of circular-spiral, and (d) SEM image of concentric-circle patterns [41]

In this study, cracking and mechanical failure of alumina substrate was observed when the temperature of the heater was increased to 450-500 °C. Therefore, the failure was attributed to the thermal stresses caused by coefficient of thermal expansion mismatch in the multi-layered sample. It was concluded that the bimorph beam bending model can be used to explain the failure caused by thermally induced stresses at elevated temperatures [41].

Killinger *et al.* [40] studied the electrical properties of both essential components of the heating systems, namely the insulator and the film heater. The nickel-chromium (Ni20Cr) coating was deposited onto the alumina coating by plasma spraying process and using spraying mask technique to form the metal-ceramic multilayer composite that is required for fabrication of the heating devices. The layout of the developed heater and the micrographs taken from the cross-section of the coated samples are shown in Fig. 1-4 and Fig. 1-5, respectively.

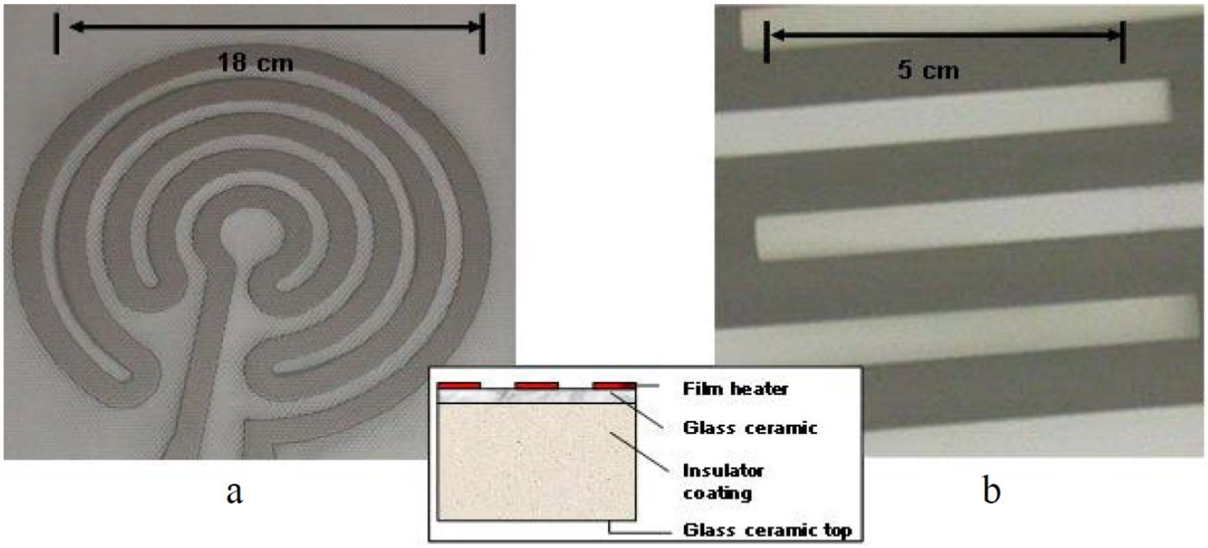

Figure 1-4 Examples of film heater layouts [40]

Figure 1-5 shows the microstructure of the deposited multi-layered coating that was deposited onto both glass ceramic and steel substrates. The thickness of the alumina and NiCr coatings were measure to be 200 and 30-50 µm, respectively. It was found that the tensile residual stresses reach very high values at the surface of the NiCr coating and deposition of thicker coatings (more than 50 µm) would lead to delamination of the metal film [40].

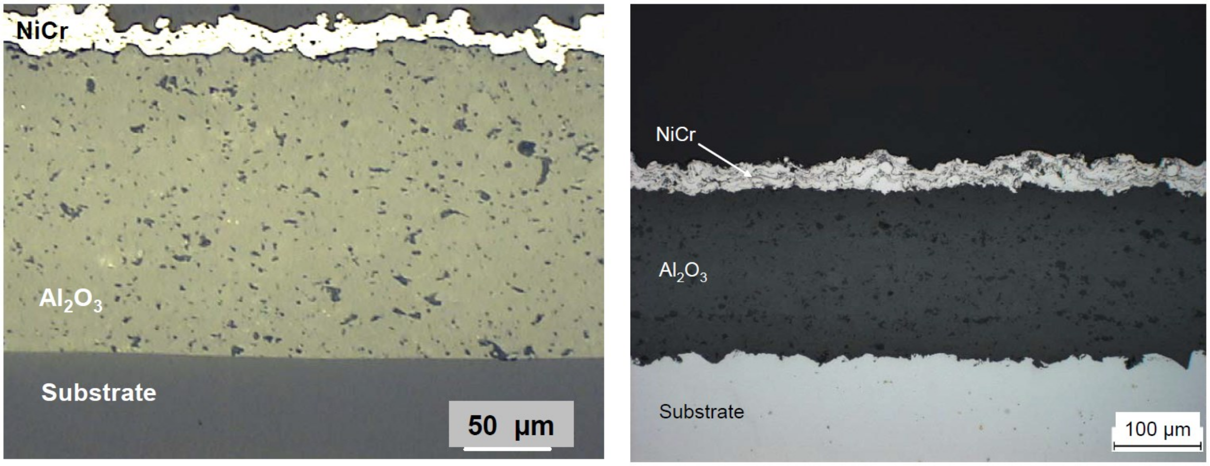

Figure 1-5 Micrographs taken from the plasma-sprayed metal-ceramic multilayer composites. Ni20Cr/Al_2O_3 on (a) glass ceramic and (b) stainless steel substrates [40]

Prudenziati *et al*. [42], developed self-regulated heaters by air plasma spraying process that could operate reliably at temperatures up to 600°C over long periods of time. In this study, the heaters were designed for both planar and cylindrical geometries. Engraved metal masks were used to fabricate the heating elements (Ni, Ni-20Cr, and Ni-5Al) in the shape of meanders as shown in Fig. 1-6.

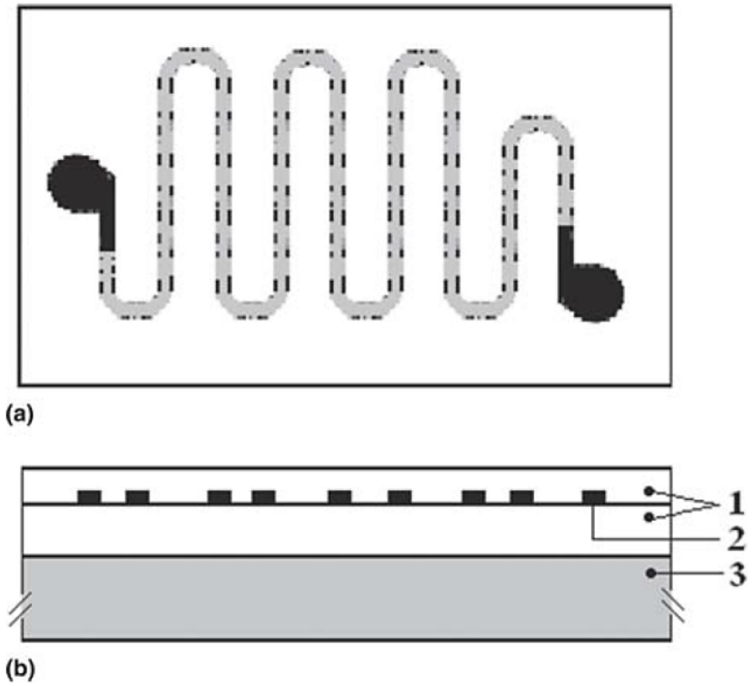

Figure 1-6 Schematic of the heating plate that consists (1) alumina coatings, (2) heating meander, and (3) metal coupon (substrate) from (a) top view and (b) cross-sectional view [42]

Two fabricated heating elements, heating plate and a runner nozzle for a polymer injection moulding apparatus, are shown in Fig. 1-7. Due to the dependence of the heating element electrical resistance on temperature, it was claimed that the metallic heating element could also be used as a smart sensor for direct reading of the heater temperature. Therefore, there would be no need to install a separate temperature sensor. Based on the claimed wide operation temperature range (20-600 °C) and the industrial reliability of the fabricated coating systems, it was concluded that the developed self-regulated heating platforms can be used for applications in the field of high-temperature operating sensors [42].

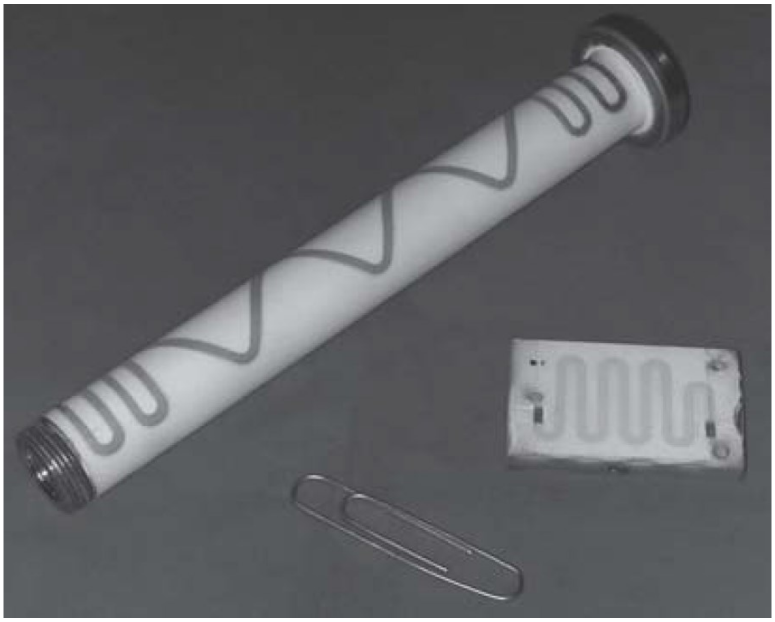

Figure 1-7 Cylindrical and Planar heaters developed by air plasma spray (APS) process [42]

In another study by the same author [43], the failure of the heating element and the insulating layer was investigated. It was found more serious failure modes were associated with use of NiCr- and NiAl-based heating elements than Ni-based ones. Electrical properties of both thermal-sprayed Ni and Ni20Cr heating elements and the correlation between the microstructure of the coating and the electrical properties of the metal alloys that were deposited by atmospheric plasma spray (APS) and HVOF processes were investigated by Prudenziati and Gualtiei [44]. It was observed that use of fine powders, oxygen-rich atmosphere in the plume, and high temperature flames of APS and HVOF lead to preferential oxidization of Cr and formation of oxide phases (mainly chromite $NiCr_2O_4$ and NiO) that are high resistive materials. The Ni/Cr ratio in the oxidized regions was found to be lower than the value in the surrounding matrix. This indicates that oxidation results in enrichment of Cr in the oxidized areas, which leads to depletion of Cr and enrichment of Ni in the surrounding areas resulting in composition change from 80Ni20Cr to xNiyCr with $x/y > 4$. This forces the electrical transport in the surrounding metal matrix with higher Ni/Cr ratio resulting in higher temperature coefficient of resistance (TCR) values. Furthermore, it was found that the TCR of NiCr that was deposited by APS was considerably less than the HVOF-sprayed NiCr [44].

Lamarre *et al.* [45] developed a multi-layered thermal-sprayed cylindrical resistive heater. In this study, alumina dielectric insulator with a thickness of 250-300 µm was deposited onto metallic substrates by plasma spray process. Then, a wire flame-sprayed iron-based alloy (FeCrAl) resistive element with thickness in the range of 75-100 µm was deposited onto the alumina coating with a specific pattern that is shown in Fig. 1-8 by masking technique. The performance and the microstructure of the heating system were analyzed after energizing and maintaining the cylindrical heater at a constant temperature of 425°C for up to four months.

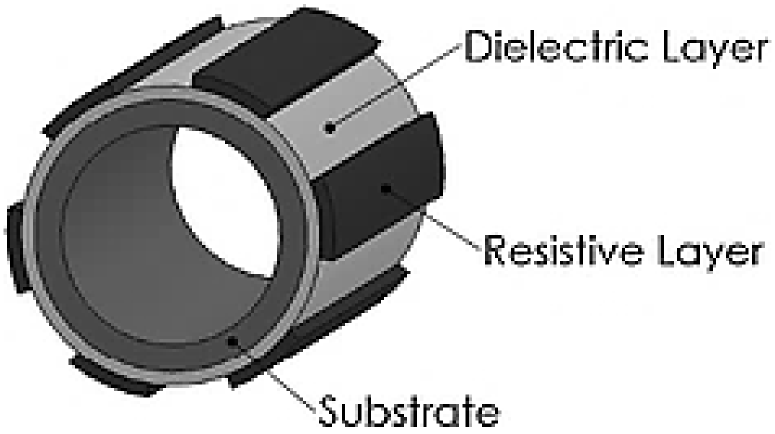

Figure 1-8 Schematic of a portion of the cylindrical resistive heating system (not to scale) [45]

A localized high-stress zone was observed at the intersection point of FeCrAl, alumina, and ambient air, which is highly due to the discontinuity of the applied force on the surface of the alumina coating. Formation of cracks in the alumina layer, which is of great importance in deterioration of alumina layer and failure of the insulator can lead to short circuiting between the conductive substrate and the heating element, can be observed in Fig. 1-9. Based on the results obtained from the simulation model, it was concluded that reducing the thickness of alumina can decrease the maximum stress, but it increases the average stress in alumina layer.

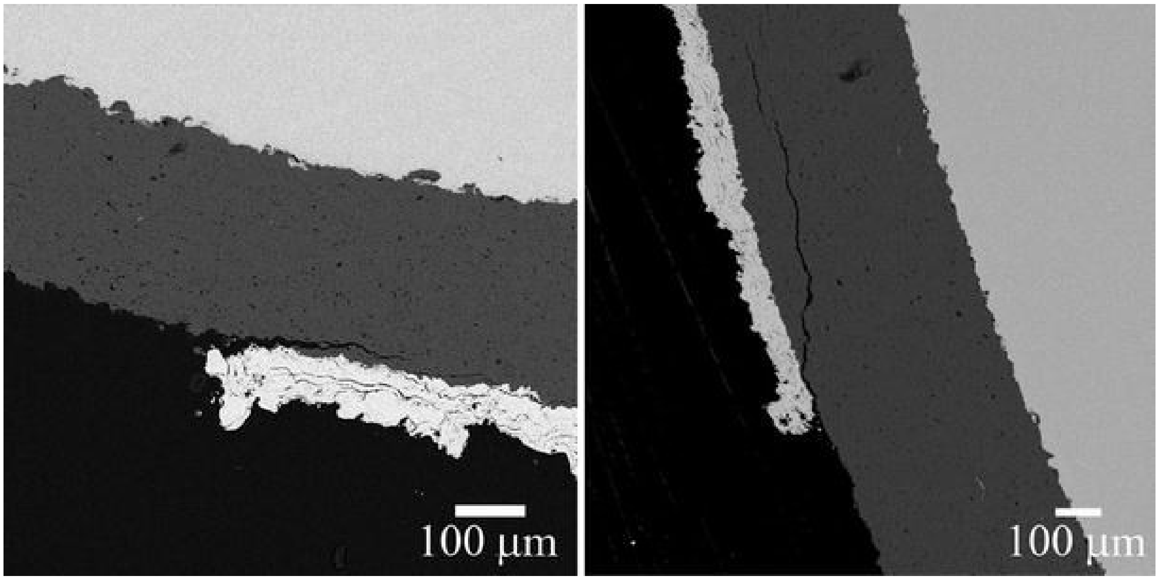

Figure 1-9 Cross-sectional SEM images taken from the multi-layered heating sample showing formation of cracks at the intersection point after conducting the thermal tests [45]

Flamed-sprayed coatings as novel heating elements with the potential impact of eliminating the formation of ice on wind turbine blades were proposed by Lopera-Valle and McDonald [46, 47]. It was found that flame spraying process could be used to deposit both coating-based heating elements, namely nickel-chromium-aluminum-yttrium (NiCrAlY) and nickel-chromium (NiCr) coatings, on top of the fibre-reinforced polymer composite (FRPC) substrate successfully without any damage to the substrate. In order to prevent damage to the fibres of the composite substrate due to the deposition of high-temperature molten powder particles, a layer of garnet sand was used as an intermediary layer between the FRPC and the metal alloy coating. Furthermore, the garnet sand layer that was formed by sparkling garnet on top of the last layer of epoxy prior to the curing process was also used as the roughening agent. It was found that the use of the garnet sand layer was beneficial for both deposition of the flame-sprayed coatings and also protecting the substrate against thermal damages due during the flame spraying deposition process. The NiCrAlY and Ni-20Cr coatings that were fabricated in this research were as thin as 80 ± 15 µm (*n* = 20) and 100 ± 15 µm (*n* = 20), respectively. The SEM images that were taken from the cross-section of the coated FRPC sample are shown in Figs. 1-10(a) and 1-10(b).

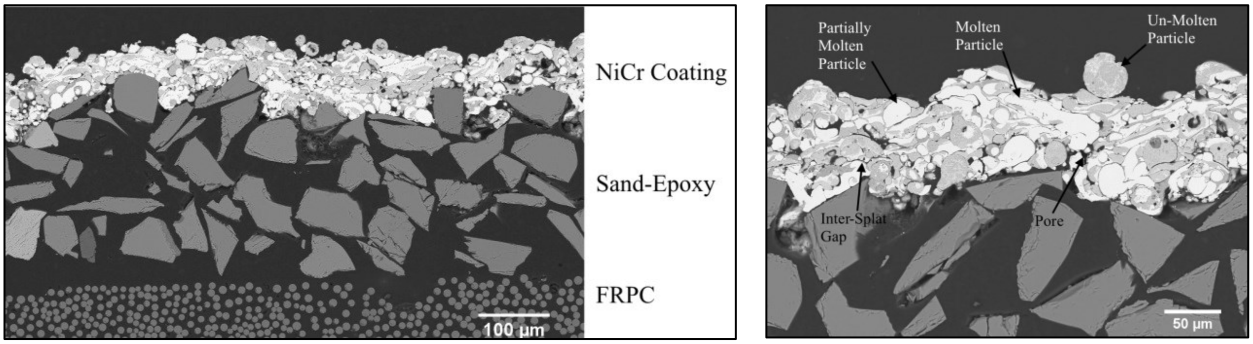

(a) (b)

Figure 1-10 (a) Low- and (b) high-magnification SEM images taken from the cross-section of the coated FRPC [46]

It was observed that with a supplied power as low as 2.5 W over 3 V the temperature of the FRPC sample was 15°C above the ambient temperature when no air was flowing over the sample [46]. In addition, application of the efficient coating-based heating element was successful in increasing temperature of the FRPC sample under forced convective conditions. In another study by the same authors [47], it was shown that the embedded coating-based de-icing element was also able to melt the ice that was formed on top of the coated polymer-based composite while the sample was exposed to forced convection conditions.

1.4 Development of Mathematical Models for Phase Change of Water/Ice

The modeling of the phase change of the materials has been the subject of extensive research studies. In an early study by Poots [48], approximate integral methods were used to determine the transient location of solid-liquid interface during the unidimensional solidification of liquids that were initially at the fusion temperature. Due to the non-linearity of the interface energy equation, obtaining the temperature distribution by using the analytical solutions was very difficult. To overcome this challenge, use of computer-aided numerical solutions and mathematical techniques such as variational technique, the heat-balance integral technique, and the Riemann-Mellin contour integral technique were suggested as outlined in a review by Muehlbauer and Sunderland [49]. Determination of the time required for solidification of food-based materials was studied by Pham [50]. In this study, Planck's equation was extended to include the sensible heat effects for predicting the freezing times of foodstuffs of simple shapes. Cleland *et al.* [51] used finite element method to predict the duration of phase change time in solids of arbitrary geometry. The flexibility of the method allowed for prediction of rates of freezing or thawing for wide variety of geometries and external heat transfer conditions [51].

Mathematical modelling of phase change problems has also been conducted in previous studies [47, 52, 53]. It has been found that the models that were developed based on one-dimensional transient conduction theory for finite length-scale media were able to estimate the duration of the phase change of water/ice to within 15% of that which was observed in experiments. In one study, Yan, *et al.* [54] developed a model that was based on the quasi-steady-state approximation to investigate the thermal characteristics of phase change material enclosed in a pipe in both freezing and melting processes. It was concluded that the quasi-steady-state model was highly efficient and reliable in determining the transient temperature of the water during the phase change process.

Other mathematical models that pertain to formation of ice have been developed to determine the transient thickness of ice [55 - 58]. As an example, a one-dimensional model for ice accretion that was caused by in-flight supercooled droplets impacting on a thin substrate was developed by Brakel, *et al.* [55]. The model was based on heat equations that were reduced to pseudo-steady forms. It was found that the results of this model were in good agreement with those that were obtained by a numerical scheme that solved the full Stefan problem. In addition, a one-dimensional mixed ice accretion model was developed by Janjua, *et al.* [56], which was capable of predicting the composition of the overall ice structure and transient ice thickness for the case of formation of rime ice and glaze ice on aircraft wings. Furthermore, Zhang, *et al.* [57] developed an improved one-dimensional model to describe the aircraft icing process. In this model, the ice property variability and runback water were also taken into account. The icing process was also investigated based on theories of phase change and film flow theories by Yanxia, *et al.* [58]. In this study, the growth of ice was determined by coupling the solid/liquid phase change with runback water flow. It was found that consideration of the flow of runback water on the icing surface accelerated the phase change process and ice growth rate.

1.5 Techno-Economic Assessment of Thermal-Sprayed Coating Systems

The initial monetary investment and the long-term expenses including the maintenance and electricity consumption of the systems should be determined to assess the feasibility and the economic benefit of utilization of the newly developed coating-based heating system in the industry for protection of pipelines against freezing of the enclosed liquid and the following failure. Furthermore, the technical performance of both heating systems should also be evaluated and be taken into consideration. In this regard, conducting a techno-economic analysis (TEA) that is composed of both technical and life-cycle cost analyses could be very informative and helpful as it may be characterized as a systematic tool, which is utilized to analyze the economic viability, opportunities, and negative economic effects of manufacturing processes, by accounting for the overall variable, capital, and fixed costs [59]. TEAs have played an integral part in determining which materials provide the greatest economic incentives for a particular product or process [60].

A concurrent issue in conducting a life-cycle cost analysis (LCCA) is the challenge of managing uncertainty in the assessment of emerging technologies. Therefore, selecting the appropriate uncertainty assessment technique depending on the various nature, location and level of uncertainty is important to guarantee effective decision-making [61]. A few assessment techniques include sensitivity analysis, scenario analysis, and Monte Carlo analysis. Sensitivity analysis determines how dependent variables are impacted by changes in the input variables of a model. Scenario analysis is a process of examining and evaluating possible future events by considering various feasible results or outcomes. Monte Carlo analysis evaluates the impact probability distributions based on input independent variable uncertainties [61].

The LCCA consists of two stages. In the first stage, the reason and the purpose of a LCCA are indicated, and the system boundaries and the functional unit are defined [62]. The functional unit is the unit that can be quantitatively calculated to represent the function provided by a product or a service. The second stage is to locate and quantify the inputs and outputs within the system boundaries [62]. Once the technological aspects are coupled with the cost metrics of the developed economic model based on the defined functional unit, a scalable view of the technical and economic implications can be obtained [63].

To design a commercially viable system, and to make appropriate investment decision, accurate facility, equipment, material and labour information must be collected first, and investment and profits must be calculated. Techno-economic analysis (TEA) is a tool to evaluate the potential cost and profits based on assumed equipment and facility characters and costs [64]. Since TEA can combine engineering design, technical information, and costs and profits together, it can provide support not only for a long-term business strategic decision, but also for on-going operation and improvement [65].

Given the importance of protection of pipes against freezing and rupture, comparison of the technical and economic implications of use of conventional tracers and multi-layered coating systems is needed for integration into industrial operations. Despite the importance of developing economic models for comparison of the costs of fabrication of coatings based on different spraying processes, the total cost associated with production and utilization of coating systems is still not clear and only a paucity of techno-economic cost analysis studies are available. One major barrier has been the reticence of companies and researchers to disclose confidential financial and technical performance data [66].

Several probabilistic cost analyses have been performed to estimate the total cost of thermal-sprayed coating systems. In a study conducted by Glatzmaier and Gomez [67], a bi-layered coating system was fabricated on wetted surfaces of stainless-steel tank walls. The coating system in this study was fabricated for use in concentrating solar power thermal storage applications. The coating system was comprised of a nickel-chromium alloy as bond coat, which was used to promote adhesion between the top layer and the substrate, and a top coat of α-alumina, which was used for protection of the substrate against corrosion due to contact with the liquid inside the tank. All the costs, including powder, gas, energy, equipment, and labor for fabrication of the coating system were estimated and the range of the cost of the coating system was determined based on the surface area in $\$/m^2$. As a result of the developed model, a cost benefit was found for fabrication of the bi-layered coating system for wetted surface tanks and other components of concentrating solar power plants. Sensitivity analysis was also performed to rank the significance of each of the parameters on the total cost of each system to understand and to revise and improve the items that were of most impactful from a financial perspective [67]. This study, however, still left unanswered questions on impact of performance of the coating systems when balanced with the cost of fabrication and implementation in industrial settings. Very little work has been done so far to assess the life cycle costs of thermal-sprayed coatings. In particular, no studies have been conducted to compare the costs of coatings used as heating elements and conventional heating systems. No techno-economic studies have been conducted wherein the costs of the coatings-based heating systems have been benchmarked against their performance.

1.6 Summary

Formation and accumulation of ice inside pipes are undesired phenomena for above-ground water distribution pipelines that are exposed to cold environments. Transformation of water into ice, which is accompanied by volume expansion, causes pressurization and bursting of the pipes. Freezing experiments were conducted to study the dependence of the freezing temperature of the enclosed water on several parameters such as pipe mechanical properties, pipe wall thickness, and the work hardening the pipe has underwent in previous loading and unloading cycles. The novelty of this section was finding the relation between the yielding of the pipe material and beginning the second phase change stage. The findings can inform on the beginning of the plastic deformation of the pipe before which a heating element must be utilized to compensate the heat dissipation to the environment.

Therefore, the necessity of using a heating system for prevention of pipe failure due to freezing of the enclosed liquid is obvious. In this regard, various thermal-spraying techniques were employed to fabricate the next generation of heating systems for temperature protection of pipelines. The obtained promising results show that the novel coating-based systems can be used on large scale to heat and melt the ice within the steel pipes. Furthermore, it was found that the coatings are even more efficient than conventional heating cables thanks to the intimate contact with the surface of the pipe. The novelty of this study was fabrication of multi-layered thermally sprayed coating systems for pipelines based on the actual environmental conditions during wintertime to avoid bursting and failure of the steel pipes. Furthermore, the link between the spraying process, spraying parameters, coating microstructure, electrical resistance, and heating performance of the fabricated coatings were investigated in detail. Therefore, the findings of this study can inform on the relationship between the material science and heat transfer for the developed coating systems.

Furthermore, two one-dimensional transient heat conduction models were developed to predict the heating and melting times of the ice inside a closed pipe that was coated with a multi-layered thermal-sprayed coating system. The developed model for phase change of a finite-length scale medium was able to determine the transient location of the solid-liquid interface and predict the transient thickness of the enclosed ice. The results show that the mathematical models that were developed based on one-dimensional transient conduction theory can be employed as a reliable tool to predict the heating and melting times of the solid ice within coated carbon steel pipes relatively accurately. Therefore, the proposed heating system, coupled with the model, can be used as an effective and predictable means to mitigate the ice accumulation inside closed metallic pipes. The novelty of this study was development of an analytical model for phase change in a finite-length medium by utilization of superposition and separation of variables method. Prior to this study, the exact solutions were only used for semi-infinite and infinite regions and numerical and approximate solutions were suggested for finite regions. Furthermore, the results of this study were also shown based on unitless phrases so that they can be used for different pipe geometries and power supplies.

Techno-economic analysis (TEA) is a tool to evaluate the potential cost and profits based on assumed equipment and facility characters and costs. Since TEA can combine engineering design, technical information, and costs and profits together, it can provide support not only for a long-term business strategic decision, but also for on-going operation and improvement. In this regard, a techno-economic model was also developed to assess the feasibility of fabrication and utilization of the coating-based heaters on an industrial scale. Based on the obtained results, the improved performance of the coating systems should be viewed in light of the increased fabrication and installation costs by end users for large-scale protection of steel pipes against bursting during freeze events. However, the coating-based heating system can still be further developed and modified so that the required microstructure can be achieved at a lower cost either by modifying the spraying process or spraying parameters. The novelty of this study was investigating the economic viability of fabrication and utilization of coating systems for protection of pipelines. The findings of this study inform on both higher efficiency of the coating system and higher cost of fabrication of the coatings compared to the heating cables. Furthermore, the heating performance of the proposed coating system was compared with the convention heating cables in the actual environmental conditions for the first time.

1.7 Objectives

The objectives of this doctoral research project were to:

i) Analyze the failure mechanism of the pipes due to freezing of the enclosed water.

ii) Develop suitable spraying parameters and procedures to fabricate functional coatings on flat and cylindrical samples.

iii) Analyze qualitatively the adhesion, microstructure, and homogeneity of the deposited coatings by taking micrographs from cross sections of coatings by using a scanning electron microscope (SEM).

iv) Assess the performance and functionality of each coating layer in providing the electrical insulation, favorable electrical resistance, and proper electrical contact.

v) Develop two mathematical models based on transient one-dimensional heat conduction to estimate the times that are required for heating and melting of ice inside a closed pipe.

vi) Develop a comprehensive model to calculate the approximate overall expenditures of fabrication, installation, operation, and maintenance of thermal-sprayed electric resistance heating systems and conventional heat tracers.

vii) Compare the performance of the coating-based heating system with conventional tracers based on actual low-temperature working conditions.

1.8 Thesis Organization

The present thesis document has several chapters with the following structure: Chapter 2 focuses on the failure of steel pipes due to the freezing of the enclosed water and ice accumulation. The experimental setup that was employed for conducting the freezing tests and the procedure for analyzing the failure of the pipes are included in this chapter. In Chapter 3 of this thesis document, the fabrication of multi-layered coating-based heating systems was studied. Discussion about the impact of spraying parameters on the microstructure of the fabricated coatings and their electrical performance has been included in this chapter. Furthermore, the performance of the developed coating systems, as de-icing elements, was discussed in detail in this chapter. Chapter 4 presents the details related to the development of the mathematical models that were used for prediction of heating and melting times of the ice inside the steel pipes. Evaluation of the accuracy of the obtained results, which was conducted by comparing the predictions of models and the experimental measurements, has also been included in this chapter. In Chapter 5, details about the development of a techno-economic model are provided.

Furthermore, the comparison of the techno-economic implications of fabrication and utilization of coating-based heating system with those of conventional tracers has been provided in this chapter. Chapter 6 summarizes the conclusions from this thesis. Finally, Chapter 7 provides the suggestions for future work for extension and modification of this research work.

Chapter 2

Failure of Steel Pipes Due to Ice Accumulation

Solidification of water in closed piping systems is a common phenomenon in both the industrial and residential sectors. In some cases, the resulting damage may be both costly and dangerous and thus warrants attention. Therefore, further study of the cooling and freezing behavior of stagnant water within closed pipes seems to be necessary. In this regard, several experiments were performed to investigate the freezing behavior of water in pipes. The inelastic deformation, work hardening, and fracture of the pipes that were caused by volume expansion due to the freezing of the water were also studied. Two conventional steel pipe materials, namely ASTM A333-6 and ASTM A106-B, were used in the freezing tests. The fracture surfaces of the pipes were analyzed by using both macroscale and microscale images of the surfaces. Fractography analysis of the fractured regions was also performed by using a scanning electron microscope. It was found that the damage caused during freezing to the A106-B pipe was considerably more than that in the A333-6 pipe. The results confirm that A333-6 should be used instead of A106-B in pressure equipment, such as pipes, that are exposed to low temperatures.

The presented work in this chapter has been published in the proceedings of The Canadian Society for Mechanical Engineering (CSME) International Congress, Toronto, ON, Canada, May 27-30, 2018.

2.1 Experimental Method

Two 254-mm (10-inch) long, 51-mm (2-inch) diameter carbon steel pipes were used in the freezing experiments. The steel pipes were of two different materials namely ASTM A333-6 and ASTM A106-B. However, the wall thickness of both of the pipes was the same. Schedule 40 pipes, which are widely used in industry, were selected for the tests. The pipes were chosen to study the effects of pipe material on the resulting failure.

Each pipe assembly included a 254-mm (10-inch) long pipe with two A420 WPL6 butt-welded end caps, each including a 19-mm (¾-inch) Class 3000 A350 LF2 threadolet. Welding consisted of a typical SMAW P1-P1 procedure using E6010 for the root and E7018 for the cap. The total length of the assembly that consisted of the pipe, the two end caps, and the two threadolets was approximately 381 mm (15 inches). A pipe assembly, which is related to a Schedule 40 ASTM A333 Grade 6 pipe, is shown in Fig. 2-1.

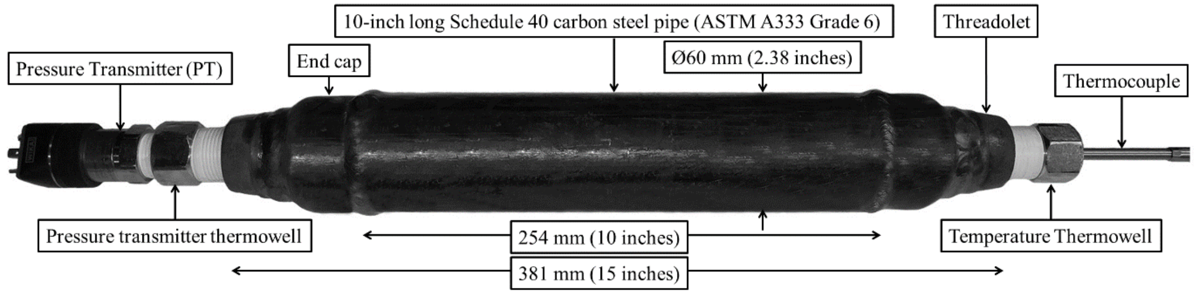

Figure 2-1 Pipe assembly, complete with the installed thermowells, thermocouple, and pressure transmitter

A thermowell (TW15, WIKA Instruments, Edmonton, AB, Canada) was installed into the threadolets at each end of the pipe. The thermowells were used for positioning the type T thermocouple (TC40, WIKA Instruments, Edmonton, AB, Canada) and the pressure transmitter (PT) (S-20, Klingenberg, Germany). The tip of the thermowell used for the PT was drilled through to enable pressure to be measured. A balloon filled with antifreeze was installed on the tip of the PT thermowell to ensure that no ice would form inside the pressure sensing pathway and to ensure that the peak pressure in the pipe, which occurs in the liquid phase, would be measured.

Temperature and pressure data were collected at regular time intervals from the thermocouples and the pressure transmitter by using two data acquisition systems. One data acquisition system (SCXI-1600, National Instruments, Austin, TX, USA) was used to measure the ambient and water/ice temperatures and a second data acquisition system (cDAQ-9171, National Instruments, Austin, TX, USA) was utilized to collect and record pressure measurements. The NI MAX software was used to collect all the measurement readings. The rate at which data was collected from all the mentioned devices was one data point per second (1 Hz).

In order to assess the freezing behavior of water inside the closed pipes, several freezing tests were performed in an 18.2 m^3 (640 ft^3) cold room freezer (Foster Refrigerator USA, Kinderhook, NY, USA) that was equipped with a temperature controller. The experiments were all conducted with pipes that were oriented horizontally and under the same environmental ambient conditions. The pipes were placed in the cold room in advance of conducting the tests so that both the ambient and the water inside the pipe were at steady state. Care was taken to start all the tests at approximately the same temperature (27°C). The cold room set-point temperature was -25°C and the tests were stopped when the water inside the pipe reached -15°C.

All of the experiments involved leaving a small pre-determined percentage of air space inside the pipe, rather than filling it completely with water. The reason for having air in the system was twofold. First, the first solidification plateau and ice cooling can only be seen when some air is entrapped in the closed system. Second, some air in the system prevents the pipe from yielding excessively and allows the pipe to be used for more freezing tests and, therefore, work hardening of the pipe material can be better observed and assessed. As a result, the amount of entrapped air in the pipe assemblies was set to a constant value of 5 vol.% for all the tests so that the work hardening behavior of the pipe materials was studied without introducing the effect of variation in the air content.

Considering the volume expansion of the pipes due to inelastic deformation, the volume of the pipe assemblies was measured after each test. Then, the pipe assemblies were refilled with water so that the increase in the volume of the pipe assembly was filled with water and the volume percent of air could be maintained constant in all the freezing tests.

Eventually, after conducting repeated freezing tests, the piping assemblies failed. The fracture surfaces were cleaned in order to study the microscopic features of the fracture surfaces. The sectioned samples of the pipes were placed in an ultrasonic cleaner (Haver USC 200, HAVER & BOECKER, Oelde, NRW, Germany) and cleaned with corrosion inhibited detergent solution (Citranox, Alconox, NY, USA) for 30 minutes to ensure that the oxide scale and deposits were removed from the fracture faces. The microstructure of the fracture surfaces was then examined by using a scanning electron microscope (Zeiss Sigma 300 VP-FE, Carl Zeiss Canada Ltd., Toronto, ON, Canada).

2.2 Results and Discussion

2.2.1 Freezing Behavior

The temperature and pressure traces of water/ice for the first freezing test that was conducted on ASTM A333 Grade 6, hereafter referred to as A333-6, Schedule 40 steel pipe in which 5 vol.% of air was entrapped in the pipe are shown in Fig. 2-2. The graph includes five stages, namely water cooling, the first solidification plateau, cooling of the mix of water and ice, the second solidification plateau, and the solid ice cooling. The first stage, which was related to the liquid cooling, began when the fans in the cold room started cycling (dropping the temperature in the room) and finished after a short supercooling period. The nucleation and growth of plate-like solid crystals known as dendritic ice occur at this stage and during the supercooling [68]. The length of the first solidification plateau in the second stage indicates the time needed for some of the liquid water in the pipe assembly to solidify so that a mixture of water and ice fills the entire volume of the pipe assembly. As the solidification proceeded through this stage, the annular ice formed inward and the dendritic ice was engulfed by solid ice [69]. At this point, solidification of water was paused due to the pressure increase. At the end of the first solidification plateau, all the water had not been transformed into solid ice and some water was still entrapped in the middle of the pipe assembly.

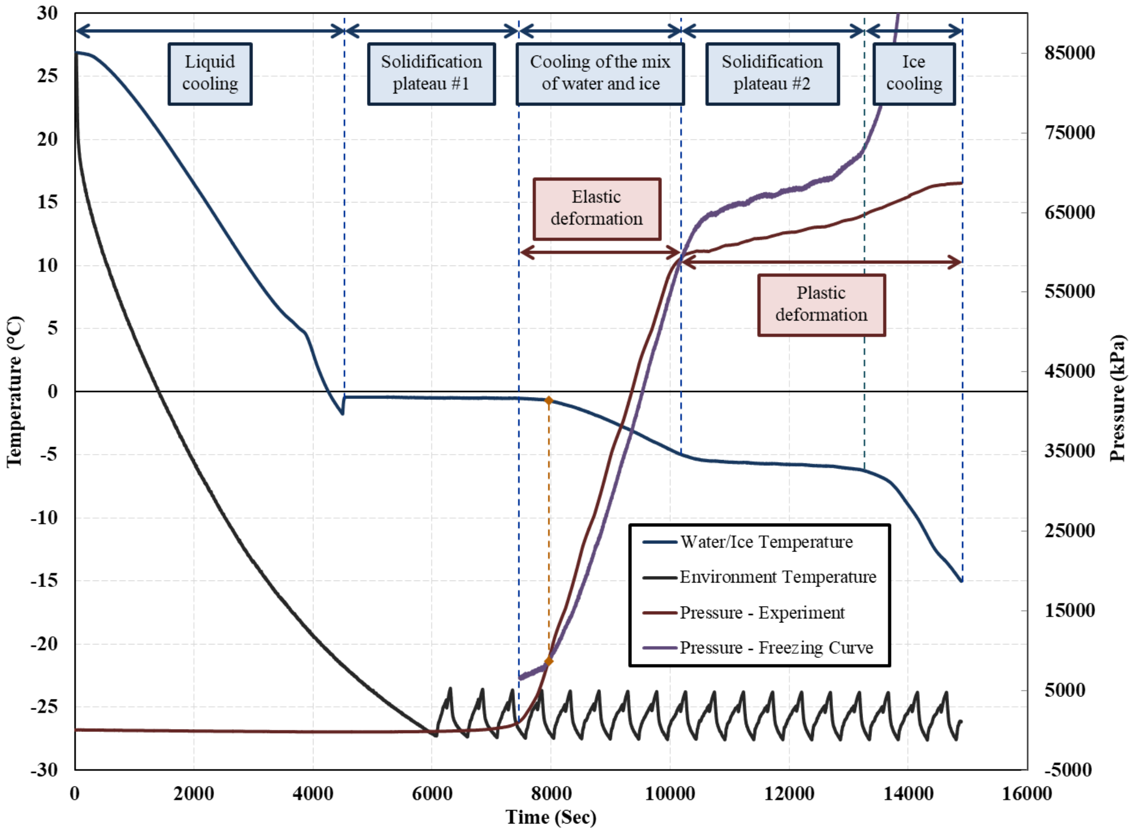

Figure 2-2 Curves of temperature and pressure versus time for water/ice in A333-6 Schedule 40 low carbon steel pipe

In the third stage and during the elastic deformation of the pipe, the pressure of water within the pipe increased sharply. As shown in Fig. 2-2, at the beginning of this stage, the average rate at which the water temperature decreased in this period was very low (order of -0.02ºC/min) because the pressure of the water was lower than the pressure that was calculated from the non-linear freezing relation for the hexagonal ice, which is given by Eq. (2-1) [70] as

$$P_f=6.11657\times 10^{-4}-414.5\times\left[\left(\frac{T_f}{273.16}\right)^{8.38}-1\right]. \tag{2-1}$$

The values of pressure obtained from Eq. (2-1) were based on the transient temperature of the freezing water inside the pipe (see Fig. 2-2). Further transformation of the water into ice caused an increase in the pressure of the freezing water such that the experimentally determined transient pressure curve intersected and crossed the transient pressure curve that was obtained from the non-linear freezing relation, which was representative of the magnitude of pressure that was required to maintain the freezing water in its liquid form. This point and its analogous point on the water temperature trace have been connected to each other with a dashed line (see Fig. 2-2) in order to highlight the interaction between water pressure and temperature. After this point, the high rate of increase in the pressure of the water caused a decrease in the rate of solidification of the rest of the pressurized water due to a continuous depression of the freezing point. Therefore, the heat loss in this period was mainly sensible as observed from the decrease in temperature of the ice-water mixture and consequently, the average rate of decrease of the water temperature changed noticeably from -0.02ºC/min before 7,960 seconds after the start of the experiment to -0.12ºC/min after 7,960 seconds after the start of the experiment.

Once the carbon steel pipe entered the plastic deformation region, the pressure increased with time at a lower rate than that which occurred earlier in the elastic deformation region. As a result of further cooling of the freezing water when the pipe material was deforming plastically, the pressure on the water was not sufficiently high to maintain the freezing liquid in its liquid form and, therefore, the remaining water started transforming to solid ice. The average pressure that was obtained from the experiment during this period (solidification plateau #2) was 5.2 MPa lower than the average pressure that was obtained from the freezing curve for the given temperatures (see Fig. 2-2). The transformation of water to ice, when the temperature trace plateaued again, was clearly observed at the time when the pipe material started deforming plastically.

The magnitude of freezing point depression correlates with the pressure of the freezing water, which itself is a function of the yield strength of the pipe and the pipe wall thickness according to the von Mises yield criterion and thick-walled pressure vessel theory relations, respectively. The yield strength of the pipe is not a constant value and varies due to work hardening from one test to another.

At the end of the second plateau, all the water in the pipe had been transformed into hexagonal ice. In the last stage, further cooling resulted only in temperature decrease of the solid ice. The increasing deviation of theoretical pressure values from the experimental values in this stage was likely due to a lack of pressurized water in the closed pipe. Therefore, comparison of pressure values between the non-linear freezing relation and the experiment is not valid in this stage.

2.2.2 Inelastic Deformation and Work Hardening

The inelastic deformation of the pipes that occurred during each freezing test was determined by measuring the diameter of the pipes by using a Pi-tape. The outer diameter of the pipes was measured before each test and after the failure of each pipe in the last test. The transverse strain values were calculated by comparing the current diameter of the pipe with its actual original value. As expected, the highest strains occurred near the middle of the pipe where the reinforcing effects of the circumferential welds had the lowest impact.

It was found that the maximum strain values that A106-B and A333-6 steel pipes could accommodate before rupture was 13.3% and 11.3%, respectively. It should be noted that the minimum transverse elongation required before failure according to the standard respecting ASTM A106 Grade B steel, hereafter referred to as A106-B, is 16.5% [71]. Therefore, the material did not meet the criteria under the frozen pipe tests. However, the requirement of the minimum transverse elongation at failure for A333-6 steel is 11.4% [72], which is very close to the strain value at which the pipe failed.

The number of loading/unloading cycles had a profound impact on the pressure values that were required to promote plastic deformation of the pipe material in each freezing test. The work hardening of both A106-B and A333-6 Schedule 40 steel pipes, which was caused by generation and movement of dislocations within the pipe material, can be observed clearly in Figs. 2-3 and 2-4, respectively.

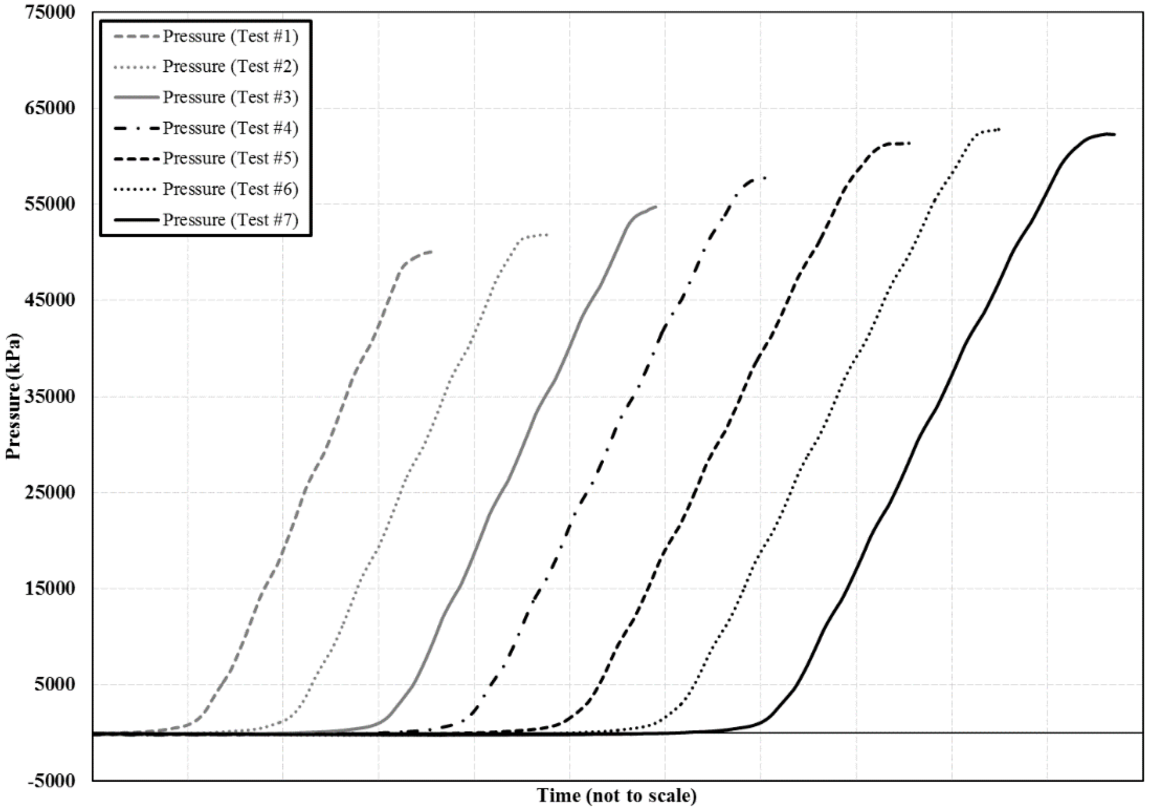

Figure 2-3 Effect of freezing/thawing cycles on yield pressure of A106-B Schedule 40 low carbon steel pipe

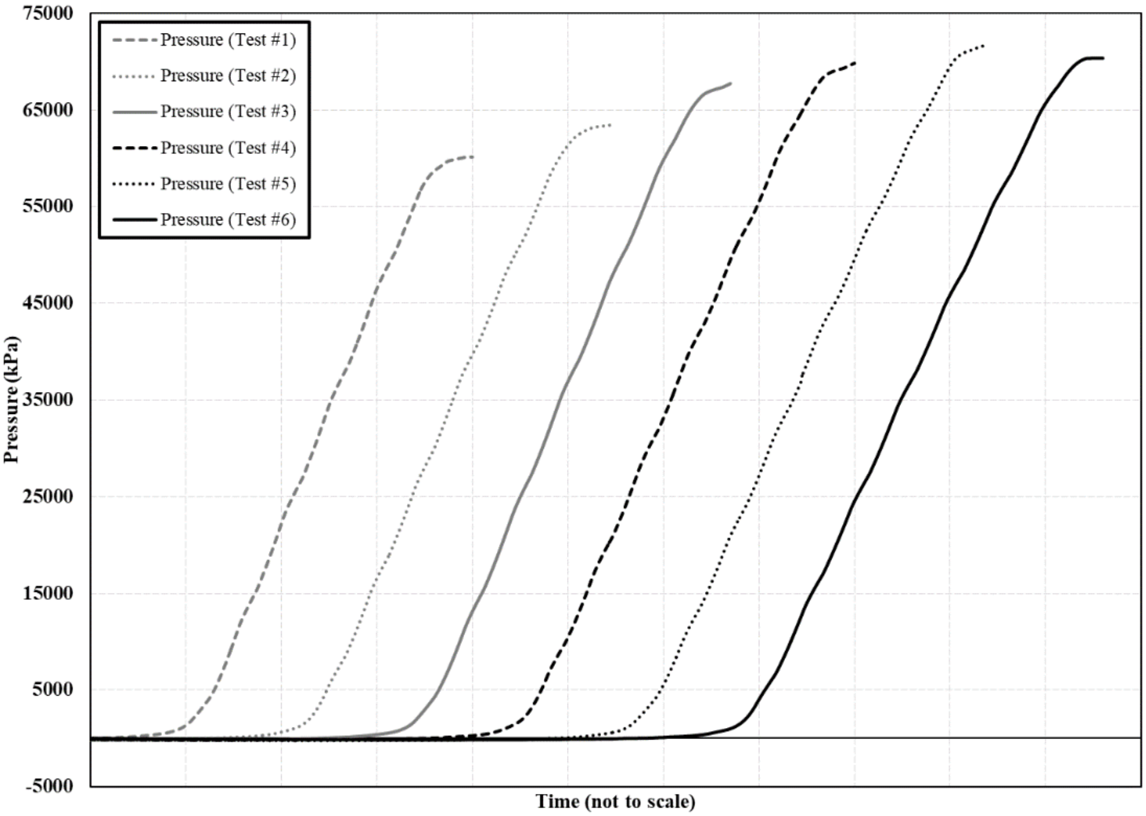

Figure 2-4 Effect of freezing/thawing cycles on yield pressure of A333-6 Schedule 40 low carbon steel pipe

A comparison of the peak pressures in the elastic region between the first and the last tests for both pipes shows approximately 23% and 17% increase in the pressure at which the pipe material started to deform plastically for A106-B and A333-6 Schedule 40 steel pipes, respectively (see Figs. 2-3 and 2-4). Therefore, the number of freezing/thawing (loading/unloading) cycles and the resulting work hardening of the pipe material had an impact on the increase of the peak pressures in the elastic region and, consequently, further depression of the freezing point of the remaining water in the closed system during the second solidification plateau according to Eq. (2-1).

A comparison of the temperature and pressure data of the first and the last tests that were performed with A333-6 steel pipe is shown in Fig. 2-5. The increase in the yield pressure and the decrease in the temperature at which temperature curve plateaued again can be clearly observed in Fig. 2-5.

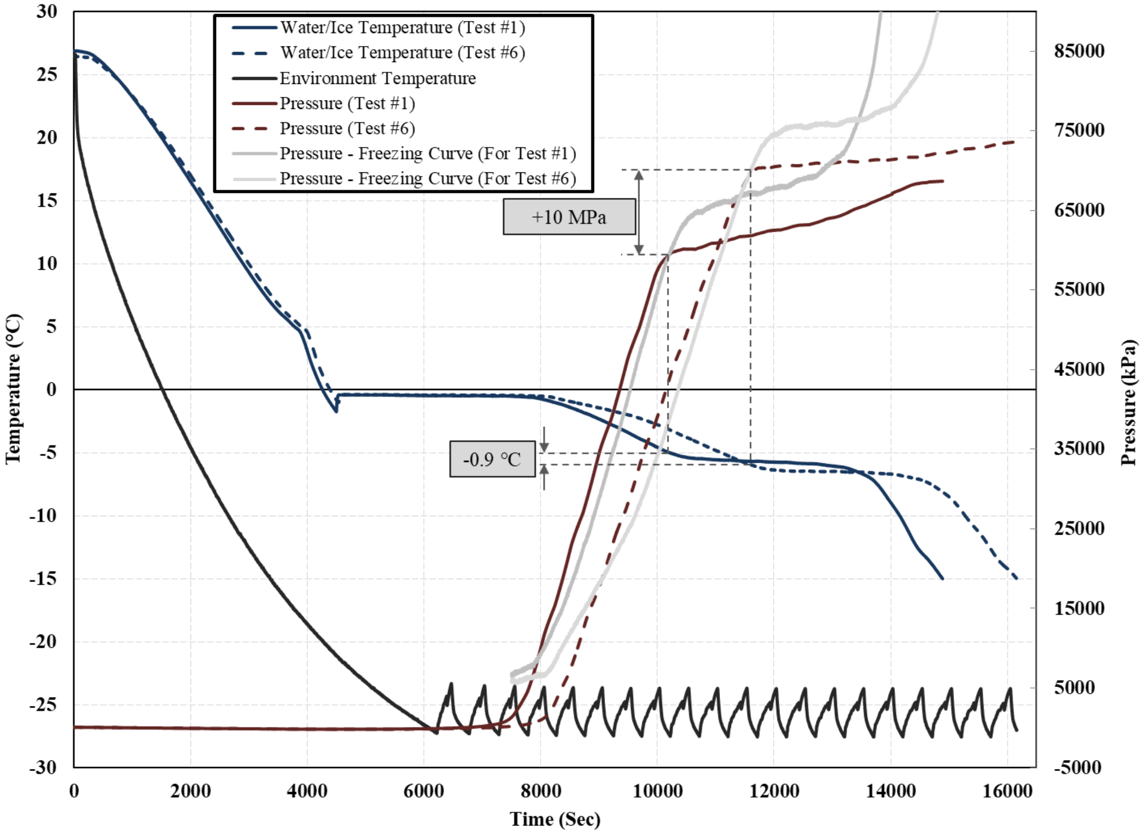

Figure 2-5 Effect of loading/unloading cycles on further depression of the freezing point at the beginning of the second solidification plateau

The relatively lower rate of temperature decrease in Test #6 compared to that of Test #1 at the beginning of the third stage (cooling of the mix of water and ice) was an indirect consequence of non-uniform bulging of the pipe assembly during the previous freezing tests, which resulted in the increase of the volume of the closed pipe from 649 ml to 718 ml. Therefore, more ice was required to be formed to compensate for the 10.6% increase in the volume of the pipe assembly and caused an increase in the water pressure to that which was required according to the freezing curve.

2.2.3 Pipe Rupture

Failure of the pipes occurred after conducting several tests. The pattern of failure that is shown in Fig. 2-6 is very common in pipe rupture cases. As expected, both pipe assemblies fractured along the axial direction, which was perpendicular to the direction of the applied hoop stress where the maximum principal stress for the case of the cylindrical pressure vessel was located. Considering the geometry of the pipe assembly with thermowells installed, the center of the pipe is the part that froze last. It was the expansion of the ice plugs in the axial direction and the low compressibility of the entrapped water that caused freeze-induced pipe failure [1].

The gap at the failure site of the A333-6 steel pipe was remarkably narrower and shorter than that of the A106-B steel pipe. It is believed that the longer axial crack for the A106-B pipe compared to that of the A333-6 pipe was due to the decrease in the amount of energy that was absorbed by the pipe material during propagation of the crack, which was due to the lower toughness of A106-B material at low temperatures. While not dramatically obvious in these specific tests due to the low amount of stored energy released at failure, the improved toughness properties of A333-6 is expected to be much more relevant and evident in actual field conditions where large amounts of stored energy is released at failure. The higher toughness of A333-6 provides better resistance to a brittle fracture developing following a ductile overload. The dependency of the absorption energy in Charpy impact tests on temperature for an A106-B pipe can be found in literature [73].

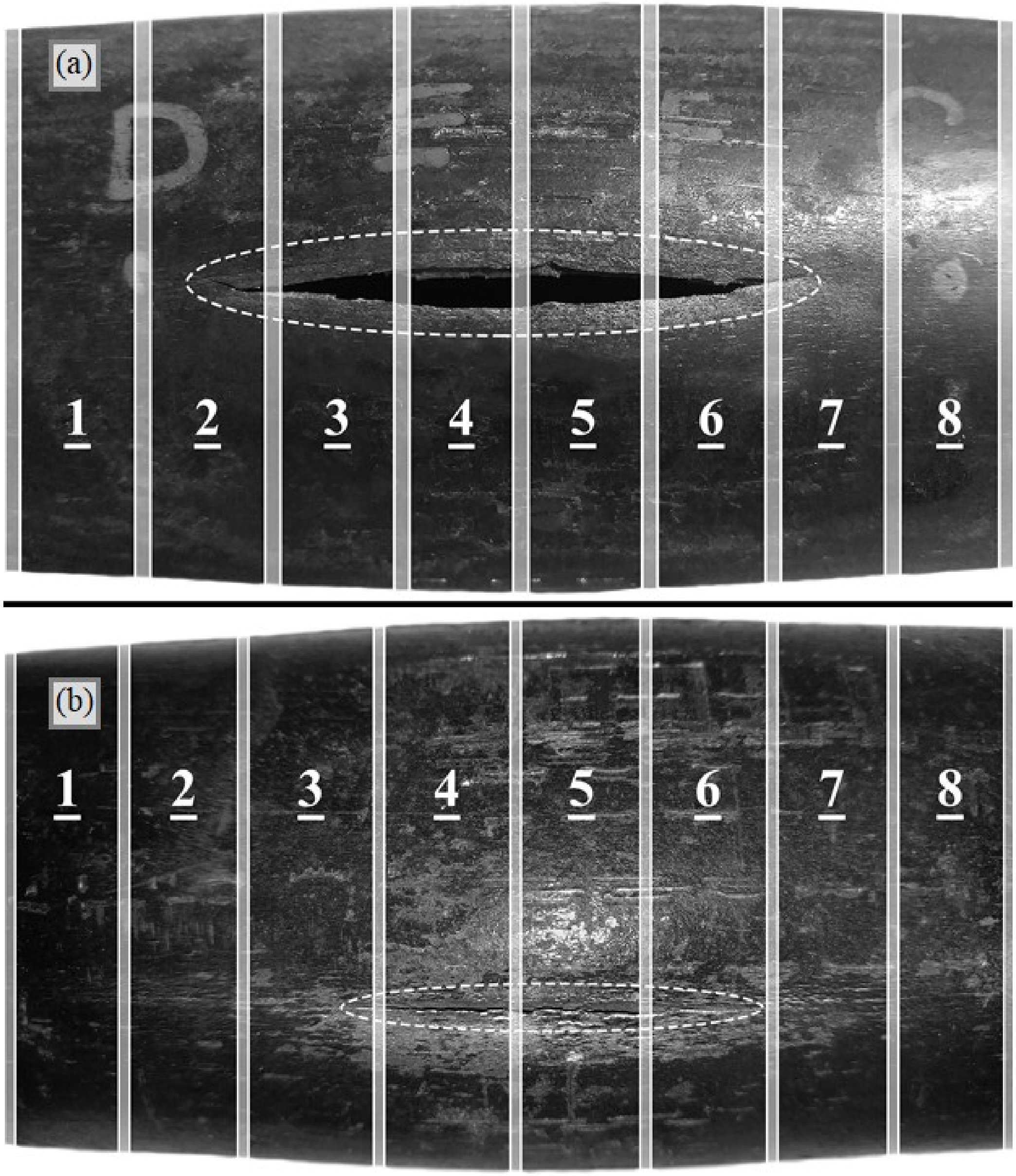

Figure 2-6 Failure of (a) A106-B and (b) A333-6 Schedule 40 low carbon steel pipe due to internal over-pressurization

The pipes were cut open after failure so that the fracture surfaces could be better observed. Eight rings, each one centimeter wide, were cut from the middle section of the pipe to study the fracture at different locations. The exact locations from which these eight rings were cut are shown in Fig. 2-6.

2.2.4 Failure Analysis

In order to study the macroscopic features of the fracture surfaces, images of the sides of the fractured regions were taken, which can be seen in Figs. 2-7 and 2-8. The geometry and appearance of the fractured regions are the characteristics that may be used to determine the fracture mechanism and the failure mode of the pipe material. Both slant fracture and double-slant fracture features, which are typical of planes-stress loading conditions in ductile materials [74] and are common failure modes in pressure vessel and in the piping industry [75], can be observed in cross-sectional views of the sectioned rings from the fractured portions.

These types of fractures, which are common in tubes with low wall thicknesses due to their minimum through-the-thickness stresses, are known to be ductile in nature [74]. It is well known that the tearing process is initiated by local thinning. The localization of two shear bands oriented at 45° angles occurs inside the necked region [76, 77]. The resulting slant failure and the necked regions can be observed in Figs. 2-7 and 2-8, in the middle and in front of the axial cracks, respectively.

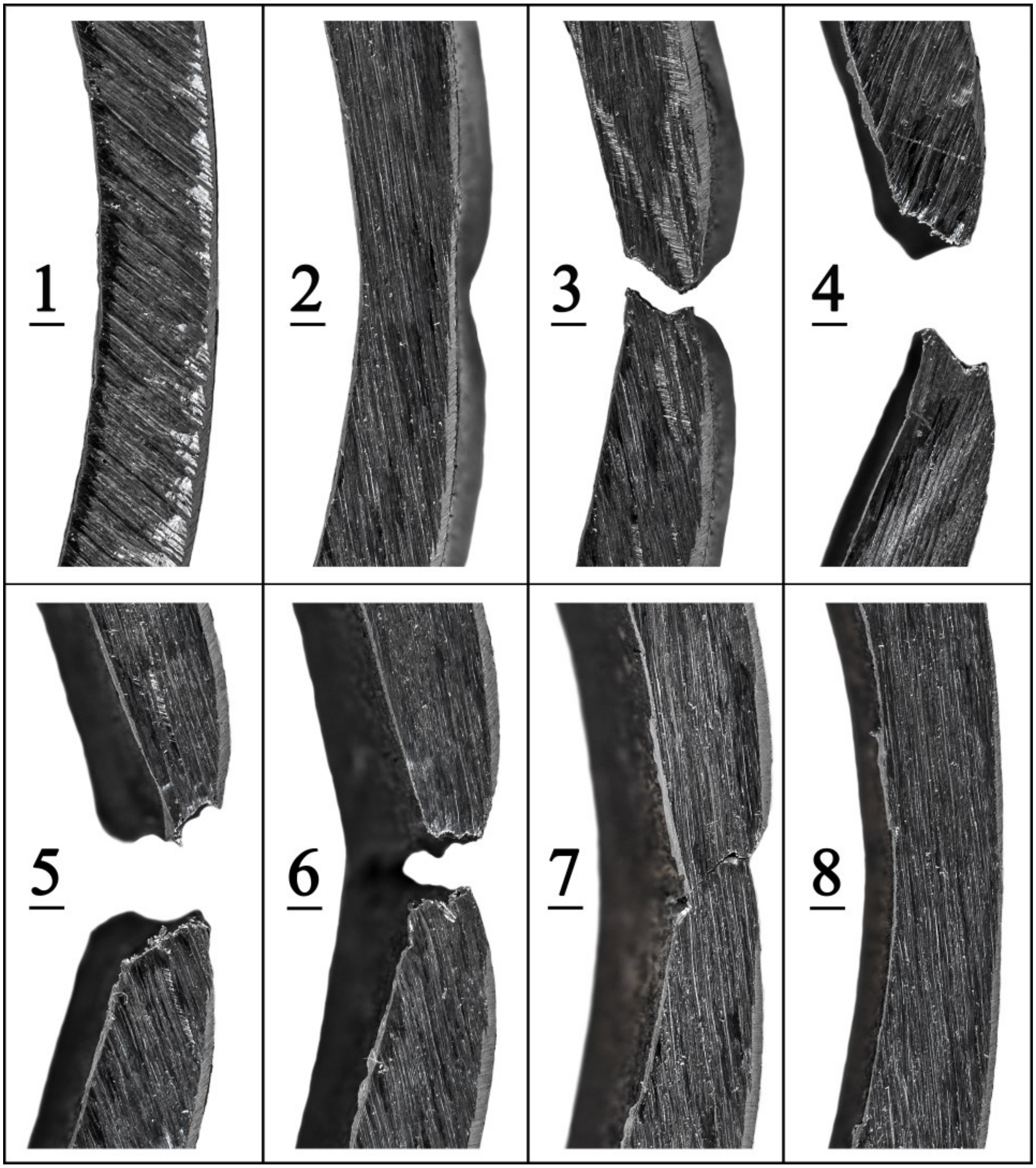

Figure 2-7 Cross-sectional views of the rings sectioned from A106-B Schedule 40 low carbon steel pipe

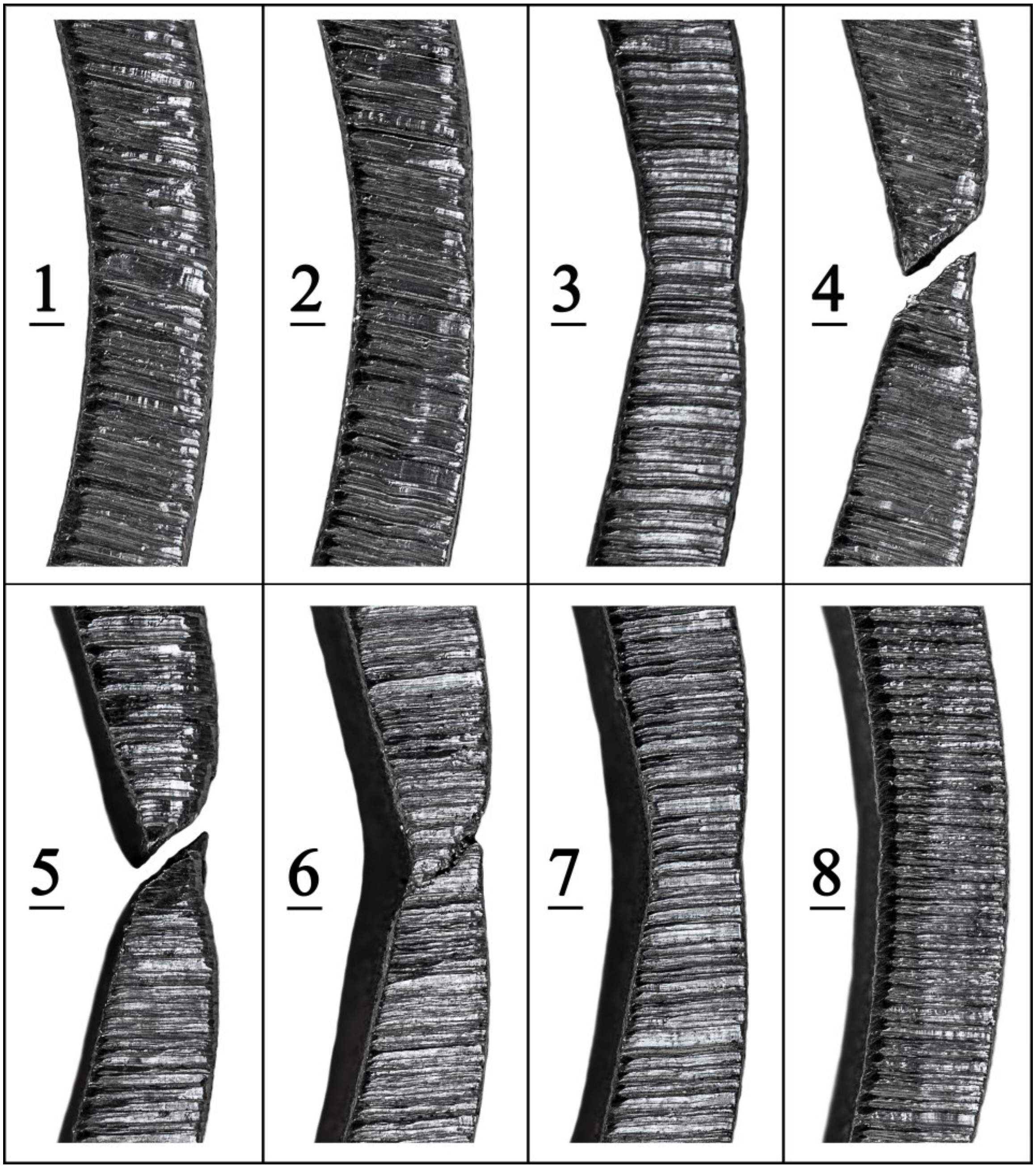

Figure 2-8 Cross-sectional views of the rings sectioned from A333-6 Schedule 40 low carbon steel pipe

2.2.5 Fractography

The higher magnification fractographs show that the mode of failure was ductile tearing from void coalescence induced microcracks, which is characteristic of ductile fracture. This can be observed from coalescence of adjacent microvoids in the axial direction (see Fig. 2-9). The dull and fibrous surfaces of the fracture that contained many dimples are indicative of dimpled rupture fracture.

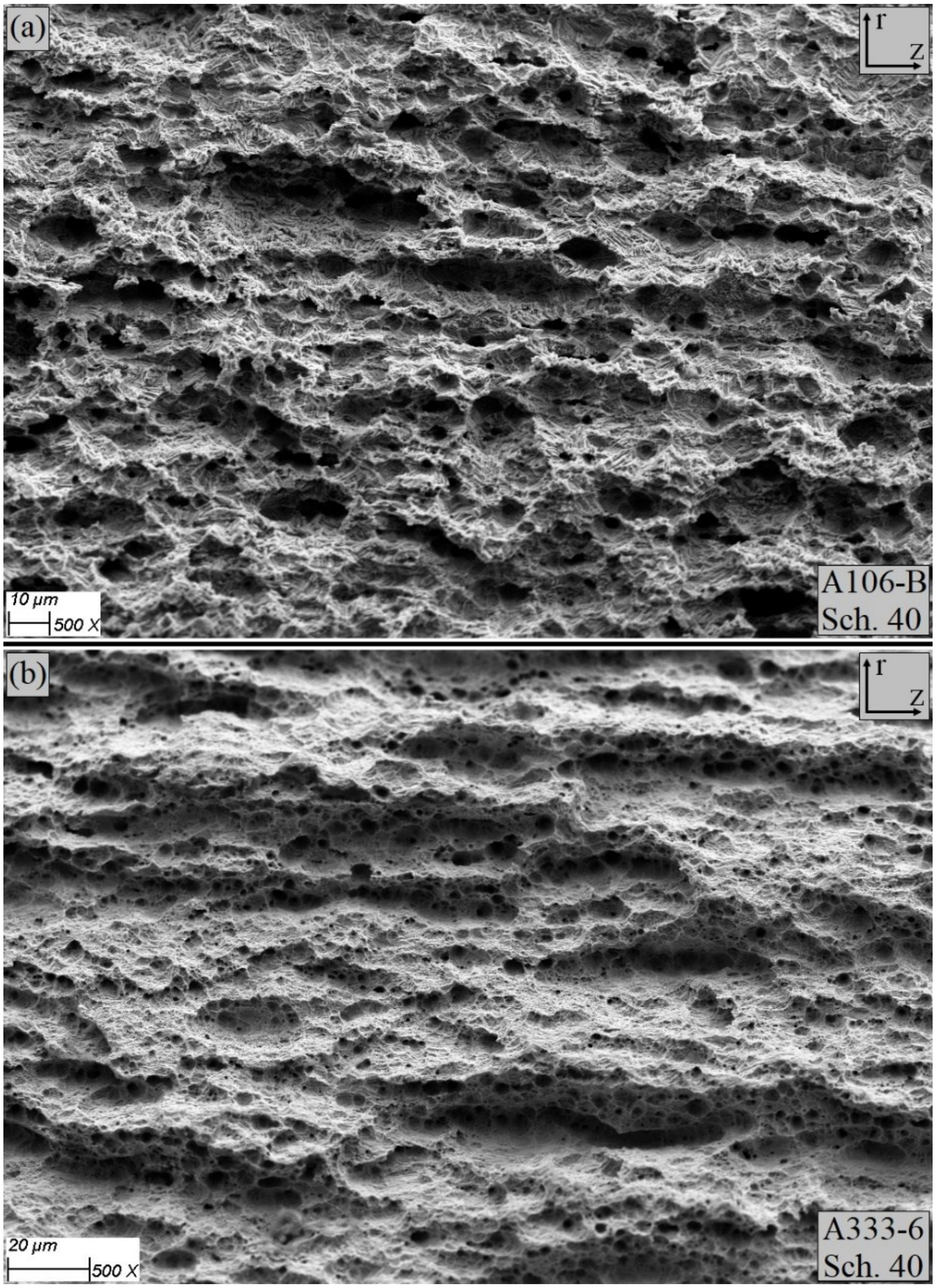

Figure 2-9 Micrograph of the fracture faces of (a) A106-B and (b)A333-6 Schedule 40 low carbon steel pipe (500X magnification)

2.3 Conclusions

Several freezing tests were performed on two steel pipe assemblies with the same dimensions, but with two different steel materials. By comparing the data, the following conclusions can be drawn.

- The freezing point depression of the water depended on the fluid pressure, which itself was a function of pipe material yield strength and wall thickness.

- The amount of work hardening mainly depended on the number of freezing/thawing cycles that the closed pipes had experienced. After performing several freezing tests, the pressure at which both A106-B and A333-6 steel pipes started deforming plastically was increased 23% and 17%, respectively.

- Work hardening of the material caused depression of freezing point in the second solidification plateau. It was found that an increase in the yield pressure of A333-6 steel pipe material on the order of 10 MPa (1,450 psi) resulted in a 0.9°C decrease in the temperature at which the remaining entrapped water started to freeze to solid ice.

- Failure and bursting of the pipes occurred after several loading/unloading (freeze/thaw) cycles. Double-slant and slant fracture appearances were observed in the macroscopic examination of the cross-sectional views of the sectioned rings.

- Higher-magnification views of the fracture surfaces of both pipes confirmed dimpled rupture fracture, which was indicative of ductile fracture. It was observed that the axial cracks were formed by coalescence of adjacent microvoids in the axial direction.

- As expected, the resulting damage in A333-6 pipe was less noticeable than that in A106-B pipe due to decreased toughness of the A106-B material at low temperatures.

Chapter 3

Fabrication of Multi-Layered Coating-Based Heating System

Various multi-layered thermal-sprayed coating systems were developed as resistive heating elements for temperature control of the carbon steel pipes. Feasibility and reliability of fabrication of different resistive heating coatings, namely Ni-20Cr and Ni-50Cr deposited by flame spraying onto the carbon steel samples were studied. Given the electrical conductivity of carbon steel, an electrically insulating layer, namely alumina or alumina-13 wt.% titania, was deposited by flame spraying process between the conductive resistive heating coating and the substrate to prevent short circuiting and flow of electrons between these layers. Fabrication of the coating systems was considered for both flat and cylindrical samples. Afterwards, the coated samples were sectioned and prepared for microstructural examination and elemental composition. The homogeneity, continuity, adhesion, and microstructural features of each coating system were examined by using a scanning electron microscope. The impact of various spraying parameters on the structure of the developed coating systems was investigated. It was found that the proposed heating system was able to generate the heat that was required to prevent formation and accumulation of ice, thus avoiding detrimental effects of bulging and ultimate bursting on the pipe due to internal pressurization. Furthermore, it was also found that the selection of a thermal spraying process and spraying parameters can have a noticeable impact on the electrical performance and the resistance of the coating system against electrical and mechanical failure modes. The obtained promising results indicate the potential utilization of these coatings in industry on mass scale.

Sections 3.1.2, 3.1.3, 3.1.4, 3.1.5, 3.1.7, 3.2.1, 3.2.2, and 3.2.4 of the work presented in this chapter, especially with regards to the cylindrical samples, have been published in:

M. Rezvani Rad, A. McDonald, "Development of a flame-sprayed coating system to mitigate ice accumulation and freezing damage in carbon steel pipes", in: *International Thermal Spray Conference*, May 7-10, 2018 (Orlando, FL, USA), ASM International, (2018), #44600, 8 pages on compact disk.

In addition, sections 3.1.1, 3.1.7, and 3.2.3, of this chapter have been published in:

Morvarid Mohammadian Bajgiran, Milad Rezvani Rad, André McDonald, Christian Moreau, "On Reliability of Thermally-Sprayed Alumina Dielectric Layers in a Multi-layered Coating-based Heating System", in: Proceedings of the Joint Canadian Society for Mechanical Engineering and CFD Society of Canada International Congress 2019, June 2-5, 2019 (London, ON, Canada), The Canadian Society for Mechanical Engineering, (2019), 8 pages on compact disk.9

Furthermore, some parts of sections 3.1.2, 3.1.3, 3.1.4, 3.1.5, 3.1.6, 3.1.7, 3.2.1, 3.2.2 and 3.2.4 of the work presented in this chapter, especially with regards to flat samples, have been published in:

M. Rezvani Rad, M. Mohammadian Bajgiran, C. Moreau, A. McDonald, "Microstructural and performance analyses of thermal-sprayed electric resistance heating systems deposited onto steel pipes as de-icing elements", in: *International Thermal Spray Conference*, May 26-29, 2019 (Yokohama, Japan), ASM International, (2019), # 47189, 8 pages on compact disk.

The extended version of these papers that includes sections 3.2.5 and 3.2.6 will be submitted to Surface and Coatings Technology Journal.

3.1 Experimental Method

Details regarding the spraying process, microstructure of the developed coating, electrical performance, and the challenges of fabrication of high-quality heaters are discussed in the following sections.

3.1.1 Feedstock Powder

In this study, various powder materials, namely aluminum oxide (Al_2O_3, AMDRY 6060, Oerlikon Metco, Westbury, NY, USA), alumina-13 wt.% titania (Al_2O_3-13TiO_2, ALO-187, Praxair Surface Technologies, Indianapolis, IN, USA), nickel-50wt.% chromium (50 Nickel-50 Chromium, 1260F, Praxair, Concord, NH, USA), nickel-20wt.% chromium (Metco 43F-NS, Oerlikon Metco, Westbury, NY, USA), and copper (SST-C5003, CenterLine, Ltd., Windsor, ON, Canada), were used to fabricate the coatings by using flame spraying (FS) and cold spraying (CS) processes. The morphology of the powder materials that were utilized in this study are shown in Figs. 3-1(a) - 3-1(e). All micrographs were taken at 500X magnification in secondary mode by using a scanning electron microscope (Zeiss Sigma 300 VP-FE, Carl Zeiss Canada Ltd., Toronto, ON, Canada).

The size distribution of alumina and alumina-titania powder particles that were used for FS process were 5 to 45 µm (-45+5 µm) and 11 to 45 µm (-45+11 µm) and their angular/blocky morphology that is shown in Figs. 3-1(a) and 3-1(b) was because of the manufacturing process that was selected for their fabrication that was fusing and crushing [78, 79].

The size of the Ni-50Cr particles were between 22 to 53 μm (-53+22 μm) and the spheroidal shape of the powder that can be observed in Fig. 3-1(c) was due to the gas atomization manufacturing process of the powder [80]. The water atomized Ni-20Cr powder that was used for the FS process was fabricated in irregular shape as shown in Fig. 3-1(d) with the size distribution of 10 to 63 μm (-63+10 μm) [81]. Dendritic copper powder with minimum purity of 99.7 % and size distribution of 5 to 45 μm (-45+5 μm) [82], which was manufactured by electrolysis process and can be seen in Fig. 3-1(e), was used in cold spraying process in this study to fabricate the desirable electrical contacts.

(a)

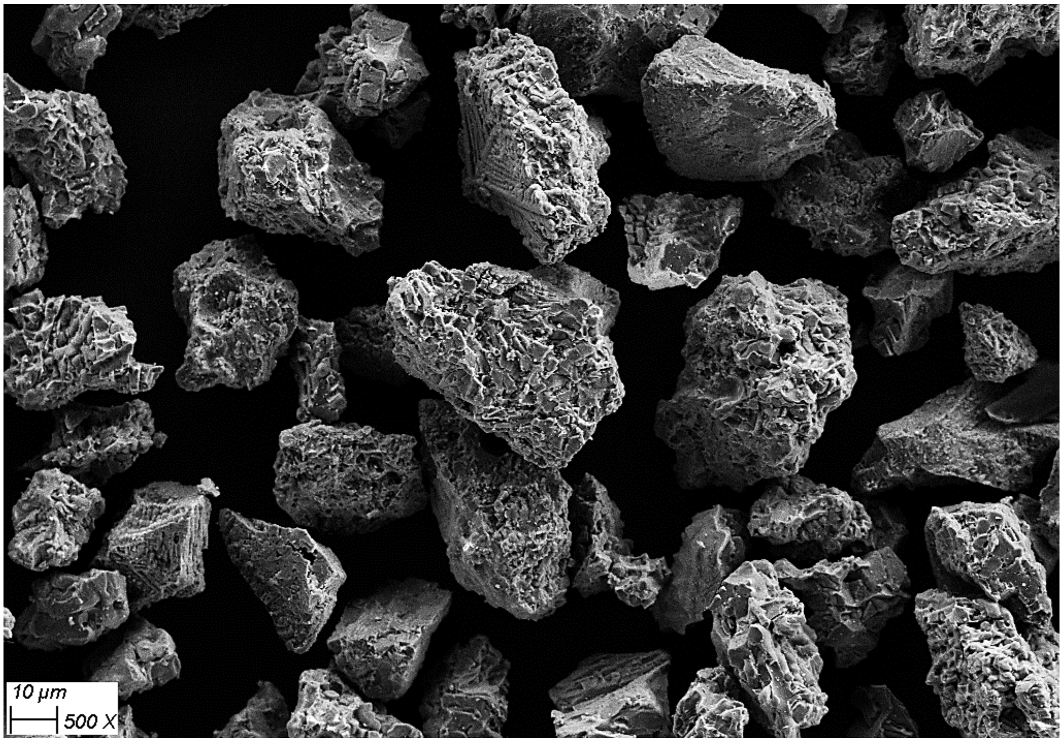

(b)

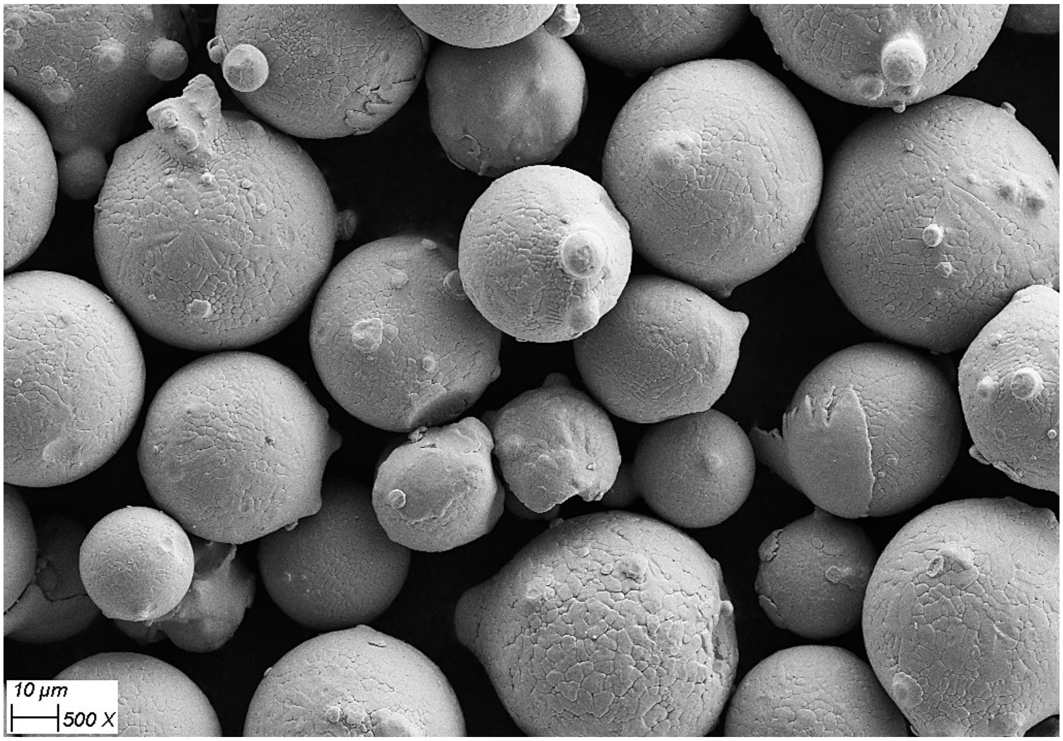

(c)

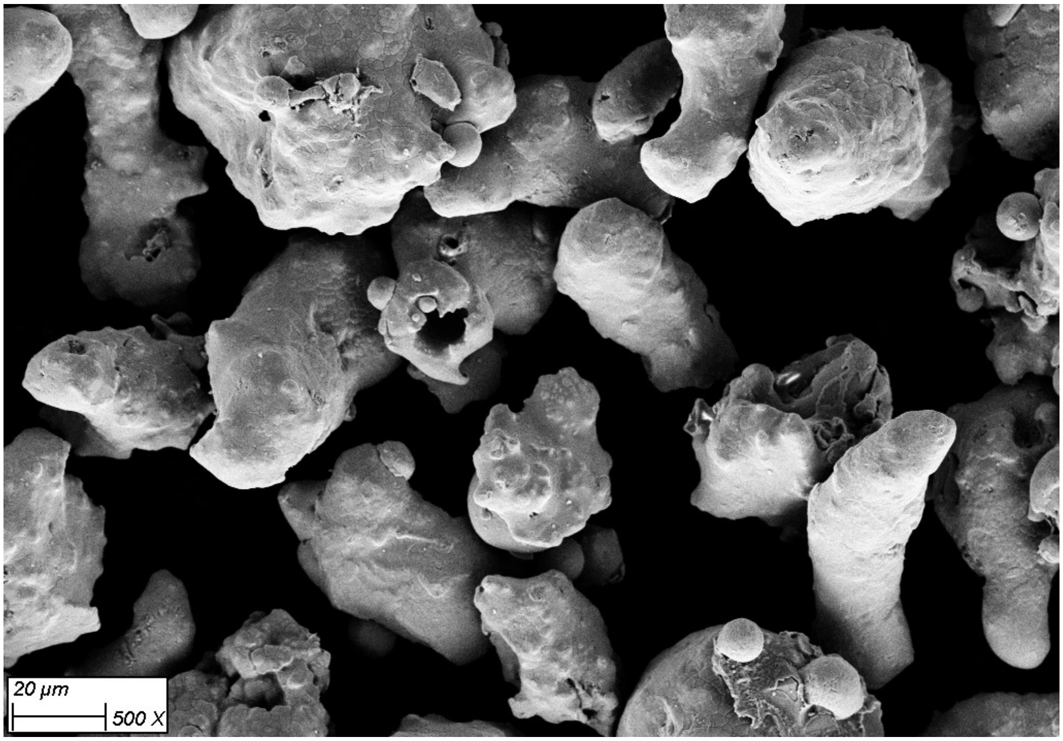

(d)

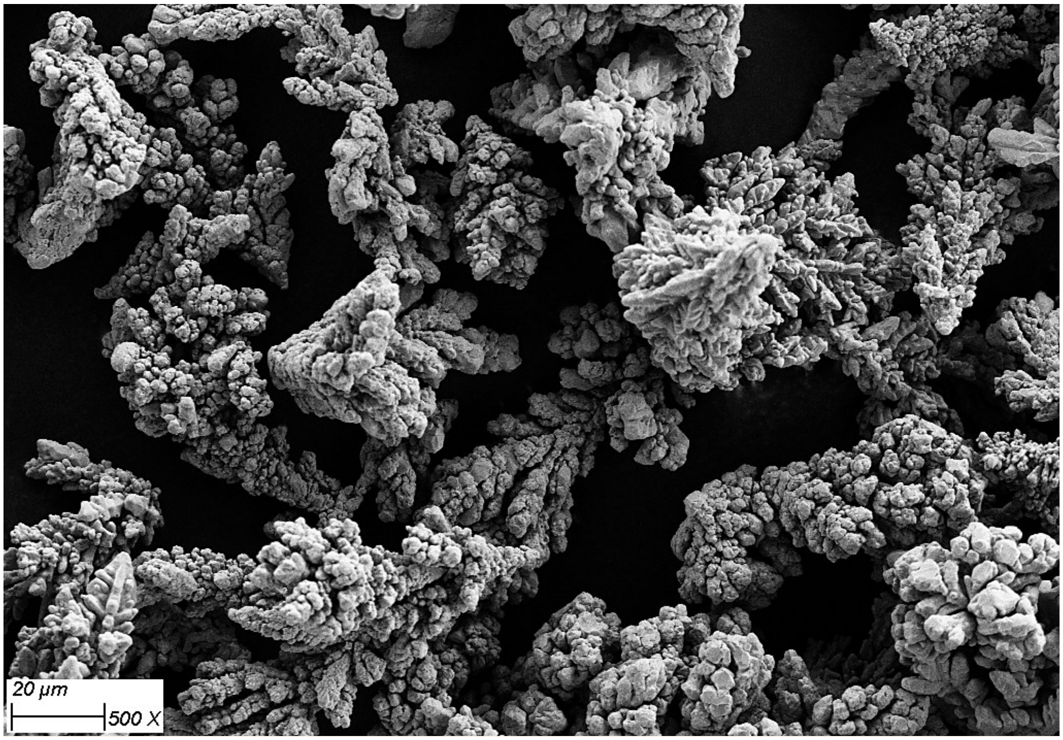

(e)

Figure 3-1 Micrographs taken at 500 X magnification from (a) Al_2O_3 powder, (b) Al_2O_3-13%TiO_2 powder, (c) Ni-50Cr powder, (d) Ni-20Cr powder, and (e) Copper powder

3.1.2 Substrate Preparation

Both flat and cylindrical carbon steel samples were used as the substrate in this study. First, the coating system was deposited on a pipe to study the feasibility and functionality of the proposed system as a de-icing element. Then, numerous coating systems with different spraying parameters and thermal spraying procedures were fabricated on flat samples to study the effect of different parameters on the electrical performance of the coating systems. This could potentially lead to optimization and improvement of the ultimate thermally-sprayed coating-based heating system that can be deposited onto pipes to act as de-icing or anti-icing elements based on actual working conditions.

A 254-mm (10-inch) long, 51-mm (2-inch) diameter carbon steel pipe (ASTM A333-6) as the substrate was taken into consideration in this study to investigate the application of the coating system based on actual working conditions. A pipe assembly was made by welding two A420 WPL6 butt-welded end caps, each including a 19-mm (0.75-inch) Class 3000 A350 LF2 threadolet, to the ends of the pipe. The total length of the pipe assembly that consisted of the 254-mm (10-inch) long pipe section, the two end caps, and the two threadolets was approximately 381 mm (15 inches). The pipe assembly that was used as the substrate is shown in Fig. 3-2.

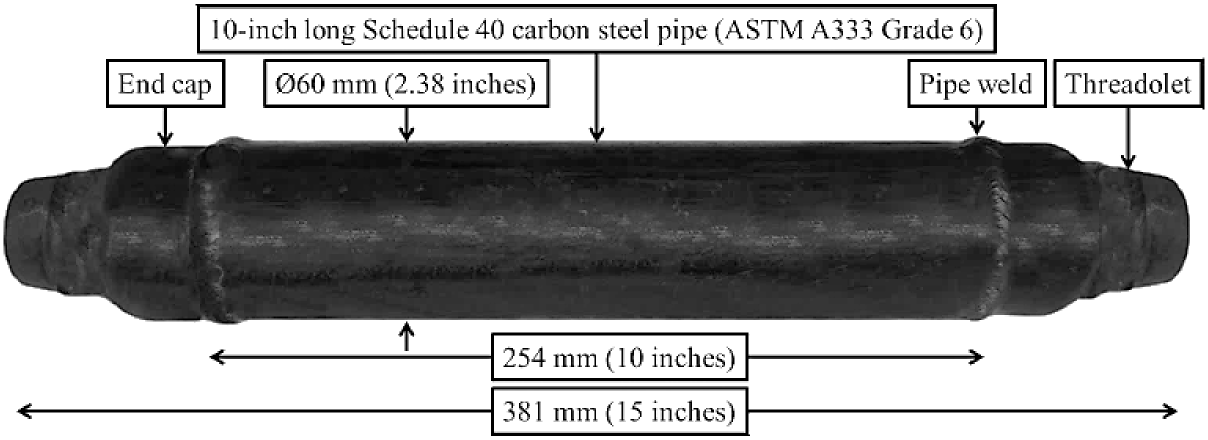

Figure 3-2 The components of the pipe assembly that was used as the substrate

The flat samples, which were also used as other substrates, were water jet cut in two different sizes from 6-mm (0.25-inch) thick steel plates (A36/44w mild steel hot rolled flat bar, Metal Supermarkets, Edmonton, AB, Canada). The larger rectangular 127-mm (5-inch) long and 25-mm (1-inch) wide samples were employed for the heating tests. However, the smaller square 25 mm x 25 mm (1 inch x 1 inch) samples were utilized for microstructural analyses. Both samples were mounted for coating deposition in each trial to ensure the identical and indistinguishable coating structure.

All flat and cylindrical samples were grit-blasted with #24 alumina grit (Manus Abrasive Systems Inc., Edmonton, AB, Canada) at an air pressure of 586 kPa (85 psig) to create the roughness that was required to cause the adhesion between the FS alumina or FS alumina-titania coatings to the substrate. For the case of the pipe substrate, just the middle section of the pipe assembly including the 254-mm (10-inch) pipe section and the pipe welds, which is shown in Fig. 3-2, was grit-blasted. To ensure that the coating layers does not deposit on the end caps of the pipe assembly, these areas were covered by using a masking tape (170-10S Red, Green Belting Industries, Mississauga, ON, Canada) during the grit blasting stage.

To decrease the tensile residual stresses that were generated during the cooling stage and solidification of the alumina molten droplets, both flat and cylindrical substrates were preheated by passing the plasma over the samples several times. The ratios that were used for mixture of the oxygen and the gas in the torch for the preheating process were the same as the ones that were used for the deposition of the alumina and alumina-titania layers.

3.1.3 Deposition of Coating Layers

Fabrication of coating system for cylindrical sample

For the case of cylindrical sample, alumina powder with the composition of Al_2O_3 99.5+ wt.%, Na_2O 0.3 wt.%, Fe_2O_3 0.05 wt.%, CaO 0.05 wt.%, and SiO_2 0.02 wt.% was fed continuously to an oxy-acetylene flame spray torch (6P-II, Oerlikon Metco, Westbury, NY, USA) based on a series of spraying parameters that are listed in Table 3-1 by using a volumetric powder feeder (5MPE, Sulzer Metco, Westbury, NY, USA). For the flame spraying process, different volume flow rates of acetylene, oxygen, and air, were provided to the torch to bring about the combustion flame that was required to melt and accelerate the powder particles. In addition, argon gas with the flow rate of 0.56 m^3/h (20 standard cubic feet per hour) was selected to act as the carrier gas.

The oxy-acetylene flame spray torch was installed on a programmable robot (HP-20, Motoman, Yaskawa Electric Corp., Waukegan, IL, USA) to ensure a consistent and repeatable deposition. To deposit the coating layers, the pipe assembly was held by a rotating chuck. While the rotating chuck was made to move at the speed of 600 rpm, the torch was moved in a linear fashion over the middle of the sample in the axial direction. Relatively high rotational speed of 600 rpm and low linear speeds of 10 mm/s and 24 mm/s were chosen for deposition of Al_2O_3 and

Ni-50Cr coatings onto the pipe, respectively, to ensure that helical pattern for the coatings would not be obtained and a homogenous coating will be fabricated, especially in the axial direction. The higher linear speed and the stand-off distance (SOD) for deposition of Ni-50Cr compared to those of the Al_2O_3 was due to the much larger flame that was achieved for deposition of Ni-50Cr. To increase the homogeneity and continuity of the coating layers, low powder feed rates and a high number of passes were used. The relative rate at which powder was conveyed to the torch by the volumetric powder hopper is given by flow meter reading (FMR) parameter, which is a dimensionless parameter and is listed in Table 3-1. The density of the powders affects the powder flow rate in the carrier gas (Ar). That said, the FMR parameter was used in this study to be indicative of different flow rates for different powders because of the variations on material densities.

Table 3-1 Flame spraying parameters for deposition of coatings on flat and pipe samples.

Coatings and geometry / Spraying Parameters	Alumina						Alumina-13 wt.% titania				Nickel-Chromium							
	Pipe	Flat					Flat				Pipe (Ni-50Cr)	Flat (Ni-20Cr)						
		S1	S2	S3	S4	S5	S1	S2	S3	S4		S1	S2	S3	S4	S5	S6	S7
Acetylene flow [m^3/h]	1.3	1.3	1.1	1.3	1.5	1.5	1.3	1.5	1.5	1.1	0.9	0.9	1.5	0.9	0.9	0.9	1.3	0.9
Oxygen flow [m^3/h]	1.9	2.1	2.4	2.1	1.8	1.8	2.1	1.8	1.8	2.4	1.9	1.9	1.5	1.9	1.9	1.9	2.4	1.9
Argon pressure [m^3/h]	0.56	0.56	0.56	0.56	0.56	0.56	0.56	0.56	0.56	0.56	0.56	0.56	0.56	0.56	0.56	0.56	0.56	0.56
Flow Meter Reading (FMR)	100	100	100	100	100	100	100	100	100	100	70	65	65	65	65	65	65	65
Robot speed [mm/s]	10	250	250	250	250	250	250	250	250	250	24	250	250	250	250	250	250	250
Stand-off distance [mm] (in)	102 (4)	127 (5)	127 (5)	77 (3)	77 (3)	127 (5)	127 (5)	77 (3)	127 (5)	127 (5)	254 (10)	152 (6)	152 (6)	229 (9)	77 (3)	152 (6)	152 (6)	152 (6)
Number of passes	14	5	5	5	5	5	3	3	3	3	8	2	2	2	2	2	2	2
Number of preheating passes	6	1	1	1	1	1	1	1	1	1	0	0	0	0	0	0	0	0
Air pressure (psi)	5	5	5	5	5	5	5	5	5	5	5	5	5	5	5	10	5	0
Increment (mm)	NA	3	3	3	3	3	3	3	3	3	NA	5	5	5	5	5	5	5

For the case of the cylindrical sample, Ni-50Cr with a composition of Cr 46 wt.%, Fe 1.0 wt.%, and Ni 53 wt.% was deposited onto the FS alumina coating by flame spraying process to fabricate the heating element. The final structure and geometry of the bi-layered coating system completed with copper strips at the ends of the pipe section can be observed in Fig. 3-3. It should be noted that the length of the pipe on which alumina coating was deposited was more than the length onto which Ni-50Cr was sprayed. The reason for that was to avoid short circuiting between the conductive heating element and the conductive substrate that can lead to the malfunction of the heating system by depositing the Ni-50Cr coating directly on top or very close to the steel substrate. To prevent any deposition of Ni-50Cr coating near the ends of the alumina coating, those regions were covered by wrapping several layers of masking tape around the pipe welds.

To fabricate the copper rings for proper electrical contact between the heating element and the power supply, a low-pressure cold spray system (SST series P, CenterLine, Ltd., Windsor, ON, Canada), with a converging-diverging de Laval nozzle and compressed air as the working fluid, was utilized to preheat and accelerate copper powder particles based on the spraying parameters listed in Table 3-2. Copper is well-known for its favorable electrical properties, which makes this material ideal for electrical contacts [82]. Similar to the flame spray torch, the cold spray nozzle was also mounted on the automatic robot to ensure reproducibility of the fabricated coatings by maintaining the transverse speed and the stand-off distance of the nozzle during spraying. The micron-sized dendritic copper powder particles were then preheated and projected onto the Ni-50Cr coating to form a dense copper coating. Given the rotational speed of the pipe assembly, the robot was programmed in such way to fabricate the copper coating in the form of a ring at each end of the pipe assembly.

Table 3-2 Low-pressure cold spraying parameters for deposition of copper on cylindrical and flat samples

Parameters \ Coating	Copper
Compressed air pressure (kPa)	634
Powder feeder opening	10%
Compressed air temperature (°C)	400
Stand-off distance (mm)	5
Number of layers	2

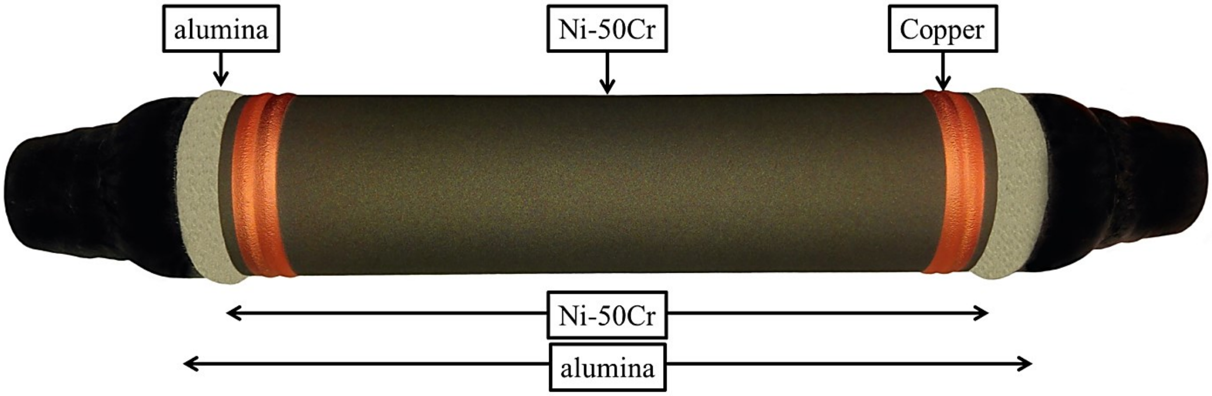

Figure 3-3 The pipe assembly coated with functional bi-layered coating system and completed with cold-sprayed copper rings at the ends of the pipe section

Fabrication of Coating System for Flat Samples

For the case of the flat samples, ten different electrically insulating layers, namely five FS alumina coatings and five FS alumina-titania were deposited onto the flat steel substrates. FS process was also employed to deposit the resistive heating layer (Ni-20Cr) on the alumina and alumina-titania coatings. The spraying parameters for deposition of the electrically insulating layer and the heating element by FS process are listed in Table 3-1. The coating systems that were fabricated on flat samples and their geometry and dimensions are shown in Fig. 3-4.

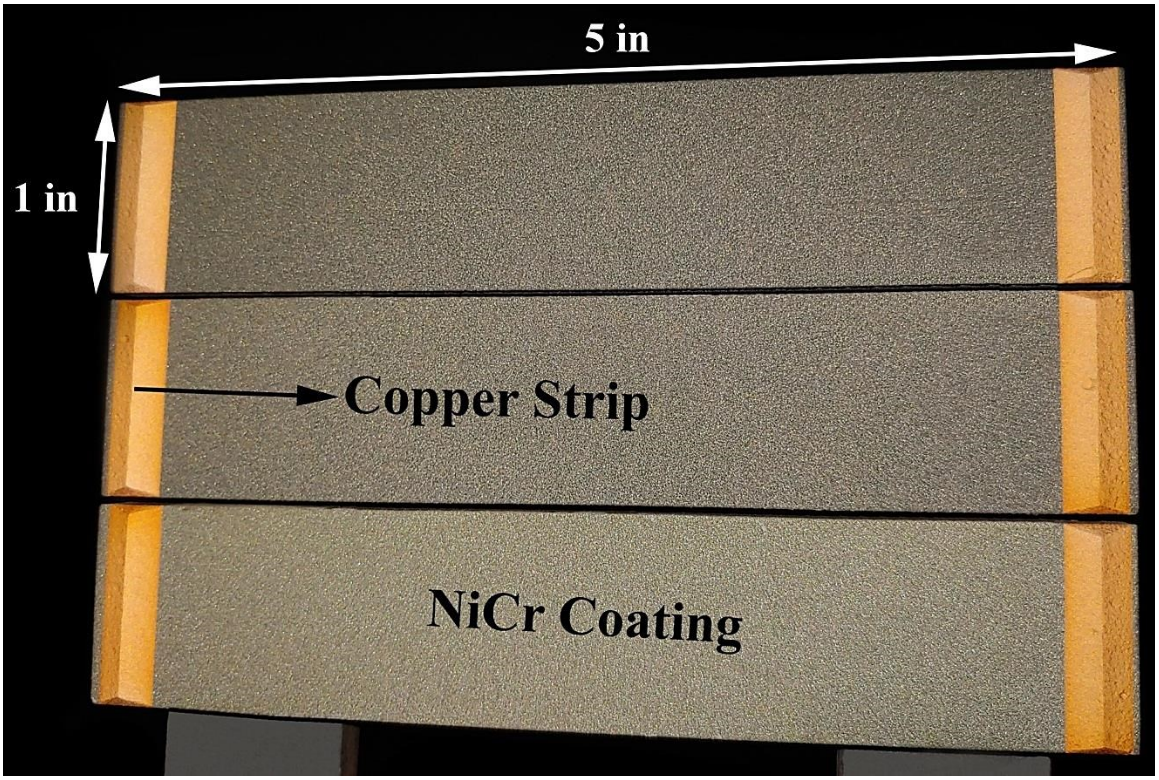

Figure 3-4 Fabricated coating systems on flat samples

3.1.4 Installation of Fittings and Sensors

Fittings and temperature sensors were utilized in order to assess the heating performance of the fabricated coatings. For the case of the pipe sample, it was filled with water to study the efficacy of the developed heating system in melting the enclosed ice within the pipe. To ensure that the pipe assembly does not undergo plastic deformation and bulging during the freezing process due to the expansion in the volume of the water during transformation into ice that is around 9 vol.%, a 10 vol.% air gap was included in the pipe assembly to prevent internal pressurization and possible damage to the coating system.

Two thermowells (TW15, WIKA Instruments, Edmonton, AB, Canada) were fastened and tightened into the threadolets at each end of the pipe. The reason for utilizing the thermowells was twofold. First, installation of the thermowells was essential for sealing the pipe assembly, which was necessary for conducting the freezing and heating test. Second, it allowed insertion of industrial thermocouples that could measure the temperature of ice or water inside the pipe assembly at the middle section. In this regard, two T-type thermocouples (TC40, WIKA Instruments, Edmonton, AB, Canada) were placed inside the thermowells whose stem length and insertion length were 209.5 mm (8.25 inches) and 165.1 mm (6.5 inches), respectively. In order to measure and collect the surface temperature of the heating element, a T-type surface thermocouple (TC50, WIKA Instruments, Edmonton, AB, Canada) was also attached to the NiCr surface in the middle of the pipe. To ensure that its temperature readings would not be perturbed by circulation of air over the pipe, the surface thermocouple was covered with glass wool thermal insulation.

The pipe assembly completed with the installed fittings and sensors is shown in Fig. 3-5. The transient ambient temperature inside the cold room was also measured by using another Type-T thermocouple. For the case of the flat samples, a similar scenario was repeated. The only difference was that the heating tests were performed without consideration of water/ice. Therefore, the temperature measurements were only conducted to collect the transient temperature of the Ni-20Cr coating (the heating element) during the heating tests.

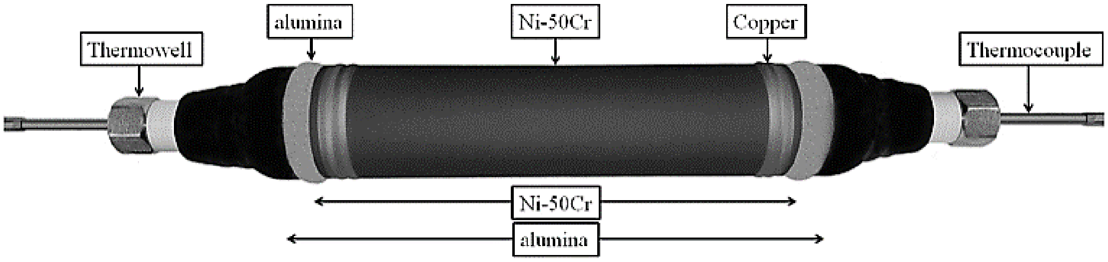

Figure 3-5 The coated pipe assembly completed with installed fittings and temperature sensors

3.1.5 Joule Heating Test

To perform the heating tests, the fabricated samples were placed inside an 18.2 m^3 (640 ft^3) cold room freezer (Foster Refrigerator USA, Kinderhook, NY, USA). The set point temperature and the bandwidth were selected as -25°C and ±2°C, respectively. All cylindrical and flat samples were positioned horizontally inside a 2 m × 0.66 m × 0.48 m closed galvanized sheet metal duct. Not only did the utilization of the closed duct reduce the effect of circulation of air over the sample in the free convection tests, but it also resembled the forced convection condition by turning on the fan at the end of the duct. To simulate the severe environmental conditions when pipes are exposed to external wind flow, forced convective cooling was caused by movement and circulation of air within the galvanized sheet metal duct by utilization of a 0.25 kW (0.33 hp) direct-drive tube-axial fan (DDA-12-10033B, Leader Fan Industries, Toronto, ON, Canada). The geometry, dimensions, and the main components of the apparatus that was used for simulation of the forced convection condition can be found in previous studies [47, 52]. The location at which the coated pipe assembly was placed during the heating tests can be seen in Fig. 3-6.

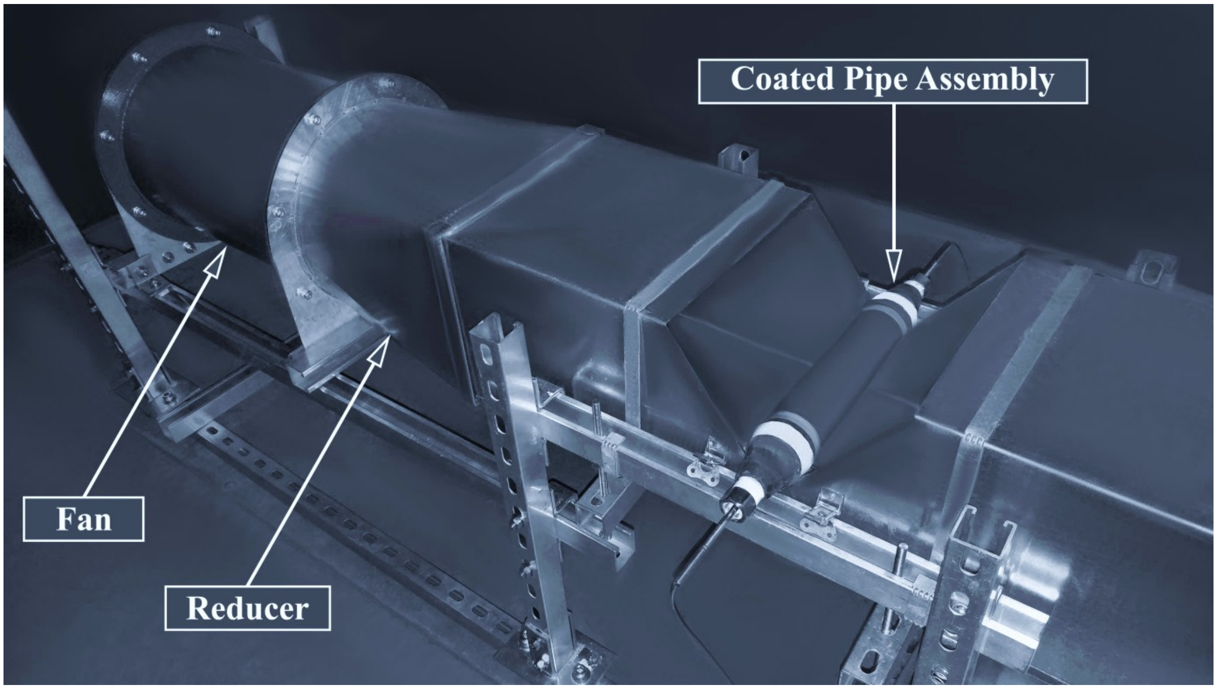

Figure 3-6 Placement of the coated pipe assembly inside a galvanized duct for conducting the heating tests

Several electric resistive heating tests were conducted to confirm the functionality of the fabricated coating systems. In this respect, a direct current (DC) power supply (1902B DC, B&K Precision Corporation, Yorba Linda, CA, USA) was employed to supply the required voltage and move the negatively charged electrons through the metal alloy coating. The wires connected to the power supply were directly soldered from the other end to the copper rings/strips to minimize the electrical resistance. Heat was generated by way of Joule heating by passing electrical current through the Ni-20Cr/Ni-50Cr coating (heating element). Most of the generated heat was transferred to the substrate by conduction and some of it was also dissipated to the environment by convection. Given the application of the coating system that is melting the ice within the pipe, alumina coating was specifically chosen as the dielectric layer to conduct the heat properly to the substrate and the enclosed freezing liquid for the case of pipe samples and minimize the dissipated heat to the ambient environment.

Various powers of 20 W, 45 W, 80 W, 125 W, 180 W and 500 W were supplied to the fabricated coating systems to assess the performance of the coating-based heating system. In all the tests, the data that was measured by the temperature sensors were collected at a frequency of 1 Hz (1 measurement per second) by using NI MAX software and a data acquisition system (SCXI-1600, National Instruments, Austin, TX, USA). For the case of the cylindrical sample, the heating tests were conducted with and without thermal insulation and under both free and forced convection heat transfer conditions to study the efficacy and practicality of the developed systems under severe climatic conditions and thermal loadings.

3.1.6 Electrical Resistivity

To compare the electrical resistivity of the heating elements, a 6.5-digit bench multimeter (34461A, Keysight Technologies, TX, USA) was used to measure the precise electrical resistance of the Ni-20Cr coating that was deposited on flat samples based on four-wire sensing (Kelvin sensing) method. Then, the acquired electrical resistance values were converted to electrical resistivity by taking into account the dimensions of the coating, namely width, length, and thickness. In this regard, several SEM images were taken from the cross section of each fabricated coatings and the average thickness was calculated by using image analysis software (ImagePro, Media Cybernetics, Bethesda, MD, USA). For each of the images, the thickness of the coating was acquired by dividing the cross-sectional area of the coating by its width.

3.1.7 Preparation of Samples for SEM

Both cylindrical and flat samples were water jet cut and cold-mounted in an epoxy resin (LECO, Mississauga, ON, Canada) for microstructural examination. Samples were cut from both middle and end sections of the samples where cold-sprayed copper was deposited to observe the interaction between all the coating layers. The sectioned samples were ground comprehensively with 180, 240, 320, 400, 600, 800, and 1200 silicon carbide grit papers (LECO, Mississauga, ON, Canada) and polished afterwards by using both 3 and 1 μm diamond slurry suspensions (LECO, Mississauga, ON, Canada) to achieve the desirable high quality that was required for taking the SEM images. To avoid having any surface charging on the non-conductive alumina coating and to eliminate the accumulation of static electric charges, the samples were coated with a thin layer of carbon by using a sputter coater (EM SCD 005, Leica Baltec Instrument, Balzers, Liechtenstein). The porosity percentages were obtained by using image analysis software (ImagePro, Media Cybernetics, Bethesda, MD, USA). To achieve a reliable value, the porosity was obtained by calculating the average between the findings from five (n = 5) different SEM images.

3.2 Results and Discussion

3.2.1 Coating Characterization

To study the microstructure of the samples, micrographs were taken in both backscattered electron and secondary modes by using a scanning electron microscope (Zeiss Sigma 300 VP-FE, Carl Zeiss Canada Ltd., Toronto, ON, Canada). To observe the topography of the powder particles and the top surfaces of the coatings properly, the secondary electron mode was employed. However, the backscattered mode was utilized for the images that were taken from the cross section of the samples so that the elemental composition of the coatings can be observed in a clearer manner due to the higher contrast between different constituent materials.

The micrographs that are taken from the cylindrical sample are shown in Fig. 3-7. Given the brittle nature of the alumina coating and placement of this ceramic layer between two metallic layers and probable generation of significant thermal stresses at the interfaces, cracking and even delamination of this layer was likely. However, after conducting several experiments in which the sample underwent repetitive heating and cooling cycles, the failure of this layer was not observed during the microstructural analysis.

Regarding the deposition of alumina, it should be noted that this specific coating material was chosen in this study due to its desirable electrical and mechanical properties. Although this material has favorable dielectric properties, it can conduct heat well compared to the other ceramic materials [78]. Therefore, not only does selection of this material prevent the short circuiting between the heating element and the substrate, but also it facilitates the transfer of heat from the heating element to the pipe and the enclosed freezing water/ice.

Penetration of the Ni-50Cr coating into the alumina coating can be seen in Fig. 3-7(a), which was mainly due to the presence of the network of connected pores. Therefore, the molten Ni-50Cr particles found their way through these channels to reach to the lower parts of the alumina coating. Although this is not desirable from the electrical perspective due to the reduction in the effective thickness off the dielectric layer, it may be considered as a plus point from mechanical viewpoint as it can provide better bonding and interlocking between the coating layers. However, it should be noted that in this case a relatively thick alumina coating should be deposited to ensure that a continuous pathway of Ni-50Cr is not generated through the alumina coating because it can lead to the malfunction of the coating system. The higher magnification micrographs from the interfaces of the coating system are shown in Figs 3-7(b) and 3-7(c). No evidence of delamination was detected at the interfaces between the layers, which speaks to the proper adhesion between the layers.

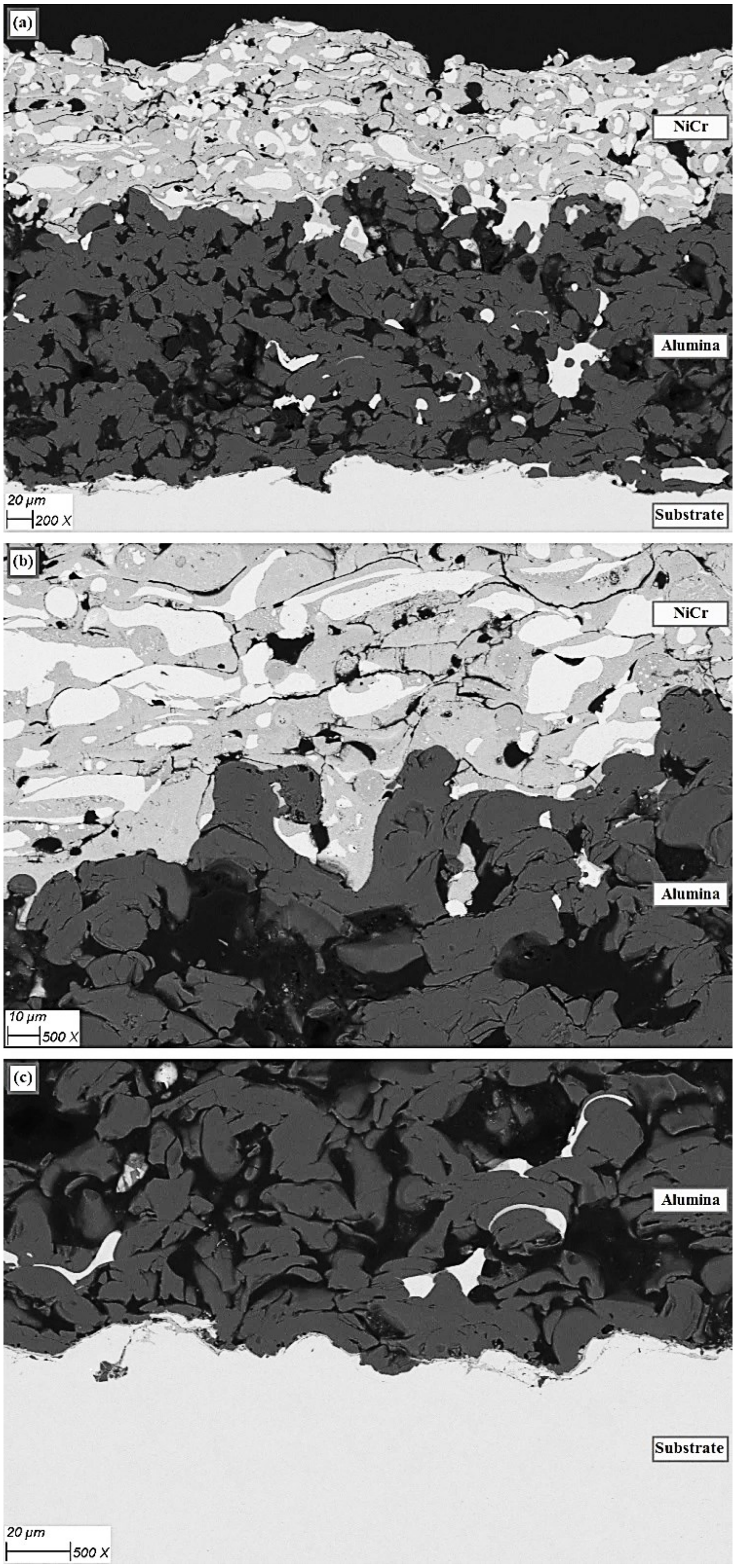

Figure 3-7 Micrographs taken from the coated pipe: (a) multi-layered coating system and (b) NiCr-alumina, and (c) alumina-substrate interfaces at higher magnification

It is well-known that the electrical properties of the coatings are dependent on their microstructure. In this regard, defects including pores, microcracks, and oxides in the Ni-50Cr can affect the electrical resistance of the coating noticeably. The porous structure of the Ni-50Cr that was deposited by flame spraying process, which is shown in Fig. 3-7(a), results in increase of the electrical resistance of this coating, in comparison with the bulk material, as it reduces the effective cross-sectional area of the coating through which the electrons can flow [83]. The same effect has been observed for presence of cracks within the coating-based heating element [84]. That said, this structure might be even advantageous in reaching high values for the electrical resistance. Moreover, the presence of the pores might arrest the cracks and prevent them from further propagation. This may result in higher integrity of the heating element, especially when it needs to undergo many heating-cooling cycles.

In order to study the mechanism for penetration of the Ni-50Cr coating into the alumina layer during the spraying process, images from the top surface of the FS alumina, FS alumina-titania, and SPS alumina, which were deposited on flat samples, were taken in secondary electron mode. Open pores were observed on the top surface of the alumina and alumina-titania coatings that were deposited by FS process during the microstructural evaluation. As can be seen in the high-magnification (1000X) micrographs that are shown in Figs. 3-8(b) and 3-8(d), some of the open pores are not superficial and may be connected to a network of connected pores that can channel and direct the molten particles of the top coat to the lower parts of the alumina/alumina-titania coatings.

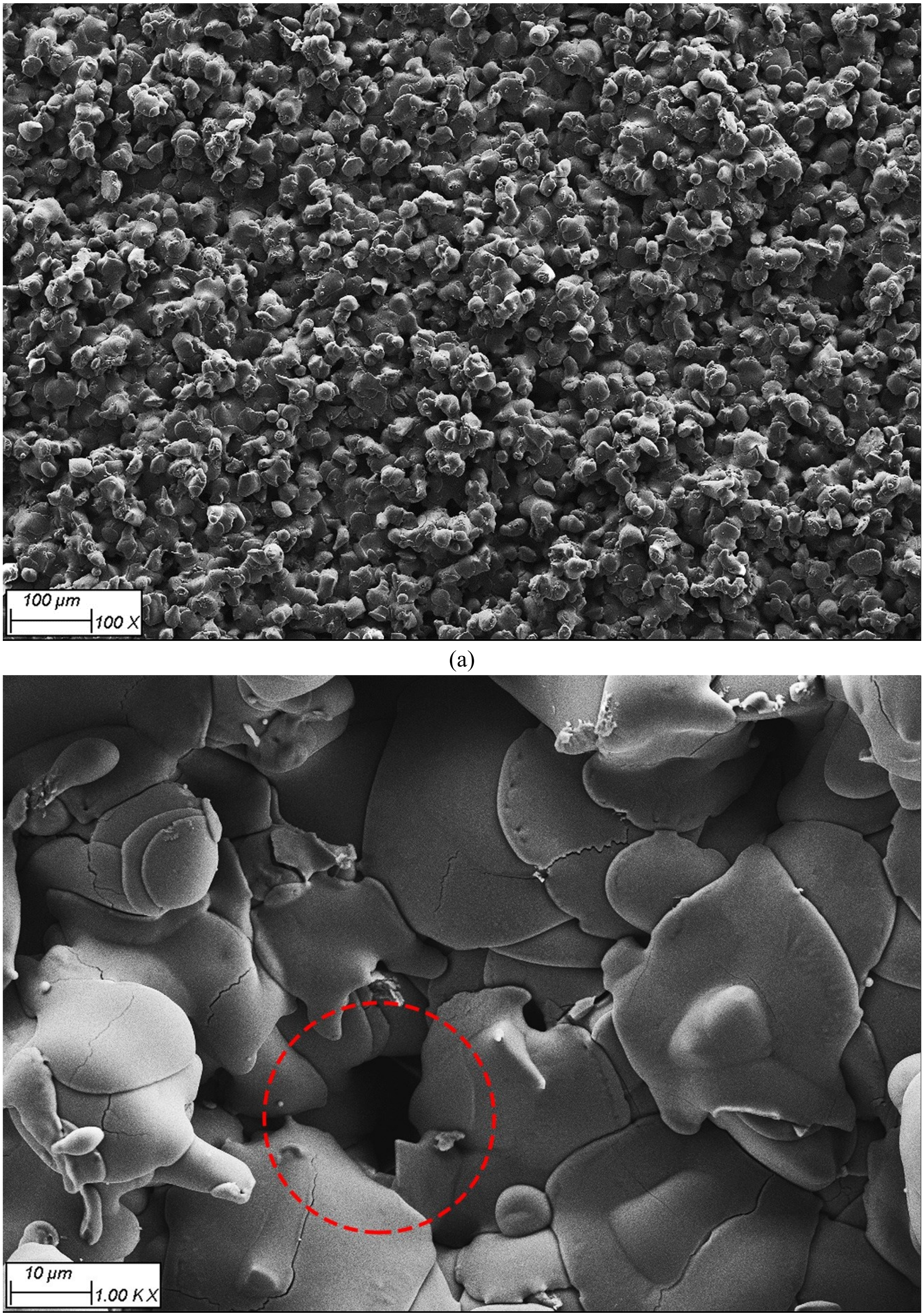

(a)

(b)

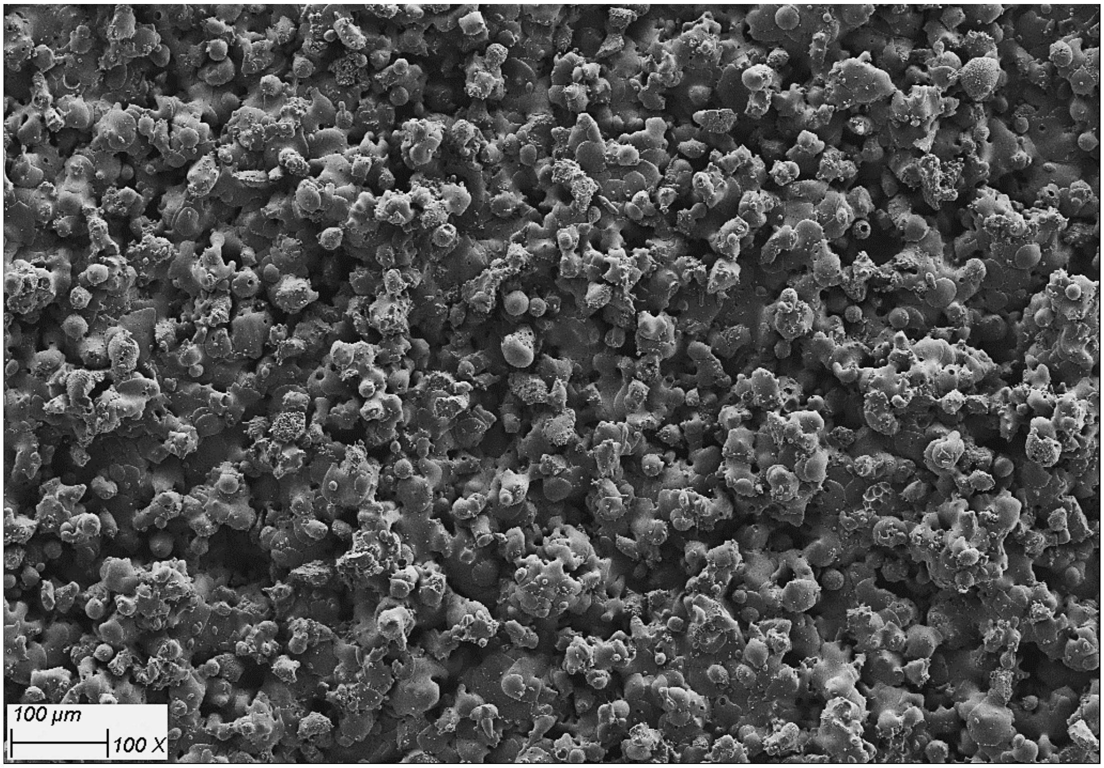

(c)

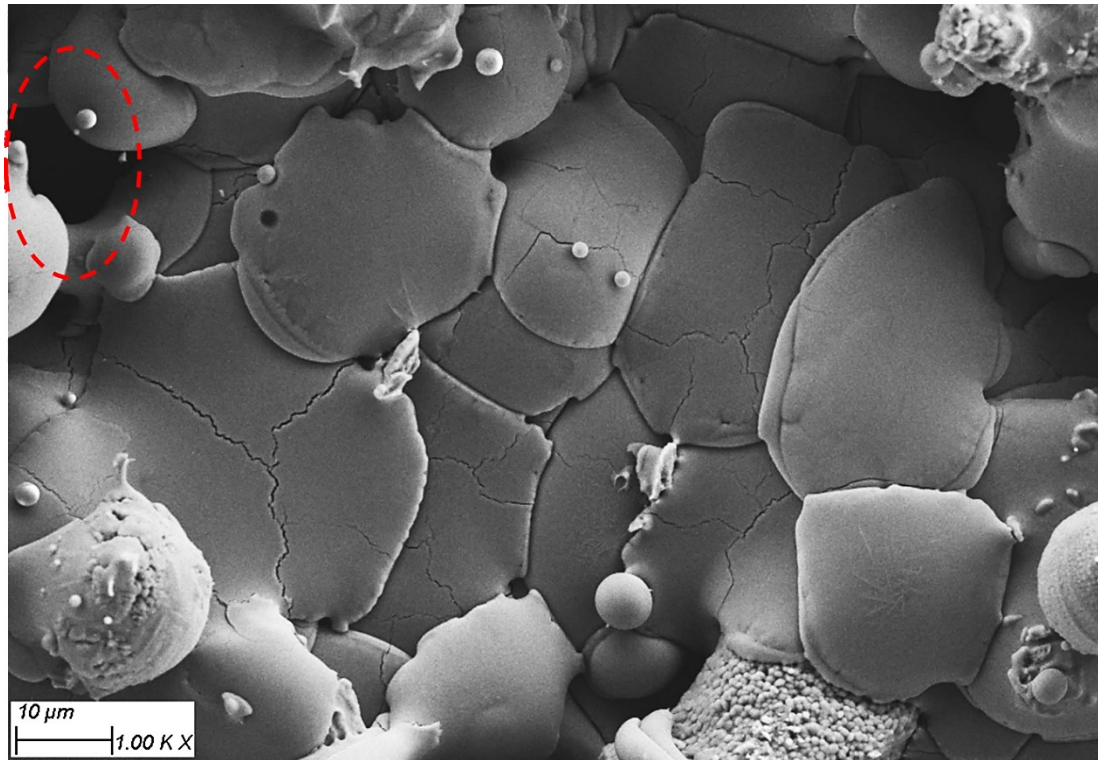

(d)

Figure 3-8 Secondary SEM images from top surface of the electrically insulating layers at 100X and 1000X magnifications; (a)-(b) FS alumina and (c)-(d) FS alumina-titania

The microstructure of the coatings that were fabricated by choosing different spraying parameters on the flat mild steel samples by using flame spraying process, can be seen in Fig. 3-9. From among all the spraying parameter, only the contents of acetylene and oxygen and the stand-off distance (SOD), which are of utmost importance, were varied so that the impact of these parameters on the microstructure of the coating systems could be investigated. Since the impact of changing the parameters were similar for both alumina and alumina-13 wt.% titania coatings, the effect of SOD and oxygen/acetylene ratio are shown only for Al_2O_3-13%TiO_2 and Al_2O_3, respectively. Given the lower melting point of the Al_2O_3-13%TiO_2 (1675 °C [79]) compared to that of the alumina (2054 °C [78]), a denser coating was obtained for alumina-13 wt.% titania coating based on the same spraying parameters even with lower number of passes.

The effect of SOD on the microstructure of the alumina-titania coating can be seen in Figs. 3-9(a) and 3-9(b). It was observed that reducing the SOD from 127 mm (5 in) for the case of S3 to 76 mm (3 in) based on S2 set of parameters resulted in noticeable increase in the porosity of the coating from 15 % to 19 %. The same effect, which was also observed in alumina coating, was due to less exposure time of the powder particles to the high-temperature flame. As a result, the powder particles were melted to a lesser extent leading to a more porous structure. The comparison of the Ni-20Cr S1 and Ni-20Cr S2 in Figs. 3-9(a) and 3-9(b) reveals the effect of oxygen/acetylene ratio on the porosity and oxidation content of the heating element. For the case of Ni-20Cr S2, due to the higher content of acetylene flow, a higher temperature for the flame was obtained that resulted in a denser coating. Furthermore, due to lower flow of oxygen (1.5 instead of 1.9 m3/h), oxidation that can be found in the darker regions was generated to a lesser extent.

Alumina coatings that were fabricated based on S2 and S4 set of parameters are shown in Figs. 3-9(c) and 3-9(d), respectively. A relatively thick, but porous, microstructure was obtained for the case of FS alumina S4. However, the alumina coating that was deposited based on S2 set of parameters, which was close to the stoichiometric ratio of acetylene's combustion, was not satisfactory due to the low deposition efficiency that was caused by lower temperature of the flame that was a result of higher flow of oxygen and lower flow of acetylene into the flame. Further, the microstructure of the FS Ni-20Cr coatings based on S3 and S6 set of spraying parameters can be seen in Figs. 3-9(c) and 3-9(d). Low thickness and remarkable oxidation content of the FS Ni-20Cr S3 coating was due to the increased stand-off distance. Given the more distance that the molten particles had to traverse to reach the sample, they had more interaction with the ambient air within the flame, and as a result of which more oxidation was generated. Increased content of oxidation can also be seen in the FS Ni-20Cr that was deposited based on S6 parameters, which was mainly due to the increased flow of oxygen to 2.1 m^3/h.

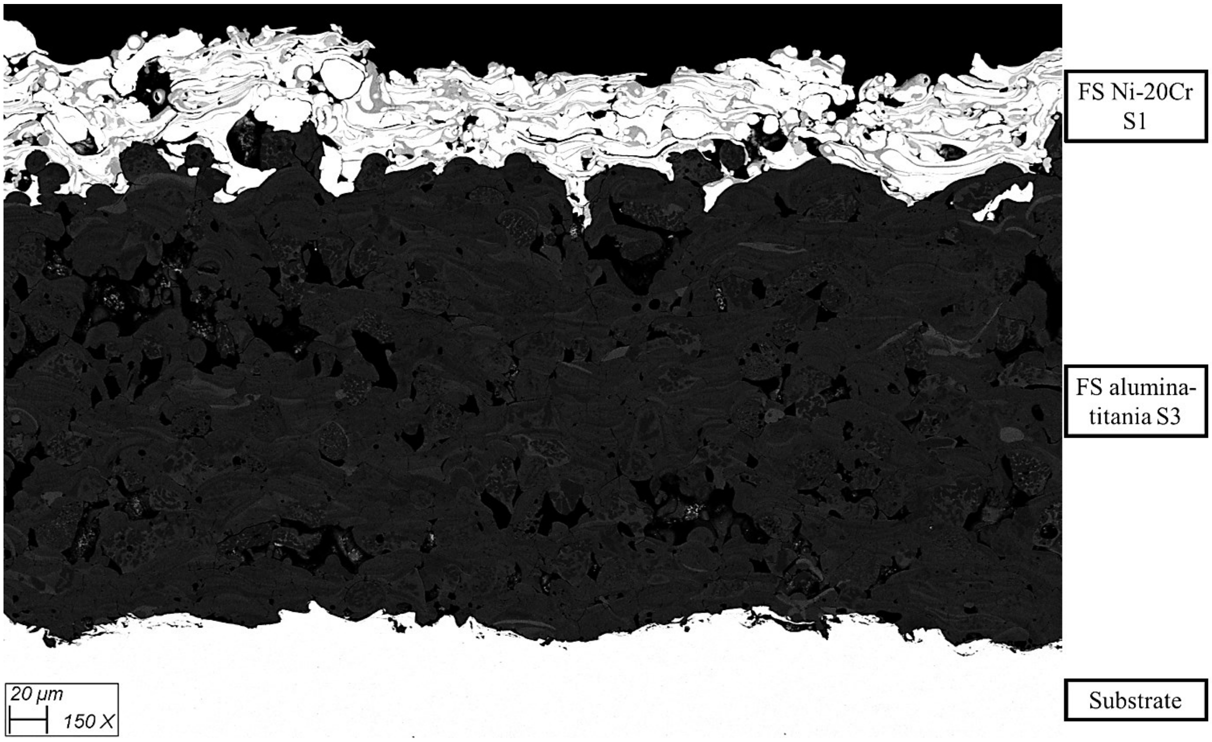
FS Ni-20Cr S1
FS alumina-titania S3
Substrate
20 µm
150 X

(a)

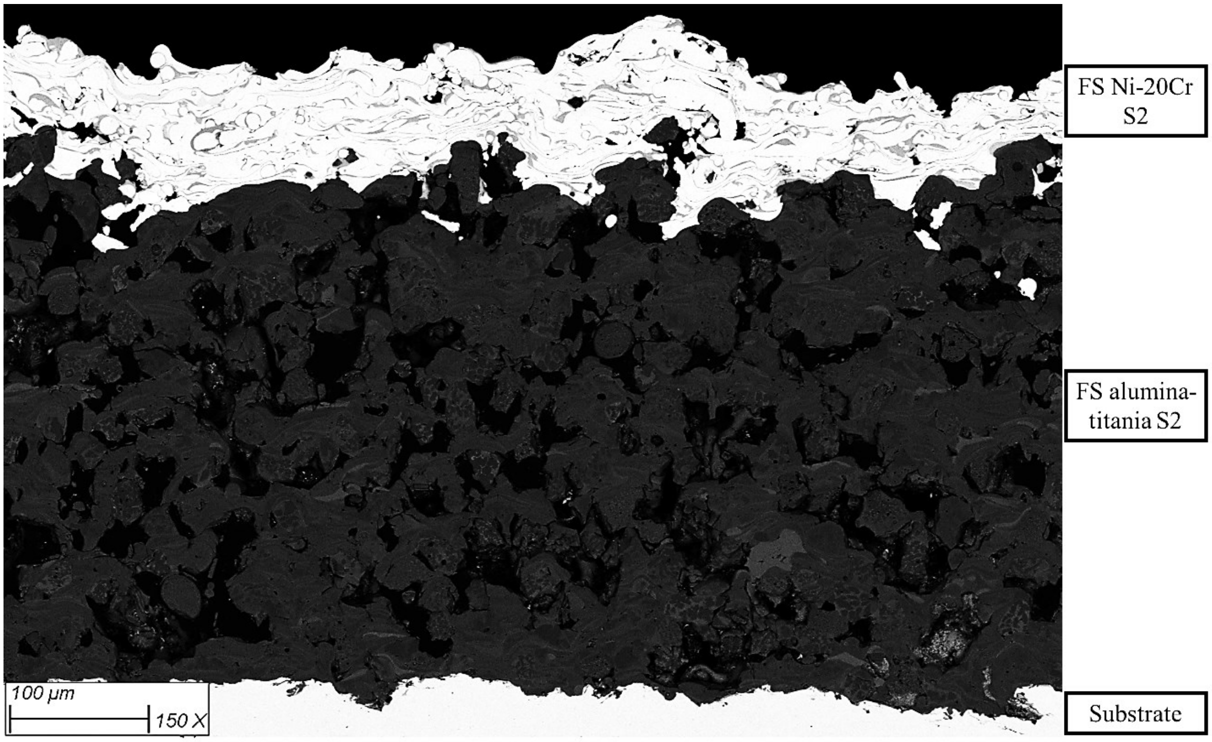
FS Ni-20Cr S2
FS alumina-titania S2
Substrate
100 µm
150 X

(b)

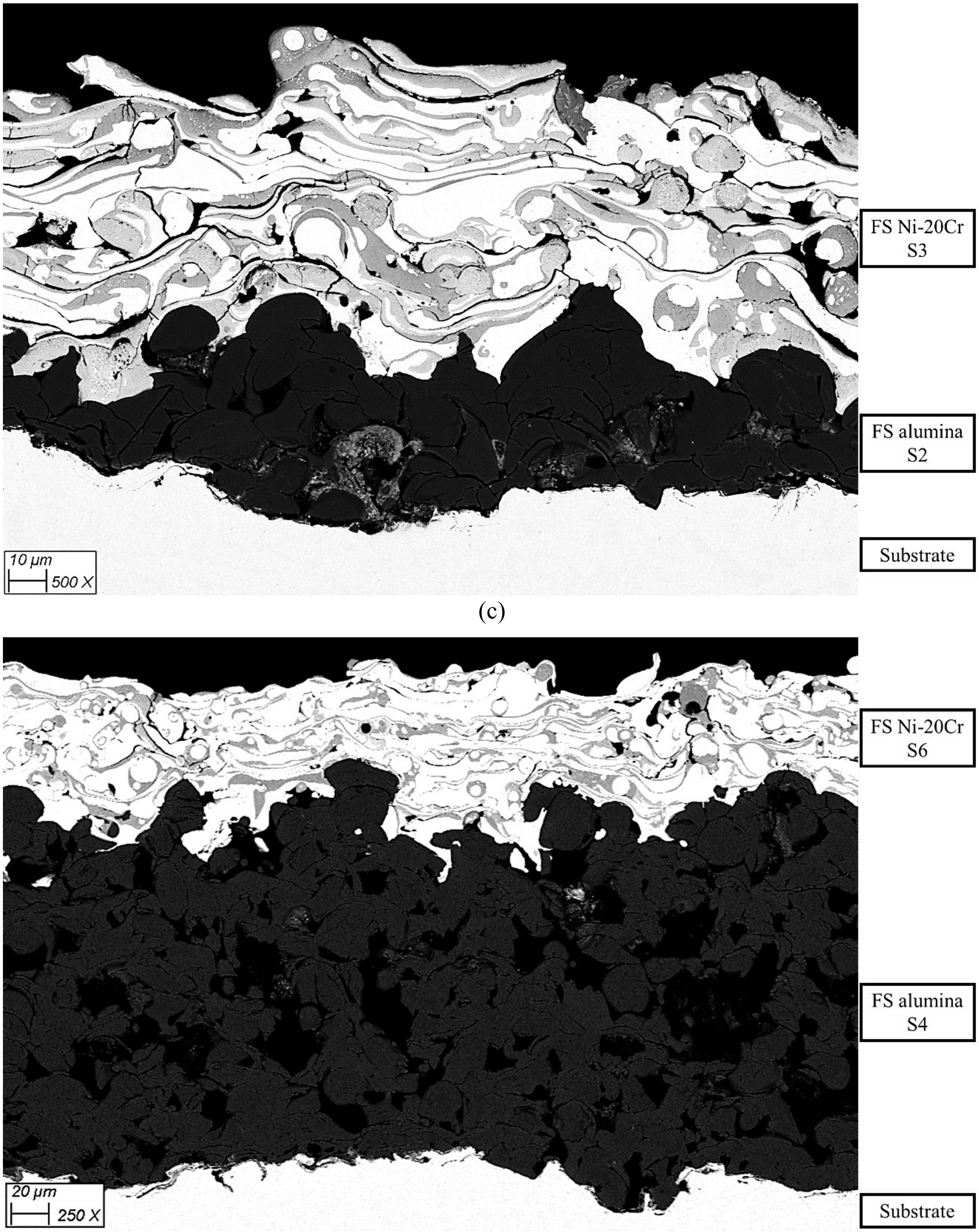

(c)

(d)

Figure 3-9 SEM image taken in backscattered mode from the cross section of the coating systems fabricated by FS process based on different spraying parameters, namely (a) Al_2O_3-TiO_2 (S3)—Ni-20Cr (S1), (b) Al_2O_3-TiO_2 (S2)—Ni-20Cr (S2), (c) Al_2O_3 (S2)—Ni-20Cr (S3), and (d) Al_2O_3 (S4)—Ni-20Cr (S6)

The microstructure of the FS Ni-20Cr coating that was deposited based on S1 set of spraying parameters can be seen in Fig. 3-9(a). However, in order to understand the elemental composition and oxidation content of this coating in a clearer manner, EDS analysis was performed. The distribution of the constituent elements of the FS Ni-20Cr S1 coating can be seen in the elemental maps shown in Figs 3-10(a) - 3-10(d). The bright regions indicate presence of nickel and the dark regions are indicative of formation of chromia (Cr_2O_3) [43], where both chromium and oxygen contents can be found. Further, some regions of light grey color are representative of another impurity phase (chromite ($NiCr_2O_4$) [43]) in which all elements of nickel, chromium, and oxygen can be found. That said, comparison of the SEM images shown in Figs. 3-9(c) and 3-9 (b) indicates the highest and the lowest contents of oxidation for the Ni-20Cr coatings deposited based on S3 and S2 set of parameters, respectively.

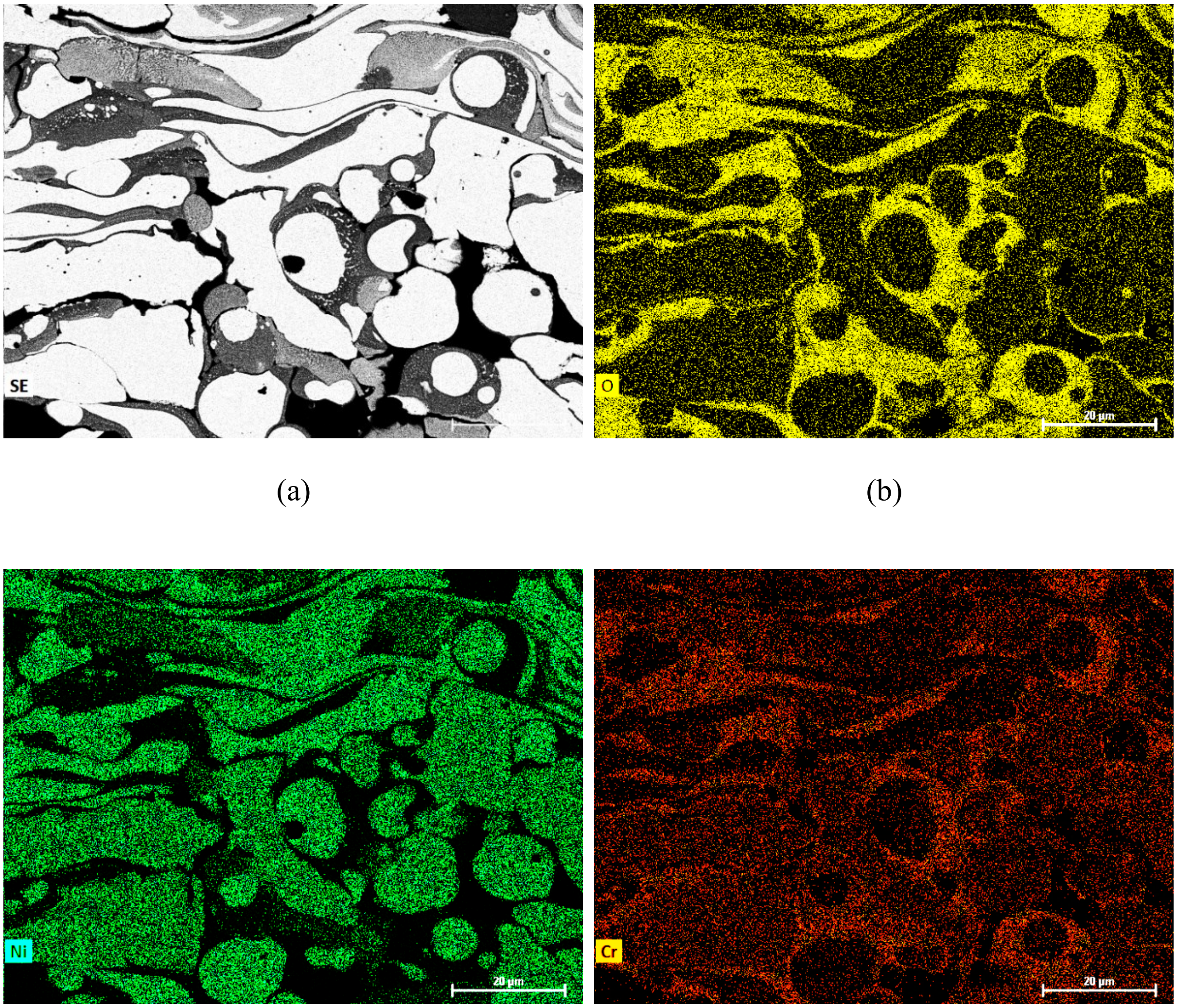

(a) (b)

(c) (d)

Figure 3-10 Representative (a) SEM images in backscattered electron mode and EDS mapping images of (b) oxygen, (c) nickel, and (d) chromium

3.2.2 Electrical Performance

The electrical resistivity of the fabricated heating element was calculated to assess the electrical performance of the fabricated coating systems. In this regard, the dimensions of the samples were taken into calculation to convert the electrical resistance to electrical resistivity, which is a material property, so that the obtained values could be comparable regardless of the dimensions of the samples. The thickness of the coatings were measured by calculating the average value from at least five SEM images (*n* = 5). As an example, the average thickness of the FS Ni-20Cr S1 on flat samples was calculated to be 43 ± 4 µm. The electrical resistivity of the Ni-20Cr heating elements that were deposited on flat samples by FS process are listed in Table 3-3.

Table 3-3 Measured bulk resistivity of the NiCr coatings

Insulating Layer	***Heating Element***	***Resistivity* (Ω-µm)**
FS alumina (S4)	FS NiCr (S6)	4.7
FS alumina-titania (S3)	FS NiCr (S1)	5.0
FS alumina-titania (S2)	FS NiCr (S2)	5.6
FS alumina (S3)	FS NiCr (S4)	6.6
FS alumina (S5)	FS NiCr (S7)	7.9

As shown in Table 3-3, the resistivity of the flame-sprayed Ni-20Cr was found to be 4.7 Ω-µm based on the S6 set of spraying parameters. In contrast, the resistivity of the same material deposited based by way of the same process, albeit with different spraying parameters (S7), was found to be 7.9 Ω-µm, which indicates a 68% relative difference between the obtained values. The higher content of both acetylene (1.3 m^3/h compared to the 0.9 m^3/h of the S1 reference spraying parameters) and oxygen (2.4 m^3/h compared to the 1.9 m^3/h of the S1 reference spraying parameters) in S6 spraying parameters resulted in a higher combustion flame temperature, which led to a dense and uniform microstructure as shown in Fig 3-9(d). This resulted in the reduced resistivity that was obtained from all sets of flame spraying parameters.

3.2.3 Challenges Associated with Fabrication of the Coating System

Brittleness of alumina is one of the design-limiting factors that restrict usage of this material in many engineering applications. This becomes a challenge when maximum functionality is required without comprising the mechanical integrity of this material [85]. In this specific study, alumina layer is deposited between two metallic layers, namely the substrate (low-carbon steel) and a heating element (nickel-chromium). Given the different thermal and physical material properties of these layers, some challenges may be associated with the fabrication and operation of the multi-layered coating-based heating system. One of the main challenges is possible cracking and delamination of the alumina coating from the substrate, which is mainly caused by the generation of thermal stresses at the interfaces with the heating element and the substrate.

The top views of the FS-sprayed alumina and alumina-titania coatings, which can be seen in Figs 3-8(b) and 3-8(d)) reveal cracking within the solidified splats due to the quenching stress even prior to deposition of the NiCr coating. In addition to the quenching stress, thermal stress was also generated during the deposition of the NiCr coating and the following cooling and solidification period. Therefore, in addition to the fine cracks that were formed after deposition of the first layer, some relatively long cracks were generated within the alumina coating, especially at the interfaces, likely because of the generated thermal stresses, the particular positioning of the adjacent pores and merging of the finer cracks as shown in Fig. 3-11 in which presence of cracks both within coating and at the interface can be observed.

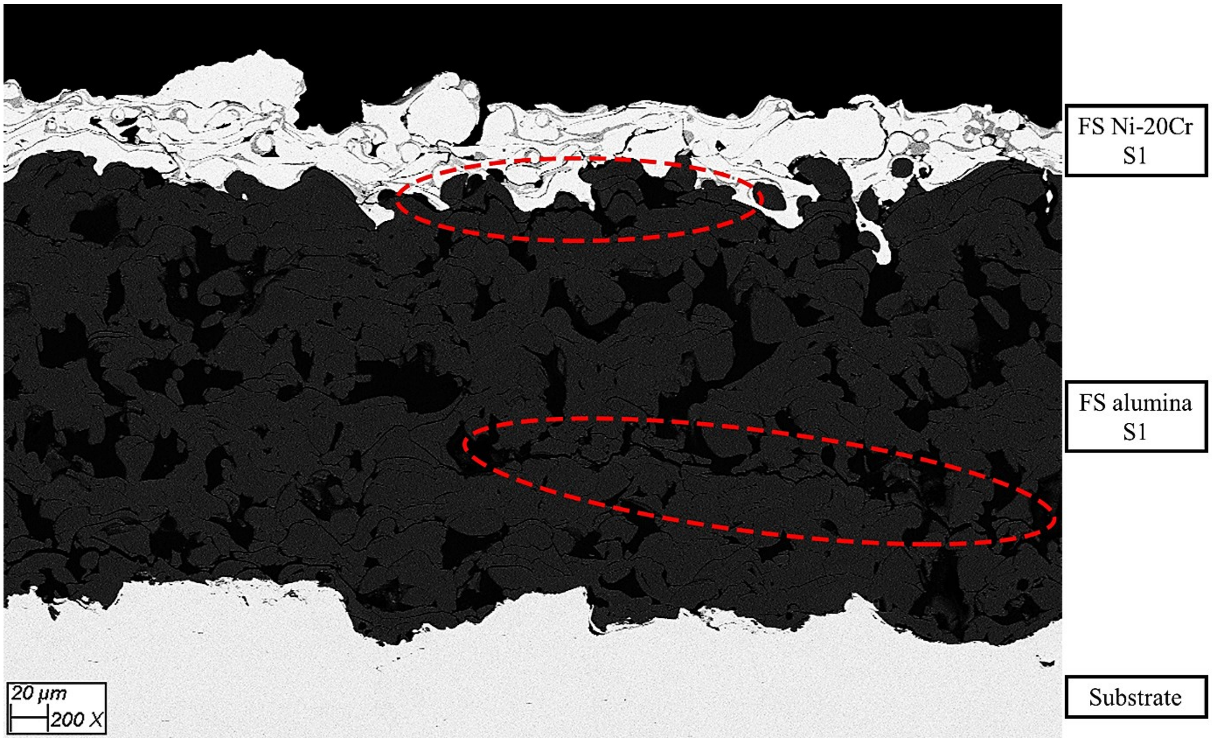

Figure 3-11 Backscattered SEM image of the cross section of the coating systems composed of FS Al_2O_3 S1—FS Ni-20Cr S1

3.2.4 Heating Performance

For the case of pipe sample, various powers were supplied to the heating element (Ni-50Cr coating) over different voltages of 10 V, 15 V, 20 V, 25 V, and 30 V under free convection heat transfer conditions. The performance of the heating element was assessed based on the temperature of the heating element and the duration of time that was needed to heat and melt the ice within the pipe. The transient temperatures of the coating surface and ice/water inside the pipe for the test in which 80 W at 20 V was provided to the Ni-50Cr is shown in Fig. 3-12. Furthermore, the times required for heating and melting of ice inside the pipe are listed in Table 3-4 as a function of the supplied power.

To compare the results between different tests, the duration of test was divided into two different stages heating and melting. Due to the curved form of the ice temperature trace, specifying the precise moment at which the melting stage began may not be possible. It should be noted that the melting process begins from the inner surface of the pipe where measuring the temperature was not possible due to practical restrictions. Therefore, the classification of the different portions of the test to heating and melting stages was subjected to some uncertainty. In order to determine the beginning of the melting stage roughly, the temperature of the coating surface was taken into consideration as a close value to the actual temperature of outer surface of the enclosed ice/water in contact with the pipe. This assumption is defensible because of the negligible thermal resistance value between the heating element and the outer surface of the ice in the pipe, which is a result of high thermal conductivity of the coating layers (13.7 W/m-K for NiCr [86] and 35 W/m-K for alumina [87]) and the steel pipe (order of 50 W/m-K [88]) and the small thicknesses of all the layers (110 µm for Ni-50Cr, 180 µm for alumina, and 3.9 mm for the steel pipe).

That said, the heating period was defined as the duration of time between supplying power to the heating element and the time the coating surface reached the temperature at which the enclosed ice experienced phase change. The melting stage was also defined as the period between the end of the heating phase and beginning of temperature rise at the end of the melting plateau where all the liquid underwent phase transformation. It should be noted that in practice, there was an overlap between the end of heating and beginning of melting stages. In other words, when the outer surface of the ice was melting, the ice at the core of the pipe was still heating up. This can be seen in the lower rate at which the coating surface temperature rises at the beginning of the melting stage, which is mainly because of the reduction in the portion of the sensible heat as the latent heat, which causes the phase change of ice, increases.

The classification of the stages was conducted only for comparison purpose to investigate the performance of the heating system based on different conditions. During the melting stage, the solid-liquid interface that was formed at the inner surface of the pipe at the beginning of the melting period traversed radially inward to the center of the pipe and therefore, the ice transformed into liquid completely. Once all the ice was melted, further transfer of the generated heat manifested itself in the form of sensible heat, which resulted in sharp increase of the water temperature.

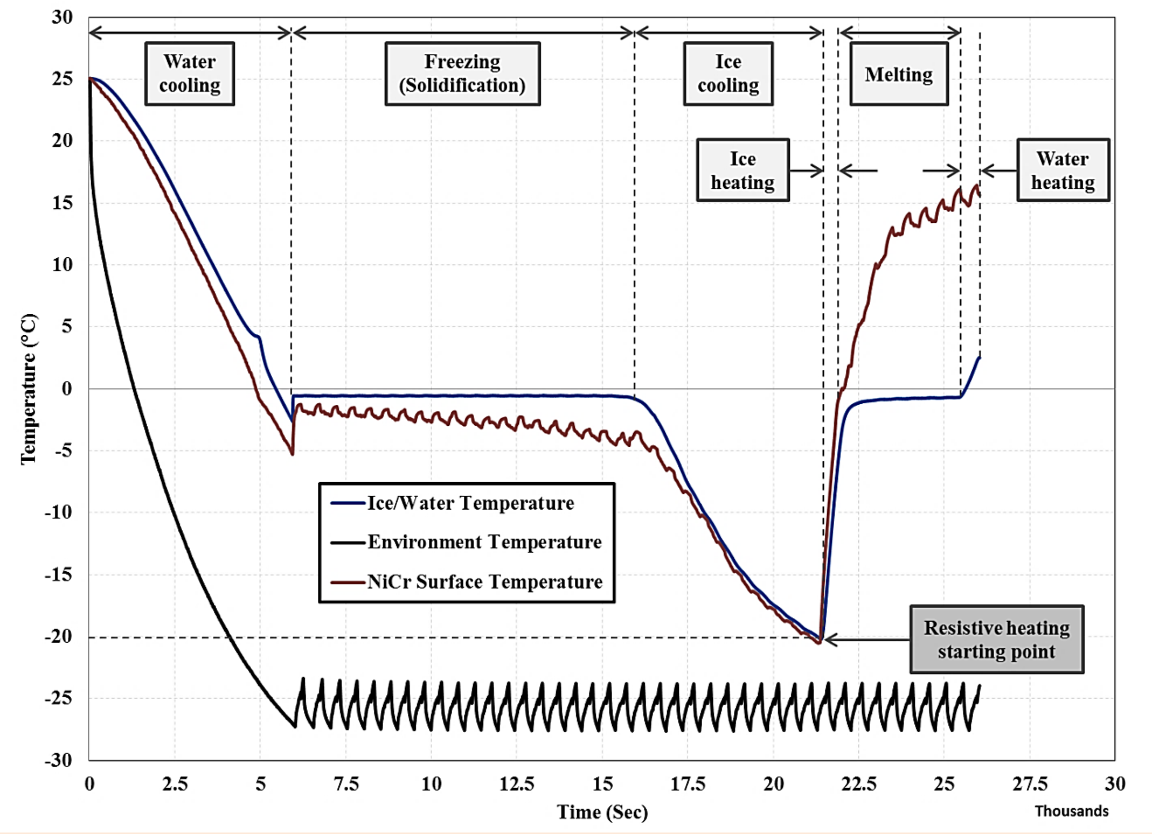

Figure 3-12 Temperature measurements from a heating test under free convection condition in which 80 W over 20 V was provided

Table 3-4 Heating and melting times of ice within a coated 60-mm nominal diameter low carbon steel pipe under free convection heat transfer conditions

Test No.	Voltage (V)	Current (A)	Supplied power (W)	Ice heating time (min)	Melting time (min)
1	10	2	20	121 ± 3	1024 ± 5
2	15	3	45	31 ± 1	158 ± 3
3	20	4	80	10 ± 1	61 ± 1
4	25	5	125	6 ± 1	35 ± 1
5	30	6	180	4 ± 1	26 ± 1

Before conducting the heating tests for the pipe sample the electrical resistance of the heating element (Ni-50Cr coating) was measured to be 5 **Ω**. It was observed that this value was constant in all the heating tests. The values for current, which are listed in Table 3-4 and Table 3-5, were measured during each heating test. It was observed that the coating was performing based on the Ohm's law in which the applied voltage was proportional to the current. That said, it was concluded that the heating element (Ni-50Cr coating) that was deposited on the cylindrical sample was an Ohmic material as previously found by Lopera-Valle and McDonald [46]. During the heating tests, due to the increase in the temperature of the flame-sprayed Ni-50Cr (heating element), the electrical resistance of the coating was increased [46], as a result of which slight (≤ 2 %) decrease in the values of the current was observed.

It was observed that even 20 W over 10 V was sufficient for the developed heating system to heat and melt the ice inside the bare pipe that was located in the cold room and was directly exposed to stagnant cold air at -25°C. This speaks to the high efficiency of the fabricated heating system on the pipe that has been proven to be noticeably higher than the conventional tracers. The reason for that is the intimate contact between the heating system and the substrate.

Furthermore, homogenous temperature distribution over large surface can be obtained from such heating systems [42] that could not be obtained for ordinary tracers that are widely used in the industry. As can be seen in Table 3-4, the durations of heating and melting were dependent on the supplied power. However, the impact of supplied power on duration of the heating test was less for high powers such as 180 W over 30 V. The reason for that was more sensible heat that was transferred to the coating, which resulted in increased coating surface temperature that led to more dissipation of heat to the ambient cold air.

In order to assess the performance of the heating system under critical environmental conditions, the Joule heating test was also conducted under forced convection heat transfer condition. Utilization of the fan in the duct increased the speed of the free-stream airflow to 31 km/h, which was even more than the outdoor wind speeds in winter that are typically around 24 km/h according to American Society of Heating, Refrigeration, and Air-conditioning Engineers (ASHRAE) and Canadian Wind Energy Atlas [89]. Six different voltages were applied to the heating element to assess the performance of the developed coating-based heating system under forced convection heat transfer conditions. Aside from the same five voltages that were also provided in the free convection heating tests, a relatively high power of 500 W over 50 V was also given to the heating element to study the sustainability of the developed coating system to perform well under severe electric power input. Based on calculations, continuous provision of 10 W should be sufficient for anti-icing of a meter of thermally insulated 2-inch diameter pipe. Given the length of the coated pipe in this study, the supplied power of 500 W was 200 times greater than the necessary supplied power. The duration of times for heating and melting stages for each of the electric loading conditions under forced convection heat transfer scenario is listed in Table 3-5.

Table 3-5 Heating and melting times of ice within a coated 60-mm nominal diameter low carbon steel pipe under forced convection heat transfer conditions

Test No.	Voltage (V)	Current (A)	Supplied power (W)	Ice heating time (min)	Melting time (min)
1	10	2	20	NA	NA
2	15	3	45	NA	NA
3	20	4	80	NA	NA
4	25	5	125	11 ± 1	157 ± 3
5	30	6	180	5 ± 1	55 ± 1
6	50	10	500	1	12 ± 1

The temperature traces of the heating element surface and ice/water within the pipe for the case of 500 W supplied power are shown in Fig. 3-13. Due to the provision of high electric power input to the bare pipe that was exposed to cold ambient air, the heating and melting stages only took only about 13 minutes. However, supplying high powers is not suggested as it produces a noticeable temperature gradient within the coated pipe as evidenced by the remarkable gap between the temperatures of the coating and ice at the centerline of the pipe. The disadvantages of such an action are twofold. First, the rate of heat loss to the cold ambient environment is increased. Second, the temperature gradient within the coating system can increase the thermal stresses between the nickel-chromium and alumina coatings and, as a result, threaten the sustainability and useful lifetime of the coating system.

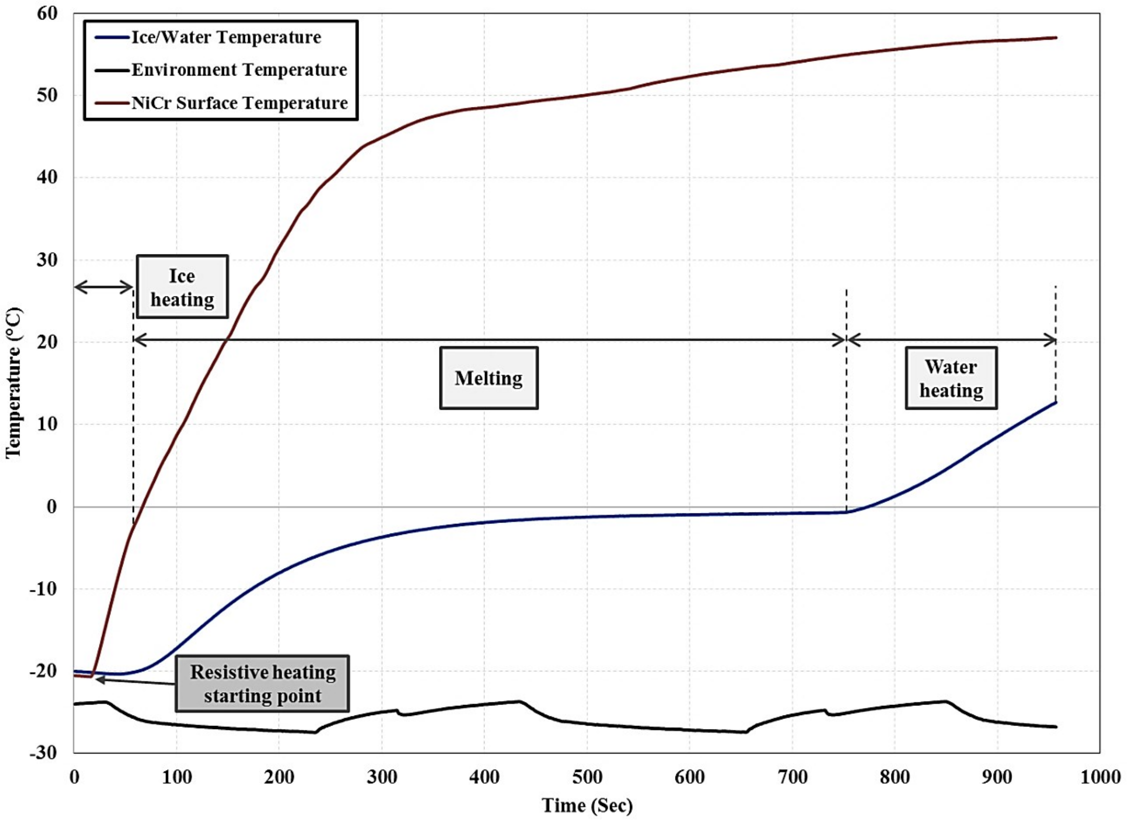

Figure 3-13 Temperature measurements from a heating test under forced convection condition in which 500 W over 50 V was supplied

Due to the manipulation of motion of air inside the duct and around the pipe, the heat transfer coefficient was increased and caused increased surface heat transfer rate based on Newton's law of cooling [90], which resulted in higher rate of heat loss and longer durations of heating and melting compared to the case in which fan at the end of the duct was not employed. As can be seen in Table 3-5, in the first three tests (No. 1, 2, 3) the power was not sufficient to heat and melt the entire ice. For instance, the temperature of the ice could not increase from -20°C when 20 W was provided to the heating element. Further, for the cases in which 45 W and 80 W were supplied the system reached equilibrium state at -13°C and -2°C, respectively.

The temperature gradient between the heating element and the center of pipe was lower during the ice heating stage compared to the melting stage. This could be observed in heating experiments in which high electric powers were supplied. Although the thermal diffusivity of the ice is relatively low (1.194×10-6 m^2/s) [52], it is more than eight times greater than that of water [91]. Therefore, once a portion of annular ice at inner surface of the pipe was melted and transformed to water, the rate of heat transfer to the ice at the core of the pipe was reduced due to the reduction in the thermal diffusivity and resulting reduced ability of the material to conduct thermal energy through itself by conduction, because of higher thermal inertia of the water compared to that of the ice. As a result, the gap between the temperature traces of the coating and ice became much wider as can be seen in Figs. 3-12 and 3-13.

In addition to the cylindrical sample, the heating tests were also conducted for the flat samples under both free convection heat transfer conditions. The performance of the FS Ni-20Cr coatings were evaluated by conducting heating tests. Due to the different microstructures and thicknesses of the Ni-20Cr coatings, which resulted in variable electrical resistances for the fabricated heating elements, care was taken to supply proportional voltages to the coating systems such that the generated powers were the same for all coating systems. In this regard, the same power of 10 W, 20 W, and 50 W was supplied to the flat samples, which were placed inside a cold room that was equipped with a temperature controller. The transient temperature of the coatings surfaces was measured from the middle of the samples where temperature was the highest during the heating test [46]. The electrical resistance of the heating elements did not vary noticeably (less than 4%) during the heating in the temperature range between -20 °C and 20 °C that is a common range for above-ground bare pipes. As can be seen in Fig. 3-14, both coating systems behaved similarly. The slight deviations between the temperature graphs in Figs. 3-14(a) and 3-14(b) were likely due to the relative difference in the electrical resistance of the heating element and the circulation of the air within the cold room and inside the closed galvanized duct for the tests that were performed under free and forced convective heat transfer conditions.

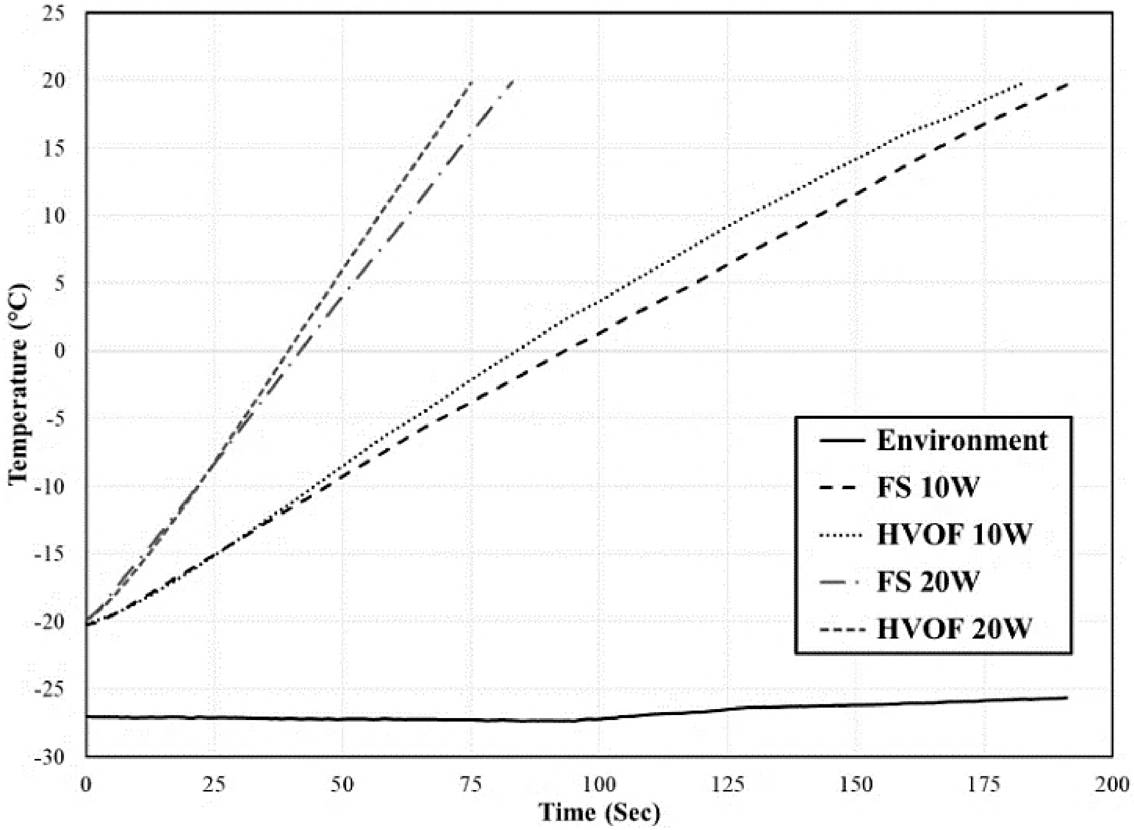

(a)

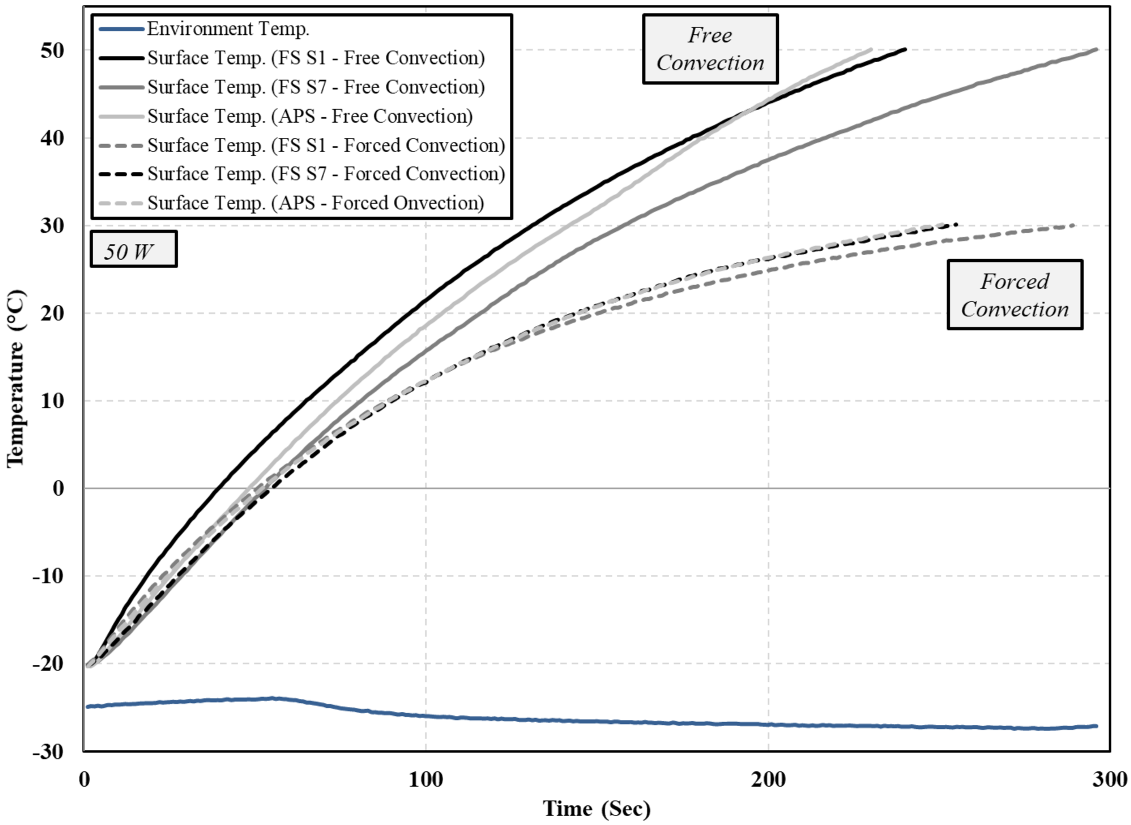

(b)

Figure 3-14 The transient surface temperature of the FS-, APS-, and HVOF-sprayed Ni-20Cr coatings during the heating test under free convective heat transfer condition and supplied powers of (a) 10/20 W, and (b) 50 W

In order to ensure proper performance of the coating system and its structural integrity under several loading conditions and high supplied powers, a power of 150 W was supplied to one of the 127 mm x 25.4 (5 in x 1 in) flat samples. The temperature trace of the heating element, which can be seen in Fig. 3-15, shows functionality of the coating system even at much higher temperature ranges that are required for de-icing application. Given the melting point of the tin solder material, which was used for electrical connection of the copper strips to the connecting wires of the power supply, is about 190 °C, the test was stopped when the surface temperature reached 200 °C. Provision of the high power of 150 W to a bare small scale sample that is exposed directly to the cold ambient air and proper functionality of the coating system even at temperature that are much higher than the actual requirement of the heating system can ensure the end users about proper performance of the developed heating system. A relative increase of 21% was observed in the electrical resistance of the flame-sprayed coating-based heating element during the heating test, which clearly shows the dependency of the electrical resistance of the Ni-20Cr coating on temperature.

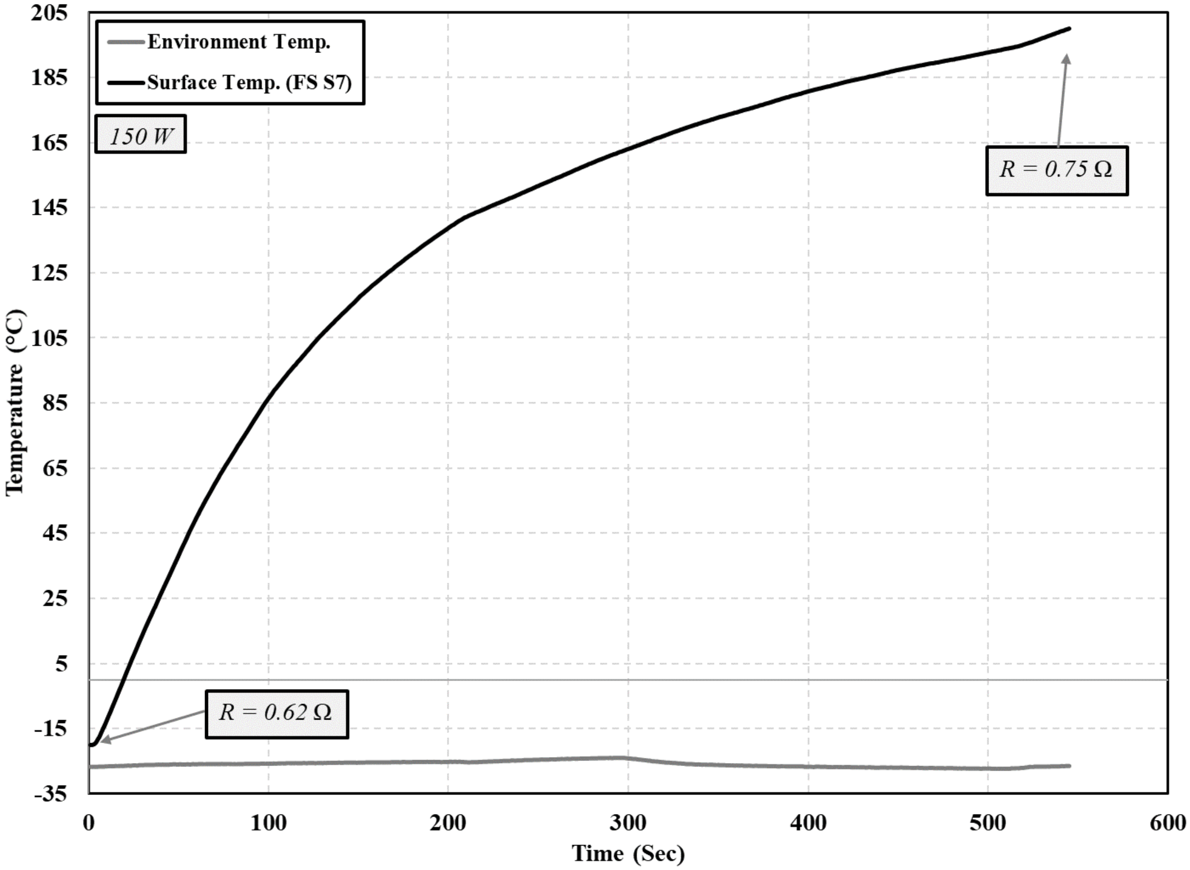

Figure 3-15 Functionality of the developed coating system at relatively high temperatures and the resulting impact on the resistance of the heating element

3.2.5 Challenges Associated with Utilization of the Coating System

In order to assess the reliability of the developed coating systems, high power inputs up to 500 W were supplied the coated pipe while it was placed in front of the axial fan inside the closed duct and was directly exposed to the circulation of the cold air. The purpose was to provide the coated pipe with the most severe environmental and electrical loading conditions to see investigate its probable failure. Obviously, the coating-based heating system would not be exposed to such critical conditions in case it is used properly for temperature protection of pipelines in the industry. After the heating system operated more than 100 hours and experienced at least 30 different heating tests under severe conditions of high-power input and direct exposure to the cold ambient air, several axial cracks were observed on the surface of the heating element. The coated pipe assembly was then sectioned and a portion from the damaged area was removed for microstructural analysis. The micrographs taken from the cross-section of the damaged part are shown in Figs. 3-16(a) and 3-16(b).

Given the noticeable difference in the thermal expansion coefficient of the alumina coating and that of the carbon steel pipe, thermal stresses were generated at the interface that resulted in formation and propagation of cracks along the interface as shown in Fig. 3-16(a). Expansion of the pipe in the circumferential direction, especially in the experiments in which noticeable increase was caused due to the high supplied power, resulted in complete separation of the bi-layered coating in the circumferential direction as shown in Fig. 3-16(b). It is noteworthy that even under this circumstance, partial detachment of Ni-50Cr coating from alumina was not observed. Based on the micrographs that were taken from the damaged zone, in all the cases, the delamination occurred at the alumina-substrate interface, which is mainly because of remarkable difference in the material properties of the afore-mentioned layers. Given the novelty of the application of the developed coating system on steel pipes, no methodical study has been done on the failure of these coatings under thermal cyclic loadings yet. In this regard, further study of the durability of the developed coating system and its reliability in service for relatively long runtime would be the subject of the next study.

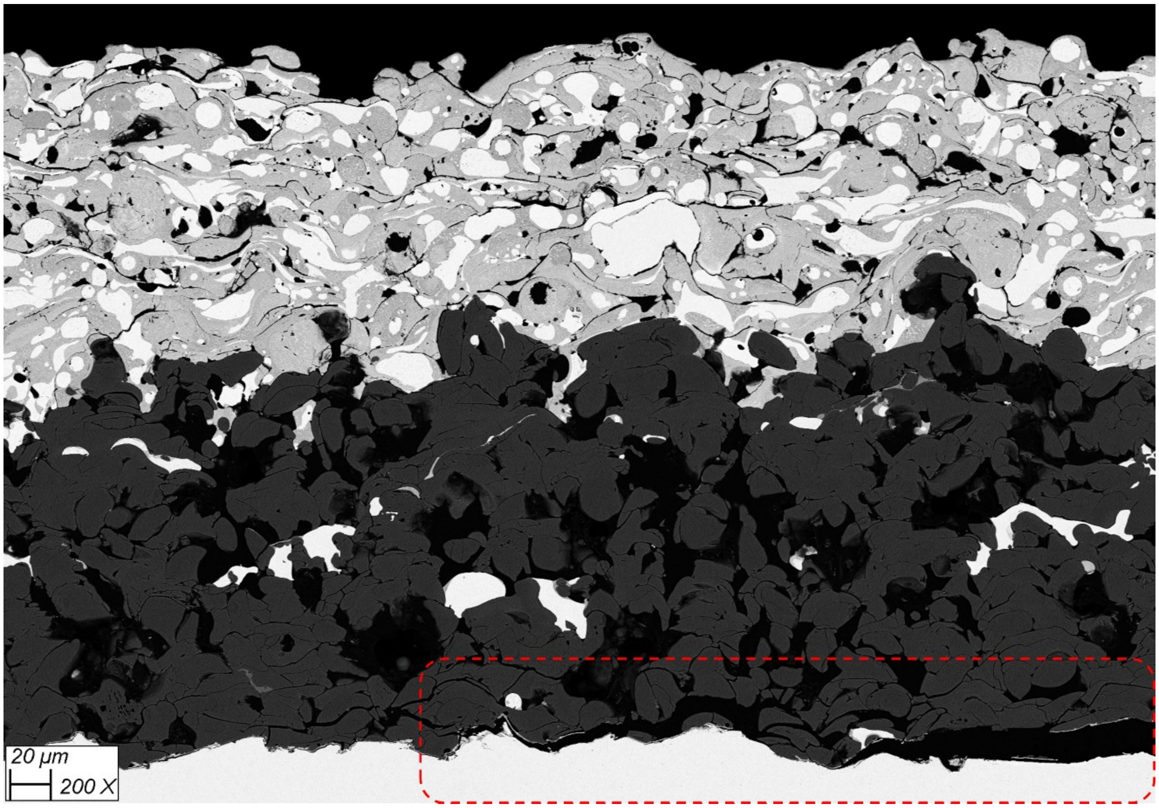

(a)

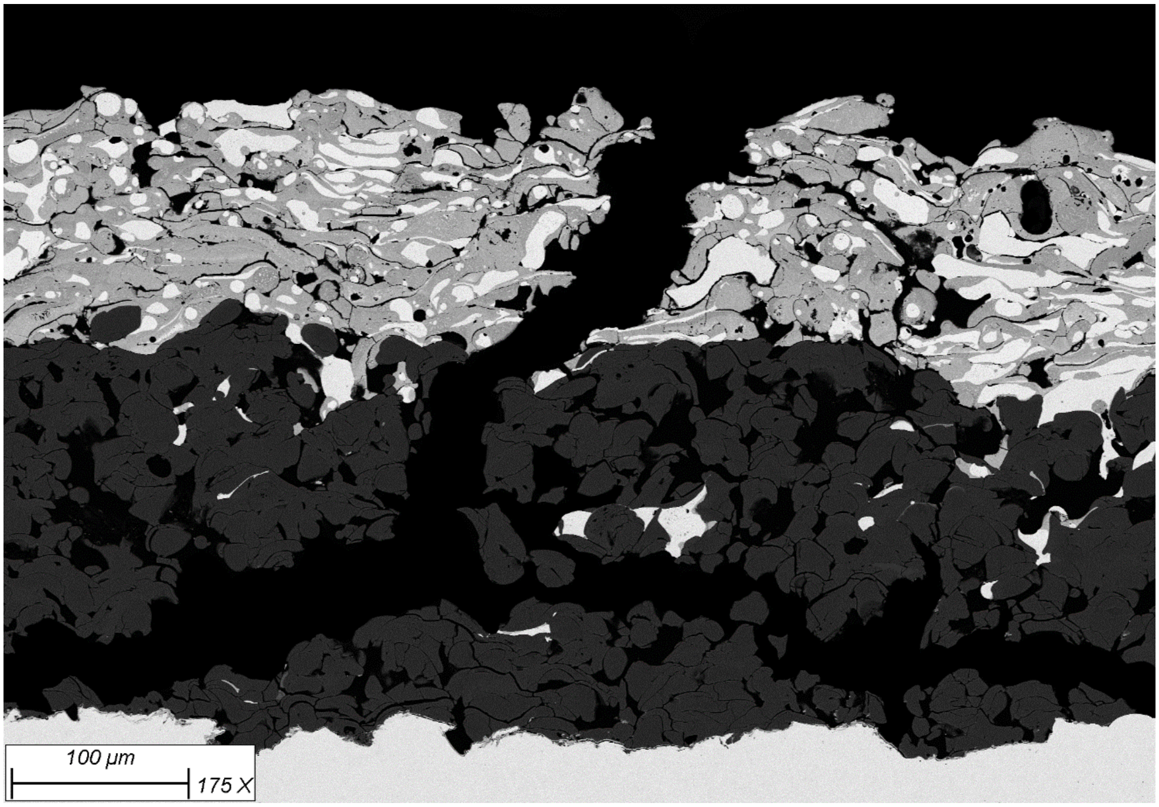

(b)

Figure 3-16 SEM images of flame-sprayed bi-layered Ni-50Cr-alumina coatings after thermal loading cycles at (a) the alumina-substrate interface and (b) the damaged cross section

3.2.6 Temperature Distribution of the Coated Pipe Surface

A high-speed thermal imaging camera (FLIR X8500sc MWIR, FLIR Systems, Inc., Wilsonville, Oregon, USA) was employed to get the temperature contour of the Ni-50Cr coating during the heating test. The camera was placed at the end of the duct to capture a full view of the coated section of the pipe. Due to the restrictions for operation of the thermal camera, the environment temperature was set to -15°C and the fan at the end of the duct was not employed to cause any interruption or disturbance in the data collection process by the thermal imaging camera. The images that are taken from the camera at specific intervals are shown in Fig. 3-17.

The power of 100 W was continually supplied to the heating element until the surface of the coating reached the maximum temperature of 50°C.

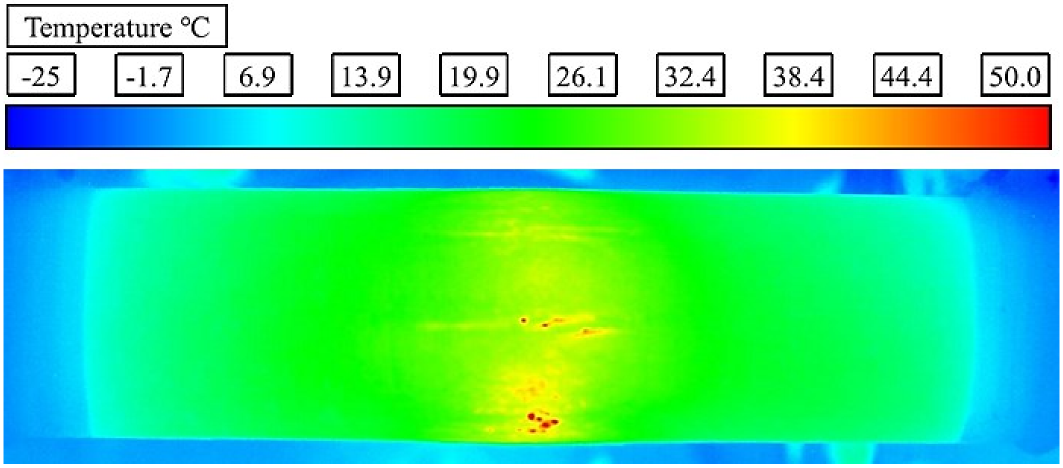

(a)

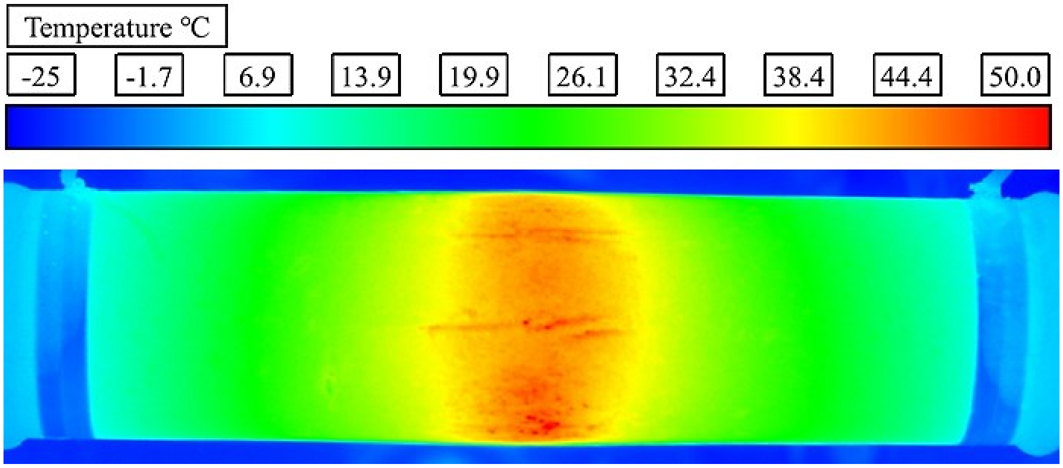

(b)

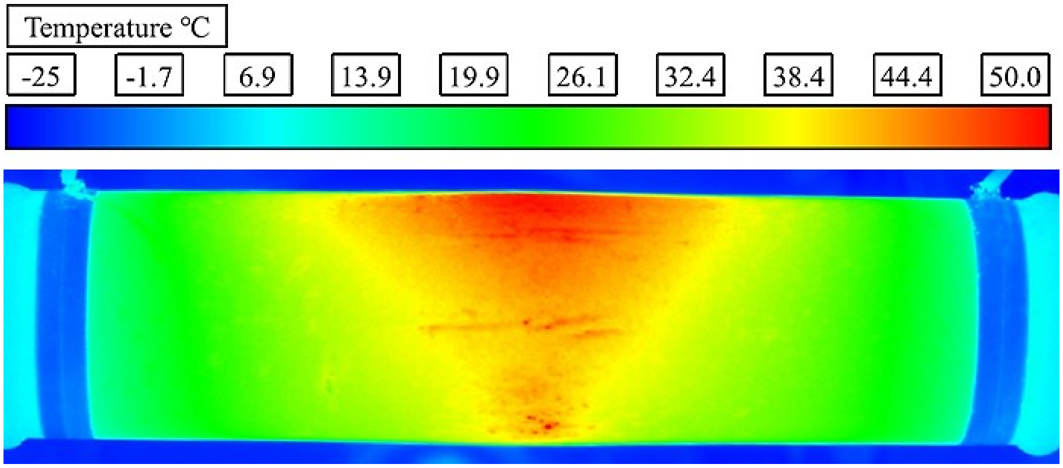

(c)

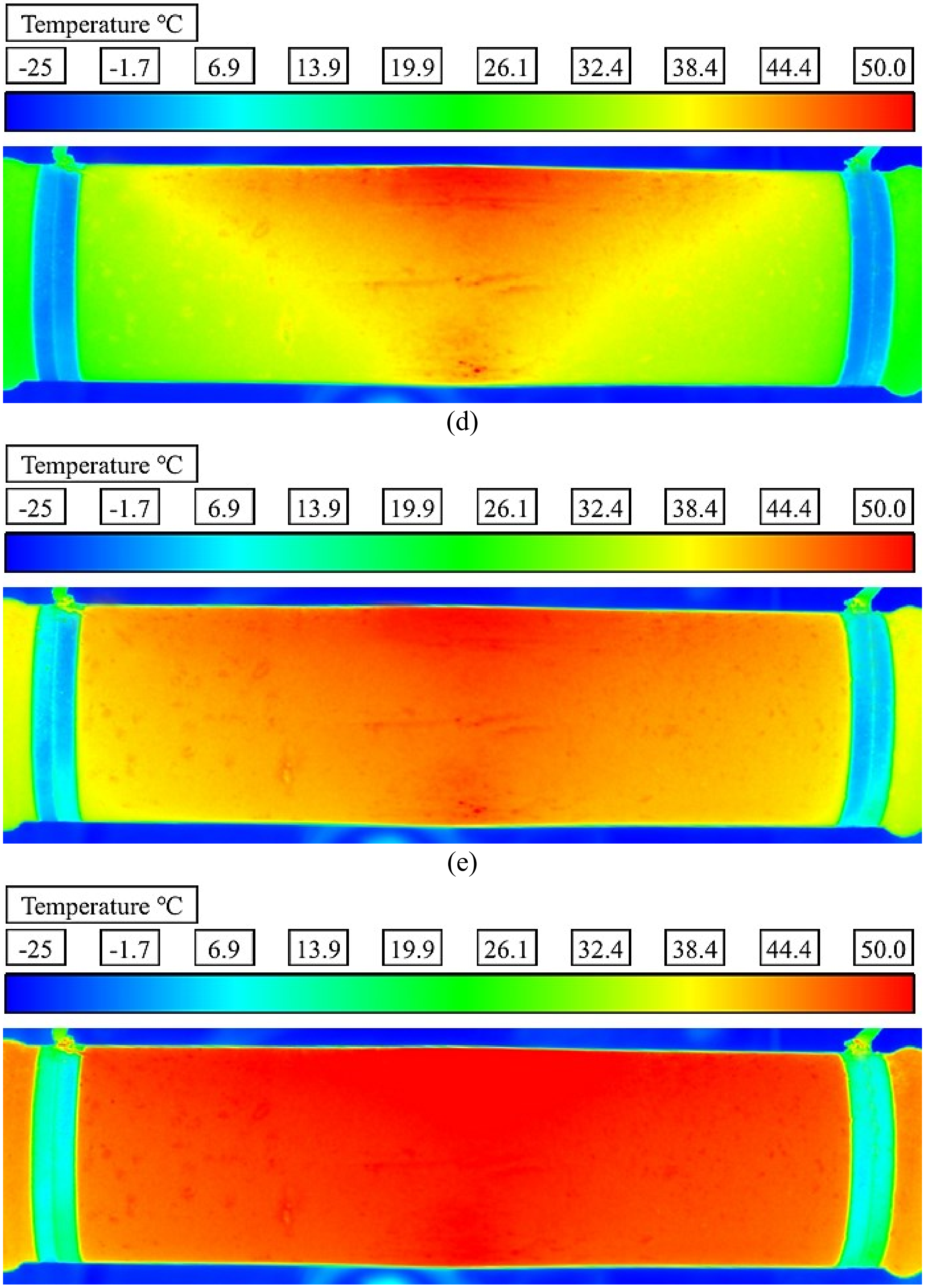

(d)

(e)

(f)

Figure 3-17 The temperatures contours taken from the coated pipe surface during the heating test at (a) 60 s, (b) 600 s, (c) 1,200 s, (d) 3,600 s, (e) 4,800 s, and (f) 6,000 s

The maximum temperature of the heating element was achieved at the middle of the heating element as shown in Figs. 3-17(a) to 3-17(f). The main reason for the temperature gradient along the surface of the coated pipe here was likely the heat dissipation through the end caps in the pipe assembly, which acted as heat sinks. Higher temperature was also observed at the upper parts of the coated pipe, which was because the 10 vol.% of air that was included in the pipe prior to fastening and tightening of the thermowells to prevent internal pressurization and possible damage to the coating system due to the volume expansion after formation of ice inside the pipe. Therefore, during and after the melting stage, which are shown in Figs. 3-17(a) - 3-17(d), the upper part of the pipe was warmer because of the shrinkage in the volume of the mixture of ice and water during the melting stage and the resulting lack of intimate contact between the inner surface of the pipe and the enclosed ice/water.

Minor axial cracks can be observed clearly in the middle of the pipe section in the images that were taken by the thermal camera, which are shown in Figs. 3-17(a) and 3-17(f). These images speak to the functionality of the coating system even after formation of relatively large cracks. The developed coating system would be operational until the heating element or the bi-layered coating system is removed entirely from the circumference of the pipe even in a short length of pipe, which can bring about discontinuity between discrete sections of the coating system. Based on visual inspection of the coating system and examination of the microstructure of the coating system, and the direction of the generated cracks that are formed along the axial direction of the pipe rather than circumferential direction, the possibility of total failure of the coating system is too low. Therefore, it is expected that misuse of the coating system and exposure to critical environmental conditions only affect the resistance of the heating element and do not result in the failure of the coating system.

In order to have a better understanding of the temperature distribution on the surface of the heating element, the temperature profiles along the axial direction of the pipe from one copper ring to the other one were obtained from the temperature contours as shown in Fig, 3-18(a). The increase in the temperature of the heating element can be seen in Fig. 3-18(b) at different time intervals. At the early stages of the heating stage, higher temperature gradient can be observed in the temperature profiles. However, due to the circulation and the resulting free convection of the water inside the pipe during and after the melting stage, more uniform temperature was achieved on the surface of the heating element.

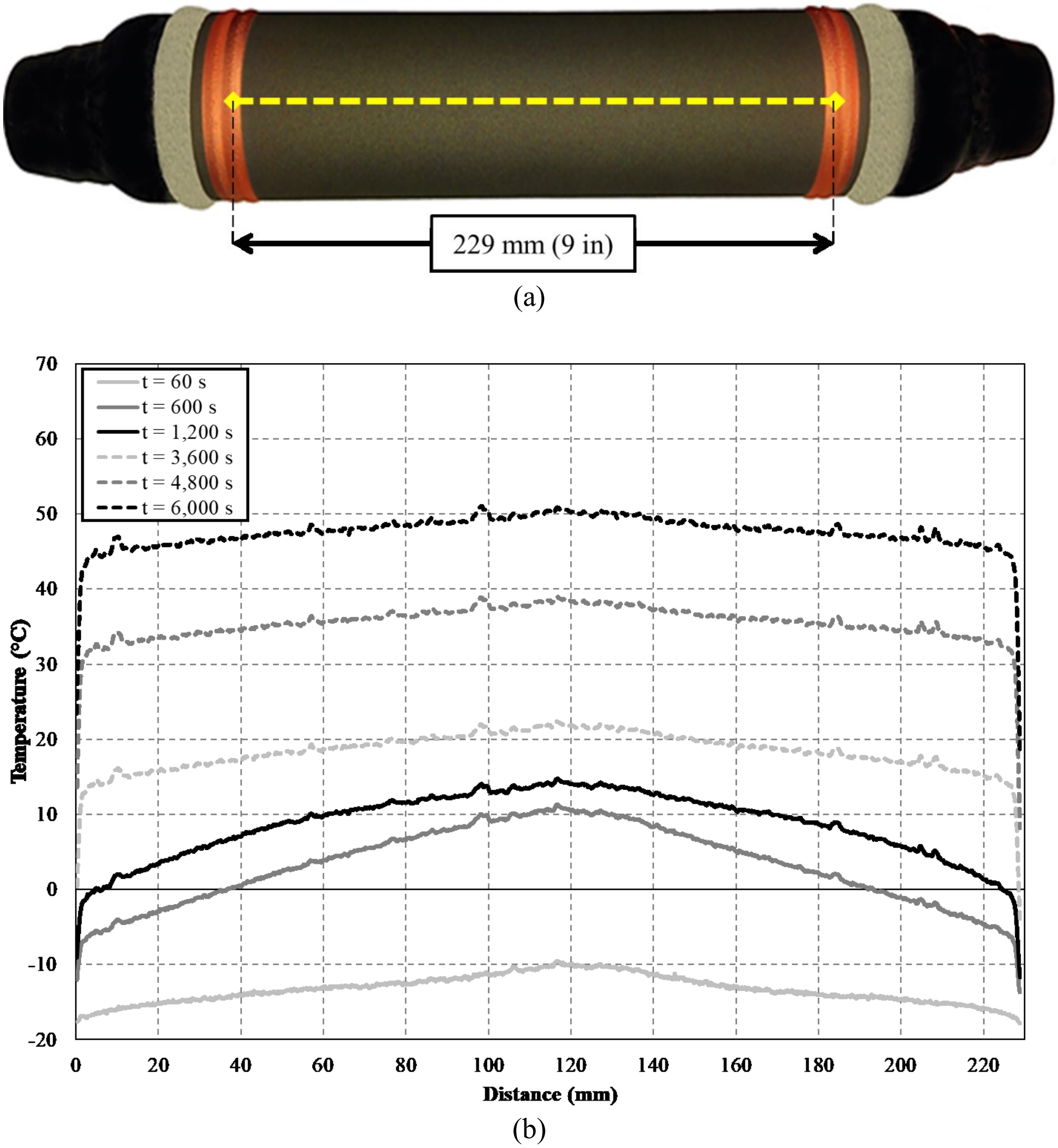

Figure 3-18 Representative (a) the line from which the temperature profiles were obtained, (b) temperature profiles obtained at various times

3.3 Conclusions

Flame spraying and cold spraying processes were employed in this study to fabricate multi-layered coating-based heating systems on flat and cylindrical samples for de-icing purpose.

The fabricated coatings were also characterized by using scanning electron microscopy (SEM) and energy-dispersive X-ray spectroscopy (EDX). The performance of the coating-based heating systems that were fabricated by using different thermal spraying processes was assessed by conducting heating tests under various environmental and electrical loading conditions. The microstructure of the fabricated coating systems was examined after conducting the heating tests by using scanning electron microscopy (SEM) to observe the extent of exerted damage to the bi-layered coating. Based on the observations, obtained results, and microstructural analyses, and in the view of foregoing discussion, the following conclusions can be drawn:

- The feasibility of utilization of the multi-layered thermally-sprayed coatings as resistive heating systems for prevention of formation of ice within the pipes and protection of them against bursting was studied. It was found that the compound of the selected materials, namely alumina, as an electrically insulating layer, nickel-chromium, as a heating element, and copper, as an electrical contact, were satisfactory for the given Joule heating task.

- Penetration of flame-sprayed NiCr into the flame-sprayed alumina and alumina-titania coatings was observed in the SEM images from the cross-section of the coating systems. This may be considered as an advantage from mechanical viewpoint thanks to the enhanced adhesion and interlocking between the coating layers. On the other hand, it may be considered as a drawback due to the decreased effective thickness of the dielectric layer. Therefore, FS alumina coatings should be deposited with higher thicknesses compared to the SPS alumina coatings to protect this layer against dielectric failure and the whole coating system against short circuiting and malfunction.

- It was observed that only 20 watts was sufficient to heat about 600 cm3 of ice from -20°C to 0°C and, more importantly, melt it when the bare pipe was directly exposed to the cold air at -25°C. This speaks to the high efficiency of the developed heating system. Further, testing of the coating system under high power input of 500 W was also successful and it took only 13 minutes for the entire ice within the bare pipe to heat and melt when pipe was tested under forced convection condition.

- Formation of axial cracks on the heating element was observed after conducting numerous heating tests under severe environmental and thermal loading conditions. The supplied power in these tests was up to 200 times greater than the necessary power that should be provided in actual working conditions in the field. It was found that generation of even relatively large cracks does not impede the functionality of the heating system and it only affects the electrical resistance of the heating system.

Chapter 4

Development of a Mathematical Model for Prediction of Performance of the Coating System

The heating and melting processes of solid ice inside a closed pipe were investigated by performing experiments and developing mathematical models. Several experiments were conducted in a cold room to measure the transient temperature and the times that were required to heat and melt ice inside a nominal 51-mm (2-inch) diameter Schedule 40 carbon steel pipe. By passing current through the coating heating system, sufficient heat was generated by way of Joule heating to heat and melt the ice in the closed pipe. One-dimensional transient heat conduction models were developed in cylindrical coordinates to predict the transient temperature of the ice during the heating process and the transient location of the moving solid-liquid interface during the melting process. The models were developed based on the separation of variables and the superposition methods. The data obtained from the models were compared with the results that were from the experiments. It was found that the models predicted the solid ice heating times to within 16%, 12%, and 15% and the melting times to within 6%, 8%, and 9% of those that were measured in experiments with supplied powers of 10 W, 20 W, and 40 W, respectively. The results suggest that the developed models based on one-dimensional transient heat conduction in cylindrical coordinates can be employed to provide reasonable predictions of the times required for a coating-based heating system to heat and melt the ice within steel pipes.

The materials presented in this chapter were published in the International Journal of Heat and Mass Transfer, (138) 923-940, 2019.

Nomenclature

$\boldsymbol{A}_{\mathbf{inn}}$	area of the inner surface of the pipe (m^2)
$\boldsymbol{A}_{\mathbf{NiCr}}$	area of the outer surface of the NiCr coating (m^2)
$\boldsymbol{B}_{\mathbf{k}}$	set of constants in function $\Re_{\mathrm{k}}$
$\boldsymbol{C}_{\mathbf{k}}$	set of constants in function $\Re_{\mathrm{k}}$
$\boldsymbol{C}_{\mathbf{p}}$	specific heat capacity ($Jkg^{-1}K^{-1}$)
$\boldsymbol{D}$	diameter (m)
$\boldsymbol{E}$	integration constant in function ϕ_{S}
$\boldsymbol{F}$	integration constant in function ϕ_{S}
$\boldsymbol{G}_{\mathbf{k}}$	set of constants in function χ_{k}
$\boldsymbol{H}_{\mathbf{k}}$	set of constants in function χ_{k}
$\boldsymbol{h}$	heat transfer coefficient ($Wm^{-2}K^{-1}$)
$\boldsymbol{I}$	electric current (A)
$\boldsymbol{J}_{\mathbf{0}}$	Bessel function of order 0 of the first kind
$\boldsymbol{J}_{\mathbf{1}}$	Bessel function of order 1 of the first kind
$\boldsymbol{k}$	thermal conductivity ($Wm^{-1}K^{-1}$)
$\boldsymbol{l}$	substrate length (m)
$\boldsymbol{M}_{\mathbf{k}}$	constant of integration in function Γ_{k}
$\boldsymbol{N}$	constant of integration in function ϕ_{L}
$\boldsymbol{P}$	electrical power (W), $P = VI$
Pr	Prandtl number, $\mathrm{Pr} = \dfrac{C_p \mu}{k}$
Ste	Stefan number, $\mathrm{Ste} = \dfrac{C_{\mathrm{pL}}\left(T_{\mathrm{NiCr}} - T_{\mathrm{f}}\right)}{\hbar}$
$\boldsymbol{q}_{\mathbf{g}}$	generated heat due to Joule heating (Wm^{-2})
$\boldsymbol{r}$	radial coordinate
$\boldsymbol{r}_{\mathbf{i}}$	location of liquid-solid interface (m)
$\boldsymbol{R'}$	electrical resistance (Ω)
$\boldsymbol{R''}$	thermal resistance (K/W)
$\mathbf{Re}_{\mathbf{Do}}$	Reynolds number, $\mathrm{Re}_{\mathrm{D_o}} = \rho u D_{\mathrm{o}} / \mu$
$\boldsymbol{T}$	temperature (°C)

t	time (s)
u	free stream air velocity (ms^{-1})
V	voltage (V)
W	constant of integration in function ϕ_{L}
Y_0	Bessel function of order 0 of the second kind
Y_1	Bessel function of order 1 of the second kind

Greek symbols

α	thermal diffusivity (m^2s^{-1})
ρ	density (kgm^{-3})
χ	function dependent on *r*, only
Γ	function dependent on *t*, only
Λ_{k}	set of constants in function τ_{k}
λ	characteristic values for the heating stage (m^{-1})
γ	characteristic values for the melting stage (m^{-1})
μ	dynamic viscosity ($kgm^{-1}s^{-1}$)

Φ	function dependent on *r*
τ	function dependent on *t*, only
υ	dimensionless parameter, ratio of the supplied thermal energy to the dissipated heat, $\upsilon = \dfrac{V^2/R'_{\mathrm{NiCr}}}{UA_{\mathrm{NiCr}}\left(T_{\mathrm{f}} - T_{\infty}\right)}$
Ψ	function dependent on *r* and *t*
$\hbar$	latent heat of fusion (Jkg^{-1})
∞	ambient

Subscripts

F	fusion
i	initial
L	liquid phase
k	number
O	outer
S	solid phase
insul	insulation
alum	alumina

4.1 Experimental Method

The coating system that was deposited onto the pipe assembly (see Fig. 3-3) was used in this study as the heating system for conducting the heating test. The coated pipe assembly was then placed in a closed duct in a cold room freezer (Foster Refrigerator USA, Kinderhook, NY, USA), which was equipped with a temperature controller. Further information regarding the experimental assembly for the freezing tests can be found in previous chapter.

In this study, a 25-mm thick insulation layer was utilized to reduce the rate of heat loss from the coating heating element to the cold ambient air. According to ASHRAE Standard 90.1-2013 [92], the minimum thickness of insulation for steel pipes with nominal pipe size between 40 and 100 mm is 25 mm with the thermal conductivity between 0.029 and 0.037 $Wm^{-1}K^{-1}$ for cooling systems working at temperatures below 4°C.

In order to study the heating and melting processes of the ice inside the pipe, direct electric current was applied to the heating element (the NiCr coating) under forced convection heat transfer conditions when the temperature of the ice inside the pipe reached -20°C. Relatively low powers of 10 W, 20 W, and 40 W were supplied to the heating element by a direct current (DC) power supply (1902B DC, B&K Precision Corporation, Yorba Linda, CA, USA) in order to prevent significant temperature gradients in the solid ice along the radial direction. The heat that was generated by way of Joule heating was transferred to the solid ice within the pipe assembly by conduction, which resulted in temperature increases, and eventually melting of the ice. The wires that were employed to connect the DC power supply to the heating system were soldered to the cold-sprayed copper coatings to make a functional electrical connection and minimize the electrical contact resistance between the power supply and the heating element.

In order to collect the temperature data from the ice, two T-type thermocouples (TC40, WIKA Instruments, Edmonton, AB, Canada) were placed inside thermowells (TW15, WIKA Instruments, Edmonton, AB, Canada) that were tightened to the threadolets at the ends of the pipe assembly. Furthermore, a T-type surface thermocouple (TC50, WIKA Instruments, Edmonton, AB, Canada) was attached to the NiCr surface in the middle of the pipe to measure the transient temperature of the coating surface. In order to ensure that the temperature measurements from the surface thermocouple would not be perturbed by the flow of frigid air over the pipe that was located inside the galvanized duct (see Fig. 3-6), insulation was attached to the outer surface of the thermocouple to cover it. The transient temperature of the ambient cold air was also measured by using a Type-T thermocouple, which was installed in the cold room. All the temperature data were collected and recorded by a data acquisition system (SCXI-1600, National Instruments, Austin, TX, USA) at a rate of one Hz (one data point per second).

4.2 Development of Mathematical Models

4.2.1 Heating Stage

The separation of variables method with application of superposition was used to solve the heat conduction problem in cylindrical coordinates and to determine the transient temperature of ice during the heating stage. Theoretically, the length of the pipe must be considerably greater than its diameter so that the assumption of one-dimensional conduction is justified. In this case, the length of the pipe section was about four times greater than its diameter. Therefore, some error was introduced into the model by this simplification when the heat transfer along the axial direction of the pipe assembly was neglected. A schematic of the cross-section of the coated pipe is shown in Fig. 4-1, which may be used for both the heating and melting stages.

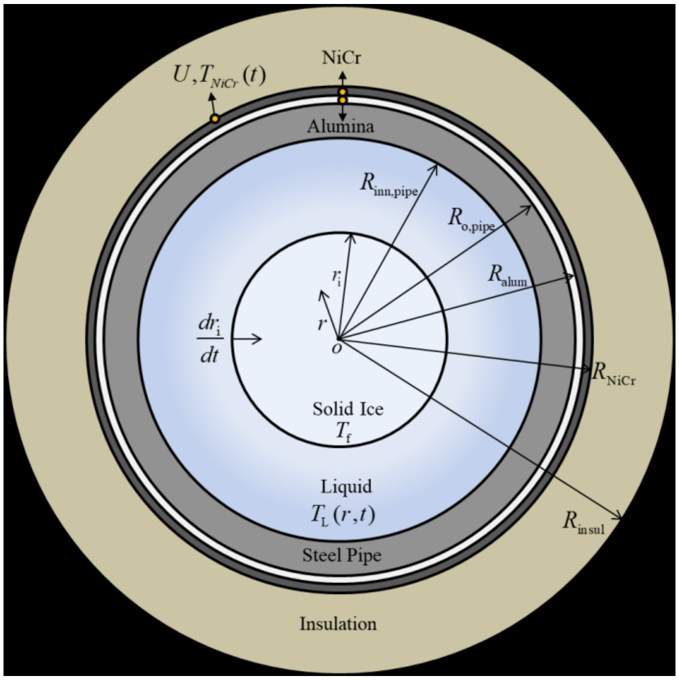

Figure 4-1 Schematic of the cross section of the coated pipe with an insulation layer during the melting process

Assuming that the properties of ice are constant in the temperature range that was studied (-20 to 0°C), the governing equation is

$$\frac{1}{r}\frac{\partial}{\partial r}\left(r\frac{\partial T_{\mathrm{S}}(r,t)}{\partial r}\right)=\frac{1}{\alpha_{\mathrm{S}}}\frac{\partial T_{\mathrm{S}}(r,t)}{\partial t}. \tag{4-1}$$

The boundary and initial conditions are

$$\frac{\partial T_{\mathrm{S}}(0,t)}{\partial r}=0, \tag{4-2}$$

$$k_{\mathrm{S}}A_{\mathrm{inn}}\frac{\partial T_{\mathrm{S}}\left(R_{\mathrm{inn}},t\right)}{\partial r}=\beta\left(q_{\mathrm{g}}-UA_{\mathrm{NiCr}}\left[T_{\mathrm{NiCr}}\left(t\right)-T_{\infty}\right]\right)\square\left(\left[\frac{V^{2}}{R'_{\mathrm{NiCr}}}\right]-UA_{\mathrm{NiCr}}\left[T_{\mathrm{S}}\left(R_{\mathrm{inn}},t\right)-T_{\infty}\right]\right), \tag{4-3}$$

$$T_{\mathrm{S}}\left(r,0\right)=T_{\mathrm{i}}. \tag{4-4}$$

where q_g is the heat energy generated by way of Joule heating by passing current through the heating element. Given that the heating element was Ohmic [46], the heat that was generated by the coating was represented as a function of the supplied voltage (V) and the electrical resistance of the heating element (R'). The power that was supplied to the coating-based heating element resulted in heating of all the components including the solid ice, the pipe, the thermowells, the coating layers, and the industrial thermocouples. Therefore, not all of the generated heat was absorbed by the ice. Given the installation of a 25-mm thick insulation layer around the pipe assembly and the provision of low powers, the difference among the transient temperatures of the pipe, fittings, and the ice was negligible. Therefore, the portion of the generated energy that was required to heat the ice was calculated by dividing the product of mass and specific heat of ice by the sum of the product of the mass and specific heat of each component, which is shown as β in Eq. (4-3). The energy that was dissipated through the wires, which were used to connect the heating element to the direct current (DC) power supply, to the ambient cold air in the cold room was calculated to be 1.8% of the total supplied power. Given that this portion was not significant, it was not taken into account when comparing the experimental results with those obtained from the model.

The $UA_{\mathrm{NiCr}}\left[T_{\mathrm{NiCr}}(t)-T_{\infty}\right]$ term in Eq. (4-3) was the amount of heat that was dissipated from the heating element to the ambient air, resulting in energy transfer that was determined by an expression that is analogous to Newton’s law of cooling. The thermal conductivity of the steel pipe (order of 50 W/m-K) [88], NiCr coating (11.3 W/m-K) [86], and the alumina coating (35 W/m-K) [87] were small, and when coupled with thicknesses that are usually small for the pipe and coating layers, the thermal resistance to heat transfer across the coating-pipe ensemble was low. Due to the low thermal resistance of the pipe material and the coating layers, there was negligible temperature difference between the temperature of the ice at the inner surface of the pipe and the temperature of the NiCr coating surface. Thus, the $T_{\mathrm{NiCr}}(t)$ term in Eq. (4-3) was replaced by the $T_{\mathrm{s}}(R_{\mathrm{inn}},t)$ term so that the transient temperature of ice was the only dependent variable in the problem. This simplification is justified by the small total thermal resistance of the coated pipe (R''), which takes into account the separate thermal resistances [93], and it is given by

$$R'' = R''_{\mathrm{pipe}} + R''_{\mathrm{alum}} + R''_{\mathrm{NiCr}} = \frac{\ln\left(\dfrac{R_{\mathrm{NiCr}}}{R_{\mathrm{alum}}}\right)}{2\pi l k_{\mathrm{NiCr}}} + \frac{\ln\left(\dfrac{R_{\mathrm{alum}}}{R_{\mathrm{o,pipe}}}\right)}{2\pi l k_{\mathrm{alum}}} + \frac{\ln\left(\dfrac{R_{\mathrm{o,pipe}}}{R_{\mathrm{inn,pipe}}}\right)}{2\pi l k_{\mathrm{pipe}}}. \tag{4-5}$$

where l is the length of the pipe section, $R_{\mathrm{inn,pipe}}$ is the inner radius of the pipe, and $R_{\mathrm{o,pipe}}$, R_{alum}, and R_{NiCr} are the outer radii of the pipe, alumina coating, and the NiCr coating, respectively. The term U in Eq. (3) is the overall heat transfer coefficient, which can be obtained from Eq. (4-6) by taking into account the thermal resistance associated with the layers as

$$U = \frac{1}{\dfrac{R_{\mathrm{NiCr}}}{R_{\mathrm{insul}}}\dfrac{1}{h} + \dfrac{R_{\mathrm{NiCr}}}{k_{\mathrm{insul}}}\ln\left(\dfrac{R_{\mathrm{insul}}}{R_{\mathrm{NiCr}}}\right)}. \tag{4-6}$$

where h is the forced convective heat transfer coefficient and R_{insul} is the outer radius of the insulation layer. Owing to the low temperature of the coating system during the tests, the heat loss from the NiCr coating to the cold ambient air inside the cold room by radiation was considered to be negligible and was not included in Eq. (4-3).

Correlation equations that were developed in other studies [94, 95] were used to estimate the forced heat transfer coefficient for flow over the pipe that was installed inside the duct. Perkins and Leppert [94] studied the local heat transfer coefficients for external flow over a uniformly heated cylinder and compared the values that were obtained with analytical predictions. They also investigated the influence of variation of dynamic viscosity with temperature across the boundary layer. According to their findings, the average heat transfer coefficient can be estimated from the correlation equation, which is given as

$$\bar{h}_{\text{o,convection}} = \frac{k_{\text{air}}}{D_{\text{insul}}}\left(0.31\text{Re}_{\text{D}_{\text{insul}}}^{0.50} + 0.11\text{Re}_{\text{D}_{\text{insul}}}^{0.67}\right)\text{Pr}^{0.40}. \tag{4-7}$$

where the equation is valid only for Reynolds numbers that are lower than 2×10^5. Due to the marginal effect of temperature on the viscosity of the air that flows over the pipe in the tests that were conducted in this study, the ratio of dynamic viscosity at the wall to the bulk dynamic viscosity of the air in the undisturbed free flow was assumed to be unity. In another study, Robinson, *et al.* [95] took into account the effect of blockage on the average heat transfer coefficient by making a correction to the Reynolds number for use in the correlations. It is well known that blockage directly affects the flow velocity and pressure distributions of the external fluid and, as a result, changes the location of the separation point over the cylinder. This will in turn affect the heat transfer coefficient of the flow over the cylinder. In this regard, an empirically-determined factor $(1+\sqrt{\frac{D_{\text{insul}}}{H}})$ was proposed for the average heat transfer coefficient over a non-isothermal cylinder. Therefore, by applying the correction, Eq. (4-7) becomes

$$\bar{h}_{\text{o,convection}} = \frac{k_{\text{air}}}{D_{\text{insul}}}\left(1+\sqrt{\frac{D_{\text{insul}}}{H}}\right)\left(0.31\text{Re}_{\text{D}_{\text{insul}}}^{0.50} + 0.11\text{Re}_{\text{D}_{\text{insul}}}^{0.67}\right)\text{Pr}^{0.40}. \tag{4-8}$$

where H is the height of the duct, which was 254 mm (10 in). In this study, the insulated pipe was placed in a closed duct. Therefore, the effect of blockage caused by placement of the pipe in the flow of air in the closed duct on the average heat transfer coefficient was predicted more accurately by consideration of the correction factor that was proposed by Robinson, *et al.* [95].

Given the non-homogeneity of one of the boundary conditions (see Eq. (4-3)), superposition was used to solve Eq. (4-1). In this method, it is assumed that the solution for T_S is the sum of two separate functions, namely $\Psi_S\,(r,t)$, which depends on both the cylinder radius and time, and $\phi_S\,(r)$, which is only a function of the radius. Therefore, $T_S\,(r,t)$ was defined as

$$T_S(r,t)=\psi_S(r,t)+\phi_S(r). \tag{4-9}$$

Substituting Eq. (4-9) in Eq. (4-1) gives

$$\frac{1}{r}\frac{\partial}{\partial r}\left(r\frac{\partial\psi_S(r,t)}{\partial r}\right)+\frac{1}{r}\frac{d}{dr}\left(r\frac{d\phi_S(r)}{dr}\right)=\frac{1}{\alpha_S}\frac{\partial\psi_S(r,t)}{\partial t}. \tag{4-10}$$

Separation of independent terms in Eq. (4-10) gives

$$\frac{1}{r}\frac{\partial}{\partial r}\left(r\frac{\partial\psi_S(r,t)}{\partial r}\right)=\frac{1}{\alpha_S}\frac{\partial\psi_S(r,t)}{\partial t}, \tag{4-11}$$

$$\frac{1}{r}\frac{d}{dr}\left(r\frac{d\phi_S(r)}{dr}\right)=0. \tag{4-12}$$

Function $\Psi_S\,(r,t)$ can be solved by employing the separation of variables method in which the partial differential equation given in Eq. (4-11) can be replaced by sets of ordinary differential equations. The proper form of the solution for the given function $\Psi_S\,(r,t)$ is assumed to be the product of two functions with independent variables as

$$\psi_S(r,t)=\Re(r)\tau(t). \tag{4-13}$$

Substituting Eq. (4-13) in Eq. (4-11) and separating into two sets of ordinary differential equations specific to the independent variables gives

$$\frac{d^2\Re_{\mathrm{n}}}{dr^2}+\frac{1}{r}\frac{d\Re_{\mathrm{n}}}{dr}+\lambda_{\mathrm{n}}^2\Re_{\mathrm{n}}=0\,. \tag{4-14}$$

$$\frac{d\tau_{\mathrm{n}}}{dt}+\alpha_{\mathrm{S}}\lambda_{\mathrm{n}}^2\tau_{\mathrm{n}}=0\,. \tag{4-15}$$

For the special case in which $\lambda_{\mathrm{n}} = 0$, Eqs. (4-14) and (4-15) become

$$\frac{d^2\Re_0}{dr^2}+\frac{1}{r}\frac{d\Re_0}{dr}=0\,. \tag{4-16}$$

$$\frac{d\tau_0}{dt}=0\,. \tag{4-17}$$

Performing the integration for Eqs. (4-14) – (4-17) yields the solutions as

$$\Re_{\mathrm{n}}\left(r\right)=B_{\mathrm{n}}J_0\left(\lambda_{\mathrm{n}}r\right)+C_{\mathrm{n}}Y_0\left(\lambda_{\mathrm{n}}r\right). \tag{4-18}$$

$$\tau_{\mathrm{n}}\left(t\right)=\Lambda_{\mathrm{n}}\exp\left(-\alpha_{\mathrm{S}}\lambda_{\mathrm{n}}^2t\right). \tag{4-19}$$

$$\Re_0\left(r\right)=B_0\ln r+C_0\,. \tag{4-20}$$

$$\tau_0\left(t\right)=\Lambda_0\,. \tag{4-21}$$

Substitution of Eq. (4-9) into Eqs. (4-2) – (4-4) transforms the boundary and initial conditions to

$$\frac{\partial\psi_{\mathrm{S}}(0,t)}{\partial r}=0\,. \tag{4-22}$$

$$\frac{d\phi_{\mathrm{S}}(0)}{dr}=0\,. \tag{4-23}$$

$$k_{\mathrm{S}}A_{\mathrm{inn}}\frac{\partial\psi_{\mathrm{S}}\left(R_{\mathrm{inn}},t\right)}{\partial r}=-\beta UA_{\mathrm{NiCr}}\psi_{\mathrm{S}}\left(R_{\mathrm{inn}},t\right). \tag{4-24}$$

$$k_{\mathrm{S}} A_{\mathrm{inn}} \frac{d\phi_{\mathrm{S}}\left(R_{\mathrm{inn}}\right)}{dr} = \beta\left(\left[\frac{V^2}{R'_{\mathrm{NiCr}}}\right] - UA_{\mathrm{NiCr}}\left[\phi_{\mathrm{S}}\left(R_{\mathrm{inn}}\right) - T_{\infty}\right]\right). \tag{4-25}$$

$$\psi_S\left(r,0\right) + \phi_S\left(r\right) = T_{\mathrm{i}}. \tag{4-26}$$

Application of the first boundary condition for function $\Psi_{\mathrm{S}}(r,t)$ (Eq. (4-22)) yields $C_{\mathrm{n}} = 0$. The characteristic values can be obtained by applying the second boundary condition for the $\Psi_{\mathrm{S}}(r,t)$ function (Eq. (4-24)) as

$$\lambda_{\mathrm{n}} = \frac{\beta UA_{\mathrm{NiCr}} J_0\left(\lambda_{\mathrm{n}} R_{\mathrm{inn}}\right)}{A_{\mathrm{inn}} k_{\mathrm{S}} J_1\left(\lambda_{\mathrm{n}} R_{\mathrm{inn}}\right)} \qquad B_{\mathrm{n}} \neq 0. \tag{4-27}$$

Furthermore, application of boundary conditions (Eqs. (4-22) and (4-24)) for the special case of $\Psi_0(r,t)$ in which $\lambda_{\mathrm{n}} = 0$ yields $\Psi_0(r,t) = 0$. Therefore, $\Psi_{\mathrm{S}}(r,t)$ can be written as

$$\psi_{\mathrm{S}}\left(r,t\right) = \sum_{\mathrm{n}=1}^{\infty} b_{\mathrm{n}} J_0\left(\lambda_{\mathrm{n}} r\right) \exp\left(-\alpha_{\mathrm{S}} \lambda_{\mathrm{n}}^2 t\right). \tag{4-28}$$

where $b_{\mathrm{n}} = B_{\mathrm{n}} \Lambda_{\mathrm{n}}$. In order to obtain the temperature distribution in the ice, the solution for the $\phi_{\mathrm{S}}(r)$ function is required. Performing the integration of Eq. (4-12) yields

$$\phi_S\left(r\right) = E \ln r + F. \tag{4-29}$$

Applying the boundary conditions for $\phi_{\mathrm{S}}(r)$ (Eqs. (4-23) and (4-25)) yields

$$\phi_{\mathrm{S}}\left(r\right) = \frac{V^2}{UR'_{\mathrm{NiCr}} A_{\mathrm{NiCr}}} + T_{\infty}. \tag{4-30}$$

Substituting Eqs. (4-28) and (4-30) into Eq. (4-9) gives $T_{\mathrm{S}}(r,t)$ as

$$T_{\mathrm{S}}\left(r,t\right) = \frac{V^2}{UR'_{\mathrm{NiCr}} A_{\mathrm{NiCr}}} + T_{\infty} + \sum_{\mathrm{n}=1}^{\infty} b_{\mathrm{n}} J_0\left(\lambda_{\mathrm{n}} r\right) \exp\left(-\alpha_{\mathrm{S}} \lambda_{\mathrm{n}}^2 t\right). \tag{4-31}$$

Application of the initial condition (Eq. (4-26)), which is required to determine the set of constants, b_{n}, yields

$$T_{\mathrm{S}}(r,0)=T_{\mathrm{i}}=\frac{V^2}{UR'_{\mathrm{NiCr}}A_{\mathrm{NiCr}}}+T_\infty+\sum_{\mathrm{n}=1}^{\infty}b_{\mathrm{n}}J_0(\lambda_{\mathrm{n}}r), \tag{4-32}$$

where set of constants, b_{n}, has to be determined. Eq. (4-32) can be written in the form of

$$T_{\mathrm{i}}-T_\infty-\frac{V^2}{UR'_{\mathrm{NiCr}}A_{\mathrm{NiCr}}}=\sum_{\mathrm{n}=1}^{\infty}b_{\mathrm{n}}J_0(\lambda_{\mathrm{n}}r). \tag{4-33}$$

It is noteworthy that Eq. (4-33) was obtained by separation of variables method to replace the partial differential equation (Eq. (4-1)) with sets of ordinary differential equations (Eq. (4-14) and Eq. (4-15)). In this regard, Eq. (4-14) is a Sturm-Liouville equation that belongs to a class of second order ordinary differential equations. It is known that the general form of the Sturm-Liouville equation is as

$$\frac{d^2\phi_{\mathrm{n}}}{dx^2}+a_1(x)\frac{d\phi_{\mathrm{n}}}{dx}+\left[a_2(x)+\lambda_{\mathrm{n}}^2a_3(x)\right]\phi_{\mathrm{n}}=0. \tag{4-34}$$

where solutions for ϕ_{n} are known as characteristic functions [96]. The weighting function that is necessary for solving the Sturm-Liouville boundary-value problem can be obtained as

$$w(x)=a_3(x)\times e^{\int a_1(x)dx}. \tag{4-35}$$

Comparing Eq. (4-14) with Eq. (4-34), the values of a_1, a_3 can be obtained. The weighting function can also be determined by solving Eq. (4-35). For this specific case, the weighting function was calculated as $w(r) = r$. One of the noticeable features of the Sturm-Liouville equations that are invoked in the application of the separation of variables method is orthogonality. The functions of $\phi_{\mathrm{n}}(x)$ and $\phi_{\mathrm{m}}(x)$ are orthogonal in the range (a,b) with respect to the weighting function $w(x)$, if

$$\int_{a}^{b}\left[\phi_{\mathrm{n}}(x)\times\phi_{\mathrm{m}}(x)\times w(x)\right]dx=0 \qquad n\neq m. \tag{4-36}$$

Furthermore, the boundary conditions at $x = a$ and $x = b$ should be homogeneous. With that in mind, orthogonality can be applied to Eq. (4-33) as the governing Eq. (4-14) was a Sturm-Liouville equation and the boundary conditions (Eq. (4-22) and Eq. (4-24)) were homogeneous at $r = 0$ and $r = R_{\mathrm{inn}}$. Multiplication of both sides of Eq. (4-33) by the weighting function $w = (r)$ and the characteristic function of $J_0(\lambda_{\mathrm{m}}r)$ and integrating from $r = 0$ to $r = R_{\mathrm{inn}}$ gives

$$\int_{0}^{R_{\mathrm{inn}}}\left(T_{\mathrm{i}}-T_{\infty}-\frac{V^2}{UR'_{\mathrm{NiCr}}A_{\mathrm{NiCr}}}\right)J_0(\lambda_{\mathrm{m}}r)rdr=\int_{0}^{R_{\mathrm{inn}}}\left[\sum_{\mathrm{n}=1}^{\infty}b_{\mathrm{n}}J_0(\lambda_{\mathrm{n}}r)\right]J_0(\lambda_{\mathrm{m}}r)\times rdr. \tag{4-37}$$

Interchanging the integration and summation signs and noting that the integral under the summation signs vanishes except when $n = m$ gives

$$\left(T_{\mathrm{i}}-T_{\infty}-\frac{V^2}{UR'_{\mathrm{NiCr}}A_{\mathrm{NiCr}}}\right)\int_{0}^{R_{\mathrm{inn}}}J_0(\lambda_{\mathrm{n}}r)rdr=b_{\mathrm{n}}\int_{0}^{R_{\mathrm{inn}}}J_0^{\,2}(\lambda_{\mathrm{n}}r)rdr. \tag{4-38}$$

Therefore, the values for b_{n} can be determined by performing the integration as

$$b_{\mathrm{n}}\approx\frac{\left(T_{\mathrm{i}}-T_{\infty}-\frac{V^2}{UR'_{\mathrm{NiCr}}A_{\mathrm{NiCr}}}\right)\int_{0}^{R_{\mathrm{inn}}}J_0(\lambda_{\mathrm{n}}r)rdr}{\left[\int_{0}^{R_{\mathrm{inn}}}J_0^2(\lambda_{\mathrm{n}}r)rdr\right]}=\frac{\left(T_{\mathrm{i}}-T_{\infty}-\frac{V^2}{UR'_{\mathrm{NiCr}}A_{\mathrm{NiCr}}}\right)\left(\frac{1}{\lambda_{\mathrm{n}}}R_{\mathrm{inn}}J_1(\lambda_{\mathrm{n}}R_{\mathrm{inn}})\right)}{\frac{1}{2\lambda_{\mathrm{n}}^2}\left[\left(\frac{\beta UR_{\mathrm{NiCr}}}{k}\right)^2+(\lambda_{\mathrm{n}}R_{\mathrm{inn}})^2\right]J_0^2(\lambda_{\mathrm{n}}R_{\mathrm{inn}})}. \tag{4-39}$$

where the value of the normalizing integral $\left(\int_{0}^{R_{\mathrm{inn}}}J_0^2(\lambda_{\mathrm{n}}r)rdr\right)$ in the denominator of the first phrase leads to a characteristic equation that is dependent on the form of the homogeneous boundary condition of the conduction problem. Given the Robin boundary condition of Eq. (4-24), the value for the normalizing integral was obtained from Jiji [97]. Therefore, the complete solution for $T_{\mathrm{S}}(r,t)$ becomes

$$T_{\mathrm{S}}\left(r,t\right)=\frac{V^2}{UR'_{\mathrm{NiCr}}A_{\mathrm{NiCr}}}+T_\infty+\sum_{\mathrm{n=1}}^{\infty}\frac{2\lambda_{\mathrm{n}}R_{\mathrm{inn}}J_1\left(\lambda_{\mathrm{n}}R_{\mathrm{inn}}\right)\left(T_{\mathrm{i}}-T_\infty-\dfrac{V^2}{UR'_{\mathrm{NiCr}}A_{\mathrm{NiCr}}}\right)}{\left[\left(\dfrac{\beta UR_{\mathrm{NiCr}}}{k}\right)^2+\left(\lambda_{\mathrm{n}}R_{\mathrm{inn}}\right)^2\right]J_0^2\left(\lambda_{\mathrm{n}}R_{\mathrm{inn}}\right)}J_0\left(\lambda_{\mathrm{n}}r\right)\exp\left(-\alpha_{\mathrm{S}}\lambda_{\mathrm{n}}^2t\right). \tag{4-40}$$

Equation (4-40) was used to estimate the transient temperature of the solid ice at any radius at a given time during the ice heating process. Furthermore, the time required to heat the solid ice from its initial temperature, T_{i}, to its melting point, T_{f}, can be calculated by using Eq. (4-40) with substitution of T_{f} for T_{S} (r,t). The general properties of ice that were used in the model regarding the heating stage are shown in Table 4-1.

Table 4-1 Properties for solid ice at 0°C [98]

Property, symbol	Value
Specific heat capacity, $c_{\mathrm{p,s}}$	2010 J/kg-K
Density, ρ_{s}	917 kg/m^3
Thermal conductivity, k_{s}	2.2 W/m-K
Thermal diffusivity, α_{s}	1.19×10^{-6} m^2/s
Melting point, T_{f}	0°C

4.2.2 Melting Stage

A one-dimensional transient heat conduction model for phase change of a finite-length scale medium was used to determine the transient location of the solid-liquid interface. The schematic of the movement of the solid-liquid interface is shown in Fig. 4-1. It was assumed that during the melting process, the properties of both ice and water were constant and the decrease in the thickness of the ice was axisymmetric. It was also assumed that the temperature of the ice after the heating stage was constant and remained at the fusion temperature. The governing equations for the temperature distribution in the solid and the liquid phases are

$$T_{\mathrm{S}}\left(r,t\right)=T_{\mathrm{f}}\,, \quad 0\leq r<r_{\mathrm{i}}\left(t\right) \tag{4-41}$$

$$\frac{1}{r}\frac{\partial}{\partial r}\left(r\frac{\partial T_{\mathrm{L}}}{\partial r}\right)=\frac{1}{\alpha_{\mathrm{L}}}\frac{\partial T_{\mathrm{L}}}{\partial t}\,, \quad r_{\mathrm{i}}\left(t\right)<r\leq R_{\mathrm{inn}} \tag{4-42}$$

The boundary and initial conditions for the phase change problem are

$$T_{\mathrm{L}}\left(r_{\mathrm{i}},t\right)=T_{\mathrm{f}}\,. \tag{4-43}$$

$$k_{\mathrm{L}}A_{\mathrm{inn}}\frac{\partial T_{\mathrm{L}}\left(R_{\mathrm{inn}},t\right)}{\partial r}=\frac{V^{2}}{R'_{\mathrm{NiCr}}}-UA_{\mathrm{NiCr}}\left[T_{\mathrm{L}}\left(R_{\mathrm{inn}},t\right)-T_{\infty}\right]. \tag{4-44}$$

$$r_{\mathrm{i}}\left(0\right)=R_{\mathrm{inn}}\,. \tag{4-45}$$

$$T_{\mathrm{L}}\left(r,0\right)=T_{\mathrm{f}}\,. \tag{4-46}$$

where r_{i} (t) is the transient location of the solid-ice interface. Unlike the heating stage in which the generated heat caused the temperature rise of all the components of the coated pipe assembly, the majority of the heat that was generated by the coating in the melting stage caused the melting of the ice and, therefore, the ratio of the sensible heat to the latent heat was considerably low. Therefore, the term β that was used in the boundary condition of Eq. (4-3) for the heating stage, was not used in the case of melting. Application of conservation of energy at the solid-liquid interface yields the non-linear interface energy equation that will be used to determine the transient location of the moving boundary, r_{i} (t). The interface energy equation for the case of melting is expressed as

$$-k_{\mathrm{L}}\frac{\partial T_{\mathrm{L}}\left(r_{\mathrm{i}},t\right)}{\partial r}=\rho_{\mathrm{L}}\hbar\frac{dr}{dt}\,. \tag{4-47}$$

where $\hbar$ is the latent heat of fusion. The temperature distribution in the liquid water can be derived by applying both superposition and the separation of variables method. It was assumed that the transient temperature of the liquid phase was the sum of two separate functions as

$$T_{\mathrm{L}}\left(r,t\right)=\psi_{\mathrm{L}}\left(r,t\right)+\varphi_{\mathrm{L}}\left(r\right). \tag{4-48}$$

Substitution of Eq. (4-48) into Eq. (4-42) and splitting the independent variables yield

$$\frac{1}{r}\frac{\partial}{\partial r}\left(r\frac{\partial\psi_{\mathrm{L}}}{\partial r}\right)=\frac{1}{\alpha_{\mathrm{L}}}\frac{\partial\psi_{\mathrm{L}}}{\partial t}, \quad r_{\mathrm{i}}\left(t\right)<r\leq R_{\mathrm{inn}}. \tag{4-49}$$

$$\frac{1}{r}\frac{d}{dr}\left(r\frac{d\phi_{\mathrm{L}}}{dr}\right)=0. \quad r_{\mathrm{i}}\left(t\right)<r\leq R_{\mathrm{inn}}. \tag{4-50}$$

It was assumed that the solution to function $\Psi_{\mathrm{L}}(r,t)$ was product of two independent functions, namely $\chi(r)$ and $\Gamma(t)$ as

$$\psi_{\mathrm{L}}\left(r,t\right)=\chi\left(r\right)\Gamma\left(t\right). \tag{4-51}$$

Substituting Eq. (4-51) into Eq. (4-49) and separation of functions with independent variables give

$$\frac{d^2\chi_{\mathrm{n}}}{dr^2}+\frac{1}{r}\frac{d\chi_{\mathrm{n}}}{dr}+\gamma_{\mathrm{n}}^2\chi_{\mathrm{n}}=0. \tag{4-52}$$

$$\frac{d\Gamma_{\mathrm{n}}}{dt}+\alpha_{\mathrm{L}}\gamma_{\mathrm{n}}^2\Gamma_{\mathrm{n}}=0. \tag{4-53}$$

where γ_{n} are characteristic values that must be determined by applying the boundary conditions. For the special case of $\gamma_{\mathrm{n}}=0$, Eqs. (4-52) and (4-53) become

$$\frac{d^2\chi_0}{dr^2}+\frac{1}{r}\frac{d\chi_0}{dr}=0. \tag{4-54}$$

$$\frac{d\Gamma_0}{dt} = 0\,. \tag{4-55}$$

The solutions to Eqs. (4-52) and (4-53) are

$$\chi_\mathrm{n}(r) = G_\mathrm{n} J_0(\gamma_\mathrm{n} r) + H_\mathrm{n} Y_0(\gamma_\mathrm{n} r), \quad r_\mathrm{i}(t) < r \le R_\mathrm{inn}\,. \tag{4-56}$$

$$\Gamma_\mathrm{n}(t) = M_\mathrm{n} \exp\left(-\alpha_\mathrm{L} \gamma_\mathrm{n}^2 t\right). \tag{4-57}$$

Furthermore, the solutions for the special case given in Eqs. (4-54) and (4-55) are

$$\chi_0(r) = G_0 \ln r + H_0\,. \tag{4-58}$$

$$\Gamma_0(t) = M_0\,. \tag{4-59}$$

In addition to the solutions for $\Psi_\mathrm{L}(r,t)$, the solution to $\phi_\mathrm{L}(r)$ is

$$\phi_\mathrm{L}(r) = N \ln r + W, \quad r_\mathrm{i}(t) < r \le R_\mathrm{inn}\,. \tag{4-60}$$

Substitution of Eq. (4-48) into Eqs. (4-43) and (4-44), the boundary conditions become

$$\psi_\mathrm{L}(r_\mathrm{i}, t) = 0\,. \tag{4-61}$$

$$\phi_\mathrm{L}(r_\mathrm{i}) = T_\mathrm{f}\,. \tag{4-62}$$

$$k_\mathrm{L} A_\mathrm{inn} \frac{\partial \psi_\mathrm{L}(R_\mathrm{inn}, t)}{\partial r} = -U A_\mathrm{NiCr} \psi_\mathrm{L}(R_\mathrm{inn}, t)\,. \tag{4-63}$$

$$k_\mathrm{L} A_\mathrm{inn} \frac{d\phi_\mathrm{L}(R_\mathrm{inn})}{dr} = \frac{V^2}{R'_\mathrm{NiCr}} - U A_\mathrm{NiCr}\left[\phi_L(R_\mathrm{inn}) - T_\infty\right]. \tag{4-64}$$

Application of the transformed boundary conditions for $\Psi_\mathrm{L}(r,t)$ (see Eqs. (4-61) and (4-63)) gives the set of constants H_n and characteristic values γ_n in Eq. (4-56) as

$$H_{\mathrm{n}} = -G_{\mathrm{n}} \frac{J_0\left(\gamma_{\mathrm{n}} r_{\mathrm{i}}\right)}{Y_0\left(\gamma_{\mathrm{n}} r_{\mathrm{i}}\right)}, \tag{4-65}$$

$$\gamma_{\mathrm{n}} \frac{\left[J_1\left(\gamma_{\mathrm{n}} R_{\mathrm{inn}}\right) - \frac{J_0\left(\gamma_{\mathrm{n}} r_{\mathrm{i}}\right)}{Y_0\left(\gamma_{\mathrm{n}} r_{\mathrm{i}}\right)} Y_1\left(\gamma_{\mathrm{n}} R_{\mathrm{inn}}\right)\right]}{\left(J_0\left(\gamma_{\mathrm{n}} R_{\mathrm{inn}}\right) - \frac{J_0\left(\gamma_{\mathrm{n}} r_{\mathrm{i}}\right)}{Y_0\left(\gamma_{\mathrm{n}} r_{\mathrm{i}}\right)} Y_0\left(\gamma_{\mathrm{n}} R_{\mathrm{inn}}\right)\right)} = \frac{UA_{\mathrm{NiCr}}}{k_{\mathrm{L}} A_{\mathrm{inn}}}. \qquad G_{\mathrm{n}} \neq 0. \tag{4-66}$$

The characteristic values (γ_{n}) were obtained by solving Eq. (4-66) numerically based on the transient locations of the solid-liquid interface, which were provided as model input. The interface locations were defined such that the distance between each of two consecutive interfaces was only 1 mm. Only the first ten (10) characteristic values for each interface location were taken into account. It was observed that the contribution of the terms with higher values of *k* was decreased rapidly. Therefore, the contribution of terms with $k > 10$ was not considered because they were negligible. The application of the transformed boundary conditions for the special case in which $\gamma_{\mathrm{n}} = 0$ (Eqs. (4-61) and (4-63) for Eqs. (4-58) and (4-59)) yields $\psi_0\left(r,t\right) = \Re_0\left(r\right)\tau_0\left(t\right) = 0$. Therefore, the solution for the $\psi_{\mathrm{L}}(r,t)$ function becomes

$$\Psi_{\mathrm{L}}\left(r,t\right) = \sum_{\mathrm{n}=1}^{\infty} g_{\mathrm{n}} \left[Y_0\left(\gamma_{\mathrm{n}} r_{\mathrm{i}}\right) J_0\left(\gamma_{\mathrm{n}} r\right) - J_0\left(\gamma_{\mathrm{n}} r_{\mathrm{i}}\right) Y_0\left(\gamma_{\mathrm{n}} r\right)\right] \exp\left(-\alpha_{\mathrm{L}} \gamma_{\mathrm{n}}^2 t\right). \tag{4-67}$$

where $g_{\mathrm{n}} = \frac{G_{\mathrm{n}} \times M_{\mathrm{n}}}{Y_0\left(\gamma_{\mathrm{n}} r_{\mathrm{i}}\right)}$. In addition, application of the boundary conditions for $\phi_L(r)$ (see Eqs. (4-62) and (4-64)) yields

$$\varphi_{\mathrm{L}}\left(r\right) = \frac{\frac{V^2}{R'_{\mathrm{NiCr}} A_{\mathrm{NiCr}} U} - T_{\mathrm{f}} + T_{\infty}}{\frac{k_{\mathrm{L}} A_{\mathrm{inn}}}{UA_{\mathrm{NiCr}} R_{\mathrm{inn}}} + \ln\left(\frac{R_{\mathrm{inn}}}{r_{\mathrm{i}}}\right)} \ln\left(\frac{r}{r_{\mathrm{i}}}\right) + T_{\mathrm{f}} \cdot \tag{4-68}$$

Substituting Eqs. (4-67) and (4-68) into Eq. (4-48) gives the temperature of the liquid phase, $T_{\mathrm{L}}(r,t)$, as

$$T_{\mathrm{L}}\left(r,t\right)=\frac{\dfrac{V^2}{R'_{\mathrm{NiCr}}A_{\mathrm{NiCr}}U}-T_{\mathrm{f}}+T_{\infty}}{\dfrac{k_{\mathrm{L}}A_{\mathrm{inn}}}{UA_{\mathrm{NiCr}}R_{\mathrm{inn}}}+\ln\left(\dfrac{R_{\mathrm{inn}}}{r_{\mathrm{i}}}\right)}\ln\left(\frac{r}{r_{\mathrm{i}}}\right)+T_{\mathrm{f}}+\sum_{\mathrm{n}=1}^{\infty}g_{\mathrm{n}}\left[Y_0\left(\gamma_{\mathrm{n}}r_{\mathrm{i}}\right)J_0\left(\gamma_{\mathrm{n}}r\right)-J_0\left(\gamma_{\mathrm{n}}r_{\mathrm{i}}\right)Y_0\left(\gamma_{\mathrm{n}}r\right)\right]\exp\left(-\alpha_{\mathrm{L}}\gamma_{\mathrm{n}}^2t\right). \quad (4\text{-}69)$$

In order to determine the set of constants (g_{n}), the initial condition (Eq. (4-46)) was applied. Application of the initial condition yields

$$\sum_{\mathrm{k}=1}^{\infty}g_{\mathrm{n}}\left[Y_0\left(\gamma_{\mathrm{n}}r_{\mathrm{i}}\right)J_0\left(\gamma_{\mathrm{n}}r\right)-J_0\left(\gamma_{\mathrm{n}}r_{\mathrm{i}}\right)Y_0\left(\gamma_{\mathrm{n}}r\right)\right]=-\left[\frac{\dfrac{V^2}{R'_{\mathrm{NiCr}}A_{\mathrm{NiCr}}U}-T_{\mathrm{f}}+T_{\infty}}{\dfrac{k_{\mathrm{L}}A_{\mathrm{inn}}}{UA_{\mathrm{NiCr}}R_{\mathrm{inn}}}+\ln\left(\dfrac{R_{\mathrm{inn}}}{r_{\mathrm{i}}}\right)}\right]\ln\left(\frac{r}{r_{\mathrm{i}}}\right). \quad (4\text{-}70)$$

Given that the $\left[Y_0\left(\gamma_{\mathrm{n}}r_{\mathrm{i}}\right)J_0\left(\gamma_{\mathrm{n}}r\right)-J_0\left(\gamma_{\mathrm{n}}r_{\mathrm{i}}\right)Y_0\left(\gamma_{\mathrm{n}}r\right)\right]$ term is the solution obtained from a Sturm-Liouville equation (see Eq. (4-52)) and the boundary conditions for function Ψ_{L} are homogeneous at $r = r_{\mathrm{i}}(t)$ and $r = R_{\mathrm{inn}}$ (see Eqs. (4-61) and (4-63)) orthogonality was invoked to obtain the values of m_{n} at each interface location and for all the characteristic values. Given that the Bessel function of the second kind ($Y_0\left(\gamma_{\mathrm{n}}r\right)$) is singular at $r_{\mathrm{i}}(t) = 0$, the results obtained from this point were not taken into account.

Invoking orthogonality over the region that was bounded by $r_{\mathrm{i}}\left(t\right)<r\le R_{\mathrm{inn}}$ gives

$$g_{\mathrm{n}}\int_{r_{\mathrm{i}}}^{R_{\mathrm{inn}}}r\left[Y_0\left(\gamma_{\mathrm{n}}r_{\mathrm{i}}\right)J_0\left(\gamma_{\mathrm{n}}r\right)-J_0\left(\gamma_{\mathrm{n}}r_{\mathrm{i}}\right)Y_0\left(\gamma_{\mathrm{n}}r\right)\right]^2dr=-\left[\frac{\dfrac{V^2}{R'_{\mathrm{NiCr}}A_{\mathrm{NiCr}}U}-T_{\mathrm{f}}+T_{\infty}}{\dfrac{k_{\mathrm{L}}A_{\mathrm{inn}}}{UA_{\mathrm{NiCr}}R_{\mathrm{inn}}}+\ln\left(\dfrac{R_{\mathrm{inn}}}{r_{\mathrm{i}}}\right)}\right]\int_{r_{\mathrm{i}}}^{R_{\mathrm{inn}}}r\ln\left(\frac{r}{r_{\mathrm{i}}}\right)\left[Y_0\left(\gamma_{\mathrm{n}}r_{\mathrm{i}}\right)J_0\left(\gamma_{\mathrm{n}}r\right)-J_0\left(\gamma_{\mathrm{n}}r_{\mathrm{i}}\right)Y_0\left(\gamma_{\mathrm{n}}r\right)\right]dr. \quad (4\text{-}71)$$

The integral of the right hand side of Eq. (4-71) may demand the use of integration by parts, which in the case of Eq. (4-71) would likely be arduous and onerous. Thus, the integral was solved numerically in order to expedite the solution. However, the solution for the integral in left hand side of Eq. (4-71) is known based on the given Dirichlet and Robin boundary conditions (see Eqs. (4-61) and (4-63)) [99]. Therefore, evaluating the integral and solving for g_n gives

$$g_\mathrm{n} \approx \frac{-\left[\dfrac{\dfrac{V^2}{R'_\mathrm{NiCr} A_\mathrm{NiCr} U} - T_\mathrm{f} + T_\infty}{\dfrac{k_\mathrm{L} A_\mathrm{inn}}{U A_\mathrm{NiCr} R_\mathrm{inn}} + \ln\left(\dfrac{R_\mathrm{inn}}{r_\mathrm{i}}\right)}\right]\left(\displaystyle\int_{r_\mathrm{i}}^{R_\mathrm{inn}} r \ln\left(\frac{r}{r_\mathrm{i}}\right)\left[Y_0(\gamma_\mathrm{n} r_\mathrm{i}) J_0(\gamma_\mathrm{n} r) - J_0(\gamma_\mathrm{n} r_\mathrm{i}) Y_0(\gamma_\mathrm{n} r)\right] dr\right)}{\left(\dfrac{2}{\pi^2}\right)\dfrac{J_0^2(\gamma_\mathrm{n} r_i)\left(k_\mathrm{L}^2 + \gamma_\mathrm{n}^2\right) - \left[-\gamma_\mathrm{n} J_1(\gamma_\mathrm{n} R_\mathrm{inn}) + k_\mathrm{L} J_0(\gamma_\mathrm{n} R_\mathrm{inn})\right]^2}{\gamma_\mathrm{n}^2\left[-\gamma_\mathrm{n} J_1(\gamma_\mathrm{n} R_\mathrm{inn}) + k_\mathrm{L} J_0(\gamma_\mathrm{n} R_\mathrm{inn})\right]^2}}. \tag{4-72}$$

The interface energy equation that was represented by Eq. (4-47) was applied to determine the transient location of the liquid-solid interface. Differentiation of Eq. (4-69) with respect to *r* gives

$$\frac{\partial T_\mathrm{L}(r_\mathrm{i}, t)}{\partial r} = \frac{1}{r_\mathrm{i}}\left[\frac{\dfrac{V^2}{R'_\mathrm{NiCr} A_\mathrm{NiCr} U} - T_\mathrm{f} + T_\infty}{\dfrac{k_\mathrm{L} A_\mathrm{inn}}{U A_\mathrm{NiCr} R_\mathrm{inn}} + \ln\left(\dfrac{R_\mathrm{inn}}{r_\mathrm{i}}\right)}\right] + \sum_{\mathrm{n}=1}^{\infty} g_\mathrm{n} \gamma_\mathrm{n}\left[J_0(\gamma_\mathrm{n} r_\mathrm{i}) Y_1(\gamma_\mathrm{n} r_\mathrm{i}) - Y_0(\gamma_\mathrm{n} r_\mathrm{i}) J_1(\gamma_\mathrm{n} r_\mathrm{i})\right]\exp\left(-\alpha_\mathrm{L} \gamma_\mathrm{n}^2 t\right) \cdot \tag{4-73}$$

Substitution of Eq. (4-73) into Eq. (4-47) gives the energy equation as

$$-k_\mathrm{L}\left(\frac{1}{r_i}\left[\frac{\dfrac{V^2}{R'_\mathrm{NiCr} A_\mathrm{NiCr} U} - T_\mathrm{f} + T_\infty}{\dfrac{k_\mathrm{L} A_\mathrm{inn}}{U A_\mathrm{NiCr} R_\mathrm{inn}} + \ln\left(\dfrac{R_\mathrm{inn}}{r_\mathrm{i}}\right)}\right] + \sum_{\mathrm{n}=1}^{\infty} g_\mathrm{n} \gamma_\mathrm{n}\left[J_0(\gamma_\mathrm{n} r_\mathrm{i}) Y_1(\gamma_\mathrm{n} r_\mathrm{i}) - Y_0(\gamma_\mathrm{n} r_\mathrm{i}) J_1(\gamma_\mathrm{n} r_\mathrm{i})\right]\exp\left(-\alpha_\mathrm{L} \gamma_\mathrm{n}^2 t\right)\right) \approx \rho_\mathrm{L} \hbar \frac{dr}{dt}. \tag{4-74}$$

Since Eq. (4-74) cannot be solved explicitly, the integration was performed numerically to obtain the transient location of the solid-liquid interface. It was observed that only the first value (for *n* = 1) for the summation term was significant and contribution of the other terms (for *n* ≥ 2) were negligible. It was also found that the summation term on the left side of Eq. (4-74) was small compared to the other term so that it could be neglected. Therefore, Eq. (4-74) was simplified to

$$\frac{-k_{\mathrm{L}}}{r_i}\left[\frac{\dfrac{V^2}{R'_{\mathrm{NiCr}}A_{\mathrm{NiCr}}U}-T_{\mathrm{f}}+T_{\infty}}{\dfrac{k_{\mathrm{L}}A_{\mathrm{inn}}}{UA_{\mathrm{NiCr}}R_{\mathrm{inn}}}+\ln\left(\dfrac{R_{\mathrm{inn}}}{r_{\mathrm{i}}}\right)}\right]\approx\rho_{\mathrm{L}}\hbar\frac{dr}{dt}. \tag{4-75}$$

Eq. (4-75) produces the same results that would be obtained from the quasi-steady approximation in which the temperature distribution is assumed to depend only on the radius and is independent of time. The general properties of water that were used in the model regarding the melting stage are presented in Table 4-2.

Table 4-2 Properties for water [98, 100]

Property	Value
Thermal diffusivity, α_{L}	1.4×10^{-7} m^2/s
Specific heat capacity, $c_{\mathrm{p,L}}$	4200 J/kg-K
Density, ρ_{L}	1000 kg/m^3
Thermal conductivity, k_{L}	0.59 W/m-K
Latent heat of fusion, $\hbar$	334,000 J/kg

4.2.3 Non-Dimensional Solution for the Melting Stage

In an effort to generalize the solution that was obtained for the specific case of a 51-mm (2-inch) nominal diameter steel pipe, a non-dimensional model was also developed so that the solution can be utilized for other similar pipe diameters, supplied powers, and overall heat transfer coefficients. Non-dimensional terms on which the model was developed are given as

$$\xi = \frac{r}{R_{\mathrm{inn}}}, \tag{4-76}$$

$$\tau = \frac{\alpha_{\mathrm{L}}}{R_{\mathrm{inn}}{}^{2}} t, \text{ and} \tag{4-77}$$

$$\theta_{\mathrm{L}}\left(\xi,\tau\right) = \frac{T_{\mathrm{L}}\left(r,t\right) - T_{\mathrm{f}}}{T_{\mathrm{f}} - T_{\infty}}, \tag{4-78}$$

for the non-dimensional pipe radius, time, and temperature, respectively.

The governing equation, interface energy equation, boundary conditions, and the initial condition were modified accordingly to

$$\frac{1}{\xi}\frac{\partial}{\partial\xi}\left(\xi\frac{\partial\theta_{\mathrm{L}}\left(\xi,\tau\right)}{\partial\xi}\right) = \frac{\partial\theta_{\mathrm{L}}\left(\xi,\tau\right)}{\partial\tau}, \tag{4-79}$$

$$-k_{\mathrm{L}}\frac{\partial\theta_{\mathrm{L}}\left(\xi_{\mathrm{i}},\tau\right)}{\partial\xi} = \frac{\alpha_{\mathrm{L}}\rho_{\mathrm{L}}\hbar}{\left(T_{\mathrm{f}} - T_{\infty}\right)}\frac{}{d\tau}, \tag{4-80}$$

$$\theta_{\mathrm{L}}\left(\xi_{\mathrm{i}},\tau\right) = 0, \tag{4-81}$$

$$\frac{A_{\mathrm{inn}}k_{\mathrm{L}}}{R_{\mathrm{inn}}}\frac{\partial\theta_{\mathrm{L}}\left(1,\tau\right)}{\partial\xi} = \frac{V^{2}}{R'_{\mathrm{NiCr}}\left(T_{\mathrm{f}} - T_{\infty}\right)} - UA_{\mathrm{NiCr}} - UA_{\mathrm{NiCr}}\theta_{\mathrm{L}}\left(1,\tau\right), \tag{4-82}$$

$$\theta_{\mathrm{L}}\left(\xi,0\right) = 0. \tag{4-83}$$

Given the non-homogenous boundary condition of Eq. (4-82), superposition should be applied to solve the governing equation. After using the separation of variables method and invoking orthogonality, the temperature distribution of the liquid phase was obtained. By differentiating the non-dimensional temperature term and substituting it in Eq. (4-80), the transient location of the moving boundary during the phase change can be obtained from

$$-k_{\mathrm{L}}\left(\frac{1}{\xi_{\mathrm{i}}}\left[\frac{\dfrac{V^{2}}{R'_{\mathrm{NiCr}}\left(T_{\mathrm{f}}-T_{\infty}\right)}-UA_{\mathrm{NiCr}}}{\dfrac{A_{\mathrm{inn}}k_{\mathrm{L}}}{R_{\mathrm{inn}}}-UA_{\mathrm{NiCr}}\ln(\xi_{\mathrm{i}})}\right]+\sum_{\mathrm{n}=1}^{\infty}\bar{g}_{\mathrm{n}}\bar{\gamma}_{\mathrm{n}}\left[J_{0}\left(\bar{\gamma}_{\mathrm{n}}\xi_{\mathrm{i}}\right)Y_{1}\left(\bar{\gamma}_{\mathrm{n}}\xi_{\mathrm{i}}\right)-Y_{0}\left(\bar{\gamma}_{\mathrm{n}}\xi_{\mathrm{i}}\right)J_{1}\left(\bar{\gamma}_{\mathrm{n}}\xi_{\mathrm{i}}\right)\right]\exp\left(-\bar{\gamma}_{\mathrm{n}}^{2}\tau\right)\right)\approx\frac{\alpha_{\mathrm{L}}\rho_{\mathrm{L}}\hbar}{\left(T_{\mathrm{f}}-T_{\infty}\right)}\frac{}{d\tau}, \tag{4-84}$$

It was found that the contribution of the summation term on the left hand side of Eq. (4-84) was negligible and Eq. (4-84) could be simplified to

$$-k_{\mathrm{L}}\frac{1}{\xi_{\mathrm{i}}}\left[\frac{\dfrac{V^{2}}{R'_{\mathrm{NiCr}}\left(T_{\mathrm{f}}-T_{\infty}\right)}-UA_{\mathrm{NiCr}}}{\dfrac{A_{\mathrm{inn}}k_{\mathrm{L}}}{R_{\mathrm{inn}}}-UA_{\mathrm{NiCr}}\ln(\xi_{\mathrm{i}})}\right]\approx\frac{\alpha_{\mathrm{L}}\rho_{\mathrm{L}}\hbar}{\left(T_{\mathrm{f}}-T_{\infty}\right)}\frac{}{d\tau}, \tag{4-85}$$

Given the complexity of Eq. (4-85) and the implicit nature of the solution, numerical integration was implemented to solve Eq. (4-85) and obtain the transient non-dimensional location of the interface, ξ_{i}.

4.2.4 Uncertainty in the Estimation of the Transient Ice Temperature

An error analysis was conducted to study the propagation of uncertainty in the results that were obtained from the thermal models for heating and melting of the ice. The error associated with the geometry of the problem and the thermo-physical properties of the ice, steel pipe, and the coating layers was assumed to be negligible. Mahdavi and McDonald [101] have made a similar assumption with respect to thermos-physical properties. It was observed that one of the major determining factors and a potential substantive source of uncertainty in the models was the thermal properties of the insulation layer. It is well known that the thermal conductivity and the resulting resistance value (R-value) of the glass wool insulation are greatly affected by the application of compression forces during installation, which change the physical morphology and density of the insulation. The resulting increase in the density of the insulation material results in increase of the thermal conductivity of the insulant [102]. In the models that were developed in this study, the conductivity of the insulation material was assumed to be 0.04 $\mathrm{Wm^{-1}K^{-1}}$ [103]. However, a relatively broad range for this value can be found in the literature [104]. Therefore, in order to study the effect of the thermal conductivity of the insulation material on the overall heat transfer coefficient and the resulting effect on the ice temperature estimation, an uncertainty analysis was performed. For the heating stage, the impact of uncertainty of the overall heat transfer coefficient on the eigenvalues (Eq. (4-27)) was studied, and then, the propagation of error in the temperature distribution of the ice (see Eq. (4-40)) was determined.

It was assumed that the uncertainty in the thermal conductivity of the insulation layer was $\pm$ 0.005 $\mathrm{Wm^{-1}K^{-1}}$. This was based on the range of the thermal conductivity values that were suggested for the glass mineral wool insulation, which was 0.035 and 0.045 $\mathrm{Wm^{-1}K^{-1}}$ [105]. Therefore, the resulting uncertainty in the *U*-value, which was calculated to be 2.16 $\mathrm{Wm^{-2}K^{-1}}$ from Eq. (4-6), was found to be ± 0.27 $\mathrm{Wm^{-2}K^{-1}}$. Given the dependence of the eigenvalues on the overall heat transfer coefficient (U), the resulting uncertainty in the determination of the eigenvalues (λ_n) was also calculated. In this regard, Eq. (4-27) was rewritten in the form of Eq. (4-86) as

$$\frac{\lambda_\mathrm{n} J_1\left(\lambda_\mathrm{n} R_\mathrm{inn}\right)}{J_0\left(\lambda_\mathrm{n} R_\mathrm{inn}\right)} = \frac{\beta U A_\mathrm{NiCr}}{A_\mathrm{inn} k_\mathrm{S}} \Rightarrow F\left(\lambda_\mathrm{n}\right) = \eta U, \tag{4-86}$$

where η represents all the constants in the right hand side of Eq. (4-86), and therefore, does not contribute to the propagation of uncertainty. Then, the uncertainty in the eigenvalues was estimated by taking the derivative of the function F with respect to λ_n as

$$\delta F\left(\lambda_\mathrm{n}\right) = \frac{dF\left(\lambda_\mathrm{n}\right)}{d\lambda_\mathrm{n}} \delta\lambda_\mathrm{n} = \frac{\left[J_1\left(\lambda_\mathrm{n} R_\mathrm{inn}\right) + \lambda_\mathrm{n}\left(R_\mathrm{inn} J_0\left(\lambda_\mathrm{n} R_\mathrm{inn}\right) - \frac{1}{\lambda_\mathrm{n}} J_1\left(\lambda_\mathrm{n} R_\mathrm{inn}\right)\right)\right] \times \left(J_0\left(\lambda_\mathrm{n} R_\mathrm{inn}\right)\right) + \left[R_\mathrm{inn} J_1\left(\lambda_\mathrm{n} R_\mathrm{inn}\right)\right] \times \left[\lambda_\mathrm{n} J_1\left(\lambda_\mathrm{n} R_\mathrm{inn}\right)\right]}{\left[J_0\left(\lambda_\mathrm{n} R_\mathrm{inn}\right)\right]^2} \delta\lambda_\mathrm{n} = \eta \delta U, \tag{4-87}$$

Following from Eq. (4-87), the resulting uncertainty in the eigenvalues was calculated to be 6.3%. Given that both functions $\Psi_{\mathrm{s}}(r,t)$ and $\phi_{\mathrm{s}}(r)$ (see Eqs. (4-28) and (4-30)) are mutually dependent on each other and both include the U and λ_{n} terms, the uncertainty associated with the temperature distribution of the ice was calculated by taking the summation of the uncertainty contributed by each function [106], and is given by

$$\delta T_{\mathrm{S}}(r,t) = \delta\phi_{\mathrm{S}}(r) + \delta\psi_{\mathrm{S}}(r,t), \tag{4-88}$$

The uncertainty caused by each function was calculated from Eqs. (4-89) and (4-90) and is given as

$$\delta\phi_{\mathrm{S}} = \frac{d\phi_{\mathrm{S}}(U)}{dU}\delta U = \left| -\frac{V^2}{U^2 R'_{\mathrm{NiCr}} A_{\mathrm{NiCr}}} \right| \delta U\,, \tag{4-89}$$

$$\delta\psi_{\mathrm{S}}(r,t) = \sum_{\mathrm{n}=1}^{\infty} \delta(\psi_{\mathrm{S}})_{\mathrm{n}}(r,t), \tag{4-90}$$

The uncertainty in the function was the sum of all the uncertainties that was calculated for each value of n. It was observed that only the first eigenvalue was significant to the estimation of the overall uncertainty in $\Psi_{\mathrm{S}}(r,t)$ due to the fact that for the cases in which $n > 1$, the value of $\Psi_{\mathrm{S}}(r,t)$ and the resulting uncertainty were negligible. For ease of calculation, function $\Psi_{\mathrm{S}}(r,t)$ was divided to two dependent terms of H_1 and H_2 as

$$(H_1)_{\mathrm{n}} = \frac{2R_{\mathrm{inn}}\lambda_{\mathrm{n}} J_1(\lambda_{\mathrm{n}} R_{\mathrm{inn}}) \left(T_{\mathrm{i}} - T_{\infty} - \dfrac{V^2}{U R'_{\mathrm{NiCr}} A_{\mathrm{NiCr}}} \right)}{\left[\left(\dfrac{\beta U R_{\mathrm{NiCr}}}{k} \right)^2 + (\lambda_{\mathrm{n}} R_{\mathrm{inn}})^2 \right] J_0^2(\lambda_{\mathrm{n}} R_{\mathrm{inn}})}, \tag{4-91}$$

$$(H_2)_{\mathrm{n}} = J_0(\lambda_{\mathrm{n}} r)\exp(-\alpha_{\mathrm{S}}\lambda_{\mathrm{n}}^2 t), \tag{4-92}$$

where H_1 is the term that was obtained by invoking orthogonality and H_2 is the function that consists of the Bessel and exponential functions of Eq. (4-40). Given that the variables r and t are in the H_2 function, the uncertainty must be calculated at a specific time and location. The propagation of uncertainty for $\Psi_S(r,t)$ that are related to each value of k was derived by way of summation of the fractional uncertainties [106] in H_1 and H_2 given by

$$\frac{\delta\psi_n(r,t)}{\psi_n(r,t)} = \frac{\delta(H_1)_n}{(H_1)_n} + \frac{\delta(H_2)_n}{(H_2)_n} = \frac{1}{(H_1)_n}\left|\frac{d(H_1)_n}{dU}\right|\delta U + \frac{1}{(H_2)_n}\left|\frac{d(H_2)_n}{dU}\right|\delta U, \tag{4-93}$$

where the uncertainties for terms of H_1 and H_2 are given by

$$\delta(H_1)_n = \left|\frac{d(H_1)_n}{dU}\right|\delta U = \left|\frac{\begin{array}{l}\left[\begin{array}{l}2R_{inn}\dfrac{\delta\lambda_n}{\delta U}\left[J_1(\lambda_n R_{inn}) + \lambda_n R_{inn} J_0(\lambda_n R_{inn}) - J_1(\lambda_n R_{inn})\right]\times \\ \left(T_i - T_\infty - \dfrac{V^2}{UR'_{NiCr}A_{NiCr}}\right) + 2R_{inn}\lambda_n J_1(\lambda_n R_{inn})\times\left(\dfrac{V^2}{U^2 R'_{NiCr}A_{NiCr}}\right)\end{array}\right]\times\left[\left(\dfrac{\beta U R_{NiCr}}{k}\right)^2 + (\lambda_n R_{inn})^2\right]J_0^2(\lambda_n R_{inn}) \\ + \left[\begin{array}{l}\left[2U\left(\dfrac{\beta R_{NiCr}}{k}\right)^2 + 2\lambda_n\dfrac{\delta\lambda_n}{\delta U}(R_{inn})^2\right]\times J_0^2(\lambda_n R_{inn}) \\ +2J_0(\lambda_n R_{inn})\left[-R_{inn}J_1(\lambda_n R_{inn})\right]\times\dfrac{\delta\lambda_n}{\delta U}\left[\left(\dfrac{\beta U R_{NiCr}}{k}\right)^2 + (\lambda_n R_{inn})^2\right]\end{array}\right]\times\left[2\lambda_n R_{inn} J_1(\lambda_n R_{inn})\left(T_i - T_\infty - \dfrac{V^2}{UR'_{NiCr}A_{NiCr}}\right)\right]\end{array}}{\left(\left[\left(\dfrac{\beta U R_{NiCr}}{k}\right)^2 + (\lambda_n R_{inn})^2\right]J_0^2(\lambda_n R_{inn})\right)^2}\right|\delta U, \tag{4-94}$$

$$\delta(H_2)_n = \left|\frac{d(H_2)_n}{dU}\right|\delta U = \left|\left[-rJ_1(\lambda_n r)\right]\left(\frac{\delta\lambda_n}{\delta U}\right)\times\exp\left(-\alpha_S\lambda_n^2 t\right) - 2\lambda_n\alpha_S t\left(\frac{\delta\lambda_n}{\delta U}\right)\exp\left(-\alpha_S\lambda_n^2 t\right)\times J_0(\lambda_n r)\right|\delta U, \tag{4-95}$$

It was observed that in the specific case in which the voltage difference was 7.5 V, $r = R_{inn}$, and t = 3,000 seconds, the uncertainty that propagated through the $(H_1)_k$ and $(H_2)_k$ functions were 11.6% and 1.8%, respectively. This resulted in uncertainty of 13.4% in the corresponding value of $\Psi_S(r,t)$. The uncertainty that was related to $\phi_S(r)$ was also found to be 14.8 %. These estimates are in good agreement with the resulting uncertainty in the $\phi_S(r)$ and $\Psi_S(r,t)$ functions. By substituting the maximum and minimum U-values in the model it was observed that values of the $\phi_S(r)$ and $\Psi_S(r,t)$ functions changed by ± 15% and ± 14.4%, respectively. However, the total uncertainty of 28.2% that was obtained from the sum of the uncertainties (13.4% and 14.8%) in the ice temperature distribution, which was estimated by using Eq. (4-88) was significantly overestimated. The overestimation was due to the repetition of the same terms in both the $\phi_S(r)$ and $\Psi_S(r,t)$ functions that makes them mutually dependent on each other. Given the equal, but opposite values of the estimated uncertainties, the total uncertainty was neutralized or counter-balanced, which is known as compensating error [106]. However, according to Eq. (4-88), all the uncertainties are simply added together, which has resulted in the overestimation of the total uncertainty. Therefore, the uncertainty value that was estimated from the propagation of uncertainty analysis is not accurate and reliable values of the uncertainties in the ice temperature distribution and the duration of the heating and melting times may be obtained by substituting the maximum and minimum values of the different overall heat transfer coefficient values into the models to obtain quantitative information on the possible range of the duration of time needed for heating and melting of ice in the pipe.

The uncertainty that was calculated was only related to the results that originated from the modelling procedure. However, in practice, the uncertainty was not only limited to the model. The experimental measurements were also subjected to uncertainty. Based on the specifications provided by the manufacturers of the devices that were used in this experiment, uncertainty on the order of ±1°C, ±0.2 %, ±0.1 A, were associated with measurement of temperature, supply voltage, and measurement of current, respectively. Given the wide range of measurements, the uncertainties that were claimed appear to be negligible.

4.3 Results and Discussion

The microstructure of fabricated coatings that are used as heating elements or heating films will affect the amount of energy that is generated by the coatings and the temperature distribution of the coatings. The resistivity and the measured resistance of the coatings will be dependent on, among other factors, the microstructure of the fabricated coatings. The electrical resistance of the coating heating element was measured to be 2.8 Ω. Therefore, by adjusting the voltage of the DC power supply to 5.3 V, 7.5 V, and 10.6 V, the supplied power (*P*) to the coating-based heating system was calculated to be 10 W, 20 W, and 40 W, respectively. By fabricating numerous coating systems, it was observed that the electrical resistance of the coating heating element depended greatly on the thickness of the coating and its microstructure. It is well-established that the electrical resistance of a conductive material is inversely proportional to its cross-sectional area. It is also well-known that the presence of microstructural defects, microcracks, and porosity can affect the electrical resistance by changing the effective cross-sectional area of the conductive material [83]. In this study, the average porosity of the Ni-50Cr coating was measured from high-magnification SEM images and found to be 5.6 ± 1.6 vol. % (n = 10). Furthermore, it was found that the thickness of the alumina layer was useful in avoiding malfunction of the coating system. Figure 4-2 presents a micrograph that was taken from a cross section of the coated pipe, and shows that the alumina layer that was deposited by way of the flame spraying process had a porous structure. It was found that a thickness of alumina that was on the order of 180 microns was sufficient to protect the alumina layer from dielectric breakdown and the metal coating from short circuiting at high powers.

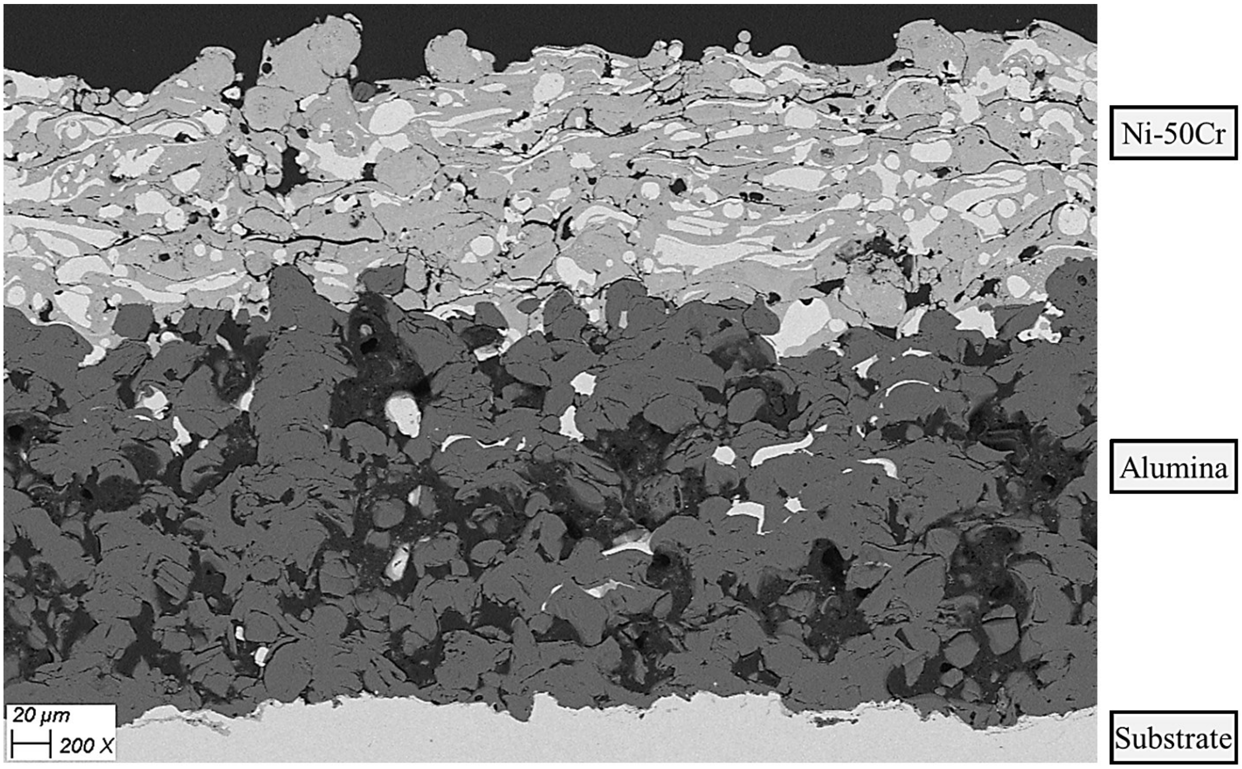

Figure 4-2 Backscattered SEM image of the coating system sectioned from the middle of the coated pipe (200X magnification)

The performance of the heating system to heat and melt ice enclosed in a steel pipe was investigated and the data from the experiments were compared with results from the models that were developed. The results that were obtained from the heating tests and the mathematical models for the supplied powers of 10 W, 20 W, and 40 W are shown in Figs. 4-3(a), 4-3(b), and 4-3(c), respectively. The beginning of the heating process was defined as the point at which electric current was supplied to the coating heating element and the end of the heating process was defined as the time at which the temperature of the coating surface reached the fusion temperature of the ice. The values of the times required to heat the ice to the fusion temperature as predicted by the model and observed from experiments are shown in Table 4-3.

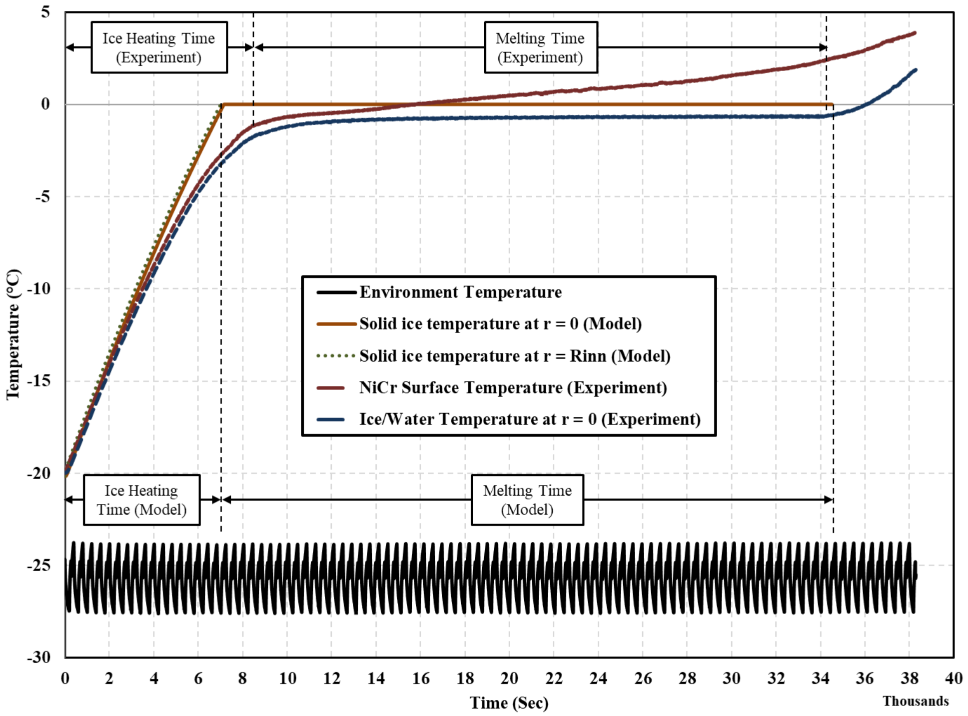
Ice Heating Time (Experiment)
Melting Time (Experiment)
Ice Heating Time (Model)
Melting Time (Model)
Environment Temperature
Solid ice temperature at r = 0 (Model)
Solid ice temperature at r = Rinn (Model)
NiCr Surface Temperature (Experiment)
Ice/Water Temperature at r = 0 (Experiment)
Temperature (°C)
5
0
-5
-10
-15
-20
-25
-30
0
2
4
6
8
10
12
14
16
18
20
22
24
26
28
30
32
34
36
38
40
Time (Sec)
Thousands

(*a*)

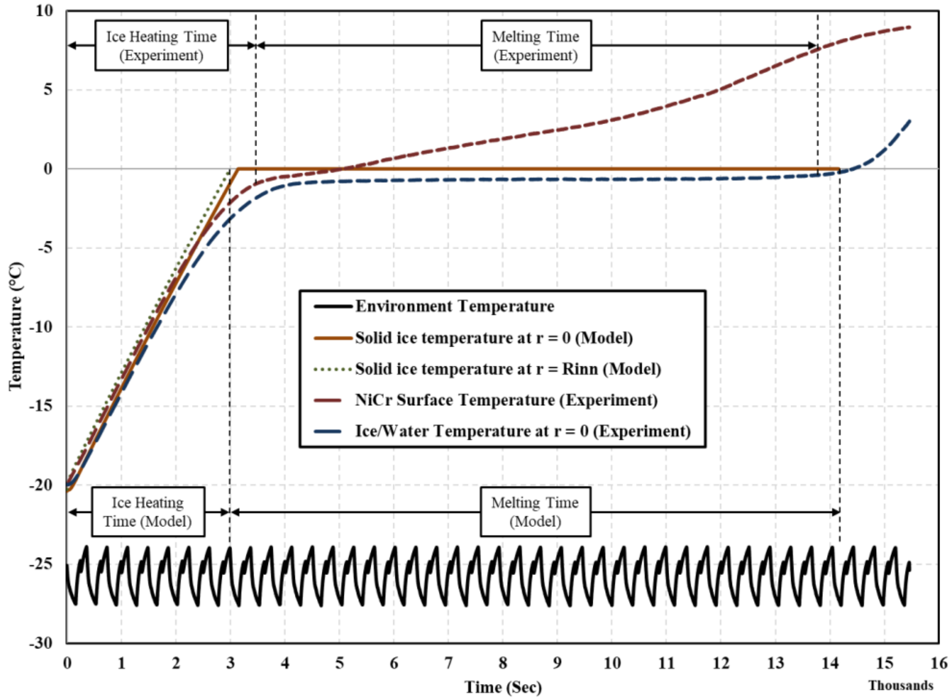
Ice Heating Time (Experiment)
Melting Time (Experiment)
Ice Heating Time (Model)
Melting Time (Model)
Environment Temperature
Solid ice temperature at r = 0 (Model)
Solid ice temperature at r = Rinn (Model)
NiCr Surface Temperature (Experiment)
Ice/Water Temperature at r = 0 (Experiment)
Temperature (°C)
10
5
0
-5
-10
-15
-20
-25
-30
0
1
2
3
4
5
6
7
8
9
10
11
12
13
14
15
16
Time (Sec)
Thousands

(*b*)

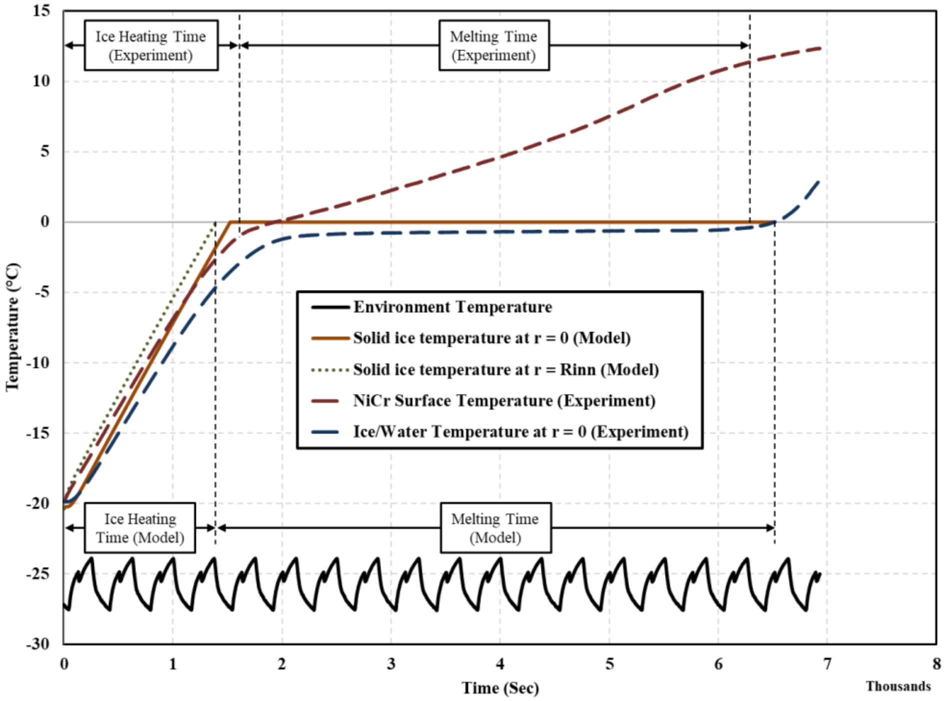

(*c*)

Figure 4-3 Experiment and model predictions of transient temperature for supplied powers of (a) 10 W, (b) 20 W, and (c) 40 W

Table 4-3 Comparison of duration of time that was obtained from the tests and the models for each stage

Stage	Source of data		Duration (min) (Relative difference %)		
			10 W	20 W	40 W
Heating of ice	Experiment		139 ± 4	57 ± 2	27 ± 1
	Model		117 ± 4 (16 %)	50 ± 1 (12 %)	23 (15%)
Melting of ice	Experiment		431 ± 8	172 ± 4	78 ± 2
	Model	Time-dependent solution	458^{+32}_{-28} (6 %)	185 ± 6 (8 %)	83 ± 2 (6 %)
		Quasi-steady approximation	458^{+32}_{-28} (6 %)	186^{+7}_{-6} (8 %)	85 ± 2 (9 %)

Due to practical limitations, the temperature of ice that was in contact with the inner surface of the pipe could not be measured. However, the temperature at the outer surface of the NiCr coating was measured instead. Considering the relatively high thermal conductivity of the steel pipe, alumina coating, and NiCr coating and the small thicknesses of the Schedule 40 steel pipe (order of 3.9 mm) and the deposited coatings (order of 180 μm for alumina and 110 μm for NiCr), the estimated thermal resistance of the coating layers and the pipe wall (see Eq. (4-6)) was found to be negligible (approximately 0.0002 K/W) and, therefore, the difference between the temperature of the outer surface of the NiCr coating and the temperature of the solid ice at the inner surface of the pipe was considered to be negligible at steady state. Given the transient nature of the problem, the validity of this assumption is undermined as the supplied power is increased. Therefore, it was assumed that the ice began to melt when the coating temperature reached the fusion temperature. The end of the melting process was defined as the moment when the temperature of the water inside the pipe began to increase from the fusion temperature at the end of the melting plateau. At that time, further heating of the water was observed as evidenced by the increase in water temperature due to sensible heating (See Fig. 4-3).

The comparison of the results that were obtained from the thermocouples for the cases in which 10 W and 20 W were supplied (see Figs. 4-3(a) and 4-3(b)) confirms the negligible temperature difference between the transient temperatures of the NiCr coating surface and the ice at the inner surface of the pipe during the heating stage. Comparison of the transient temperature of the ice at the center of the pipe from the initial temperature up to -5°C obtained from the test and model revealed that the average difference between the results were 0.8°C, 0.4°C and 1°C for the cases in which 10 W, 20 W, and 40 W were supplied to the heating element, respectively. While the transient heat conduction model predicted the transient temperature of the ice accurately up to -5°C (see Figs. 4-3(a) and 4-3(b)), the predictions of the model deviated considerably from the experimental results at temperatures close to the melting point. This deviation was caused by the reduced sensible heat absorbed by the ice.

The temperature of the heating element near the copper coating rings was slightly higher (order of 1-2°C) than that at the middle of the heating element. The reason for this observation was twofold. First, the electrical contact resistance between the connecting wires, solder material, copper coating, and the NiCr coating was low, thus allowing for increased energy generation at the copper coating rings due to the higher electron density there. Second, and more importantly, there was a lower volume of water at the ends of the pipe due to the presence of the end caps and installation of thermowells. Thus, a lower volume of water was available to absorb the heat that was generated. As a result, not all of the heat that was generated was absorbed by ice and water as sensible heat to increase the temperature of ice or water. The portion of the heat that was absorbed by ice near the copper coatings to melt the ice caused the small deviation between the model and experiment results. It is hypothesized that this difference in the obtained results, which was due to the effect of the end sections of the coated pipe, would likely be lower for longer coated pipes.

The transient temperature of the ice and the duration of time that was required to heat the ice from the initial temperature to the fusion temperature were obtained from the transient heat conduction model. Comparison of the predictions of the model and the data from the experiments shows that the model predicted the duration of ice heating to within 16%, 12%, and 15% of that which was measured from the experiments for supplied powers of 10 W, 20 W, and 40 W, respectively. The higher relative difference between the data from the experiment and prediction of the model for the case in which 10 W was supplied was likely due to the uncertainty associated with calculation of the overall heat transfer coefficient and the greater contribution of term $UA_{\text{NiCr}}\left[T_{\text{NiCr}}(t)-T_{\infty}\right]$ in Eq. (4-3) because of the lower value of the $\frac{V^2}{R'_{\text{NiCr}}}$ term. In contrast, for the case in which 40 W was supplied and the contribution of the $UA_{\text{NiCr}}\left[T_{\text{NiCr}}(t)-T_{\infty}\right]$ term was much less, the relatively high difference was likely due to the higher temperature gradient and the fact that the comparison was made between the NiCr coating surface temperature from the experiment with the temperature of the ice at the inner surface of the pipe from the model.

The determinative factor in calculation of the overall heat transfer coefficient (U) was determination of the heat transfer coefficient (h), which was estimated based on the speed of the air inside the closed galvanized duct. The speed of the free-stream airflow was measured to be 31 km/h (19.3 miles/h). This free-stream air velocity provided a stringent testing parameter since the American Society of Heating, Refrigeration, and Air-conditioning Engineers (ASHRAE) and the Canadian Wind Energy Atlas have suggested that outdoor wind speeds in the winter are typically about 24 km/h (15 miles/h) [89]. The average heat transfer coefficient that resulted from external airflow over the cylindrical pipe, and which was required in order to calculate the overall heat transfer coefficient, was estimated to be 91 $\text{Wm}^{-2}\text{K}^{-1}$ from Eq. (4-8) that was also verified with experimental data. Several experiments were conducted to obtain the heat transfer coefficient. In these experiments thermal insulation was installed at the ends of the pipe assembly to expose only the portion of the pipe that was coated with NiCr to the circulation of the cold ambient air at the same time that power was supplied to the coating. Therefore, according to the balance of the energy at steady state, the heat that was provided to the pipe was equal to the heat that was dissipated to the environment by convection. By measuring the temperature of the surface of the NiCr coating at steady state by using surface thermocouples and applying the balance of energy, the only unknown variable, which was the heat transfer coefficient, was obtained. It was observed that the values that were obtained from these tests were in close agreement with values obtained from the correlation equation of Eq. (4-8).

The other reason for the relative difference between the results from the model and the experiment for the solid ice heating stage was the fact that not all of the supplied thermal energy was absorbed by the ice. This resulted in deviations from an ideal one-dimensional heat conduction problem. Taking into account the mass and specific heat capacity of all the components in the coated pipe assembly, term β in Eq. (4-3) was calculated to be 0.37 for the heating stage. In contrast, given the low ratio of the sensible heat to latent heat in the melting stage, it was assumed that all the generated heat was absorbed by the ice that was inside the pipe (see Eq. (4-44)). The validity of this assumption will be undermined when higher powers are supplied to the coating-based heating element since higher energy input will result in higher water temperature at the inner surface of the pipe, resulting in higher sensible to latent heat ratio during the melting process.

The transient thickness of the ice within the pipe during the melting process and the time that was required to melt the ice inside the pipe completely (see Figs. 4-4(a), 4-4(b), and 4-4(c)) were acquired from the model that was based on the transient moving-boundary problem in finite-region. The total times that were required to melt the entire ice inside the pipe for the supplied powers can be measured from Figs. 4-3(a), 4-3(b), and 4-3(c). The duration of the melting process that was obtained from the model was the time that was required for the solid-liquid interface to move from the inner radius of the pipe (R_{inn}) to the centre of the pipe at $r = 0$. The values of the times required to melt the ice as predicted by the model and observed from experiment are shown in Table 4-3. Further details regarding the transient thickness of ice and comparison between the results obtained from the time-dependent solution and quasi-steady approximation given by Eqs. (4-74) and (4-75), respectively, can be seen in Figs. 4-4(a), 4-4(b), and 4-4(c).

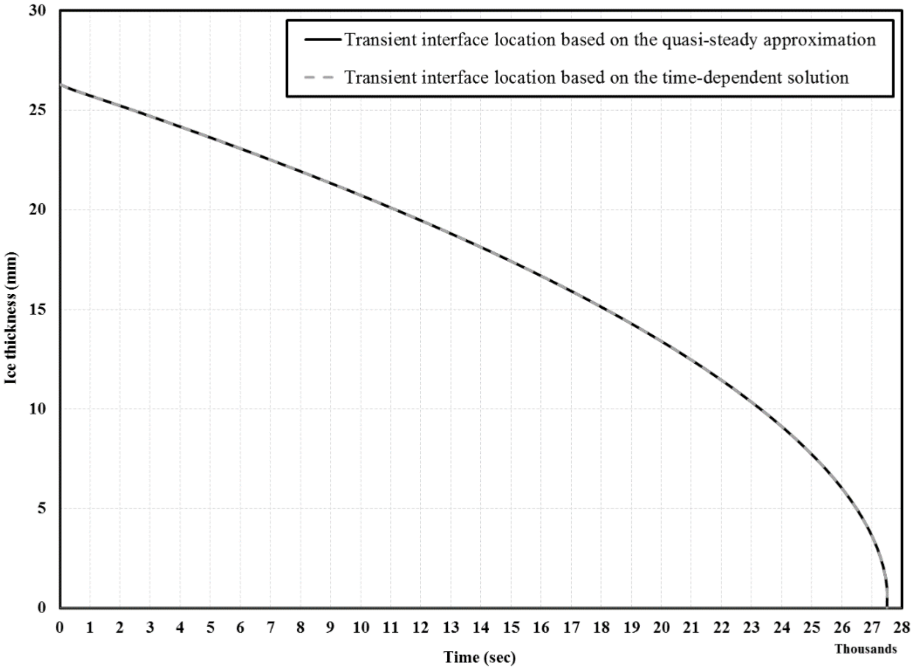

(a)

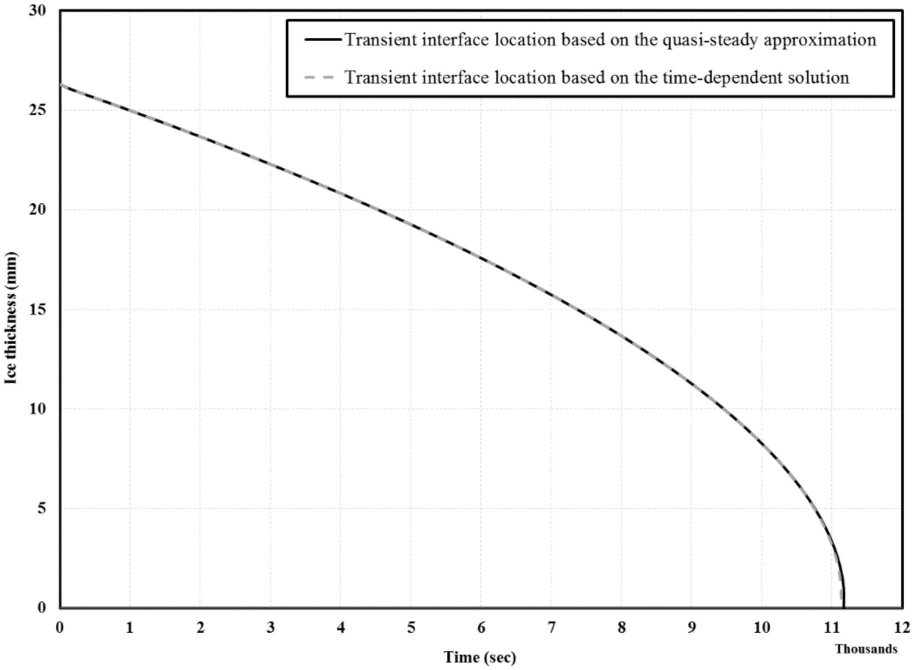

(b)

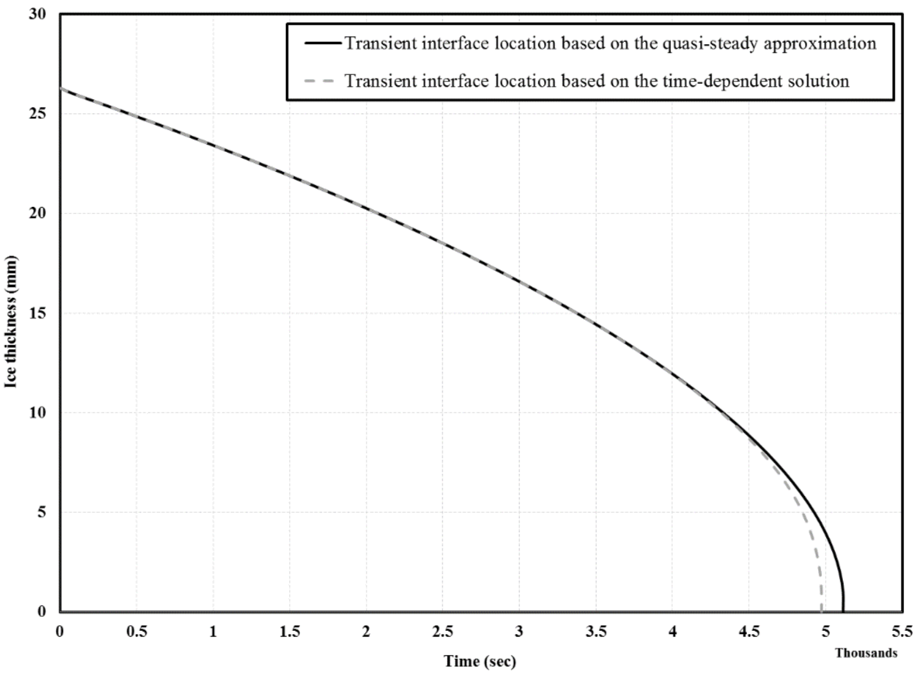

(c)

Figure 4-4 Transient location of the interface at supplied powers of (a) 10 W, (b) 20 W, and (c) 40 W

The rate at which the ice thickness decreased during the melting stage increased with time. This was due to the variable surface area at each solid-liquid interface location, $r_i(t)$. As the interface was approaching the center of the pipe, less heat was required to melt ice at the surface area of the moving interface, and, as a result, less time was required for the interface to move inward. The results show that the marginal contribution of the summation term that is shown in Eq. (4-74) is obvious when the interface radius (r_i) decreases as the interface moves towards the center of the pipe, resulting in lower characteristic values, especially for cases in which higher powers are applied. This negligible impact of the summation term, especially at the early stages of the phase change when the interface location is not close to the center of the pipe was due to the $\exp\left(-\alpha_L \gamma_n^2 t\right)$ term in Eq. (4-74) whose value was reduced because of the presence of large negative value in the exponential term. Therefore, the contribution of the results obtained from function Ψ_L was negligible compared to that obtained from the function ϕ_L (see Eq. (4-48)). That said, the solution for the transient moving boundary problem could be simplified by taking into account only the contribution of function ϕ_L, which only depends on radius. Therefore, the procedure for solving the phase change problem could be simplified by using a quasi-steady state model.

There were two challenges associated with consideration of function Ψ_L to determine the transient location of the solid-liquid interface. First, it has been stated in the literature that the superposition principle is not applicable to phase change problems due to the non-linear nature of the interface energy equation [107]. Therefore, in the absence of exact solutions, approximate and numerical methods can be used to solve the phase change problems [107]. As a result, the data obtained from consideration of Ψ_L could not easily be summed with results obtained from the function, ϕ_L. However, in this study, it has been shown that for the given problem and boundary and initial conditions, application of the superposition method was not problematic due to the negligible contribution of the summation term in Eq. (4-74). Second, the initial condition that was given by Eq. (4-43) did not fully describe the true initial condition of the problem. This could have affected the values obtained for g_k in Eq. (4-72).

The relative differences between the predictions of the model and the measurements from the experiments for the duration of the melting process were calculated to be less than 9% for all the supplied powers. Table 4-3 lists the detailed results related to the duration of each stage of the process that were obtained from the heating experiments and the models. The temperature of the surface of the coating was higher for the cases with higher supplied powers. This resulted in slightly higher proportion of sensible heating to latent heating for the cases with higher applied powers. In free boundary conduction problems of melting, the quasi-steady approximation will be valid when the Stefan number, $\mathrm{Ste} = \frac{C_{\mathrm{pL}}\left(T_{\mathrm{NiCr}} - T_{\mathrm{f}}\right)}{\hbar}$, is less than 0.1 [108]. For the cases in which 10 W and 20 W of power were supplied, the Stefan number was no more than 0.1 (0.03 for 10 W and 0.09 for 20 W), resulting in the agreement that was observed between the model predictions and the experiments as shown in Fig. 4-3. The difference between the data from the experiments and predictions of the model (quasi-steady approximation) for the duration of the melting process was slightly greater for the case in which the highest power of 40 W was supplied. Given the higher temperature gradient across the radial and along the axial directions of the coated pipe, which was caused by pipe end effect and electrical contact resistance between the connecting wire, solder material, copper coating, and NiCr coating, the melting of the ice inside the pipe likely started earlier than the time indicated by the surface thermocouple measurement and, therefore, the difference between the data from the model prediction and the experiments for the case in which 40 W was supplied was likely due, in part, to the limited length of the coated pipe sample. Further, beyond 4,500 seconds of heating with 40 W of power (see Fig. 4-4(c)), the Stefan number was as large as approximately 0.15, which is larger than 0.1, indicating that the quasi-steady approximation would no longer be valid.

The transient location of the solid-liquid moving interface during the melting process for eight cases in which different powers were supplied are shown in Fig. 4-5. The curves were created based on a dimensionless term (υ), which indicates the ratio of the thermal energy supplied to the ice to the approximate dissipated energy to the environment. The dependence of the duration of melting on the heat generated by way of Joule heating can be seen in Fig. 4-5 based on non-dimensional terms according to the non-dimensional quasi-steady approximation given in Eq. (4-85). As can be seen, the difference in the duration of the melting processes is reduced at high powers. The reason for that is the increase in the temperature of the liquid phase due to the larger temperature gradient in the radial direction, which increases the sensible to latent heat ratio. As a result, more heat is transferred to the liquid phase and then dissipated to the ambient by convection and a reduced portion of the supplied heat is absorbed by the ice for the phase change.

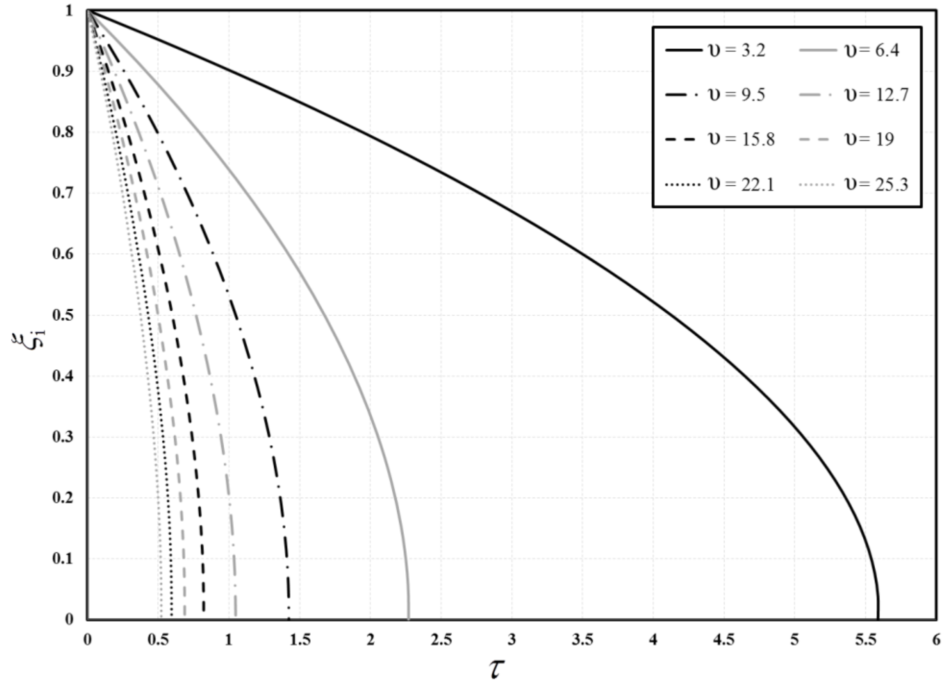

Figure 4-5 Non-dimensional transient location of the interface based on quasi-steady approximation for various non-dimensional supplied powers

The speed at which the solid-liquid interface propagated toward the center of the pipe versus the interface location for different supplied powers is shown in Fig. 4-6, which was obtained from Eq. (4-75). The speed of propagation of the liquid-solid interface increased dramatically as the interface approached the center of the pipe. Given the decrease in the lateral surface area of the solid ice in the cylindrical pipe as the interface moved toward the center of the pipe and with the approximately constant energy input from the coating-based heating system, the heat flux that was applied to the solid-liquid interface surface increased with time. Therefore, the velocity at which the moving boundary propagated increased as shown in Fig. 4-6. This increase in the interface velocity was noticeable when the interface was close to the center of the pipe (r_i □). Due to the singularity of the heat conduction solution at the center of the pipe when both the applied heat flux to the ice and the velocity of the interface approached infinity, the classical Fourier theory of heat conduction would not be valid at the time at which the interface arrived at the center of the pipe at $r_\mathrm{i} = 0$. Therefore, it is suggested that a non-Fourier conduction model, which would be based on a hyperbolic heat conduction equation, should be used to predict the temperature distribution and interface location at that particular time at the center of the pipe [109]. It was found by Sadd and Didlake [109] that the temperature of the liquid phase that is predicted by a non-Fourier model during melting is slightly higher than the temperature that is obtained based on the classical Fourier model. Furthermore, depending on the assumed relaxation time, the location of the interface would be slightly farther for the case in which the heat conduction model is developed based on a non-Fourier heat conduction behavior [109]. Although the transition from the parabolic Fourier model to the hyperbolic non-Fourier model for short time scales and its effect on the temperature response have been the subject of numerous research studies [109 - 111], it is not within the scope of the present study.

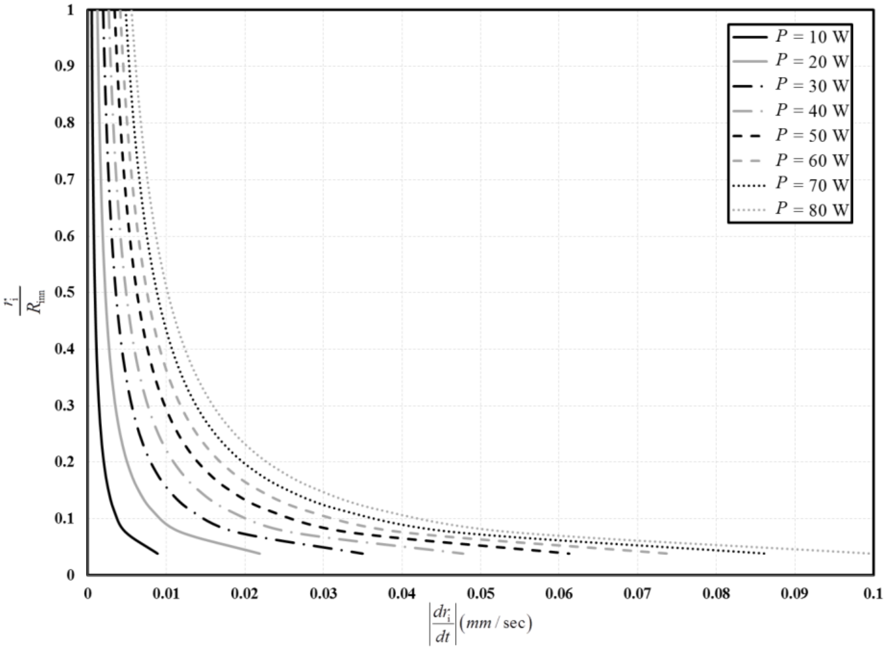

Figure 4-6 Transient speed of the moving interface versus interface location for various supplied powers

4.4 Conclusions

In this study, two one-dimensional transient heat conduction models were developed to predict the heating and melting times of the ice inside a closed pipe that was coated with a multi-layered thermal-sprayed coating system. Based on the obtained results from the models and the experiments, the following conclusions can be drawn:

- It was found that the results obtained from the model and the data collected from the heating test were in good agreement with one another. For the cases in which 20 W and 40 W powers were supplied to the heating element, the model could satisfactorily predict the transient temperature of the enclosed solid ice. However, in the case in which 10 W was applied, the prediction of model slightly differed from the experimental results due to the greater contribution of the term related to the dissipation of the heat to the ambient and the uncertainty in calculation of the overall heat transfer coefficient.

- The relative errors between the results obtained from the heating tests and the model that was developed based on one-dimension transient conduction for all the supplied powers were less than 16%. The relative differences between the duration of time obtained from the test and the model for the melting stage were calculated to be less than 9% for all the three applied powers.

- It was found that results obtained from the simplified case of quasi-steady approximation could be used solely to predict the duration of the melting stage. The impact of including the function Ψ, which was dependent on both time and radius, was insignificant, especially for the cases in which low powers of 10 W and 20 W were provided to the heating element. The reason for this negligible effect was the $\exp\left(-\alpha_{\mathrm{L}}\gamma_{\mathrm{n}}^{2}t\right)$ term in Eq. (4-74). Given the high values of the characteristic values and the time, especially for cases in which low powers are supplied, the resulting values for this term were sufficiently low to neglect the contribution of the solution obtained for function Ψ_{L}.

- The results of this study show that the mathematical models that were developed based on one-dimensional transient conduction theory can be employed as a reliable tool to predict the heating and melting times of the solid ice within coated carbon steel pipes relatively accurately. Therefore, the proposed heating system, coupled with the model, can be used as an effective and predictable means to mitigate the ice accumulation inside closed metallic pipes.

Chapter 5

Techno-Economic Assessment of Coating-Based Heating System Versus Conventional Tracers

Techno-economic assessment of the utilization of thermal-sprayed coatings for temperature control and protection of water distribution steel pipes against freezing and subsequent bursting was conducted. A data-intensive model was developed to compare the technical and economic implications associated with fabrication, installation, operation, and maintenance of multi-layered coatings, as heating systems, with those of conventional heat tracers. The total costs of the of multi-layered coating-based resistive heating system and the conventional heat tracers were obtained and converted to cost per unit length of a 50-mm (2-inch) diameter pipe to allow for scaling by engineers in the field for longer and larger pipes. From the financial perspective, it was found that the cost of material for both heating systems was approximately $25 USD per meter of 50-mm diameter steel pipe. However, the total cost of fabrication of the coating system was noticeably higher due mainly to the labor cost. After conducting the heating tests based on low-temperature working conditions in a cold room, it was found that the efficiency of the coating-based heating system was higher than conventional heat tracers, which was mainly due to intimate contact between the coating-based heating element and the pipe substrate. Based on the obtained results, the improved performance of the coating systems should be viewed in light of the increased fabrication and installation costs by end users for large-scale protection of steel pipes against bursting during freeze events.

Sections 5.1.1, 5.2.1, 5.3.1, and 5.3.4 of this chapter were published in:

M. Rezvani Rad, K. Ngaokere, D. Hayden, A. Kumar, A. McDonald, “Technoeconomic assessment of coating-based resistive heating systems versus conventional heat tracers”, in: International Thermal Spray Conference, May 26- 29, 2019 (Yokohama, Japan), ASM International, (2019), # 47224, 7 pages on compact disk.

Furthermore, the extended version that included all the sections in this chapter was submitted to *Cold Regions Science and Technology* for publication.

5.1 Experimental Method

Details regarding conducting the heating tests for both coating-based heating system and the conventional tracer, and development of a controlling system are presented in the following.

5.1.1 Utilization of the Heating Cable

A similar pipe assembly that was used as the substrate for deposition of the coating system was used for the heating test by using a tracer. The heat tracer that was employed in this study as a heating element was an 1828-mm (6-ft) self-regulating pipe tracing cable (BSX-8-2-FOJ, Thermon, TX, USA). The heating cable was directly connected to a 208 V single phase plug, resulting in heat output with power density of 19.5 W/m (6 W/ft). However, the power output of the heating cable was heavily dependent on the surrounding temperature, and the output wattage could only be obtained at 10°C (50°F). In order to compare the performance of both systems, specific lengths of the tracer based on the required output wattage were wrapped around the pipe to provide approximately 10 W and 20 W for the majority of the duration of the heating test. However, due to the high sensitivity of the self-regulating cable polymeric core and its increased electrical resistance versus temperature, the output wattage of the tracer changed often during the experiments. Therefore, it was difficult to set fixed output wattages over the course of the experiments. An alternate current (AC) power source was used to supply the voltage that was required for moving the electrons through the coating-based heating system and generate heat by way of Joule heating.

Similar to the case in which the coating-based heating system was used for generation of heat, several surface and industrial thermocouples were used to evaluate the performance of the tracer and compare it to that of the coating system. In this regard, a surface thermocouple was also installed on the surface of the heating cable to measure its transient temperature during the heating test.

5.1.2 Development of a Control Unit

A temperature controller (CN7500 ramp/soak controller, OMEGA, QC, Canada) and a high reliability solid state relay (SSRL240DC25, OMEGA, QC, Canada) was assembled to control the heating performance of the coating system and maintain the temperature of the enclosed water at a constant specified value. Not only does using the controlling system decrease the consumption of energy, but also it protects the pipe against freezing in a more efficient and safer manner as the temperature does not fluctuate around the freezing point. It is generally agreed upon that the maintenance temperature should be kept at a temperature higher than the freezing point to prevent formation of ice inside the pipe. In this regard, it has been reported in the literature that control temperature of 5°C provides the required safety factor in protection of the pipe and its content from freezing [112]. The schematic of the controlling system is shown in Fig. 5-1. The controlling unit works based on the difference between the specified set point temperature and the current temperature value, which is measured by a using an industrial thermocouple inside the pipe.

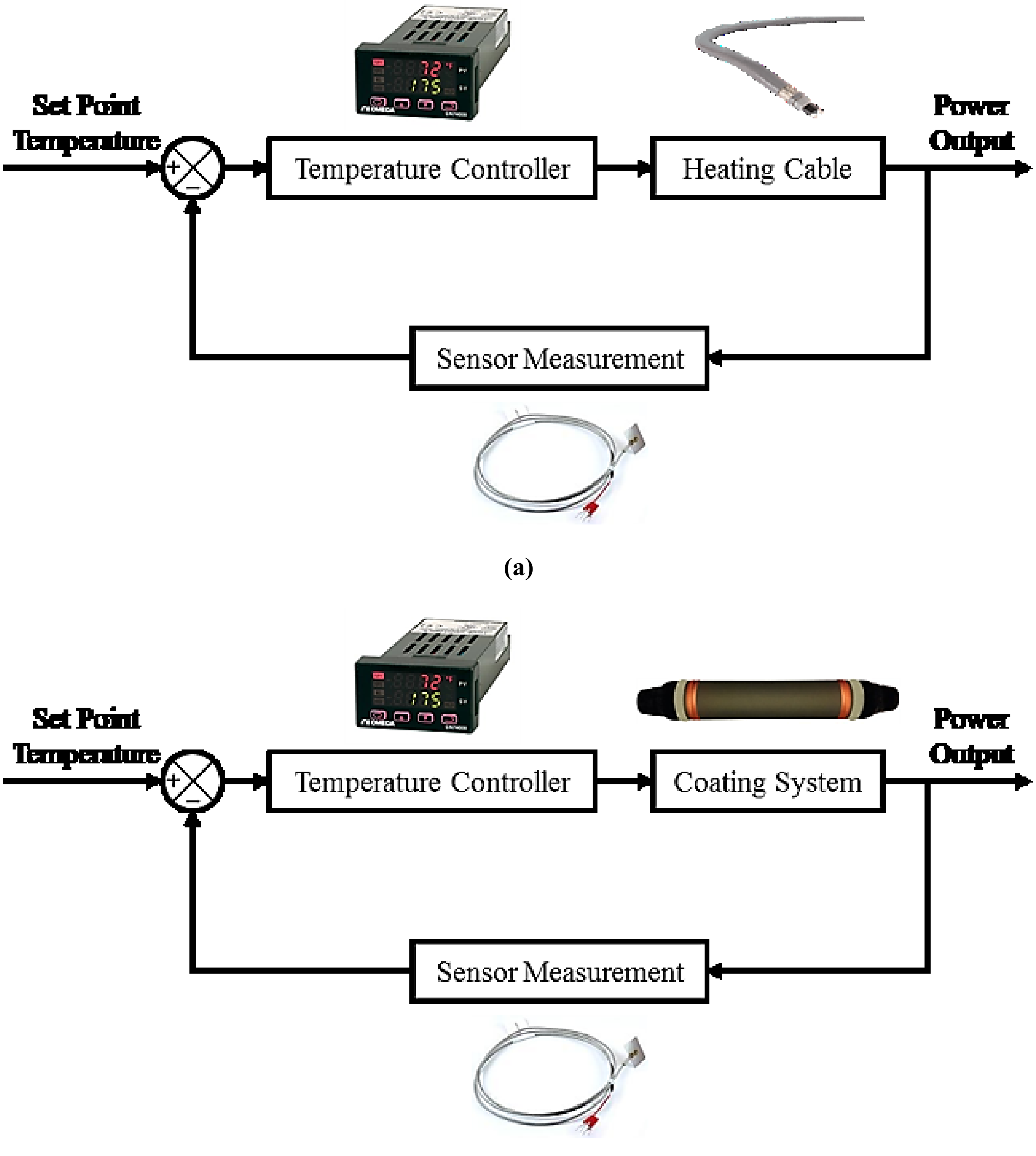

(a)

(b)

Figure 5-1 Schematic of the controlling loop developed for the temperature protection of pipelines for (a) heating cable and (b) coating-based heating system

5.2 Development of the Techno-Economic Model

Details regarding the constitutive parameters, formulations, and assumptions that were taken into account tin the model are presented in the following.

5.2.1 Economic Analysis

A data intensive economic model was developed to compare the total estimated costs of both coating-based and tracer heating systems, which are composed of fabrication, installation, operation, and maintenance expenses. All costs regarding the acquisition, operation, maintenance, and disposal of materials and goods were taken into consideration in the life-cycle cost analysis (LCCA). The advantage of conducting the LCCA is to select a design alternative that brings about the same or similar performance under the same working conditions at a lower cost. Cost parameters were developed based on a detailed literature review, in consultation with experts, and modelling, and are specific to the eastern US market. Different stages associated with application of each heating system and the required materials and procedures are shown in Fig. 5-2.

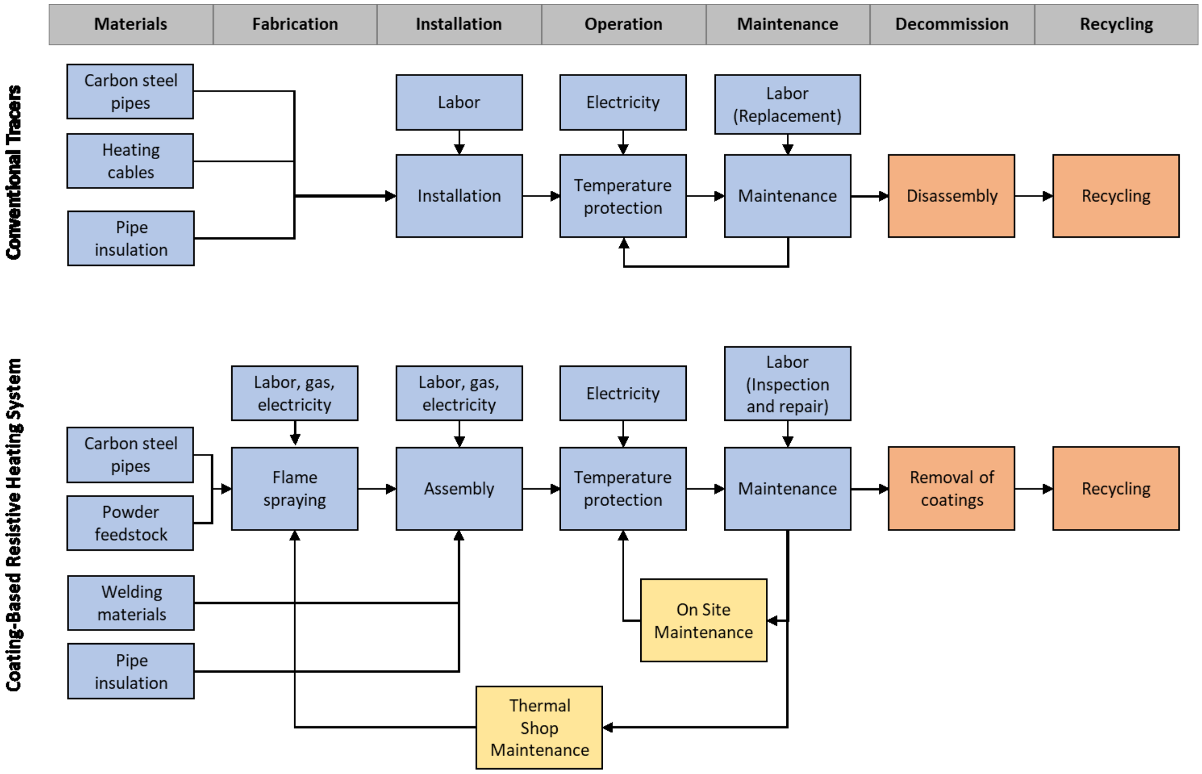

Figure 5-2 Process flow of each heating system

According to Fig. 5-2 the costs associated with all components of the LCCA can be obtained from Eq. 1 given as

$$LCC = C_{\mathrm{ic}} + C_{\mathrm{in}} + C_{\mathrm{e}} + C_{\mathrm{m}} + C_{\mathrm{d}}, \tag{5-1}$$

where C_{ic}, C_{in}, C_{e}, C_{m}, and C_{d} are initial cost, installation cost, energy cost, maintenance cost, and disposal cost, respectively.

The initial cost of the coating system includes feedstock powder, connecting wires between the power supply and the coating-based heating element, thermal insulation, controlling system, and above all, the labor cost associated with fabrication of the coatings. The cost of the powder was calculated based on the consumption of powder by measuring the weight of the powder that is used for deposition of the coating by knowing the pipe surface area, coating thickness, density of the coating material, and the deposition efficiency of the thermal spraying process. Alternatively, it could be obtained by just measuring the weight of the powder inside the powder hopper before and after spraying the coating on a specified length of pipe.

The cumulative cost related to reservation of the thermal spray shop, consumption of gases and other consumables, electricity, overheads, and the experienced technician labor, was considered to be \$300 USD per hour. The total required time for fabrication of the unit length (1 m) of the coating system was calculated based on scaling up the measured times for surface preparation (grit blasting) and deposition of the coatings for the given length of pipe (254 mm) in this study. It should be noted that the required duration of time for deposition of coating layers heavily depends on the required thickness of layers, number of passes, and the speed of the robot. Therefore, the required time depends on the thermal spraying process that is used for fabrication of the coating systems. In this study, the traverse speeds of the oxy-acetylene torch along the pipe were 10 mm/sec and 24 mm/sec during deposition of alumina and Ni-20Cr coatings, respectively. Furthermore, the number of passes that were required for preheating of substrate prior to the deposition of alumina, fabrication of alumina layer, and fabrication of Ni-50Cr layer were 6, 14, and 6, respectively. That said, the time that is needed for fabrication of the whole coating system could be calculated for greater scales. In comparison to the coating system, the initial cost of the tracer includes a self-regulating heating cable, a line connector, and thermal insulation. For the case of a smart heating system, a controlling unit including a solid-state relay, temperature sensor, and a temperature controller can be added to both systems to improve the heating systems from a passive mode to a smart mode.

The installation cost is related the labor that is required for setting up each heating system, assembling the discrete elements such as segmented coated pipes at the location where protection against freezing and accumulation of ice is needed, installation of the thermocouples, and connecting the heating systems to the power sources. For the case of the heat tracers, the installation of the heating system is noticeably easier as it does not require much expertise and specialized knowledge and the heating cables can be installed along the existing pipelines in the axial direction easily. With regards to the installation of the tracers, it was advised by the manufacturer of the heating cable (Thermon, TX, USA) that approximately 15 minutes is required for installing the heat tracer and the required temperature sensors for controlling and monitoring the performance of the heating system on a one-meter long 50-mm (2-inch) diameter pipe. The cost of labor regarding the ordinary task of installation of the cable on the pipe was considered $50 USD per hour in the model.

For the case of the coating-based heating system, coating deposition should be conducted on each pipe section separately. Then, the coated pipe sections will be shipped to the location, where the heating system is required. In this study, assembling of the pipe sections by way of welding was taken into consideration. Given the restriction on the length of the coated pipes for shipping, the potential length of the pipes for shipment was assumed to be 5 meters. The duration of time that was required to weld two pipe sections together was considered to be 10 minutes. The labor cost of $150 USD per hour was also considered for an on-site certified welder. The calculation of the exact shipping cost and its inclusion in the model was very challenging due to the noticeable uncertainty regarding the shipment of the coated sections to the potential site. Given the distance between the desired field and the thermal spray shop can very remarkably from one case to another case, it should only be considered based on specific case studies.

Therefore, the shipping cost that should have been acknowledged in the installation cost was not taken into consideration. The same assumption was made for the case of heating cable due to the unknown distance between the supplier's location and the location of the field, where tracers are needed. However, several case studies are proposed so that the approximate cost of the shipping can be estimated. Variable parameters and conditions can be considered in these cases based on different scenarios.

The cost of energy in the model was related to the energy consumption per unit of time in both heating systems. The electricity cost was calculated based on the required output wattage to prevent formation and accumulation of ice. However, the required wattage is dependent on the environmental and climatic conditions, desired temperature of the enclosed liquid, pipe diameter, and above all, the efficiency of the heating system. Based on the calculations, provision of 10 W was sufficient per meter of the pipe for only four months of a year when the pipes are exposed to the cold environment and temperature control of pipes and protection against freezing are required.

After conducting the heating tests, it was found that the coating-based heating system was noticeably more efficient than the tracer. Although the average input wattage for the case of heating cable was 20% higher than the coating system, the required time for heating and melting of ice was also longer about 10%. That said, it was assumed in the model that efficiency of the coating-based heating system was 30 % higher than the tracer, and therefore, the consumption of energy for the tracer was 1.3 times that of the coating system.

The average electricity price in major cities of United States that is $0.085USD/kWh was the value that was considered in the calculations [113]. The energy cost was calculated based on

Eq. 5-2 in which annual payment of energy was calculated based on several assumptions, namely a 10% discount rate, a 2.2% annual inflation rate in the United States [114], and assumed 10-year useful life for both heating systems. Therefore, the present value of energy is given by

$$C_{\mathrm{e}} = \sum_{\mathrm{k=1}}^{\mathrm{n}} A_e \times \left(\frac{1+e}{d-e} \right) \left[1 - \left(\frac{1+e}{1+d} \right)^n \right], \tag{5-2}$$

where C_{e}, A_{e}, d, e, and n are total energy cost, annual energy cost, discount rate, inflation rate, and the number of years, respectively [63].

The maintenance costs consist of the technician's salary, technical support regarding the problem identification and repair, and general overheads. Given the novelty of the application of the coating-based heating system for pipelines, the maintenance cost of the coating system is not known. Therefore, the annual maintenance cost was assumed to be 5% of the total capital cost. The maintenance cost was calculated based on Eq. 5-3 by considering the annual payment, discount rate and useful life as

$$C_{\mathrm{m}} = \sum_{\mathrm{k=1}}^{\mathrm{n}} A_{\mathrm{m}} \times \left(\frac{(1+d)^n - 1}{d(1+d)^n} \right), \tag{5-3}$$

where C_{m}, A_{m}, d, and n are total maintenance cost, annual maintenance cost, discount rate, and the number of years, respectively [63].

The cost of disposal, which is an incremental expense attributed to the disposal of both heating systems and all attached electrical connections and controlling units at the end each system's life cycle, should also be considered in the life cycle cost (LCC) analysis. It is generally agreed that the coating material can be recycled at the end of its useful life. That said, it was assumed that the cost of removal of coating from the pipe and its disposal was in the same order of the revenue from recycling the multi-layered coating system. Therefore, no extra expense was considered in the model regarding the disposal of the coating system. The same approach was adopted for the heating cable. All parameters and assumptions that were taken into account in the LCC model are listed in Table 5-1. Given the rapidly evolving economy in the additive manufacturing field, in general, and the thermal spraying field, in particular, the provided values and estimations in this study would be subject to change over time [66].

Table 5-1 The parameters and assumptions that were used in the LCC model

Items	***Values***	***Comments***
Discount rate	10%	Assumed
Inflation rate	2.2%	[114]
Contingency	10% of the total cost	Assumed
Useful life	10 years	Assumed
Maintenance (Coating)	5% of the total cost	Assumed
Maintenance (Tracer)	1% of the total cost	Assumed
Diameter of pipe	60.3 mm (2.4 in)	-
Thickness of insulation	12.7 mm (0.5 in)	-

5.2.2 Shipping of the Materials

The cost of shipping is dependent on many factors including, but not limited to, labor, mileage, fuel consumption, seasonality, and trucking lane availability. Due to the high complexity of assessing the actual economic implications of product shipment, making precise estimations are not possible. However, the overall shipping cost can be estimated with some degree of uncertainty. Given the fabrication of the coating layers onto the pipe surface is required to be conducted in the thermal spray shop, the shipment process is more elaborated for the heating system as shown in Fig. 5-3. Due to the greater distance that must be travelled for transportation of cargo for the case of coating-based heating system, more emission of pollutants and greenhouse gases to the environment are expected to be incurred. Further, it stands to reason that the cost of shipping would be higher for the case of coating-based heating system.

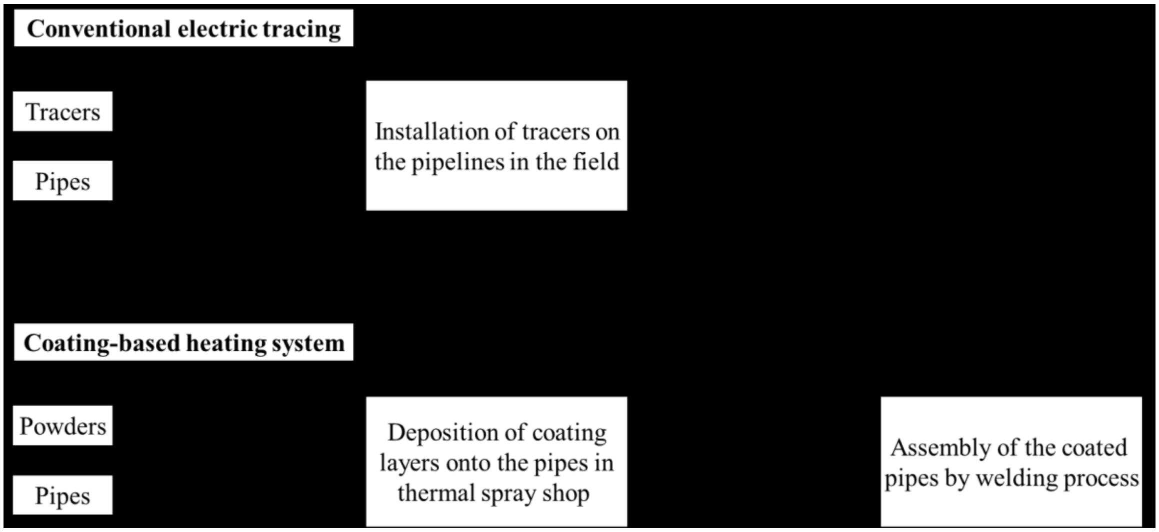

Figure 5-3 Required shipping for the raw material and the final products for both heating systems

The raw materials (powders) are shipped to the thermal spray shops from the powder suppliers that are usually far from the shops. In some cases, they are even shipped from foreign countries. Aside from the concerns related to the availability of the powder feedstock, shipping of powder feedstock to the thermal pray shop can be as costly as the cost of the powder itself. However, the major concern is related to the shipment of the coated pipe sections to the field.

This greatly depends on the distance between the thermal spray shop and the field where the coated pipes should be installed.

In order to have a better understanding of the economic impact of the shipping of the pipe sections to the thermal spray shop and the coated pipe sections to the field, ground transportation by 26 ft trucks was considered. The fuel consumption of a vehicle of this size has been reported to be around 10 miles per gallon (mpg) (23.5L/100km) for an empty car. However, for a fully-loaded vehicle, the fuel consumption can get higher to 6 mpg (39.2L/100km) according to discussion with experts in the field of shipping. Therefore, for the round trip, the average consumption of 8 mpg (29.40L/100km) was taken into calculation. The rental cost of \$40 for the truck for a day, the mileage cost of \$0.99/mile (\$0.62/km), and the labor cost of \$25/h were also considered in the calculation of the shipping cost.

Three different random distances of 25 km, 50 km, and 100 km were considered so that the approximate cost of shipping for the extra distance that is required for shipment of the coating-based heating system can be estimated. The weight of the coated pipe was calculated to be 29.9 kg for a 5-meter long 2-inch diameter schedule 40 coated pipe. Given the maximum load of the truck is 4,087 kg (9,010 lb), it can accommodate and carry 135 coated pipes with a total length of 675 m. The estimated total cost of shipping that was obtained for each scenario was then divided by the length of the pipe so that the cost of shipping per unit length of pipe (\$/m) can be found and be compared with the total cost of fabrication and utilization of the coating system.

5.2.3 Sensitivity Analysis

The data, assumptions, and scenarios in this study are subject to uncertainty. In this regard, sensitivity analysis was conducted to understand better the impact of uncertainty of each independent variable. In addition to the uncertainties in assumptions, some uncertainty also exists in the measured data due to inherent randomness and fluctuations in measured variables that might affect the model estimations partially [115]. This uncertainty was not taken into consideration in this study due to its negligible nature and for simplicity.

Among all the parameters that were investigated in this study, two items namely maintenance and shipping were subjected to noticeable uncertainty. The reason for the uncertainty in the estimated cost of maintenance of the novel coating-based heating system in the field was lack of experimental record and knowledge because fabrication of this coating system is still in the early stages of research and feasibility study. Therefore, the proposed system has not been operated in actual working conditions in the field and some of its features may not be known precisely [67]. However, the case for the shipping was different as the uncertainty was so high that assuming a reasonable value was not possible. Therefore, several different scenarios were taken into consideration to give the reader insight into the impact of the shipping cost on the total cost of fabrication and utilization of the coating system based on the unit length (1m) of the 2-inch diameter pipe. Sensitivity analysis was also conducted to understand the impact of changing each determining factor within a reasonable range on the total cost of heating systems and to introduce the weight factors in a systematic manner. The robustness of the developed model can be increased by finding the factors that cause noticeable uncertainty and variation in the outcomes or predictions of the model.

5.3 Results and Discussion

5.3.1 Technical Assessment of Performance of the Heating Systems

As explained earlier, providing the same power input to both heating systems was not possible due to the unequal change of the electrical resistance of the heating systems versus temperature. The increase in the electrical resistance of the coating system within the temperature range of -25°C and 10°C was relatively negligible (less than 4 %). This resulted in power output reduction of the coating-based heating element in the order of 7%. In comparison, the increase in the electrical resistance of the coating was more than 300% in the given temperature range of -25°C up to 30°C. Therefore, the electric current that was passed through the heating cable was measured at each second so that the transient power can be determined. Then, the average power outage was calculated to make the comparison between the coating-based heating system and the heating cable possible. The heating performance of both systems was evaluated based on the duration of time that was required for heating and melting of ice inside the pipes. The data acquired from both systems for the given powers of 10 W and 20 W are shown in Figs. 5-4(a) and 5-4 (b), respectively.

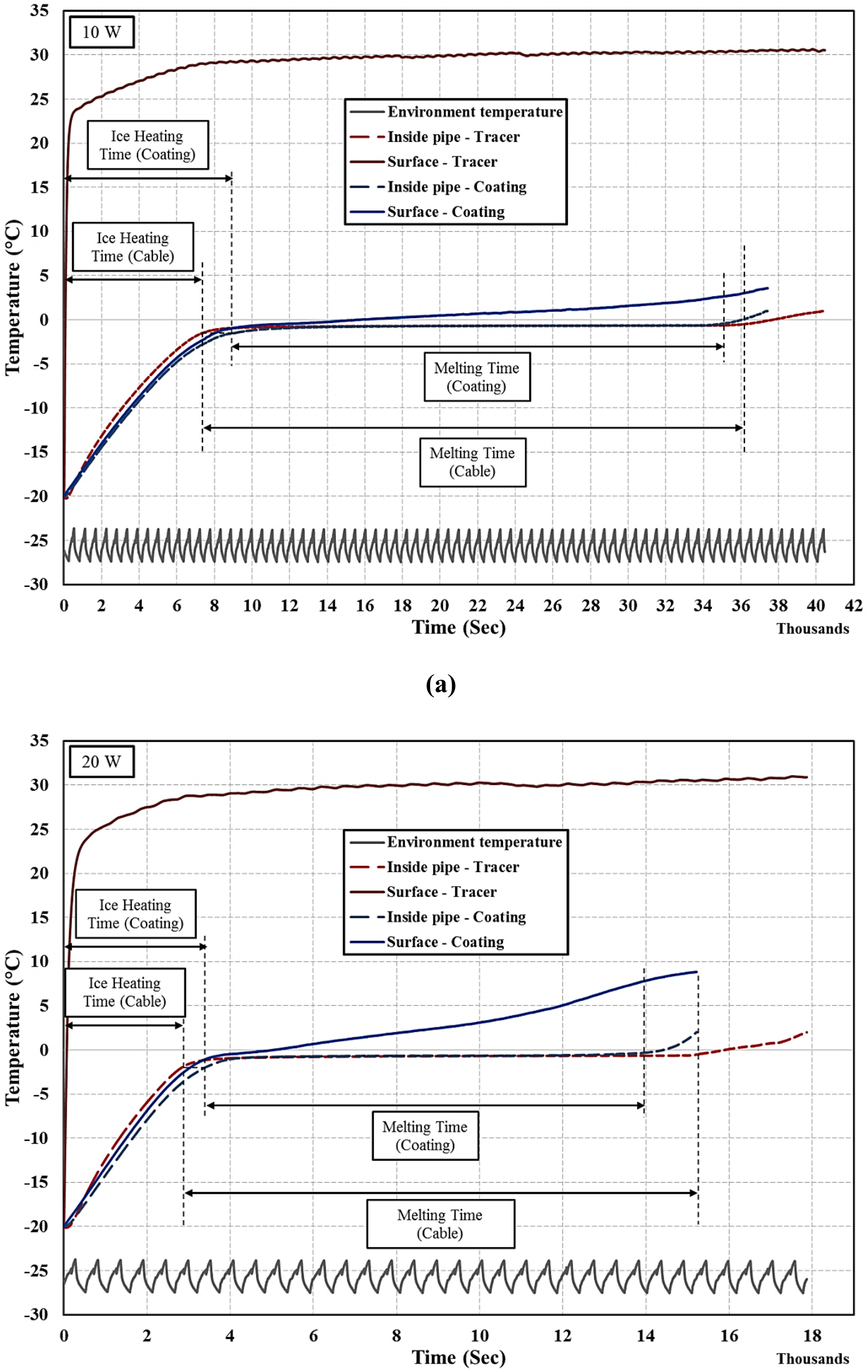

(a)

(b)

Figure 5-4 Comparison of the performance of both heating systems under free convection heat transfer condition and supplied powers of (a) 10 W and (b) 20 W

Given the variable watt output of the heating cable throughout the heating test, the comparison between the heating and melting times of both systems should be conducted with care. The heating of the ice from -20°C up to the melting point occurred faster when the heating cable was used. In contrast, the duration of the melting phase was much shorter for the case of coating system for the same supplied powers. The reason for that was the noticeably higher output wattage of the cable at sub-zero temperatures. However, once the temperature of the heating cable reached a plateau at around 30°C, the power outage was reduced as its electric resistance increased remarkably. In comparison to the heating cable, the performance of the coating system did not undergo remarkable change during the heating experiment, and the reduction of the power output was less than 7% in the given temperature range from -20°C to 20°C.

To understand better the impact of temperature on the electrical resistance of the cable and the generated power, their transient values versus temperature are shown in Fig. 5-5. As can be seen in Fig. 5-5, the electrical resistance of the wire was increased from 160 Ω to 480 Ω due to the increase in the temperature of the cable from -20 °C to 30 °C. This resulted in reduction of the outage power from 57 W to 24 W within the same temperature range. The average value of the output power for the heating cable, which was obtained from the data shown in Fig. 5-4 (b), was found to be 24 W for the entire duration of the test. However, the average power consumption was different during each stage. It was found that the average power was 25.5 W and 23.5 W for heating and melting stages, respectively. Although the average supplied power to the cable (24 W) was 20 % greater than the one the was provided to the coating system, the total duration of heating and melting was even 10 % less for the case of the coating system. This clearly speaks to the higher efficiency of the coating system.

Although the self-regulating feature is advantageous in limiting the output wattage and temperature of the cable, and as a result, prevents the cable from destruction due to overheating [116], the continuous change of the power during temperature fluctuation makes the comparison of the performances of the heating systems difficult. The detailed quantitative results regarding the approximate duration of heating and melting stages for both heating systems for the given powers are listed in Table 5-2.

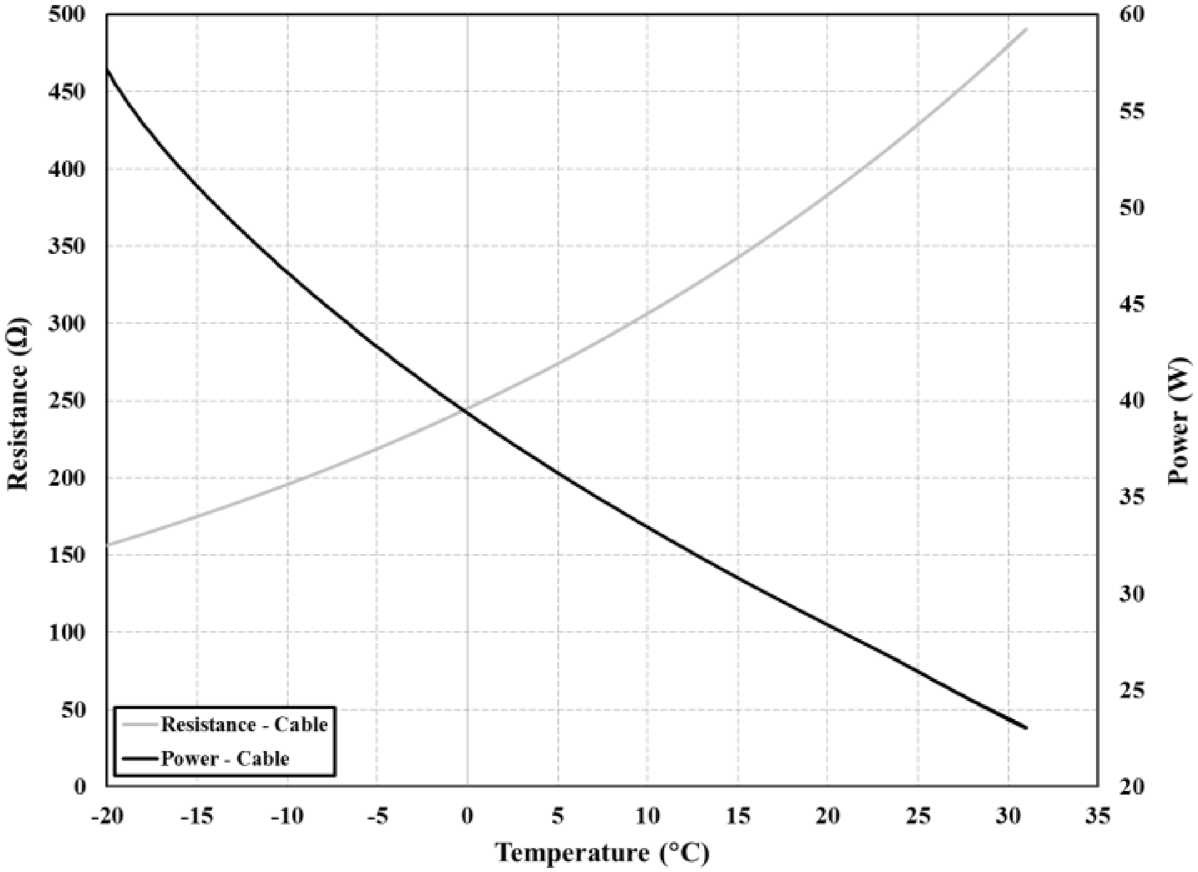

Figure 5-5 Dependence of electrical resistance and power output of the heating cable on temperature

Table 5-2 Duration of times for heating and melting stages of each heating system

System	*Phase*	*Duration of Phase (min)*	
		10 W	20 W
Heating Cable	Heating	123	48
	Melting	480	205
Coating System	Heating	150	55
	Melting	435	176

5.3.2 Microstructure of the Coating System and Calculation of Labor Cost

A micrograph that was obtained from the cross-section of the bi-layered coating system in the middle of the coated pipe section can be seen in Fig. 5-6. The average thicknesses of the coating layers were found to be 171 ± 6 µm (*n* = 5) and 128 ± 4 µm (*n* = 5) for alumina and Ni-50Cr coatings, respectively. The thickness of the coating layers was dependent on many parameters including the number of spraying passes. Therefore, more labor time, feedstock powder, gases, and electricity are required to achieve thicker layers.

The obtained microstructure for the flame-sprayed alumina was porous. Furthermore, some of the Ni-50Cr coating was penetrated into the alumina coating, which resulted in reduction of the effective thickness of this insulating layer. Therefore, high numbers of preheating passes (6) and spraying passes (14) were considered for deposition of alumina layer to achieve a thick coating that can provide the required electrical insulation. However, the required thickness for this electrically insulating layer can be reduced by application of high-temperature thermal spraying techniques that can lead to deposition of a dense alumina coating. An alternative plan would be sealing the top surface of alumina layer prior to deposition of the Ni-50Cr layer. These actions may lead to noticeable reduction in the spraying time and as a result, considerable savings in the labor cost associated with fabrication of the coating system.

Furthermore, Ni-50Cr was deposited onto the alumina coating by passing the torch six (6) times along the pipe in the axial direction while the pipe was rotating to achieve a uniform coating. Utilization of another high-temperature thermal spraying technique such as air plasma spraying or high-velocity oxy-fuel (HVOF) may bring about a more uniform and denser coating whose electrical resistivity would be lower than the flame-sprayed Ni-50Cr coating. As a result, a similar or the same electrical resistance and heating performance may be achieved by reducing the required thickness of this layer, which can result in reduction in the required spraying passes, labor time, and the final cost of fabrication of the coating system.

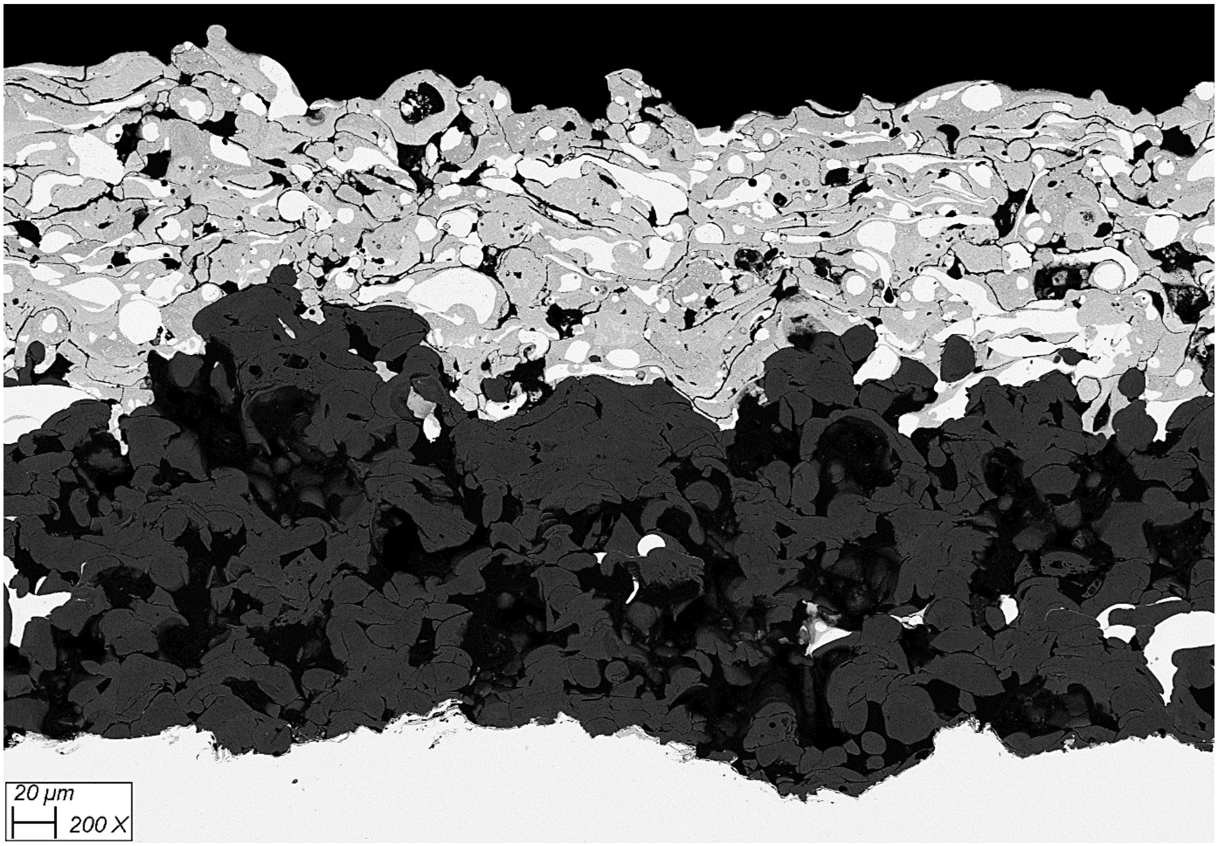

Figure 5-6 Micrograph taken from the cross section of the coating system at 200 X magnification in backscattered mode

The detailed information regarding the required time for each stage of the fabrication process of the coating system and the estimated costs are presented in Table 5-3. Based on measured times, it takes about one hour to fabricate the coating system per meter of 2-inch diameter pipe. Although the exact time of some of the stages such as deposition of alumina was known, the required time for some of the tasks such as grit blasting and mounting the samples were estimated. Therefore, the time that has been provided for the miscellaneous tasks in Table 5-3, which includes the times for mounting the sample, mounting flame spray torch and cold spray nozzle, refilling the powder hoppers for both flame spraying and cold spraying processes, and deposition of coatings on 3-inch extra sections before and after traversing the whole length of pipe to ensure uniformity and consistency, is an approximate value and therefore, is subject to some uncertainty. Although the duration of time for deposition of alumina and Ni-50Cr layers were calculated based on the traverse speed of the oxy-acetylene torch in the axial direction, the required time for deposition of the copper rings at each end of the coated section was obtained based on the traversing speed of the cold spray nozzle in the direction perpendicular to the centerline of the pipe due to the required different motion of the robot for fabrication the copper rings at the ends of the pipe section. To ensure continuity and uniformity of the deposited copper coating, about 7.6 mm (3 in) extra path was taken into consideration prior to reaching and after passing the 60-mm diameter pipe.

Table 5-3 The measured/estimated times and costs for various stages of fabrication of the coating system

Items requiring labor	*Number of passes*	*Traverse speed of gun (mm/sec)*	*Required time for 5-m section (sec)*	*Total labor cost ($/m)*	*Cost per unit length ($/m)*
Grit blasting	NA	NA	3,000	250	50
Substrate Preheating	6	10	3,000	250	50
Deposition of alumina	14	10	7,000	583.3	116.7
Deposition of Ni-50Cr	6	24	1,250	104.2	20.8
Deposition of Copper	4	5	240	20	4
Miscellaneous tasks	NA	NA	3,510	292.5	58.5
Total	NA	NA	18,000	1,500	300

5.3.3 Selection of Materials and Spraying Processes

Alumina was selected because of its unique electrical and thermal properties. Although alumina is an insulator from the electrical perspective, it is a good conductor of heat compared to other ceramics [78]. Therefore, the heat that is generated in the top metal coating layer (the heating element) was transferred to the pipe and to the enclosed ice/water. As a result, heat dissipation to the environment was reduced. Nickel chromium was also selected because of its relatively high electrical resistivity [81]. The flame spraying technique was also chosen because of the low cost of equipment, availability, ease of use, and low cost of labor compared to other high-temperature thermal spraying processes. Copper was also selected because it is a superior electrical conductor. In addition, the connecting wires that are also made of copper can be soldered easily to the dense copper ring. Cold spraying was selected for deposition of copper due to its high precision, low consumption of powder, and the resulting denser structure of the coating [82].

The main reasons for selection of the flame spraying process in this study were the inexpensive cost and easiness of utilization of this thermal spraying method. Although flame spraying process was very widespread during 1980s and 1990s, its usage got less popular by introducing newer techniques such as air plasma spray (APS) and high-velocity oxy-fuel (HVOF) spraying. As an example, the percentage of application of combustion spraying in industry was reduced from 87% in 1994 to 50% in 2000 among all the different spraying techniques including PTA, D-Gun, plasma, HVOF, and arc [66]. Despite the reduction in the usage of this spraying process in recent years, it is still one of the popular, available, and easy to use thermal spraying processes. The other important reason is the remarkable lower investment cost of this process compared to the other thermal spraying methods that makes it feasible for local or small-scale companies to purchase this equipment. For instance, the investment cost of equipment was estimated to be between $65,000 USD and $130,000 USD for HVOF/HVAF processes. However, the total investment cost of automated powder flame spraying process was estimated to be between $6,500 USD and $13,000 USD [117].

The other determinative factor in selection of the thermal spraying process for fabrication of the heating system is the consumption of the energy. Comparison of the power input for various spraying methods shows that arc and flame spraying techniques are among the lowest consumers of the energy [118]. In contrast, HVOF and high-velocity liquid fuel (HVLF) are the largest energy consumers among the thermal spraying processes and require approximately more than ten times greater power than the power input of flame spraying process [118].

This study is focused on the techno-economic implications. However, a complete assessment of the systems should include the environmental impacts of materials, processes, and services [119]. Given the novelty of this research in fabrication of the coating system for pipelines, the environmental impacts of fabrication and utilization of the proposed thermally sprayed coating system are unknown. It is known that LCA is a powerful tool to assess and quantify various environmental impacts of a process such as emissions to air, land, and water, damage to the human health, damage to the ecosystem quality, and resource depletion, to name but a few. Environmental impacts regarding utilization of different thermal spraying processes, namely wire arc, cold spray, plasma spray, and high-velocity oxygen fuel spray, which have already been studied by Moign, *et al.* [120], should also be taken into consideration in the decision-making process. Furthermore, the emission of pollutants to the environment due to the shipping or environmental impact of consumption more electricity in other thermal spraying techniques are of great importance for selecting the best heating system option. As an example, it was found by Moign, *et al.* [120] that consumption of electricity during the APS and SPS processes was of the utmost importance as it was responsible for about 70-80 % of the environmental impacts.

5.3.4 Assessment of Economic Implications

Based on the assumptions that were mentioned earlier, the total cost of each heating system was calculated. The costs associated with fabrication and installation of the coating system were estimated based on the discussions with the experts in the field. Geographical considerations must be taken into account regarding the accuracy of these numbers as these costs may vary noticeably based on the location where they are fabricated and are needed to be used. All the calculated estimations are subjected to different degrees of uncertainty. A 10% contingency was taken into account to ensure that these uncertainties are reflected in the estimated total cost.

The estimated cost of each component of the life cycle analysis is listed in Table 5-4. The total expenditures of each system for 10-year time span can also be compared clearly based on data shown in Fig. 5-7. The noticeable gap between the two graphs was because of the higher capital cost of the coating-based heating system, which was mainly caused by high labor cost of the experienced technician and noticeably high operating cost of the thermal spray shop. Furthermore, the gap even became wider in the upcoming years due to the higher assumed maintenance cost of the coating system compared to that of the tracer. Due to the high reliability and safe operation of the heating cable, the maintenance cost of the heating cable was considered to be as low as 1% in this study. The reliability and working lifespan of the heating cables are so high that manufacturers of the cables often guarantee the performance of them for 40 years.

Table 5-4 The associated costs of each component of the life cycle cost analysis for the first year

Items	*Coating ($/m)*	*Tracer ($/m)*
Capital cost		
Raw material (powder and wire)	35	22
Pipe insulation	10	10
Labor cost		
Fabrication	300	N/A
Installation cost	5	13
Total capital cost	360	45
Operating cost		
Maintenance cost (% of total capital cost)	152 (5%)	3 (1%)
Electricity cost	24	31
Total operating cost	176	34
Total Cost	524	68

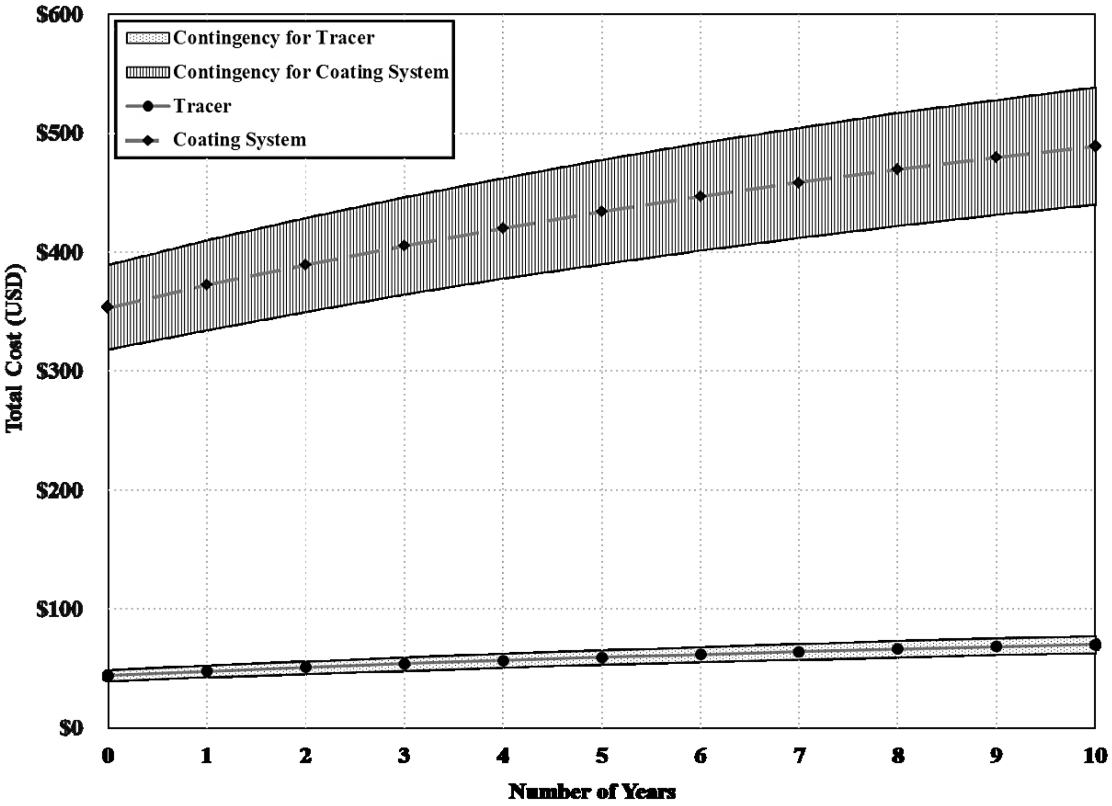

Figure 5-7 Comparison of the total cost of each heating system for an assumed 10-year lifetime

The higher efficiency of the coating system compared to the heating cable was explained and illustrated earlier. The benefit of using the coating systems for less consumption of energy was quantified. As can be seen in Table 5-4, less energy consumption of the coating system did not bring about noticeable financial benefit in the cost of energy for the given diameter of the pipe, the required power density, and the given working time per year. Therefore, the saving from the less energy consumption of the coating system was not comparable to the higher maintenance cost and a higher degree to the capital cost required for fabrication of the coating system.

That said, the tracers seem to be a much more affordable and suitable choice for temperature protection of pipes and their protection against freezing. The tracers offer other advantages, including but not limited to, lower cost, easy shipment, fast installation, no necessity for repair, no need for special expertise for installation of the cables, capability for being stored, and above all, the availability of the heating cables in the market. Furthermore, in case of failure of the tracers, they can be easily replaced. However, in case of failure of the coating system, either the coating layers have to be removed from the pipe and again be sprayed onto the pipe on-site or the pipe section with the failed coating should be cut from the pipeline and be sent back to the thermal spray shop for repair.

In comparison to the above-mentioned advantages of the tracers, coating systems offer higher thermal efficiency, better performance, and temperature uniformity over a large surface. Therefore, they can be employed in specific cases and under particular circumstances wherein high thermal efficiency of the heater and more surface temperature uniformity are required and extremely appreciated even at higher costs.

It is noteworthy that the obtained values are only applicable to 2-inch diameter pipe sections. However, in the actual working conditions, valves, supports, flanges, branches, and other geometrical complexities, increases the energy consumption. As an example, it has been found by Sandberg, *et al.* that as high as 30 % of the generated heat is dissipated through valves and supports [121]. Further, fabrication of coating on curved surfaces or on parts like valves and flanges with complex geometries require special care and will take more time and budgetary cost.

5.4 Uncertainty Assessment

5.4.1 Scenario Analysis

5.4.1.1 Labor Cost

To examine and evaluate the possible regional effects on labour and shipping costs properly, an extensive scenario analysis was conducted to estimate the total cost of each heating system. It is well-established that the labor cost for fabrication, installation, repair, and disposal of the coating vary significantly based on the location and the country based on which the assumptions are made. All the assumptions and the obtained values for total cost of the coating system in this study were obtained based on the rates of Eastern US market. Therefore, the fabrication and operation of the coating system may be more competitive and comparable from financial viewpoint with those of the tracers in other geographical regions. In this regard, two other rates of $100 USD and $200 USD per hour were also taken to account to comprehend better the effect of costs associated with reservation of the thermal spray shop and the labor required. The impact of the cumulative costs associated with fabrication of the coating system can be seen in Fig. 5-8.

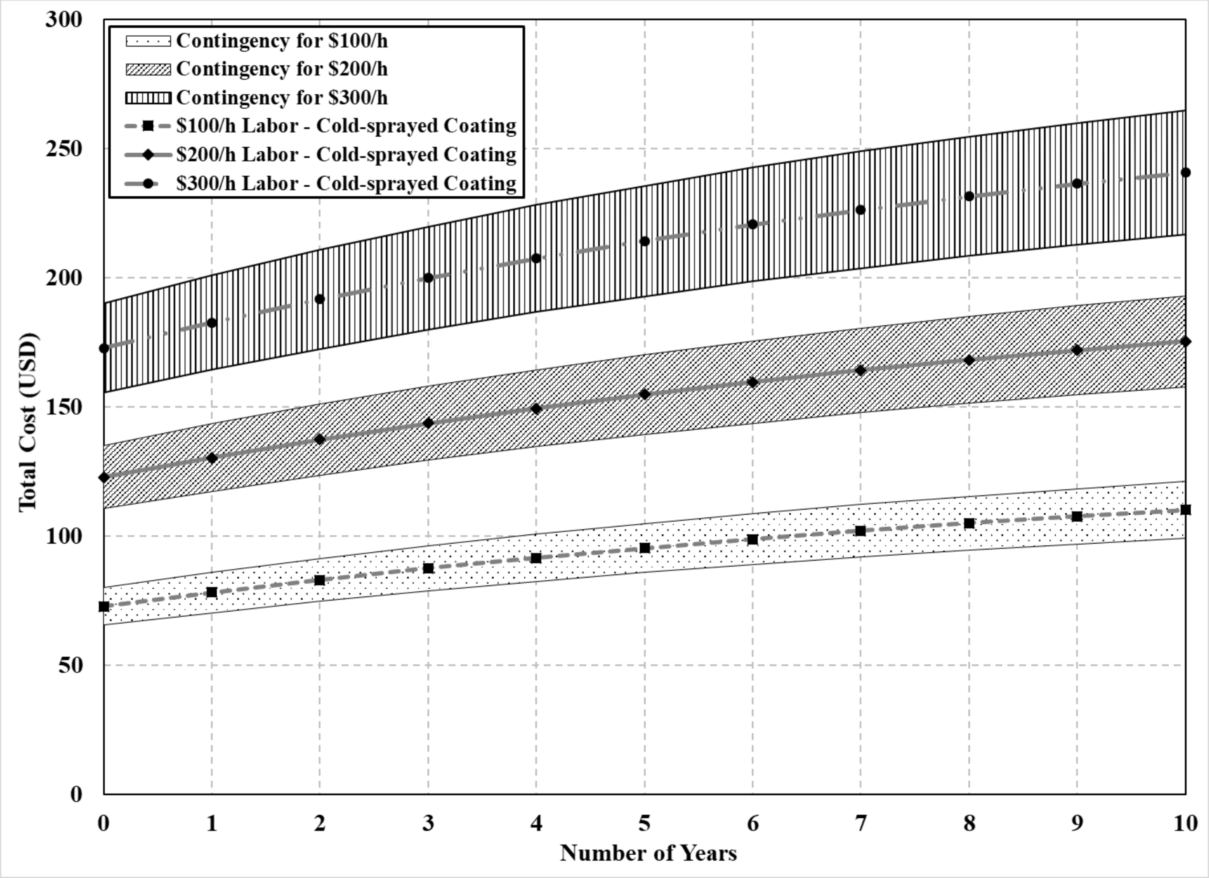

Figure 5-8 Comparison of the total cost of coating-based heating system per meter during the 10-year lifetime based on different labor costs of $100/h, $200/h, and $300/h

As shown in Fig. 5-8, the labor cost has a profound impact on the total cost associated with fabrication and utilization of the coating-based heating system. Comparison of the total cost of the coating system in which labor rate of $100/h was taken into consideration with that of the ordinary tracer shows that the systems are still not comparable as the total cost of the coatings system is about three times greater than the tracers. Therefore, further modification of the spraying parameters and selection of high-temperature thermal spraying processes are still required to reduce the labor time and the resulting cost to make the coating system competitive with the tracers from financial perspective.

5.4.1.2 Shipping Cost

As explained earlier, the shipping cost for the coated pipes and the tracers could not be predicted precisely due to the unknown distance between the thermal spray shop or the supplier of the tracers and the field where heating system is required. Given the likely extra distance that is required to be travelled for shipment of the coated pipes, the extra cost of shipping for coating system compared to the ordinary tracers can be estimated. In this regard, the extra costs of shipping and their impact on the total cost of the coating system per unit length of the pipe, which were estimated based on the imaginary scenarios, are listed in Table 5-5. It can be seen that the cost of shipping based on conservative estimations for an approximate distance of 100 km between the thermal spray shop and the field would be about \$0.46/m of 2-inch diameter pipe, which is not comparable with the fabrication cost of the pipe that is about \$300/m. This shows that the shipping of the coated pipe to the field would not be a challenge from financial viewpoint.

Table 5-5 The estimated cost of shipping from thermal spray shop to the filed based on different imaginary scenarios for the coated 2-inch diameter pipes

Items / *Case*	*Distance (km)*	*Total mileage (km)*	*Average fuel consumption (L/100km)*	*Fuel cost (\$/L)*	*Average speed (km/h)*	*Labor (\$/h)*	*Rental vehicle (\$/day)*	*Mileage rate (\$/km)*	*Total cost (\$)*	*Cost/unit length (\$/m)*
#1	25	50	29.4	0.8	50	25	40	0.62	108	0.16
#2	50	100							176	0.26
#3	100	200							311	0.46

5.4.2 Sensitivity Analysis

To better understand the impact of each of the variables on the total costs of the heating systems, sensitivity analysis was conducted. The results of this analysis are shown in Figs 5-9(a) and 5-9(b) for tracer and coating system, respectively. In an attempt to consider the global market rather than just focusing on one specific region (Eastern US area), wide potential changes in each of the independent variables were taken into consideration. It is expected that these relatively wide ranges enable the readers and engineers worldwide to calculate the approximate costs of utilization of both heating systems. As an example, the discount rate in this study was considered to be 10%. Consideration of relative differences of -30% and +50% in this value brings about a relatively wide range of discount rate from 7% to 15% that could accommodate the actual investment condition in many regions.

The other benefit of conducting the sensitivity analysis is finding the most determining parameters. As an example, the uncertainty in the cost of electricity is of utmost importance in calculation of the total cost of the tracer as the maintenance cost is negligible in this heating system. However, the uncertainty in the fabrication labor is the main parameter for consideration for the coating system. It can be seen in Fig. 5-9(b) that the contribution of electricity cost is not comparable to other determining variables for the coating system. The results shown in Figs. 5-9(a) and 5-9(b) are obtained based on potential maximum changes in the values of each parameter. To have a better understanding of the impact of uncertainty on each parameter based on the same relative percentage changes of ±50% and rank the significance of each parameter the results are shown in Figs. 5-10(a) and 5-10(b) in a different format. Although the cost of the heating cable and electricity cost are the major contributors for the tracers, the fabrication labor and maintenance are the most important factors for consideration regarding the coating systems.

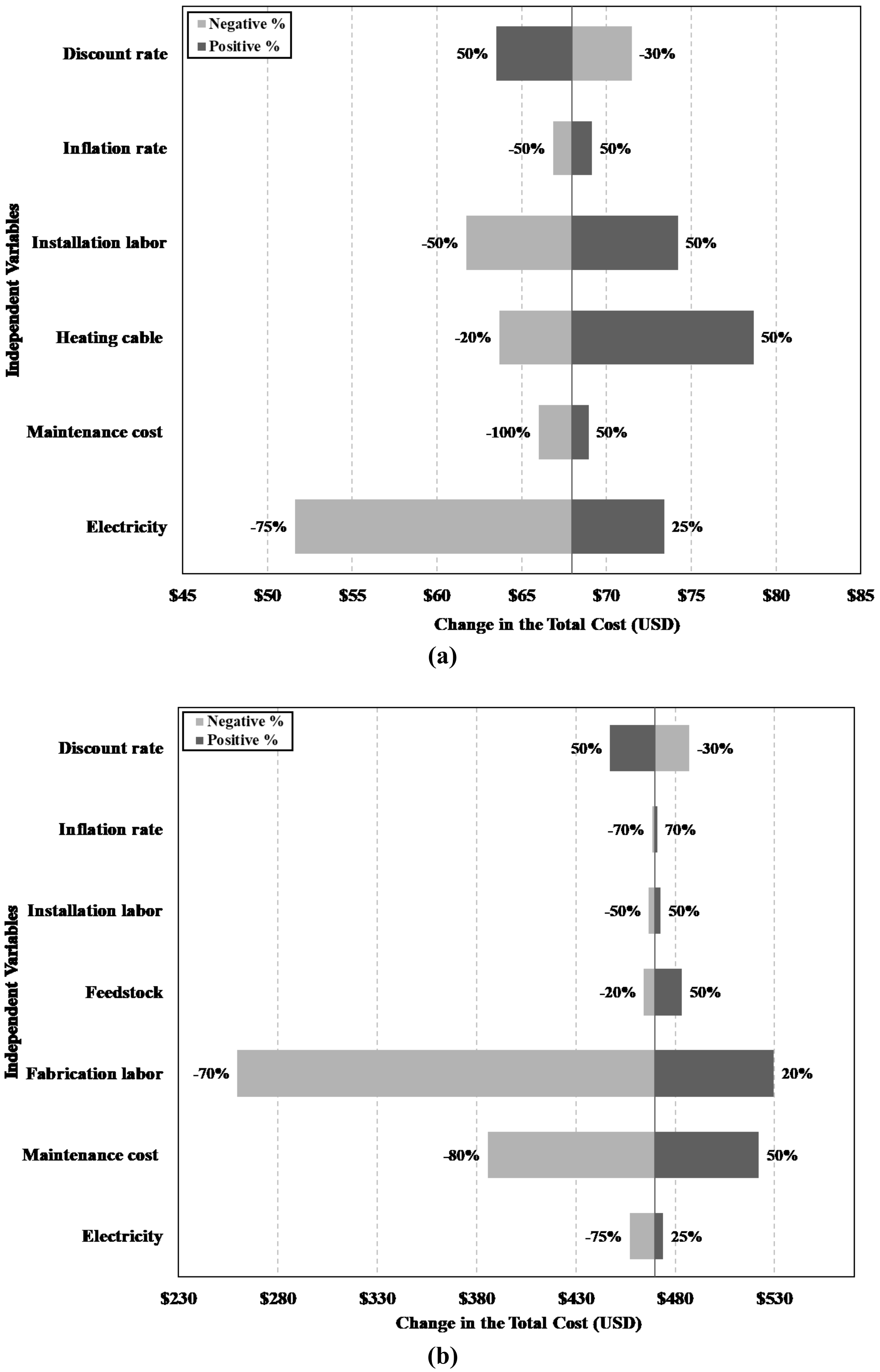

Figure 5-9 The impact of potential uncertainty on the total cost associated with fabrication and utilization of (a) tracer and (b) coating-based heating system

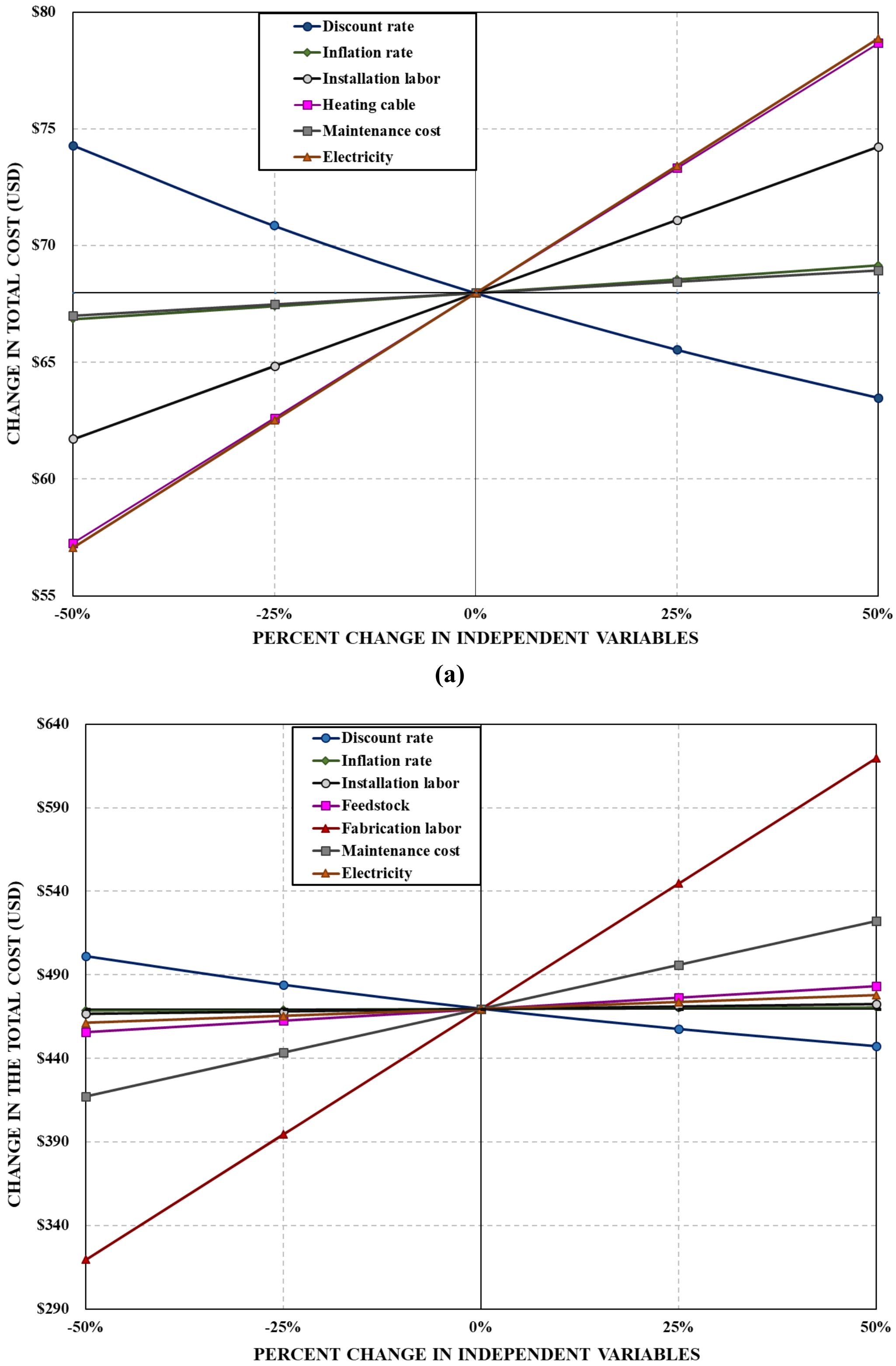

(a)

(b)

Figure 5-10 The effect of equal uncertainty percentages on the total cost associated with fabrication and utilization of (a) tracer and (b) coating-based heating system

5.5 Utilization of the Controlling System

In a test that was conducted by employing the controlling system, the temperature of the enclosed water was set at 5°C. Therefore, once the temperature was close or at the set-point temperature, the electric power to the system was not provided continuously as before. The relay was adjusting the power output by switching on and off the current. As the temperature got closer to the set-point value, the duration of time at which power was supplied to the heating element was decreased. The temperature traces collected from the industrial thermocouple within the pipe and the surface thermocouple on the heating element are shown in Fig. 5-11.

At slightly over 3,000 seconds after beginning of the heating test when the temperature of the water within the pipe reached 5°C, which is shown with the first dotted vertical line and an arrow, the temperature of the heating element began decreasing as the supplied voltage to the heating system was switched off and no heat was generated anymore. However, the temperature of the enclosed water was still rising until the point when both the outer surface of the coating and the enclosed water inside the pipe reached equilibrium at the same temperature around 16°C. After that the temperature of the pipe and the enclosed water were reduced due to the heat dissipation to the cold ambient air until the temperature of the enclosed water got below 5°C again, which is shown with the second vertical dotted line and an arrow. Then, the system reached equilibrium at 5°C. This shows that the use of controlling system based on the enclosed water in the system and provision of 80 W will reach equilibrium after about 5 hours and will stay at that specific temperature.

The temperature sensor based on which the controlling unit operates could be installed on the heating element to minimize the thermal inertia and the required time for the system to reach equilibrium. However, operation of the controlling unit based on the temperature sensor installed on the coated pipe can be misleading, especially for the larger diameter pipes as it can be noticeably different than the core of the enclosed liquid.

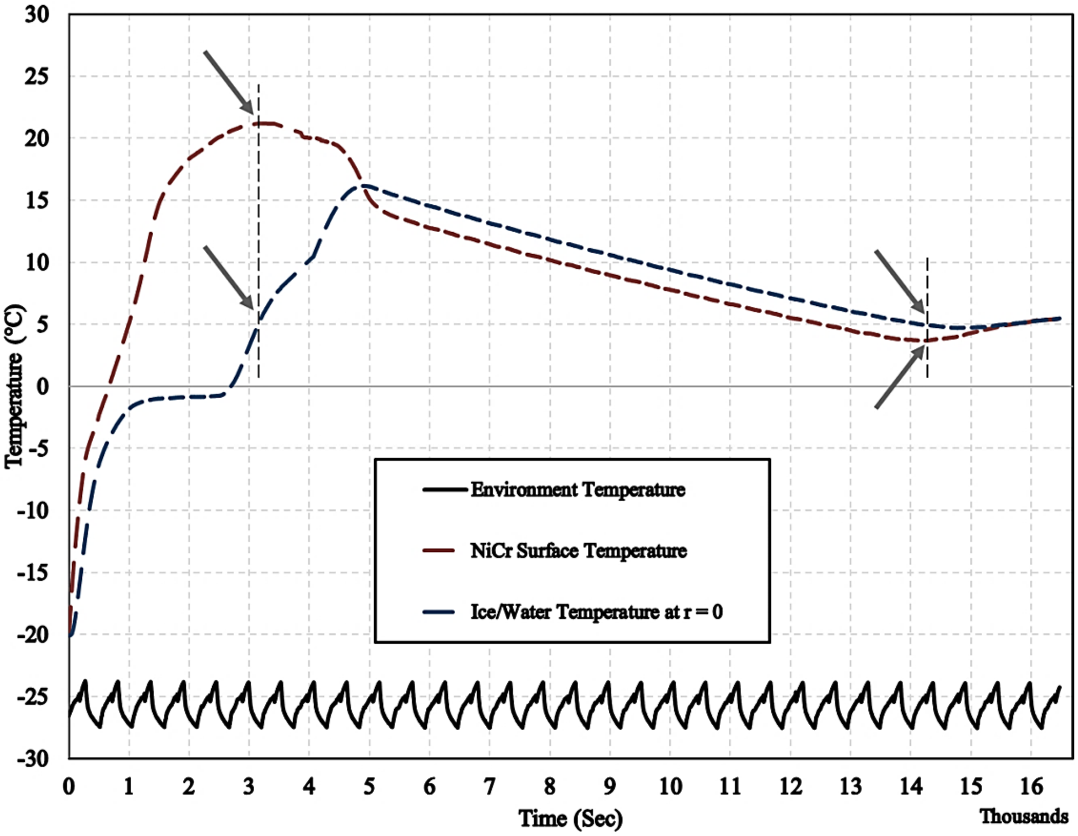

Figure 5-11 The impact of using a controlling unit on the performance of the coating-based heating system

Although addition of the controlling system can be beneficial from the technical perspective, it might be cost prohibitive. Therefore, the cost of the controlling system should be calculated and be divided by the length of the pipe section for which the controlling system was employed. In this regard, three scenarios were considered to better understand the approximate cost of controlling system per unit length of the pipe. Given the sections that were considered in this study are each five meters long, pipe assemblies composed of one section, two sections, and three sections equal to 5m, 10m, and 15m, respectively, were taken into consideration. The detailed cost analysis of the controlling system is listed in Table 5-6. It stands to reason that development of the controlling system is more beneficial for longer pipe sections. However, due to possible temperature gradients along the long pipe sections, the consumption of energy could be increased. Furthermore, to increase the safety of the operation of the controlling section and to ensure that the ice is not formed inside the pipe, several temperature sensors should be utilized to read and collect temperature data from the enclosed liquid along the pipe section. Although the cost of development of the controlling system per meter of the pipe is high for the case of 5-m pipe relative to the fabrication cost of both tracer and coating system, the obtained values for the 15-m and 25-m sections appear to be reasonable as shown in Table 5-6.

Table 5-6 The estimated cost of utilization of a controlling system per unit length of a 2-in diameter pipe

Items / *Case*	*Pipe Sections*	*Total Length (m)*	*Temperature Controller ($)*	*Solid State Relay ($)*	*Electrical connections ($)*	*Assembly Labour cost ($)*	*Total cost ($)*	*Unit cost ($/m)*
#1	1	5	162	37	50	25	274	54.8
#2	3	15						18.3
#3	5	25						11.0

5.6 CONCLUSIONS

Techno-economic implications of utilizing two heating systems for protection of pipes against freezing and bursting, namely conventional heating cable and thermal-sprayed coating system, were investigated. In the view of foregoing discussion, the following conclusions can be drawn:

- The coating-based heating system was noticeably more efficient than the heating cable in terms of heating and melting the ice within the pipe. Although the power that was provided to the cable was approximately 20 % greater than the supplied power to the coating during the experiment, it took relatively 10 % more time for the heating cable to heat and melt all the ice inside the pipe.

- The higher efficiency of the coating system is mainly because of the immediate contact between the heating element (nickel chromium coating) and the substrate (pipe) that minimizes the thermal contact resistance between them.
- The costs of fabrication and maintenance of the coating-based heaters are noticeably higher than those of the tracers. It is mainly because of the high labor rate of the experienced technician and operational cost of the thermal spray shop.
- The advantages of utilization of the cables are low capital cost, easy shipping, low maintenance cost, high reliability, capability of storage, availability in the market, and utilization for complex geometries, and no necessity for high level of knowledge or skill for installation.
- In comparison, the benefits of employing the coating system are provision of uniform heating over large surfaces, higher efficiency thanks to the immediate contact of the heating element to the substrate that leads to less consumption of energy, and easier control over the output power.
- Based on the results obtained from comparison of economic and technical implications of each heating system, the decision for utilization of the coating system should be viewed from a financial perspective and weighed with consideration of the higher heating efficiency that the coating system offers where protection of steel pipes against freezing damage and bursting is required. The better heating performance of the coatings may make them competitive too, or even more desirable than, the cables for specific and targeted applications.

Chapter 6

Conclusions

The protection of pipelines against bursting, which is caused by transformation of the enclosed water into ice, was the primary focus of this research program. In order to better understand the failure mechanism of the pipes due to exposure to cold ambient air, numerous experiments were performed on two conventional steel pipe materials, namely ASTM A333-6 and ASTM A106-B. It was found that freezing behavior of the water inside the pipe is dependent on the pipe material, pipe thickness, mechanical properties of the pipe, and the work hardening that was occurred in the previous experiments. It was also found that internal pressurization begins when the there is no more room inside the pipe to accommodate the expansion in the volume of the mixture of ice and water during the freezing stage. Sufficient heat should be provided to the pipe prior to reaching to the yielding point of the pipe when inelastic deformation occurs.

Given the necessity of supplying heat to protect the pipelines, heating systems should be employed to prevent ice accumulation, flow blockage, bulging, and ultimate failure of the pipes. In this regard, the feasibility of using a multi-layered coating-based heating system was studied. The reason for development of the heating system was the potential for achieving higher efficiency compared to the conventional tracers. To that end, the primary objective of this research was finding the materials with favorable electrical properties and developing the spraying parameters for deposition of the layers by using flame and cold spraying techniques. The feasibility of utilization of the multi-layered thermally-sprayed coatings as resistive heating systems for prevention of formation of ice within the pipes and protection of them against bursting was studied. It was found that the selected materials, namely alumina, as an electrically insulating layer, nickel-chromium, as a heating element, and copper, as an electrical contact, were satisfactory for the given Joule heating task.

The only challenge with deposition of the NiCr coating was its penetration into the insulating layer. This resulted in reduction in the effective thickness of the alumina coating, and therefore, the voltage at which the coating can be failed would be reduced. Although this was a drawback from electrical point of view, it can be viewed as an advantage from mechanical perspective thanks to the interlocking and enhanced adhesion between the coating layers. It was also observed that relatively low powers such as 20 W were sufficient to heat and melt the ice inside the bare 254-mm (10-inch) long, 51-mm (2-inch) diameter carbon steel pipe that was located in the cold room and was directly exposed to stagnant cold air at -25°C. This speaks to the high efficiency of the fabricated heating system.

Developing mathematical models to predict the transient temperature of the ice during the heating stage and the transient location of the solid-liquid interface during the melting stage was another objective of this research. The mathematical models were developed based on one-dimensional transient conduction theory for finite length-scale media. It was found that the results obtained from the model were in good agreement with the measurements from the heating experiments. Comparison of the predictions of the model and the data from the experiments shows that the model predicted the duration of ice heating to within 16%, 12%, and 15% of that which was measured from the experiments for supplied powers of 10 W, 20 W, and 40 W, respectively.

Aside from the improved performance of the coating systems, studying the economic feasibility of fabrication and utilization of the coating system was of interest. To that end, a data-intensive model was developed to compare the total costs associated with fabrication, installation, operation, and maintenance of multi-layered coatings with those of conventional heat tracers. Although the cost of the raw material for both heating systems are in the same order, the fabrication cost of the coating system is noticeably higher, which is due to the higher labor cost. However, the obtained results are based on the Eastern U.S. market values and the total cost associated with fabrication of the coating system could be more comparable to the tracers at regions where labor rate is relatively low. The results suggest that end-users must weigh the improved performance of the coating systems against the increased fabrication and installation costs for large-scale protection of steel pipes against bursting in industrial applications.

Chapter 7

Recommendations for Future Work

This research program has made significant contributions in the areas of fabrication of coating-based resistive heating systems, development of mathematical models for determination of the required times for heating and melting of the ice within the steel pipes, and assessment of techno-economic implications of fabrication and utilization of thermal-sprayed coatings for heating purpose. However, these themes can be further enhanced and expanded. Several recommendations for conducting further research in these areas can be provided as follows:

- The transient pressure of the enclosed freezing liquid inside the pipe can be determined by obtaining the temperature data from the heat transfer model and coupling it with the pressure values from the non-linear phase change curve of the phase diagram of water, the mechanical properties of the pipe, pipe geometry, and the work hardening that has already occurred during the previous loading/unloading cycles. The obtained pressure values can be related to strain by mathematical formulations. Then, the obtained strain values can be compared to the critical strain values to inform on the approximate time of rupture of pipes.
- In the fabrication of the coating-based heating systems, high-temperature thermal spray processes such as flame spraying, wire arc spraying, air plasma spraying, and high-velocity oxygen fuel spraying have been used. Fabrication of the heaters with cold-spray process offers many advantages over thermal spray for fabrication of heaters such as lower labor cost and reduced environmental impacts due to the absence of in-process combustion gases. Furthermore, the cold-sprayed coating would not penetrate into the

electrically insulating layer, and therefore, there would be no concern related to the decreased effective thickness of the insulating layer. The most important advantage of the cold-sprayed heaters is the extra design flexibility that can be achieved thanks to easier control on the length of the coating compared to its thickness when it is deposited in meander shape.

- Assessing the techno-economic implications of the coating-based heating system is of great importance because the economic feasibility and improved performance of the coatings are the determining factors in selection of the coating-based heaters for large scale industrial applications. Furthermore, optimizing the spraying parameters can result in denser, thicker, and more uniform coatings, especially for fabrication of the electrically insulating layer. This can result in reduction of the labor cost and make the coating system competitive to the conventional tracers from financial perspective.
- For utilization of the developed coating system in industry on mass scale, many environmental and technical factors should be taken into account. In the present thesis document, only economic considerations and electrical performance of the heating systems were assessed. Conducting a comprehensive life cycle analysis (LCA) is necessary to compare the environmental implications of both heating systems with one another before selecting one of them. It is well-known that LCA is a powerful tool to assess and quantify various environmental impacts of a process such as emissions to air and water, damage to the human health, damage to the ecosystem quality, and damage the resources. Furthermore, technical considerations such as corrosion resistance, wear resistance, vulnerability of the deposited coatings to possible damages during shipping and the necessity of deposition of a flexible polymer coating onto the heating element,

and on-site reparability in case of damage to the coating system could be the main focus of future studies.

- Some assumptions and simplifications were taken into account in the mathematical models that were developed based on one-dimensional transient heat conduction in cylindrical coordinates to predict the heating and melting times of the enclosed ice inside the pipe. A more accurate 3D modeling can be conducted by using CFD where the change in the volume of the ice during phase change and free convection inside the pipe due to the movement of the ice, which is caused by change in the density of the ice after transformation into water, can be simulated.
- Given the brittle nature of the ceramic layer (alumina) and the generation of thermal stresses due to positioning of this layer between two metallic layers, temperature cyclic loadings should be conducted at severe loading conditions to ensure the reliability of the developed coating system. Furthermore, it has been observed that formation of cracks would not impede the heating performance of the coating system. It only increases the electrical resistance of the heating element. The link between formation of cracks and the increase in the electrical resistance is an interesting topic that can be assessed by using a thermal imaging camera for capturing the formation of cracks and using a data logger for reading and collecting the transient electrical resistance values.
- A basic controlling unit, which was composed of a solid state relay, temperature controller, and a temperature sensor (surface thermocouple), was developed to control the heating performance of the coating system. Given the change in the electrical resistance of the heating element versus temperature, a more sophisticated controlling system can be developed that can automatically switch on and off the system based on

the electrical resistance readings from the coating-based heating element. This can bridge the gap between the passive functional coatings and the smart active coatings for the purpose of protection of pipelines against freezing and rupture.

References

[1] K.M. Smith, M.P. Van Bree, J.F. Grzetic, “Analysis and Testing of Freezing Phenomena in Piping Systems”, *Proceedings of the ASME 2008 International Mechanical Engineering Conference and Exposition*, Boston, Massachusetts, November 2008, pp. 123-128.

[2] D.B. Edwards, K.M. Smith, D.E. Duvall, J.F. Grzetic, “Analysis and Testing of Freezing Phenomena in Plastic Piping Systems”, *Proceedings of the ASME 2009 International Mechanical Engineering Conference and Exposition*, Lake Buena Vista, Florida, November 2009, pp. 201-206.

[3] E. Vine, E. Mills, A. Chen, “Energy-efficiency and renewable energy options for risk management and insurance loss reduction,” Energy, Vol. 25, Issue 2, 2000, pp.131-147.

[4] A. Carrns, “Avoiding Costly Home Damage from Winter’s Cold,” The New York Times, 02-Dec-2014.

[5] J. R. Gordon, “An Investigation into Freezing and Bursting Water Pipes in Residential Construction,” Research Report No. 96-1, Building Research Council, School of Architecture, University of Illinois at Urbana-Champaign, 2006, PP. 1-51.

[6] C. Sandberg, *et al.*, “Chapter B6: Heat Tracing of Piping Systems”, Piping Handbook, McGraw-Hill Education, 2000, pp. B.242-B243.

[7] Y. V. Deshmukh, Industrial Heating: Principles, Techniques, Materials, Applications, and Design, Boca Raton: Taylor & Francis, 2005, p. 358.

[8] C. Sandberg, *et al.*, "Panel discussion on electrical heat tracing," 1999 IEEE Power Engineering Society Summer Meeting. Conference Proceedings (Cat. No.99CH36364), Edmonton, Alta., Canada, 1999, pp. 900-903 vol.2.

[9] V. F. Petrenko, C. R. Sullivan, V. Kozlyuk, “Variable-resistance conductors (VRC) for power-line de-icing”, Cold Regions Science and Technology, Vol. 65, Issue 1, 2011, pp. 23-28.

[10] K. Zhang, B. Han, X. Yu, “Nickel particle based electrical resistance heating cementitious composites”, Cold Regions Science and Technology, Vol. 69, Issue 1, 2011, pp. 64-69.

[11] A. G. Mohammed, G. Ozgur, E. Sevkat, “Electrical resistance heating for deicing and snow melting applications: Experimental study”, Cold Regions Science and Technology, Vol. 160, 2019, pp. 128-138.

[12] O. Parent, A. Ilinca, “Anti-icing and de-icing techniques for wind turbines: Critical review”, Cold Regions Science and Technology, Vol. 65, Issue 1, 2011, pp. 88-96.

[13] C. J. Erickson, "Reliable and cost-effective electrical heating of pipelines with self-regulating heating cables," in IEEE Transactions on Industry Applications, Vol. 24, No. 6, pp. 1089-1095, Nov.-Dec. 1988.

[14] B. C. Johnson and J. E. Propst, "Technological advancement in self-limiting electric heat tracing cables, in Industrial Applications Society 35th Annual Petroleum and Chemical Industry Conference, Dallas, TX, 1988, pp. 9-13.

[15] D. Michels, J. Hadeler, and J.H. Lienhard, High-Heat-Flux Resistance Heaters From VPS and HVOF Thermal Spraying, Exp. Heat Transf., 1998, 11(4), p 341-359.

[16] A. Killinger and R. Gadow, “Thermally Sprayed Coating Composites for Film Heating Devices”, Advances in Science and Technology, Vol. 45, 2006, pp. 1230-1239.

[17] M. Prudenziati, “Development and the Implementation of High-Temperature Reliable Heaters in Plasma Spray Technology”, J. Therm. Spray Technol., Vol. 17, Issue 2, 2008, pp. 234-243.

[18] M. Floristan, R. Fontarnau, A. Killinger, and R. Gadow, Development of Electrically Conductive Plasma Sprayed Coatings on Glass Ceramic Substrates, Surf. Coat. Technol., 2010, 205(4), p 1021-1028

[19] J. Lamarre et al, "Performance Analysis and Modeling of Thermally Sprayed Resistive Heaters," J. Therm. Spray Technol., Vol. 22, (6), 2013, pp. 947-953.

[20] A. Lopera-Valle and A. McDonald, “Application of flame-sprayed coatings as heating elements for polymer-based composite structures”, J. Thermal Spray Technol., Vol. 24, Issue 7, 2015, pp. 1289-1301.

[21] D. H. Harris et al, "Polycrystalline Ferrite Films for Microwave Applications Deposited by Arc Plasma," J. Appl. Phys., vol. 41, (3), pp. 1348-1349, 1970.

[22] R. T. Smyth and J. C. Anderson, "Production of Resistors by Arc Plasma Spraying," ElectroComponent Science and Technology, vol. 2, (2), pp. 135-145, 1975.

[23] S. Sampath et al, "Thermal Spray Techniques for Fabrication of Meso-Electronics and Sensors," MRS Proceedings, vol. 624, pp. 181, 2000.

[24] H. Herman, S. Sampath and R. McCune, "Thermal Spray: Current Status and Future Trends," MRS Bull, vol. 25, (7), pp. 17-25, 2000.

[25] H. F. Younis, R. S. Dahbura and J. H. Lienhard V, "Thin film resistance heaters for high heat flux jet-array cooling experiments," vol. 353, pp. 127-134, 1997.

[26] D. Michels, J. Hadeler and J. H. Lienhard V, "high-heat-flux resistance heaters from VPS and HVOF thermal spraying," Exp. Heat Transfer, vol. 11, (4), pp. 341-359, 1998.

[27] L. Pawłowski, "The relationship between structure and dielectric properties in plasma-sprayed alumina coatings," Surface and Coatings Technology, vol. 35, (3), pp. 285-298, 1988.

[28] R. Luo et al, "Structure and electrical insulation characteristics of plasma-sprayed alumina coatings under pressure," Ceramics International, vol. 44, (6), pp. 6033-6036, 2018.

[29] F. Toma et al, "Comparative Study of the Electrical Properties and Characteristics of Thermally Sprayed Alumina and Spinel Coatings," J. Therm. Spray Technol., vol. 20, (1), pp. 195-204, 2011.

[30] B. Yan et al, "Water Adsorption and Surface Conductivity Measurements on -Alumina Substrates," vol. 10, pp. 247-251, 1987.

[31] F. Toma et al, "Comparison of the Microstructural Characteristics and Electrical Properties of Thermally Sprayed Al_2O_3 Coatings from Aqueous Suspensions and Feedstock Powders," J. Therm. Spray Technol., vol. 21, (3), pp. 480-488, 2012.

[32] C. C. Stahr et al, "Dependence of the Stabilization of α-Alumina on the Spray Process," J. Therm. Spray Technol., vol. 16, (5), pp. 822-830, 2007.

[33] M. Plummer, "The formation of metastable aluminas at high temperatures," J. Appl. Chem., vol. 8, (1), pp. 35-44, 1958.

[34] R. McPherson, "Formation of metastable phases in flame- and plasma-prepared alumina," J. Mater. Sci., vol. 8, (6), pp. 851-858, 1973.

[35] H. G. Wang and H. Herman, "Plasma-sprayed cordierite: Dielectric and electrical properties," Surface and Coatings Technology, vol. 37, (3), pp. 297-303, 1989.

[36] H. G. Wang, G. S. Fischman and H. Herman, "Plasma-sprayed cordierite: structure and transformations," J. Mater. Sci., vol. 24, (3), pp. 811-815, 1989.

[37] S. Sampath, "Thermal Spray Applications in Electronics and Sensors: Past, Present, and Future," J. Therm. Spray Technol., vol. 19, (5), pp. 921-949, 2010.

[38] L. Gołonka and L. Pawłowski, "Ceramic on Metal Substrates Produced by Plasma Spraying for Thick Film Technology," ElectroComponent Science and Technology, vol. 10, (2-3), pp. 143-150, 1981.

[39] H. Kim et al, "The electrical insulation behavior and sealing effects of plasma-sprayed alumina–titania coatings," Surface and Coatings Technology, vol. 140, (3), pp. 293-301, 2001.

[40] A. Killinger and R. Gadow, "Thermally Sprayed Coating Composites for Film Heating Devices," Advances in Science and Technology, vol. 45, pp. 1230-1239, 2006.

[41] T. Tong et al, "Ultrafast laser micromachining of thermal sprayed coatings for microheaters: design, fabrication and characterization," Sensors and Actuators A: Physical, vol. 114, (1), pp. 102-111, 2004.

[42] M. Prudenziati, G. Cirri and P. Dal Bo, "Novel high-temperature reliable heaters in plasma spray technology," J. Therm. Spray Technol., vol. 15, (3), pp. 329-331, 2006.

[43] M. Prudenziati, "Development and the Implementation of High-Temperature Reliable Heaters in Plasma Spray Technology," J. Therm. Spray Technol., vol. 17, (2), pp. 234-243, 2008.

[44] M. Prudenziati and M. L. Gualtieri, "Electrical Properties of Thermally Sprayed Ni- and Ni20Cr-Based Resistors," J. Therm. Spray Technol., vol. 17, (3), pp. 385-394, 2008.

[45] J. Lamarre et al, "Performance Analysis and Modeling of Thermally Sprayed Resistive Heaters," J. Therm. Spray Technol., vol. 22, (6), pp. 947-953, 2013.

[46] A. Lopera-Valle and A. McDonald, "Application of Flame-Sprayed Coatings as Heating Elements for Polymer-Based Composite Structures," J. Therm. Spray Technol., vol. 24, (7), pp. 1289-1301, 2015.

[47] A. Lopera-Valle and A. McDonald, "Flame-sprayed coatings as de-icing elements for fiber-reinforced polymer composite structures: Modeling and experimentation," International Journal of Heat and Mass Transfer, vol. 97, pp. 56-65, 2016.

[48] G. Poots, "On the application of integral-methods to the solution of problems involving the solidification of liquids initially at the fusion temperature", *Int. J. Heat Mass Transfer*, Vol. 5, pp. 525-531, 1962.

[49] J. Muehlbauer, J. Sunderland, "Heat conduction with freezing or melting", *Appl.Mech. Rev.*, Vol. 18, pp.951-959, 1965.

[50] Q. Pham, "Extension to Planck's equation for predicting freezing times of foodstuffs of simple shapes", *Int. J. Refrig.*, Vol. 7, pp. 377-383, 1984.

[51] D. Cleland, A. Cleland, R. Earle, S. Byrne, "Prediction rates of freezing, thawing, and cooling in solids of arbitrary shape using a finite element method", *Int. J. Refrig.*, Vol. 7, pp. 6-13, 1984.

[52] A. McDonald, B. Bschaden, E. Sullivan and R. Marsden, "Mathematical simulation of the freezing time of water in small diameter pipes", Applied Thermal Engineering, Vol. 73, Issue 1, 2014, pp. 142-153.

[53] E. Sullivan and A. McDonald, "Freezing time of water in small diameter tubes and pipes in residential and commercial HVAC applications", in Proceedings of The Canadian Society

for Mechanical Engineering International Congress, Toronto, ON, Canada, June 2014, 6 pages on compact disk.

[54] T. Yan, X. Xu, D. Qiu and W. Gang, “A Quasi-Steady-State Simplified Model for Pipe-encapsulated PCM”, Procedia Engineering, 2017, pp. 3243-3250.

[55] T.W. Brakel, J.P.F. Charpin, T.G. Myers, “One-dimensional ice growth due to incoming supercooled droplets impacting on a thin conducting substrate”, Int. J. Heat Mass Transfer, Vol. 50, Issues 9-10, 2007, pp. 1694-1705.

[56] Z.A. Janjua, B. Turnbull, S. Hibberd, K. Choi, “Mixed ice accretion on aircraft wings”, Physics of Fluids, Vol. 30, Issue 2, 2018, p. 027101.

[57] X. Zhang, X. Wu, J. Min, “Aircraft icing model considering both rime ice property variability and runback water effect”, Int. J. Heat Mass Transfer, Vol. 104, 2017, pp. 510-516.

[58] D. Yanxia, G. Yewei, X. Chunhua, Y. Xian, “Investigation on heat transfer characteristics of aircraft icing including runback water”, Int. J. Heat Mass Transfer, Vol. 53, Issues 19-20, 2010, pp. 3702-3707.

[59] F. Simba, L. Trojer, B. Mwinyiwiwa, N. Mvungi, E. Mjema, “Techno-economic analysis of UMTS900 and UMTS2100 for rural connectivity in Tanzania”, International Conference on Communication Technology Proceedings, ICCT, 2012, p. 10–15.

[60] R. A. Haylock, “Life-cycle assessment, techno-economic analysis, and statistical modeling of bio-based materials and processes”, M.Sc. Dissertation, Iowa State university, 2016.

[61] S. Parsons, “Interpreting life cycle assessment for decision-making on emerging materials”, Doctoral thesis, University of Surrey, 2016.

[62] G. Finnveden, *et al.*, “Recent developments in Life Cycle Assessment”, Journal of Environmental Management, (91), 2009, p. 1–21.

[63] P. D. Lavappa and J. D. Kneifel, “Energy Price Indices and Discount Factors for Life-Cycle Cost Analysis”, NIST Interagency/Internal Report (NISTIR) - 85-3273-30, 2015.

[64] R. Petter, W.E. Tyner, "Technoeconomic and Policy Analysis for Corn Stover Biofuels”, ISRN Economics, Article ID 515898, 13 pages, 2014.

[65] T.M. Knoll, “Techno-Economic Modelling of Mobile Access Network Alternatives”, ITG 5.2.4 Meeting. Berlin, 2012.

[66] P.L. Fauchais, J.V.R. Heberlein, M.I. Boulos, “Industrial Applications of Thermal Spraying Technology”, In: Thermal Spray Fundamentals. Springer, Boston, MA, 2014.

[67] G.C. Glatzmaier, J.C. Gomez, "Determining the Cost Benefit of High-Temperature Coatings for Concentrating Solar Power Thermal Storage Using Probabilistic Cost Analysis", Journal of Solar Energy Engineering, Vol. 137, pp. 041006, 2015.

[68] R. R. Gilpin, "The effects of dendritic ice formation in water pipes", Int. J. Heat Mass Transf., vol. 20, 1977, pp. 693–699.

[69] R.R. Gilpin, "The influence of natural convention on dendritic ice growth", J. Cryst. Growth, vol. 36, 1976, pp. 101–108.

[70] M. Choukroun and O. Grasset, "Thermodynamic model for water and high-pressure ices up to 2.2GPa and down to the metase domain", J. Chem. Phys., vol. 127, 2007, p. 124506.

[71] ASTM A106/A106M-13, "Standard Specification for Seamless Carbon Steel Pipe for High-Temperature Service", ASTM International, West Conshohocken, PA, 2013, p. 3.

[72] ASTM A333/A333M-11, "Standard Specification for Seamless and Welded Steel Pipe for Low-Temperature Service", ASTM International, West Conshohocken, PA, 2011, p. 3.

[73] PVRC Recommendations on Toughness Requirements for Ferritic Materials, WRC Bulletin 175, Welding Research Council, 1972.

[74] W.T. Becker, Fracture Appearance and Mechanisms of Deformation and Fracture, Failure Analysis and Prevention, vol. 11, ASM Handbook, ASM International, Materials Park, Ohio, 2002, pp. 1162–1327.

[75] H. Huang and L. Xue, "Prediction of slant ductile fracture using damage plasticity theory", Int. J. Press. Vessels Pip., vol. 86, 2009, pp. 319–328.

[76] S.A. El-Naaman and K.L. Nielsen, "Observations on Mode I ductile tearing in sheet metals", Eur. J. Mech. A/Solid, vol. 42, 2013, pp. 54–62.

[77] K.L. Nielsen and J.W. Hutchinson, "Cohesive traction–separation laws for tearing of ductile metal plates", Int. J. Impact Eng., vol. 48, 2012, pp. 15–23.

[78] Oerlikon Metco, Material Product Data Sheet: DSMTS-0005.6 – Aluminum Oxide Thermal Spray Powders, Oerlikon Metco, Westbury, 2017, p. 1.

[79] Praxair Surface Technologies Inc., Powder Solutions Catalog, Indianapolis, 2014, p. 17.

[80] Praxair Surface Technologies Inc., Powder Solutions Catalog, Indianapolis, 2014, p. 12.

[81] Oerlikon Metco, Material Product Data Sheet: DSMTS-0109.2 – Nickel - 20% chromium powders for thermal spray, Oerlikon Metco, Westbury, 2017, p. 1.

[82] Centerline (Windsor) Limited, Technical Data Sheet: SST-TDS-C5003-PR-1.3-0415– commercial copper powder, Windsor, Ontario, 2017, p. 1.

[83] H. Ashrafizadeh, *et al.*, "Deposition of Electrically Conductive Coatings on Castable Polyurethane Elastomers by the Flame Spraying Process," J. Therm. Spray Technol., Vol. 25, No. 3 (2016), pp. 419-430.

[84] K. Bobzin, *et al.*, "Temperature distribution on thermally sprayed heating conductor coatings", IOP Conf. Ser.: Mater. Sci. Eng. 480 012002, 2019.

[85] P. Auerkari, Mechanical and Physical Properties of Engineering Alumina Ceramics, Espoo: Technical Research Centre of Finland, 1996.

[86] Nickel-Chromium Alloys (NiCr) Properties, Reade International Corp., https://www.reade.com/products/nickel-chromium-alloys-nicr.

[87] 99.5% Alumina Material Properties, Accuratus Ceramic Corporation, https://accuratus.com/pdf/995aluminaprops.pdf.

[88] Thermo-physical Properties of Carbon Steel Pipes, Greenline Pipe and Fitting, http://greenlinepipe.com/pipes/carbonsteel-pipe.html.

[89] ASHRAE. 2005 ASHRAE Handbook of Fundamentals, American Society of Heating, Refrigeration, and Air-conditioning Engineers, Atlanta, 2005, p. 25.2, 26.15.

[90] L.M. Jiji, Heat Conduction, third edition. Berlin: Springer, 2009, p. 34.

[91] T. L. Bergman, A. S. Lavine, F. P. Incropera, D. P. DeWitt, "Fundamentals of heat and mass transfer", seventh edition. NJ: John Wiley & Sons, Inc., 2011, pp. 136-138.

[92] American Society of Heating, Refrigeration, and Air-conditioning Engineers, ASHRAE Standard 90.1 – Energy Standard for Buildings except Low-rise Residential Buildings, American Society of Heating, Refrigeration, and Air-conditioning Engineers, Atlanta, 2013, pp. 81.

[93] T. L. Bergman, A. S. Lavine, F. P. Incropera, D. P. DeWitt, "Fundamentals of heat and mass transfer", seventh edition. NJ: John Wiley & Sons, Inc., 2011, pp. 136-138.

[94] H. Perkins, G. Leppert, "Local heat-transfer coefficients on a uniformly heated cylinder", Int. J. Heat Mass Transfer, Vol. 7, Issue 2, 1964, 143-158.

[95] W. Robinson, L. Han, R. Essig, C. Heddleson, "Heat transfer and pressure drop data for circular cylinders in ducts and various arrangements", Report 41 ASTIA ATI 128 961, Ohio State University Research Foundation, 1951, pp. 1-94.

[96] L.M. Jiji, Heat Conduction, third edition. Berlin: Springer, 2009, p. 74.

[97] L.M. Jiji, Heat Conduction, third edition. Berlin: Springer, 2009, p. 102.

[98] M. Akyurt, G. Zaki, B. Habeebullah, “Freezing phenomena in ice-water systems”, Energy Convers. Manag., Vol. 43, Issue 14, 2002, pp. 1773-1789.

[99] G. Cinelli, An extension of the finite Hankel transform and applications, Int. J. Eng. Sci., Vol. 3, 1965, pp. 539–559.

[100] A. Bejan and A. D. Kraus. Heat transfer handbook. New York: J. Wiley, 2003, p. 957.

[101] A. Mahdavi, A. McDonald, “Analytical study of the heat transfer coefficient of the impinging air jet during cold spraying”, Int. J. Thermal Sci., Vol. 130, 2018, 289 – 297.

[102] J. Willoughby, 30 - Insulation, In plant engineer's reference book (Second Edition), edited by Dennis A. Snow, Butterworth-Heinemann, Oxford, 2002, Pages 30/10-30/11.

[103] A. Labbani Motlagh, High performance modular insulating panel development for a reefer van, Master’s Thesis, Simon Fraser University, 2016.

[104] E. Utochkina, Heat insulation materials from environmental aspect, Bachelor’s Thesis, Saimaa University of Applied Sciences, Lappeenranta, 2014.

[105] F. Domínguez-Muñoz, B. Anderson, J.M. Cejudo-López, A. Carrillo-Andrés, “Uncertainty in the thermal conductivity of insulation materials”, Eleventh International IBPSA Conference, Glasgow, Scotland, July 2009, pp. 1008-1013.

[106] J.R. Taylor, An introduction to error analysis: the study of uncertainties in physical measurements, second ed., University Science Books, Herndon, VA, 1996.

[107] D.W. Hahn and M. Necati Özişik, Heat Conduction, third edition, John Wiley & Sons, Inc., 2012, p. 453.

[108] L.M. Jiji, Heat Conduction, third edition. Berlin: Springer, 2009, pp. 189-191.

[109] M. Sadd and J. Didlake, “Non-Fourier melting of a semi-infinite solid”, J. Heat Transfer, Vol. 99, Issue 1, 1977, pp. 25-28.

[110] K.R. Sharma, “Comparison of Solutions from Parabolic and Hyperbolic Models for Transient Heat Conduction in Semi-Infinite Medium”, Int. J. Thermophys, Vol. 30, 2009, pp. 1671–1687.

[111] D.W. Tang, N. Araki, “Non-fourier heat conduction in a finite medium under periodic surface thermal disturbance”, Int. J. Heat Mass Transfer, Vol. 39, Issue 8, 1996, pp. 1585-1590.

[112] 3M, Self-Regulating Heat Tracing Cables for Commercial Buildings: 1507-01878e, 3M Electrical Product Division, London, ON, Canada, 2015, p. 8.

[113] Comparison of Electricity Prices in Major North American Cities, Hydro-Québec, 2017. Available at: http://www.hydroquebec.com/documents-data/official-publications.

[114] https://tradingeconomics.com/united-states/inflation-cpi.

[115] S. Lloyd, R. Ries, "Characterizing, Propagating, and Analyzing Uncertainty in Life-Cycle Assessment: A Survey of Quantitative Approaches", Journal of Industrial Ecology, Vol. 11, Issue 1, pp. 161-179, 2007.

[116] J. L. Lardear, "Control of self-regulating heating cable for use in pipeline heating applications", *37th Annual Conference on Petroleum and Chemical* Industry, Houston, TX, USA, 1990, pp. 105-113.

[117] M. Ducos, "Evaluating the costs of thermal spraying", ALIDERTE course (in French). ALIDERTE, Limoges, 2006.

[118] R. Molz, D. Hawley, "A method of evaluating thermal spray process performance", In: *Thermal spray 2007: Global coating solutions*. ASM International, Materials Park, OH, e-Proc, 2007.

[119] A. Moign, A. Vardelle, J.G. Legoux, N.J. Themelis, "LCA Comparison of Electroplating and Other Thermal Spray Processes", in: *International Thermal Spray Conference*, May 4-7, 2009, Las Vegas, NV, USA.

[120] A. Moign, A. Vardelle, N.J. Themelis, J.G. Legoux, "Life cycle assessment of using powder and liquid precursors in plasma spraying: The case of yttria-stabilized zirconia", *Surface and Coatings Technology*, Volume 205, Issue 2, 2010, pp. 668-673.

[121] C. Sandberg, G. Kuse, N.R. Rafferty, W.E. McBride, "Secondary factors in electrical heat tracing design", *Proceedings of 1996 IAS Petroleum and Chemical Industry Technical Conference*, Philadelphia, PA, USA, 1996, pp. 237-245.